



**HAL**  
open science

# Multi-scale modelling and simulations of the cbemo-mechanical behaviour of degraded cement-based materials

Eric Stora

► **To cite this version:**

Eric Stora. Multi-scale modelling and simulations of the cbemo-mechanical behaviour of degraded cement-based materials. Structural mechanics [physics.class-ph]. Université de Paris Est, 2007. English. NNT: . tel-03674716

**HAL Id: tel-03674716**

**<https://theses.hal.science/tel-03674716>**

Submitted on 20 May 2022

**HAL** is a multi-disciplinary open access archive for the deposit and dissemination of scientific research documents, whether they are published or not. The documents may come from teaching and research institutions in France or abroad, or from public or private research centers.

L'archive ouverte pluridisciplinaire **HAL**, est destinée au dépôt et à la diffusion de documents scientifiques de niveau recherche, publiés ou non, émanant des établissements d'enseignement et de recherche français ou étrangers, des laboratoires publics ou privés.

UNIVERSITE PARIS-EST

Année 2007

THESE

pour obtenir le grade de

DOCTEUR DE L'UNIVERSITE PARIS-EST

Discipline : Génie Civil

présentée par

Eric STORA

Titre :

**Modélisation multi-échelle et simulations du comportement chimie-  
mécanique des matériaux cimentaires dégradés.**

Multi-scale modelling and simulations of the chemo-mechanical behaviour of  
degraded cement-based materials.

soutenue le 5 décembre 2007

devant le jury composé de

|                    |                    |
|--------------------|--------------------|
| J. van der Lee     | Président          |
| D. Kondo           | Rapporteur         |
| G. Pijaudier-Cabot | Rapporteur         |
| B. Bary            | Examineur          |
| Q.-C. He           | Directeur de thèse |

## ABSTRACT

The assessment of the durability of cement-based materials, which can be employed in underground structures for nuclear waste disposal, requires accounting for deterioration factors, such as chemical attacks and damage, and for the interactions between these phenomena. The resistance of cement-based materials to these degradations is strongly conditioned by their mechanical and diffusive macroscopic properties. The first purpose of the thesis consists in building a multi-scale approach and an orthotropic damage model to estimate these properties and their evolution during chemical deterioration processes. The second objective is to perform simulations of chemo-mechanical degradations of leached cementitious materials to predict their long-term behavior. Starting from a non-exhaustive review of analytical homogenization techniques, new models, like the mixed composite spheres assemblage estimate, are proposed by revisiting the theories of Hashin and Shtrikman (1962) and of double-inclusion type schemes. A realistic multi-scale homogenization approach is then developed and validated for cement pastes and mortars. Simulations of chemo-mechanical degradations of leached cementitious materials are subsequently carried out by implementing these models into the platform ALLIANCES. The numerical results confronted with experimental tests give valuable information in terms of the material durability.

**Keywords:** cement-based materials; mechanical and diffusive properties; multi-scale homogenization; damage; leaching; coupled chemo-mechanical degradations.

## RESUME

L'évaluation de la durabilité des matériaux cimentaires utilisables dans les structures d'entreposage de déchets nucléaires nécessite la prise en compte de facteurs de détérioration, tels que les attaques chimiques ou la fissuration, ainsi que des interactions entre ces phénomènes. La résistance des matériaux cimentaires à ces dégradations est fortement conditionnée par leurs propriétés mécaniques et diffusives macroscopiques. Le premier objectif de la thèse vise à construire une approche multi-échelle et un modèle d'endommagement orthotrope pour estimer ces propriétés ainsi que leurs évolutions au cours de processus de détériorations chimiques. Le second est de réaliser des simulations de dégradations couplées chimie-mécanique de matériaux cimentaires lixiviés afin d'étudier leur comportement à long terme. Après une synthèse non exhaustive consacrée aux techniques d'homogénéisation analytique, de nouveaux modèles, tels que l'estimation par assemblage mixte de sphères composites, sont proposés en revisitant les théories d'Hashin et Shtrikman (1962) et les méthodes de type double-inclusion. Une approche d'homogénéisation multi-échelle est ensuite développée pour les pâtes de ciment et les mortiers et validée. Des simulations de dégradations couplées chimie-mécanique de matériaux cimentaires lixiviés sont enfin effectuées en implémentant les modèles développés précédemment au sein de la plateforme numérique ALLIANCES. Les résultats numériques confrontés avec des essais expérimentaux donnent des informations utiles concernant la durabilité de ces matériaux.

**Mots clés:** matériaux cimentaires; propriétés mécaniques et diffusives; homogénéisation multi-échelle; endommagement; lixiviation; dégradations couplées chimie-mécanique.

# CONTENTS

## 1 GENERAL INTRODUCTION

### Part I. PRESENTATION OF CEMENT-BASED MATERIALS

|   |    |
|---|----|
| 2 MICROSTRUCTURE AND PHYSICAL PROPERTIES OF CEMENT-BASED MATERIALS .....                              | 4  |
| 2.1 Presentation of the multi-scale microstructure of cement-based materials .....                    | 4  |
| 2.1.1 Microstructure of cement pastes .....   | 4  |
| 2.1.2 Microstructure of mortars and concretes.....  | 14 |
| 2.2 Microscopic and macroscopic properties of cement-based materials.....                             | 14 |
| 2.2.1 Information on the elastic properties of the HCP elementary phases .....                        | 14 |
| 2.2.2 Elastic properties of HCP.....  | 16 |
| 2.2.3 Elastic properties of mortars and concretes.....  | 17 |
| 2.2.4 Transport properties of cement-based materials .....  | 18 |
| 3 DEGRADATIONS OF CEMENT-BASED MATERIALS SUBJECTED TO LEACHING .....                                  | 19 |
| 3.1 Chemical deterioration of cementitious materials caused by leaching .....                         | 20 |
| 3.2 Experimental insights on the chemo-mechanical degradation of leached cement-based materials ..... | 23 |
| 3.2.1 Impact of leaching on the residual mechanical behaviour .....                                   | 23 |
| 3.2.2 Influence of damage on the leaching process.....  | 24 |
| 3.2.3 Fully coupled experiments .....   | 25 |

### Part II. PREDICTION OF THE EFFECTIVE ELASTIC PROPERTIES OF CEMENT-BASED MATERIALS

|  |    |
|--|----|
| 4 INTRODUCTION TO EFFECTIVE-MEDIUM THEORIES (EMTS).....  | 28 |
| 4.1 Fundamental principles of homogenization methods.....  | 28 |
| 4.1.1 General principles of homogenization methods.....  | 28 |
| 4.1.2 Presentation of the Eshelby problem.....   | 30 |
| 4.2 Presentation of some classical matrix-inclusion type EMTs .....  | 34 |
| 4.2.1 Dilute approximation.....  | 35 |
| 4.2.2 MT approximation.....  | 35 |
| 4.2.3 Generalized self-consistent scheme (GSCS).....   | 36 |
| 4.3 Presentation of double-inclusion type models .....   | 37 |
| 4.3.1 Interaction Direct Derivative (IDD) model.....   | 38 |
| 4.3.2 The Hori and Nemat-Nasser double-inclusion model (DIM) .....   | 39 |
| 4.3.3 Other double-inclusion type models .....   | 47 |
| 4.3.4 Development of a modified DIM for composites with coated spherical inclusions.....                   | 50 |
| 4.4 Accuracy of EMTs .....   | 52 |
| 4.4.1 Review on the accuracy of EMTs .....   | 53 |
| 4.4.2 Comparison with numerical simulations on cement-based materials .....                                | 53 |
| 4.5 Conclusion of chapter 4.....   | 56 |
| 5 INFLUENCE OF INCLUSION SHAPE ON THE LINEAR ELASTIC EFFECTIVE PROPERTIES OF HCP (Stora et al. 2006a)..... | 58 |
| 5.1 Definition of a shape parameter for the inclusions .....   | 59 |
| 5.2 Significance of the shape parameter for HCP elastic properties .....                                   | 65 |
| 5.3 Approximation of the particulate phases by spheroidal inclusions.....                                  | 67 |
| 5.3.1 Assessment of the spherical particle assumption .....  | 68 |

|       |   |    |
|-------|---|----|
| 5.4   | Conclusions of chapter 5 .....  | 74 |
| 6     | CONSTRUCTION OF A MULTI-SCALE HOMOGENIZATION MODEL FOR ESTIMATING THE ELASTIC PROPERTIES OF CEMENT-BASED MATERIALS..... | 75 |
| 6.1   | A multi-scale approach for estimating the elastic effective properties of HCP .....                                     | 75 |
| 6.1.1 | Review of the existing micromechanical models for cement pastes.....  | 75 |
| 6.1.2 | Construction of a multi-scale homogenization model for HCP .....  | 76 |
| 6.1.3 | Predictions of the elastic properties of sound and leached HCP.....   | 78 |
| 6.2   | A multi-scale approach for estimating the effective elastic properties of mortars .....                                 | 82 |

### **Part III. PREDICTION OF THE MACROSCOPIC DIFFUSIVITIES OF CEMENTITIOUS MATERIALS**

|       |   |     |
|-------|---|-----|
| 7     | REVIEW OF MATRIX-INCLUSION TYPE EMTS FOR PREDICTING THE DIFFUSIVITIES OF POROUS MEDIA .....                                   | 91  |
| 7.1   | Fundamental principles of matrix-inclusion type EMTs.....   | 91  |
| 7.1.1 | General principles of homogenization methods.....   | 91  |
| 7.1.2 | Presentation of the Eshelby problem.....  | 92  |
| 7.2   | Basic expressions of EMTs for estimating macroscopic diffusivities .....  | 95  |
| 7.2.1 | Classical matrix-inclusion type estimates .....   | 95  |
| 7.2.2 | Double-inclusion type schemes.....  | 96  |
| 7.3   | Significant microstructural parameters from the viewpoint of diffusion.....   | 100 |
| 7.3.1 | Importance of the percolation of the diffusive phase.....   | 100 |
| 7.3.2 | Importance of other microstructural indicators .....  | 102 |
| 7.4   | Review of matrix-inclusion type EMTs from the viewpoint of connectivity and percolation .....                                 | 103 |
| 8     | REVIEW AND DEVELOPMENT OF OTHER HOMOGENIZATION THEORIES FOR PREDICTING THE DIFFUSIVITIES OF POROUS MEDIA.....                 | 105 |
| 8.1   | Review of bounding approaches .....   | 105 |
| 8.2   | Review of SC type schemes .....   | 108 |
| 8.3   | Mixed composite spheres assemblage (MCSA) estimate (Stora et al. 2006b) .....   | 112 |
| 8.3.1 | Presentation of the estimate.....   | 112 |
| 8.3.2 | Signification and interpretation of the MCSA parameter .....  | 118 |
| 8.3.3 | Comparisons with other EMTs .....   | 119 |
| 8.4   | Conclusions of chapter 8.....   | 122 |
| 9     | CONSTRUCTION OF A MULTI-SCALE HOMOGENIZATION MODEL FOR ESTIMATING THE EFFECTIVE DIFFUSIVITIES OF CEMENT-BASED MATERIALS ..... | 123 |
| 9.1   | Multi-scale description of HCP microstructure .....   | 124 |
| 9.2   | Three-step homogenization process .....   | 125 |
| 9.3   | Estimations of the effective diffusivities of HCP.....  | 127 |
| 9.3.2 | Evaluation of the macroscopic diffusion coefficients of leached HCP.....  | 131 |
| 9.4   | Estimations of the macroscopic diffusive properties of mortars.....   | 133 |

### **Part IV. MODELLING OF DAMAGE OF CEMENTITIOUS MATERIALS**

|        |  |     |
|--------|--|-----|
| 10     | DEFINITION OF STATE VARIABLES .....                                | 141 |
| 11     | MICROMECHANICAL ESTIMATIONS OF THE DAMAGED MATERIAL BEHAVIOR ..... | 142 |
| 11.1   | General presentation.....  | 142 |
| 11.2   | Comparison of the homogenization schemes in simple cases.....      | 144 |
| 11.2.1 | Comparison for a material with aligned cracks.....                 | 144 |
| 11.2.2 | Comparison for an isotropic damaged material .....                 | 149 |

|        |  |            |
|--------|--|------------|
| 11.2.3 | Comparison for an orthotropic damaged material.....  | 150        |
| 11.3   | Link between the macroscopic behavior and the number of microcracks .....                        | 152        |
| 11.4   | Conclusion of the chapter 9.....   | 154        |
| 12     | <b>ESTABLISHMENT OF THE EVOLUTION LAWS.....</b>  | <b>155</b> |
| 12.1   | Criteria based on the generalized standard materials (GSM) formalism .....                       | 155        |
| 12.1.1 | Presentation of the GSM formalism.....   | 156        |
| 12.1.2 | Application of the GSM formalism for quasi-brittle materials .....                               | 156        |
| 12.1.3 | Development of evolution laws adopting the GSM formalism.....                                    | 157        |
| 12.1.4 | Application in the case of multi-axial tension tests.....  | 159        |
| 12.2   | Strain-based criteria.....   | 163        |
| 12.2.1 | Review of strain-based criteria.....   | 163        |
| 12.2.2 | Review of the Mazars model.....  | 164        |
| 12.2.3 | Definition of a strain-based evolution law for the micromechanically-based<br>damage model ..... | 166        |
| 12.2.4 | Positivity of the intrinsic dissipation.....   | 168        |
| 12.2.5 | Application in the case of multi-axial tension tests.....  | 169        |
| 12.3   | Conclusions of chapter 12 .....  | 172        |

## **Part V. MODELLING AND NUMERICAL SIMULATIONS OF THE CHEMO-MECHANICAL DEGRADATIONS OF CEMENTITIOUS MATERIALS**

|        |  |            |
|--------|--|------------|
| 13     | <b>MODELLING AND SIMULATIONS OF THE CHEMICAL DEGRADATION<br/>WITH ALLIANCES PLATFORM .....</b>         | <b>176</b> |
| 13.1   | Presentation of ALLIANCES.....   | 176        |
| 13.1.1 | Coupled chemical-transport problem solved by ALLIANCES .....   | 177        |
| 13.2   | Simulations of the decalcification of cement pastes .....  | 182        |
| 13.2.1 | System considered.....   | 182        |
| 13.2.2 | Input data.....  | 182        |
| 13.2.3 | Influence of the diffusion law on the chemical degradation .....                                       | 185        |
| 13.2.4 | Influence of the composition of cement pastes on the chemical degradation .....                        | 191        |
| 13.2.5 | Influence of the aggressive solution on the chemical degradation.....                                  | 193        |
| 13.2.6 | Improving the leaching simulations by adjusting the parameters of the<br>homogenization model .....    | 195        |
| 13.3   | Conclusions of chapter 13.....   | 199        |
| 14     | <b>SIMULATIONS OF THE CHEMO-MECHANICAL DEGRADATIONS BY<br/>LEACHING OF CEMENT-BASED MATERIALS.....</b> | <b>200</b> |
| 14.1   | Stiffness reduction of cement-based materials after leaching .....                                     | 200        |
| 14.2   | Simulations of the mechanical residual resistance tests on cement-based materials ...<br>.....         | 201        |
| 14.2.1 | Tensile tests on uniformly leached specimens .....   | 201        |
| 14.2.2 | Three-points flexion tests .....   | 203        |
| 15     | <b>GENERAL CONCLUSIONS AND PERSPECTIVES .....</b>  | <b>213</b> |
| 15.1   | Main conclusions.....  | 214        |
| 15.2   | Proposals for future research.....   | 215        |
| 15.3   | Perspectives .....   | 218        |

## NOMENCLATURE FOR MECHANICS

|                    |  |
|--------------------|--|
| $a_r$              | radius of the circular base of the spheroid representing particulate phase $r$   |
| $a_i$              | maximum axis of the degenerated spheroid representing type $i$ microcracks       |
| $A$                | area   |
| $b_r$              | radius of the revolution axis of the spheroid representing particulate phase $r$ |
| $c_r$              | volume fractions of phase $r$  |
| $d_i$              | damage scalar of the family $i$ of microcracks                                   |
| Dis                | intrinsic dissipation  |
| $E_r$              | Young modulus of phase $r$   |
| $f$                | damage threshold function  |
| $k$                | ratio of the compressive strength on the tensile one                             |
| $K_r$              | bulk modulus   |
| $G_r$              | shear modulus  |
| $N_i$              | volume density of the family $i$ of microcracks                                  |
| $n_r$              | number of inclusion particles of phase $r$                                       |
| $n_C$              | number of families of cracks   |
| $P_a$              | number of particulate phases in the RVE  |
| $r_r$              | aspect ratio of the spheroid representing particulate phase $r$                  |
| $R_{eq}$           | radius of the equivalent sphere of an arbitrary volume $V$                       |
| $V$                | domain occupied by the RVE   |
| $\partial V$       | external surface of the RVE  |
| $X_i$              | thermodynamic force associated with the damage variable $\beta_i$                |
| $Y_i$              | thermodynamic force associated with the damage variable $d_i$                    |
| $Y_0$              | initial damage threshold in terms of elastic energy density                      |
| $\nu_r$            | Poisson ratio of inclusion $r$   |
| $\beta_i$          | damage softening variables   |
| $\tilde{\epsilon}$ | equivalent strain  |
| $\epsilon_0$       | initial damage threshold in terms of strain                                      |
| $\lambda$          | damage multiplier  |
| $\Phi$             | thermodynamic potential or Helmholtz free energy                                 |
| $\Psi$             | dissipation potential  |
| $\zeta_r$          | morphological parameter of a particulate phase $r$                               |
| $\mathbb{B}_r$     | stress localization tensor   |
| $\mathbb{C}_r$     | stiffness tensor of particulate phase $r$  |
| $\mathbb{C}_M$     | matrix stiffness tensor of the matrix phase                                      |
| $\mathbb{C}^*$     | macroscopic stiffness tensor of the effective material                           |
| $\mathbb{D}$       | second-order damage tensor   |
| $\mathbb{H}_r$     | phase $r$ compliance fluctuations tensor   |
| $\mathbb{H}$       | compliance increment tensor  |
| $\mathbb{I}$       | fourth-order identity tensor.  |
| $\mathbb{J}$       | deviatoric operator  |
| $\mathbb{K}$       | hydrostatic operator   |
| $\mathbb{S}_M$     | macroscopic compliance tensor of the matrix material                             |
| $\mathbb{S}^*$     | macroscopic compliance tensor of the effective material                          |

### Greek symbols

|                                      |  |
|--------------------------------------|--|
| $\varepsilon$                        | microscopic strain tensor  |
| $\varepsilon$ or $\bar{\varepsilon}$ | macroscopic strain tensor  |
| $\varepsilon_p$                      | macroscopic tensor of the principal strains                                      |
| $\varepsilon_r^*$                    | eigenstrain inside the particulate phase $r$                                     |
| $\varepsilon_{Dr}^*$                 | eigenstrain inside the double-inclusion surrounding type $r$ inclusions          |
| $\sigma$                             | microscopic stress tensor  |
| $\sigma$ or $\bar{\sigma}$           | macroscopic stress tensor  |
| $\sigma^\infty$                      | stress tensor applied at infinity  |
| $\bar{\sigma}_r$                     | average stress over the inclusion $r$  |
| $\Omega_{Di}^*$                      | eigenstiffness tensor of the double-inclusion embedded in the effective material |
| $\Sigma_I^M$                         | Eshelby tensor of a homogeneous inclusion $I$ embedded in an infinite matrix     |
| $\bar{\Sigma}_I^M$                   | Eshelby tensor of an inhomogeneous inclusion $I$ embedded in the matrix          |

### subscripts or superscripts

|     |                  |
|-----|------------------|
| $M$ | matrix phase     |
| $I$ | inclusion        |
| $D$ | double-inclusion |

## NOMENCLATURE FOR CHEMISTRY AND TRANSPORT

|                      |  |
|----------------------|--|
| $c_r^{th}$           | percolation threshold of particulate phase $r$   |
| $c_r^{(p)}$          | percolating volume fraction of phase $r$   |
| $c_r^{im}$           | relative volume fraction of phase $r$ in the inner coating of a doubly coated sphere     |
| $c_r^{out}$          | relative volume fraction of phase $r$ in the outer coating of a doubly coated sphere     |
| $C_a$                | calcium concentration in the pore solution (in mol/L of solution)                        |
| $C_j$                | concentration of aqueous species $j$ in the pore solution (in mol/L of solution)         |
| $D_r$                | diffusion coefficient of an isotropic phase $r$ ( $m^2 s^{-1}$ )                         |
| $D^*$                | effective diffusion coefficient of a macroscopically isotropic material ( $m^2 s^{-1}$ ) |
| $D_{HTO}$            | diffusivity of tritiated water in bulk water at 23°C ( $m^2 s^{-1}$ )                    |
| $e_j$                | aqueous specie   |
| $e_{ja}^{z+}$        | aggressive ionic specie  |
| $e_m$                | mineral specie   |
| $f$                  | density of coated spheres with phase 2 as external coating in a MCSA                     |
| $K_m$                | equilibrium balance of the dissolution of $e_m$  |
| $M_i$                | number of mineral phases   |
| $M_t$                | total mass of CSH  |
| $M_R$                | ratio of the mass of CSH <sup>int</sup> to the total mass of CSH                         |
| $N$                  | number of aqueous species in the interstitial solution                                   |
| $p_m$                | concentration of $e_m$ (in mol/L of solution)  |
| $r_i$                | radius of the spherical core of a composite sphere                                       |
| $r_e$                | external radius of a composite sphere  |
| $S_a$                | calcium concentration in the solid phase ( $mol L^{-1}$ )                                |
| $V_m$                | molar volume of $e_m$ (in L/mol of solution)   |
| $\mathbf{1}$         | second-order identity tensor   |
| $\mathbf{J}_i$       | macroscopic flux vector of aqueous species $i$   |
| $\bar{\mathbf{J}}_i$ | microscopic flux vector of aqueous species $i$   |

$\bar{\mathbf{U}}$  average velocity vector

*Greek symbols*

$\beta_i^j$  polarizability of phase  $i$  with respect to phase  $j$

$\zeta$  hydration rate

$\chi$  stoichiometric coefficients

$\gamma_i$  activity coefficient

$\rho_m$  density of mineral phase  $r$

$\tau$  tortuosity

## ABBREVIATIONS

|                    |   |
|--------------------|---|
| Aft                | alumino-ferrite   |
| AFm                | monosulfoaluminates   |
| C <sub>3</sub> S   | tricalcium silicate   |
| CH                 | portlandite crystals or calcium hydroxide Ca(OH) <sub>2</sub> |
| CP                 | capillary pores   |
| CSH                | calcium-silicate-hydrates                                     |
| CSH <sup>int</sup> | internal (or high-density) calcium-silicate-hydrates          |
| CSH <sup>ext</sup> | external (or low-density) calcium-silicate-hydrates           |
| C/S                | calcium over silicon ratio                                    |
| CSA                | composite spheres assemblage                                  |
| CTM                | chemistry-transport-mechanics                                 |
| DIM                | double-inclusion model  |
| EMT                | effective-medium theory                                       |
| GEM                | general effective media                                       |
| GSCS               | generalized self-consistent scheme                            |
| GP                 | gel pores   |
| HCP                | hardened cement paste   |
| HTO                | tritiated water   |
| IDD                | interaction direct derivative                                 |
| KT                 | Küster - Töksöz   |
| MT                 | Mori - Tanaka   |
| OPC                | ordinary Portland cement                                      |
| MCSA               | mixed composite spheres assemblage                            |
| MIP                | mercury intrusion porosimetry                                 |
| PCW                | Ponte-Castañeda and Willis                                    |
| RVE                | representative volume element                                 |
| SC                 | self-consistent   |
| UC                 | unhydrated clinker  |
| w/c                | water to cement ratio   |

## TENSORIAL NOMENCLATURE

$$(\mathbf{A} \otimes \mathbf{B})_{ijkl} = A_{ij} B_{kl}$$

$$(\mathbf{A} \otimes \mathbf{B})_{ijkj} = A_{ik} B_{jl}$$

$$(\mathbf{A} \bar{\otimes} \mathbf{B})_{ijkl} = A_{il} B_{jk}$$

$$(\mathbf{A} \bar{\otimes} \mathbf{B})_{ijkl} = \frac{1}{2} (\mathbf{A} \bar{\otimes} \mathbf{B} + \mathbf{A} \otimes \mathbf{B})$$

## LIST OF FIGURES

|  |    |
|--|----|
| Figure I.1: Images of a CEM I 52.5 cement paste with a water to cement ratio (w/c) equal to 0.43 obtained by SEM: A/ representative area of the sample, B/ detailed image of an Outer Product Zone (taken from Béjaoui et al. 2006). .....   | 6  |
| Figure I.2: Images of the microstructure of $CSH^{int}$ and $CSH^{ext}$ in CEM I 52.5 cement pastes with diverse w/c ratios obtained by Transmission electron microscopy (TEM) (taken from Béjaoui et al. 2006). .....   | 8  |
| Figure I.3: Views of cement particles generated from the spherical harmonic expansion (taken from (Garboczi and Bullard 2004). .....   | 10 |
| Figure I.5 (semi-logarithmic scale): Evolution of the macroscopic diffusion coefficients measured experimentally for both sound CEM I and CEM V pastes with their w/c ratio, taken from diverse sources in the literature (adapted from Richet et al. 1997). .....   | 19 |
| Figure I.6: Photo of a CEM I 42.5 paste sample with w/c = 0.40 leached during 3 months by pure water (taken from Adenot 1992). .....   | 21 |
| Figure I.7: Degradation process of the main hydrated phases in terms of calcium concentration in solid phase $S_{Ca}$ as a function of calcium concentration in solution $C_{Ca}$ (line = results obtained with the chemical equilibrium code CHESS; dotted line = simplified curve) (adapted from Bary and Béjaoui 2006). ..... | 22 |
| Figure II.1: Schematic illustrating the replacement of the heterogeneous RVE by an equivalent homogeneous medium. ....   | 28 |
| Figure II.2: Schematic of a spherical inclusion with a homogeneous interphase enclosed in an infinite matrix. ....   | 32 |
| Figure II.3: Schematic picture of the equivalent homogeneous inclusion. ....   | 33 |
| Figure II.4: Two-dimensional representation illustrating the three-phase model on which is based the GSCS. ....  | 37 |
| Figure II.5: Derivation of the MT (left) and IDD (right) models for a multi-phase composite from the dilute configuration by modifying the far-field stresses. ....  | 39 |
| Figure II.6: Schematic of the original three-phase configuration a) used for the derivation of DIM and representation of the different steps b), c), d) and e) employed for its derivation. ....   | 41 |
| Figure II.7: Schematic illustrating the link between the Hori and Nemat-Nasser DIM and other micromechanical schemes (Hu and Weng 2000). ....  | 44 |
| Figure II.8: Schematic illustrating the discrepancies of the Hori and Nemat-Nasser DIM. ....   | 45 |
| Figure II.9: Schematic illustrating the effective inclusion concept employed by Kuster-Toksöz (1974) and Shen and Yi (2001). ....  | 48 |
| Figure II.10: Schematic illustrating the main steps employed to derive the modified DIM. ....  | 51 |
| Figure II.11: Evolutions of the effective Young moduli estimated by different micromechanical schemes and by FE simulations (Wriggers and Moftah 2006) for two types of concretes as functions of the volume fractions of aggregates a) type I and b) type II. ....  | 54 |
| Figure II.12: Evolutions of the effective elastic bulk (left) and shear (right) moduli estimated by different EMTs and by FE simulations (Garboczi and Berryman 2001) for both sound and degraded HCP as a function of $e = E_{ITZ} / E_{HCP}$ . ....  | 55 |

|   |    |
|---|----|
| Figures II.13: Evolutions of the effective Young moduli estimated by different EMTs and by FE simulations (Roberts and Garboczi 2000) for an elastic body weakened by oblate spheroidal voids with aspect ratio $r = 0.25$ , as a function of porosity.....   | 56 |
| Figure II.14: Schematic representation of the evolution of the dimensions of prolate spheroids corresponding to an inclusion phase $r$ with the shape parameter $\zeta$ : a) $c_r$ constant; b) $b$ constant (Stora et al. 2006a). .....  | 61 |
| Figure II.15: a) Two-dimensional representation of HCP with spheroidal inclusions based on MT and double-inclusion type schemes (left); b) Two-dimensional representation of HCP with spherical inclusions based on MT and double-inclusion type schemes (Stora et al. 2006a).....  | 62 |
| Figure II.16: Evolutions of the normalized effective Young modulus for sound CEM I pastes with capillary pores as a function of the shape parameter $\zeta$ for different volume fractions. Solid lines: $w/c = 0.50$ ( $c_{CP} = 23.7\%$ ), dashed lines: $w/c = 0.40$ ( $c_{CP} = 18.3\%$ ), dotted lines: $w/c = 0.25$ ( $c_{CP} = 11\%$ ) (Stora et al. 2006a). The subscript Sph means that the modulus has been estimated using the spherical particle approximation..... | 64 |
| Figure II.17: Evolutions of normalized effective Young modulus for sound CEM I pastes with unhydrated Clinker respectively represented by oblate and prolate spheroids, as a function of the shape parameter $\zeta$ . Solid lines: $w/c = 0.50$ ; dashed lines: $w/c = 0.40$ ; dotted lines: $w/c = 0.25$ (Stora et al. 2006a). .....  | 65 |
| Figure II.18: Evolutions of the normalized effective Young modulus for sound CEM I pastes, as a function of the morphological parameter $\zeta$ . Solid lines: $w/c = 0.50$ ; dashed lines: $w/c = 0.40$ ; dotted lines: $w/c = 0.25$ (Stora et al. 2006a). .....   | 66 |
| Figure II.19: Evolutions of the normalized effective Young modulus for leached CEM I pastes, as a function of the morphological parameter $\zeta$ . Solid lines: $w/c = 0.50$ ; dashed lines: $w/c = 0.40$ ; dotted lines: $w/c = 0.25$ (Stora et al. 2006a). .....   | 67 |
| Figures II.20: Evolutions of the effective Young moduli estimated respectively by the IDD model with spherical and spheroidal inclusions and by FE simulations (Kamali 2003) for both a) sound and b) partially degraded HCP as a function of capillary porosity volume fraction (Stora et al. 2006a). .....  | 69 |
| Figure II.21: Approximation of realistic HCP particulate phases shapes by equivalent spheroids (Stora et al. 2006a).....  | 72 |
| Figure II.22: Schematic of the levels I and II of the two-scale representation used for the estimation of the effective elastic properties of HCP.....  | 78 |
| Figure II.23: Comparison between the effective Young moduli estimated by the multi-scale model with experimental measurements (Constantinides and Ulm 2004; Gallé et al. 2004) on both sound and degraded HCP. ....   | 80 |
| Figure II.24: Evolutions of the effective Young moduli estimated by the multi-scale model and by FE simulations (Kamali 2003) for both a) sound and b) partially degraded HCP as a function of capillary porosity volume fraction.....  | 81 |
| Figure II.25: Evolutions of the effective Young moduli estimated by the Constantinides and Ulm model, by the present multi-scale one and by FE simulations (Kamali 2003) for both a) sound and b) partially degraded HCP as a function of capillary porosity volume fraction. ....  | 82 |
| Figure II.26: Schematic of the representation used for the estimation of the effective elastic properties of mortars. ....  | 84 |

|  |     |
|--|-----|
| Figure III.1: Two-dimensional representation illustrating the application of the GSCS for computing the diffusive properties of a composite with coated spherical inclusions.....  | 96  |
| Figure III.2: Schematic illustrating the main steps employed to derive the modified DIM. ...   | 98  |
| Figure III.3: Evolution of the normalized effective elastic properties a) and of the diffusivity b) of the perforated cement paste with the volume fraction of porous cylindrical tunnels....  | 102 |
| Figure III.4 (semi-logarithmic scale): Evolution of the effective diffusion coefficient of a macroscopically isotropic two-phase material with $D_2 / D_1 = 10^3$ respectively estimated by the MT (Mori and Tanaka 1973) and the IDD (Zheng and Du 2001) schemes as a function of the volume fraction of the diffusive phase. The latter phase is modeled as prolate spheroids with diverse aspect ratios $r$ . ..... | 104 |
| Figure III.5 (semi-logarithmic scale): Evolutions of HS, Beran and Bergman bounds for a macroscopically isotropic two-phase material with $D_2 / D_1 = 10^3$ as a function of the volume fraction of the high diffusive phase.....   | 107 |
| Figure III.7 (semi-logarithmic scale): Evolutions of the effective diffusion coefficient of a macroscopically isotropic two-phase material with $D_2 / D_1 = 10^3$ estimated by SC type schemes as a function of the volume fraction of the high diffusive phase.....  | 109 |
| Figure III.8: Evolutions of the effective diffusion coefficient of a macroscopically isotropic two-phase material with $D_1 / D_2 \rightarrow 0$ estimated by SC type schemes as a function of the volume fraction of the diffusive phase.....   | 109 |
| Figure III.9: Two-dimensional representations of monodisperse overlapping spherical inclusions that are randomly distributed in space. The percolation thresholds of the clusters formed by these spherical inclusions and of the remaining space differ significantly. ....   | 110 |
| Figure III.10: Two-dimensional representation of the CSA developed by Hashin and Shtrikman (1962).....   | 114 |
| Figure III.12: Two-dimensional representation of an assemblage mixing two types of composite spheres (Stora et al. 2006b).....   | 116 |
| Figure III.13: Evolutions of the effective diffusion coefficient of a macroscopically isotropic two-phase material with $D_2 / D_1 = 10^3$ estimated by the MCSA scheme as functions of the high-diffusive phase volume fraction for diverse values of the parameter $f$ .....   | 120 |
| Figure III.14: Evolutions of the effective diffusion coefficient of a macroscopically isotropic two-phase material with $D_1 / D_2 \rightarrow 0$ estimated by the MCSA scheme as functions of the high-diffusive phase volume fraction for diverse values of the parameter $f$ .....  | 120 |
| Figure III.15: Evolution of the volume fractions of the high-diffusive phase respectively dispersed in the shells of the C1 spheres (a) and in the cores of the C2 spheres (b) as functions of the total volume fraction of the high-diffusive phase for diverse contrasts between phase diffusivities, the geometric parameter $f$ being equal to 0.5.....  | 122 |
| Figure III.16: Two-dimensional representation of the assemblages mixing two types of composite spheres used for representing the microstructures of $CSH^{int}$ and $CSH^{ext}$ . ....   | 126 |
| Figure III.17 (semi-logarithmic scale): Evolutions of the diffusivities of CEM I pastes measured experimentally (Richet et al. 1997) and predicted respectively by the multi-scale model with $f = 0.546$ and by the simplified model in Stora et al. (2006b), as functions of their total porosity.....   | 129 |

|   |     |
|---|-----|
| Figure III.18: Two-dimensional representation of HCP using two scales: at the first scale, non-diffusive and little diffusive phases are modeled as spherical inclusions embedded in a solid diffusive phase; at the second scale, the homogenized solid phase and the porous one are modeled as a MCSA (Stora et al. 2006b).....   | 130 |
| Figure III.19: Evolutions of the effective diffusion coefficients of CEM I pastes with different w/c ratios as a function of calcium concentration in pore solution (Stora et al. 2006b).....   | 132 |
| Figure III.20: Schematic of the representation used for the estimation of the effective diffusive and elastic properties of mortars. ....   | 134 |
| Figure IV.1: Evolutions of the effective axial Young modulus, the longitudinal Poisson ratio and the longitudinal shear modulus of an elastic body with $\nu = 0.25$ weakened by aligned penny-shaped cracks on the $(e_2, e_3)$ plane estimated by diverse homogenization schemes as functions of the crack density parameter $p = 4\pi d/3$ (3D).....   | 147 |
| Figure IV.2: Evolutions of the effective axial Young modulus of an elastic body with $\nu = 0.25$ weakened by aligned penny-shaped cracks on the $(e_2, e_3)$ plane estimated by diverse homogenization schemes and by numerical simulations as functions of the crack density parameter $p = \pi d$ (2D).....  | 149 |
| Figure IV.3: Evolutions of the effective Young modulus (up left), the Poisson ratio (up right), the bulk (down left) and shear moduli (down right) of an elastic body with $\nu = 0.25$ weakened by randomly oriented penny-shaped cracks predicted by various homogenization schemes as functions of the crack density parameter $p$ (3D).....   | 150 |
| Figure IV.4: Evolutions of the effective Young moduli and shear moduli along the three principal axis $e_1 = e_2 = e_3$ of an elastic body with $\nu = 0.25$ weakened by three families of penny-shaped cracks oriented according to the principal directions with identical crack densities $p_1 = p_2 = p_3 = p/3$ (up) and with crack densities $p_1 = p_2 = p/2$ and $p_3 = 0$ (down) as functions of the crack density parameter $p$ ..... | 152 |
| Figure IV.5: Rosette representing the relative decrease of the effective Young modulus predicted by the IDD model for two families of cracks aligned with the $e_1$ and $e_2$ directions which crack densities are $d_1 = d, d_2 = 0$ with $d = 0.1$ (dash-dotted), $d_1 = d, d_2 = d/2$ (dashed) and $d_1 = d_2 = d$ (plain), respectively. ....   | 154 |
| Figure IV.6: Rosette representing the relative decrease of the effective Young modulus predicted by the IDD model for four families of cracks aligned with the $e_1$ and $e_2$ directions which crack densities are $d_1 = d_2 = d/2$ and $d_3 = d_4 = 0$ with $d = 0.1$ (dashed) and $d_1 = d_2 = d_3 = d_4 = d/4$ (plain), respectively. ....   | 154 |
| Figure IV.7: Comparison of the stress-strain curves predicted of a mortar subjected to uniaxial tension along the $e_1$ axis by different micromechanically based damage models with Marigo criterion with the one experimentally recorded by Le Bellégo (2001) (up); evolution for the crack density parameter $d_1$ predicted by the latter models (down). ....   | 160 |
| Figure IV.8: Comparison of the stress-strain curves predicted of a mortar subjected to uniaxial tension along the $e_1$ axis by the IDD damage model with Marigo criterion with the one experimentally recorded by Le Bellégo (2001) (up); evolution for the crack density parameter $d_1$ predicted by the latter model (down). ....   | 161 |
| Figure IV.9: Stress-strain curves along the two principal axis of a mortar subjected to biaxial tension along the two axis $e_1$ and $e_2$ with $\epsilon_{11} = \epsilon_{22}$ predicted by different homogenization   |     |

|   |     |
|---|-----|
| models with Marigo criterion (up); evolution for the crack density parameters $d_1$ and $d_2$ predicted by the latter model (down). .....   | 162 |
| Figure IV.10: Damage yield surfaces respectively representing the Mazars criterion and the De Vree one for $k = 1$ and $k = 3$ in the space of principal stresses. ....   | 164 |
| Figure IV.11: Damage yield surfaces respectively representing the Mazars criterion and the De Vree one for $k = 1$ and $k = 3$ in the space of principal strains. ....  | 164 |
| Figure IV.12: Comparison of the stress-strain curves predicted of a mortar subjected to uniaxial tension by the damage model with a strain-based criterion with the one experimentally recorded by Le Bellégo (2001) (up); evolution for the crack density parameters $d_1$ and $d_2$ predicted by the latter model (down). ....  | 170 |
| Figure IV.13: Stress-strain curves along the two principal axis of a mortar subjected to biaxial tension along the two axis $e_1$ and $e_2$ with $\varepsilon_{11} = \varepsilon_{22}$ predicted by the damage model with Marigo criterion (up); evolutions for the crack density parameters $d_1$ and $d_2$ predicted by the latter model (down). ....                                       | 171 |
| Figure IV.14: Stress-strain curves along the two principal axis of a mortar subjected to biaxial tension along the two axis $e_1$ and $e_2$ with $\varepsilon_{11} = 3\varepsilon_{22}$ predicted by the damage model with Marigo criterion (up); evolutions for the crack density parameters $d_1$ and $d_2$ predicted by the latter model (down). ....                                      | 171 |
| Figure V.1: Modelling and simulations of chemo-mechanical degradations of cement-based materials with ALLIANCES. ....   | 181 |
| Figure V.2: Schematic of the one-dimensional system employed for the simulations of pure water leaching of HCP. ....  | 182 |
| Figure V.3: Mineral compositions in terms of volume fractions inside a sample of CEM I 42.5 paste with $w/c = 0.40$ subjected to a 50 days attack by pure water simulated with ALLIANCES using a) a proportional law, b) Tognazzi's law and c) the multi-scale homogenization model, respectively. ....   | 186 |
| Figure V.4: Evolutions of the macroscopic diffusivity inside a sample of CEM I 42.5 paste ( $w/c = 0.40$ ) subjected to a 50 days attack by pure water simulated with ALLIANCES using a proportional law (red), Tognazzi's law (blue) and our homogenization model (dashed), respectively. ....   | 187 |
| Figure V.5: Evolutions of the pH of the interstitial solution and of the calcium concentrations in solid phase and in solution inside a CEM I 42.5 paste with $w/c = 0.40$ subjected to a 50 days attack by pure water simulated with ALLIANCES using a proportional law (red), Tognazzi's law (blue) and the multi-scale homogenization model (dashed), respectively. ..                     | 188 |
| Figure V.6: Evolution of the concentrations in solution of the main aqueous species compared with the initial ones as a function of the depth of the sample of CEM I 42.5 with $w/c = 0.40$ paste after 50 days of pure water degradation simulated with ALLIANCES using a proportional law (up), Tognazzi's law (middle) and the multi-scale homogenization model (down), respectively. .... | 190 |
| Figure V.7: Mineral compositions in terms of volume fractions inside a sample of CEM I 52.5 HTS paste with $w/c = 0.45$ subjected to a 50 days attack by pure water simulated with ALLIANCES. ....  | 191 |
| Figure V.8: Evolutions of the pH of the interstitial solution and of the concentrations of calcium ions in solid phase and in solution inside 42.5 ( $w/c = 0.40$ ) and 52.5 HTS ( $w/c = 0.45$ ) CEM I pastes subjected to a 50 days attack by pure water. ....  | 193 |

|   |     |
|---|-----|
| Figure V.9: Mineral compositions in terms of volume fractions inside a sample of CEM I 42.5 paste with a w/c = 0.40 (Le Bellégo 2001) subjected to a 10 days attack on its left side by pure water (left) and by a 6M NH <sub>4</sub> NO <sub>3</sub> solution (right).....   | 195 |
| Figure V.10: Evolutions of the macroscopic diffusivity inside a sample of CEM I 42.5 paste (w/c = 0.40) subjected to a 50 days attack by pure water simulated with the multi-scale homogenization model with CH modelled as a sphere (blue) and as oblate spheroids (dashed), respectively.....   | 196 |
| Figure V.11: Mineral compositions in terms of volume fractions inside a sample of CEM I 42.5 paste with w/c = 0.40 subjected to a 50 days attack by pure water simulated with the multi-scale homogenization model with CH modelled as a sphere (left) and as an oblate spheroid (right), respectively.....   | 196 |
| Figure V.12: Evolutions of the macroscopic diffusivity inside a sample of CEM I 42.5 paste (w/c = 0.40) subjected to a 50 days attack by pure water simulated with the multi-scale homogenization model by considering different quantities of additional percolating gel pores ( $\Delta c_{GP}^{(p)} = 0.04$ and $\Delta c_{GP}^{(p)} = 0.065$ )..... | 197 |
| Figure V.13: Mineral compositions in terms of volume fractions inside a sample of CEM I 42.5 paste with w/c = 0.40 subjected to a 50 days attack by pure water simulated with the multi-scale homogenization model by considering an increased quantity of additional percolating gel pores ( $\Delta c_{GP}^{(p)} = 0.065$ ).....                      | 198 |
| Figure V.14: Evolutions with square root of time of the total amount of released calcium from a CEM I 42.5 paste with w/c = 0.40 subjected to an attack by pure water simulated with the multi-scale homogenization model. ....   | 199 |
| Figure V.15: Evolution of the Young modulus inside a sample of CEM I 42.5 paste with w/c = 0.40 (Le Bellégo 2001) subjected to a 50 days pure water attack. ....  | 201 |
| Figure V.16: Stress-strain curves of a sound and an asymptotically leached cement paste with a w/c ratio equal to 0.50 (Heukamp et al. 2005) submitted to a uniaxial traction following the e <sub>1</sub> axis. ....   | 202 |
| Figure V.17: Schematic of the two-dimensional mesh employed for the simulations of mechanical resistance tests (up); mesh (200 elements) used for the computations (down)...  | 204 |
| Figure V.18: Identification of the strain damage threshold of a leached OPC type I paste (Heukamp et al. 2005) from the stress-strain curve of the damaged unleached one.....   | 206 |
| Figure V.19: Profile of the Portlandite concentration (mol/L) in a mortar beam after a 114 days attack by a NH <sub>4</sub> NO <sub>3</sub> solution (up); crack density parameter d <sub>1</sub> predicted by the IDD damage model in the leached beam submitted to a flexural displacement of 39 μm (down).   | 207 |
| Figure V.20: Profiles of the diffusion coefficients (down) and of the liquid calcium concentration (mol/L) (up) in a mortar beam after a 114 days attack by a 6M NH <sub>4</sub> NO <sub>3</sub> solution.....  | 208 |
| Figure V.21: Evolutions of the mineral compositions in terms of volume fractions inside a mortar beam after a 114 days attack by a NH <sub>4</sub> NO <sub>3</sub> solution along the vertical symmetry axis beam. ....   | 209 |
| Figure V.22: Comparison of the simulations results with the experimental curves of the vertical forces plotted against the imposed flexural displacement and of the ones recorded during a three-point flexion tests on a sound mortar beam and a leached one. ....   | 210 |

## LIST OF TABLES

|   |     |
|---|-----|
| Table I.1: Mineral composition in terms of volume fractions of standard CEM I hydrated pastes obtained by the model of Tennis and Jennings (Jennings 2000; 2000). .....   | 7   |
| Table I.2: Critical pore diameter values measured by MIP tests for various types of cements pastes in sound or leached states issued from diverse sources. ....   | 13  |
| Table I.3: Elastic properties of the main phases in a sound state present in HCP microstructure, taken from diverse sources in the literature. ....   | 16  |
| Table I.4: Young moduli measured experimentally of standard cement pastes, taken from diverse sources in the literature. ....   | 17  |
| Table I.5: Table summarizing some important experimental results of accelerated leaching tests of HCP, taken from diverse sources in the literature. ....   | 22  |
| Table II.1: Table confronting the merits of the different EMTs presently reviewed. ....   | 58  |
| Table II.2: Input volume fractions of principal hydrates, unhydrated Clinker and capillary porosity for six different HCP (Kamali 2003). ....   | 63  |
| Table II.3: Input volume fractions of principal hydrates, unhydrated Clinker and capillary porosity for two different HCP.....  | 79  |
| Table II.4: Grading of the fine Nevada sand used for the mortars (Heukamp 2002).....  | 83  |
| Table II.5: Comparison of the micromechanical estimations with experimental data on cement pastes and mortars (Heukamp 2002).....   | 85  |
| Table III.1: Comparative table aiming at testing homogenization models on three simple criteria.....  | 112 |
| Table III.2: Composition in terms of volume fractions of hydrated CEM I pastes obtained by combining the mineral compositions given in Béjaoui and Bary (2007) computed with the hydration model of Jennings (2000) and Tennis and Jennings (2000) and the experimental measurements of capillary pores (Igarashi et al. 2004)..... | 128 |
| Table V.1: Table summarizing the main input data for performing CTM coupled simulations using the homogenization model with ALLIANCES. ....   | 181 |
| Table V.2: Initial composition of the two CEM I pastes used for the simulations. ....   | 183 |
| Table V.3: Comparison of the decalcification front propagations obtained in the simulations performed with ALLIANCES of pure water leaching with experimental values.....   | 190 |
| Table V.4: Comparison of the decalcification front propagations obtained in the different simulations performed with ALLIANCES of accelerated leaching by a 6M $\text{NH}_4\text{NO}_3$ solution with experimental values (Gallé et al. 2004).....  | 192 |
| Table V.5: Comparison of the decalcification front propagations obtained in the new simulations performed with ALLIANCES of pure water leaching with experimental values. ....  | 196 |
| Table V.6: Mechanical input data adopted for the micromechanically-based damage model in the cases of a HCP sample (Heukamp et al. 2005) submitted to a uniaxial traction and of the mortar beam tested in flexion (Le Bellégo 2001). ....  | 200 |

## **ACKNOWLEDGEMENTS**

I first of all would like to acknowledge DSNI/Réacteurs Bétons for its financial support. I wish to thank B. Bary and Professor Q.-C. He, who directed in a complementary way my PhD thesis and taught me a lot of things. I thank also all the people at the LaM at the university of Paris-Est Marne-la-Vallée and at the CEA/DPC/SCCME/LECBA in Saclay.

I thank Professors D. Kondo and G. Pijaudier-Cabot, for having reviewed my dissertation in a few weeks only, and Professor van der Lee who examined my work. A special think also to L. Sanguigno and Professors A. Vautrin and G. Mensitieri, who incited me to do a PhD.

## 1 GENERAL INTRODUCTION

Due to the pluridisciplinary nature of the subject treated, the present manuscript is concerned with well separated physical problems in cementitious materials, such as chemistry, diffusion or mechanics. For conciseness, this introduction gives only a general overview of the thesis, a more specific introduction being associated with each main Part of the document.

### 1.1 Industrial and scientific context

The durability of concrete materials employed in many kinds of infrastructures, such as bridges, dams, or nuclear reactors, is an acute issue in Civil Engineering because they involve important security aspects. The cost of maintenance of these concrete structures is tremendously high. This economical factor consequently motivates scientific research allowing for better assessing how cement-based materials behave with time. Some of the primary mechanisms of deterioration of concrete facilities include cracking due to external loadings and chemical attacks. The loss of performance and sometimes the complete rupture of these infrastructures can consequently be originated by mechanical and/or chemical deteriorations of concrete.

It appears therefore a necessity to adopt multi-physical coupled approaches to deal with material durability. Besides its importance for previously mentioned concrete facilities, this topic is also of current concern in the context of nuclear waste storage. As is already the case in the experimental site of Bures in the east of France, concrete is very likely to be employed for different applications in future underground structures devoted to the storage of nuclear waste. It should be used as engineering barrier but also as outside coating in the waste containers in which vitrified waste may be stored. The life time service of these underground facilities should be about tens or hundreds of thousand of years, since the radioactivity of nuclear waste can last such a long time scale. The present manuscript is more specifically situated in this context of long-term durability of cement-based materials.

The scope of the thesis is however not only purely industrial but also scientific. Homogenization techniques have known an increasing success among researchers and their application to cement-based composites appears promising in particular for predicting with accuracy the evolutions of their properties with time. These methods indeed allow for estimating the macroscopic physical properties of a heterogeneous material from the knowledge of the microstructure and the physical characteristics of the elementary phases. In that sense, they constitute deductive approaches, since they may a priori be applied to any material provided that its composition and phase physical properties are known. These approaches that are focused on in the present manuscript furthermore represent an outstanding tool to link the microscopic phenomena, like the dissolution of a phase, to the macroscopic behaviour of the material and even of the structure.

## 1.2 Research objectives

The objective of the present manuscript is mainly two-fold. In the context of durability, two of the most essential factors that determine the service life of concrete facilities are the diffusive and mechanical characteristics of the construction material for the following reasons. The resistance of a structure to loadings is of course conditioned by the mechanical behavior of concrete and its opposition to chemical deterioration largely depends on the opportunity offered to ions to diffuse through the material.

The first objective of the thesis thus consists in building an analytical approach, based on homogenization techniques and on a multi-scale description of cement-based materials, allowing for estimating both their mechanical and diffusive properties and for predicting their evolution with time. Many empirical laws already exist for computing these quantities but they suffer some limitations. For instance, their validity range is quite restricted or they require many experimental data. To circumvent this difficulty, homogenization models have recently been proposed (e.g. Bernard et al. 2003; Constantinides and Ulm 2004; Pivonka et al. 2004). However, these models are generally only designed for determining one specific physical property of cement-based materials, such as their elastic moduli or their macroscopic diffusivity. It is consequently of high interest to develop a unified homogenization approach that is capable of predicting both the mechanical and transport properties of concrete materials on the basis of a realistic microgeometry. Furthermore, progress in experimental analysis techniques (e.g. Scrivener 2004; Garboczi and Bullard 2004) has led to a more accurate knowledge of the microstructure of these materials, which is valuable for developing a precise modelling. A damage model also gaining profit from homogenization techniques is proposed to predict the rather brittle behavior of concrete.

The second and final goal of the present manuscript is to model and carry out simulations of degradations coupling chemistry, transport and mechanics of cement-based composites. These simulations are performed with the help of a numerical integration platform ALLIANCES that allows for coupling different physical problems (Montarnal et al. 2006; 2007) developed by the French Atomic Energy Commission (CEA) in collaboration with ANDRA and EDF. The study of such deteriorations is crucial in the context of nuclear waste storage. The concrete material, assumed to be saturated in the nominal storage phase, undergoes chemical deteriorations in contact with ground water. This degradation process is ruled by the macroscopic diffusion coefficients of chemical species through the saturated cementitious material. Therefore a coupled chemical-transport approach is necessary to predict the alteration with time of its microstructure. The engineering barrier made of concrete of the underground structures serving for the disposal of nuclear wastes should also act against the propagation of radionuclide. The impact of chemical alteration of the construction material on

the global diffusive properties of this structure element is a key point for assessing its capacity to work as a radionuclide barrier.

Moreover, the chemical degradation process generating a strong augmentation of porosity inside the cementitious material affects the overall mechanical behaviour of the underground facility. Damage of the structure may then occur because of the combined solicitations due to external loadings and to chemical deterioration. This nucleation and growth of cracks in the concrete can in turn accelerate the transport phenomena and then enhance the chemical alteration process. Nevertheless, the simulations give some useful insights for other thematics, such as CO<sub>2</sub> storage or tunnels construction. But in such fields of applications, it is necessary to consider unsaturated conditions, which generally lead to particularly complicated computations. The assumption of saturated conditions is presently retained, since the degradations of concrete underground structures for the storage of nuclear waste may be envisaged at a long-term. The thermal effects are not taken into account, even though nuclear waste can induce very significant elevations of temperatures.

### 1.3 Outline of the thesis

The manuscript is composed of five Parts. The first one is dedicated to the presentation of cement-based materials and of the degradations of these materials subjected to leaching. In Parts II and III devoted to homogenization techniques, a multi-scale modeling approach based on a realistic representation of cementitious materials is developed to estimate the evolution with time of their elastic and diffusive macroscopic properties, respectively. In Part IV, a micromechanical damage model based on some simplifying assumptions is developed to predict the quasi-brittle behavior of concrete and integrated in the FE code CAST3M. Part V is finally dedicated to the modelling and the numerical simulations of chemical and of coupled chemo-mechanical degradations of leached cement-based materials. These simulations are performed by incorporating the models proposed in the previous Parts to predict the macroscopic properties of cement-based materials into the ALLIANCES platform.

## **Part I**

# **PRESENTATION OF CEMENT-BASED MATERIALS**

Cement-based materials are massively employed in the domain of construction. A country like China consumes more than one hundred millions of tons of concrete per year. Three types of cementitious materials are studied in the present manuscript: hardened or hydrated cement paste (HCP), mortar and concrete. A particular emphasis is put on the cement pastes that constitute the matrix in mortars and concretes and that are very sensitive to degradations. Reinforced concretes are also commonly used in constructions but phenomena like corrosion are out of our scope.

A good knowledge of the microstructure of cementitious materials and of its impact on their macroscopic properties is a prerequisite for properly predicting their physical deteriorations. A detailed investigation of HCP microstructure is fundamental to better understand the mechanisms of degradation of cement-based materials and explain the differences of properties from one material to another. This investigation constitutes furthermore the cornerstone for the construction of the homogenization model treated in the following Parts of the thesis. The present Part gathers experimental results and observations that are useful for understanding the microstructure of cementitious materials, for knowing its basic properties and assessing the material durability.

## **2 MICROSTRUCTURE AND PHYSICAL PROPERTIES OF CEMENT-BASED MATERIALS**

### **2.1 Presentation of the multi-scale microstructure of cement-based materials**

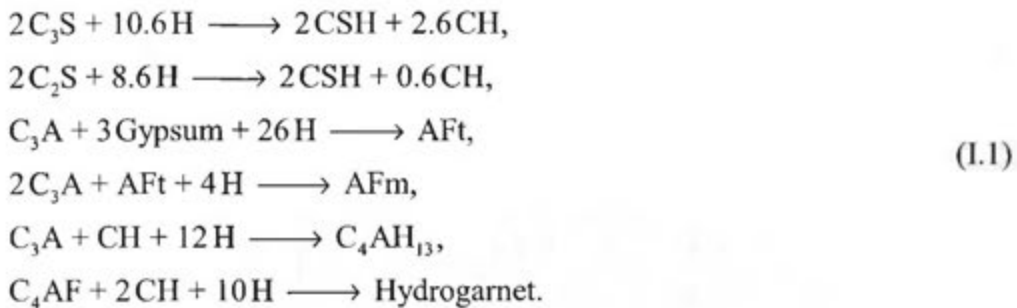
#### *2.1.1 Microstructure of cement pastes*

##### *2.1.1.1 Hydration of cement pastes*

Cement pastes are complex, multiphase, porous materials, which microstructure evolves with time. The material primarily consists in anhydrous cement grains mixed with water. These grains called clinker are fabricated from a mix of limestone and clay transformed by heating them at about 1450°C and by crushing. Their diameter can vary from 1 to 100  $\mu\text{m}$ . A basic Portland clinker is generally composed of four dominant compounds: tricalcium silicate ( $\text{C}_3\text{S}$ ), dicalcium silicate ( $\text{C}_2\text{S}$ ), tricalcium aluminate ( $\text{C}_3\text{A}$ ) and calcium aluminoferrite ( $\text{C}_4\text{AF}$ ). For simplicity, the following cement chemists' notations are used: C = CaO; S =  $\text{SiO}_2$ ; A =  $\text{Al}_2\text{O}_3$ ; F =  $\text{Fe}_2\text{O}_3$ ; H =  $\text{H}_2\text{O}$ ). Some additives, such as Gypsum, fly ash or slag, may

be also adjoined to this clinker, base of the standard Portland cement, to modify the paste microstructure and thus its macroscopic properties.

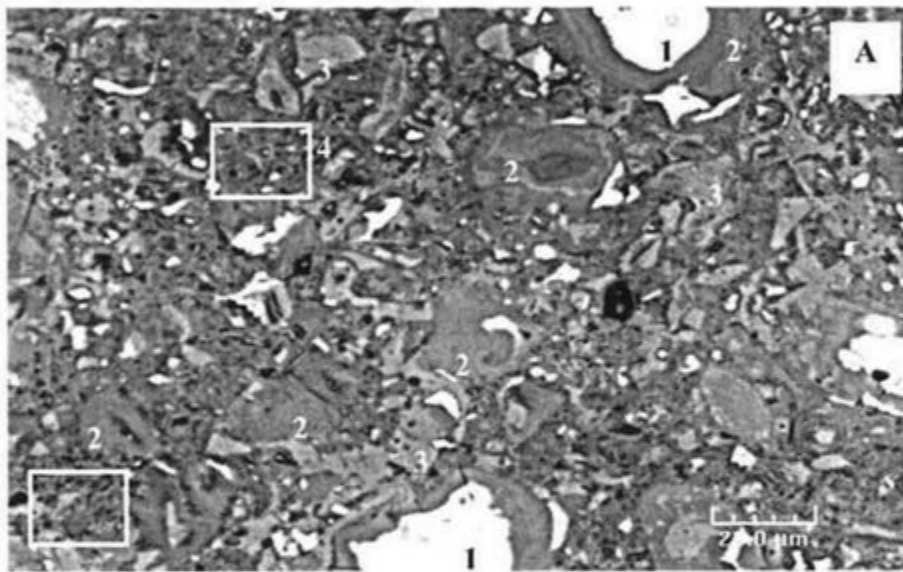
A complex microstructure then forms due to hydration of cement grains, the reaction of cement particles with water initially taking place at the particle surface. The microstructure obtained is usually described as a complex mixture of pores (P), calcium-silicate-hydrates (CSH), unhydrated clinker (UC), portlandite or calcium hydroxide (CH) and aluminates (AF), such as ettringite or alumino-ferrite (AFt), monosulfoaluminates (AFm). The chemical composition of these mineral phases is given at the end of the page<sup>1</sup>. The relative proportions of these phases in HCP may significantly vary from one paste to another and strongly depend from the mineral composition of the cement grains and on the water/cement (w/c) ratio. Tennis and Jennings (2000) proposed the following equations to model the hydration of the cement grains and compute the resulting volume fractions of the hydrated phases:



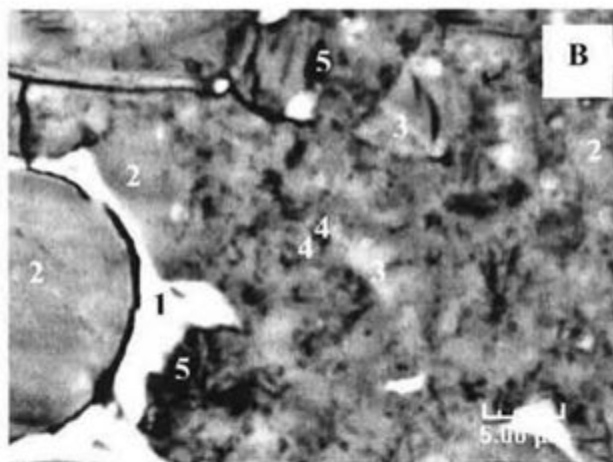
Other hydration models exist in the literature such as CEMHYD3D developed by the NIST (Bentz 1997) but the Tennis and Jennings model (2000) is adopted in the ensuing to estimate the volume fractions of the mineral phases composing the microstructure of HCP.

During hydration of cement particles, it is generally asserted (Richardson 2000) that two diffusive layers presently defined as inner and outer layers form successively from cement grains surface. The inner layer is less porous than the outer one, since the first one results from higher confinement conditions and from poorer water accessibility during hydration process. An image provided by scanning electronic microscopy (SEM) is proposed to illustrate the HCP heterogeneous microstructure (see Fig. I.1).

<sup>1</sup> CSH =  $x \text{ CaO} - \text{SiO}_2(\text{aq}) - x \text{ H}_2\text{O}$ , where  $x$  varies between 0 and 2.3; CH =  $\text{Ca}(\text{OH})_2$ ;  
 AFt =  $6 \text{ CaO} - \text{Al}_2\text{O}_3 - 3 \text{ SO}_3 - 24 \text{ H}_2\text{O}$ ; AFm =  $4 \text{ CaO} - \text{Al}_2\text{O}_3 - \text{SO}_3 - 12 \text{ H}_2\text{O}$ ;  
 Hydrogarnet =  $3 \text{ CaO} - \text{Al}_2\text{O}_3 - 6 \text{ H}_2\text{O}$ ; Gypsum =  $\text{Ca}(\text{SO}_4) - 2 \text{ H}_2\text{O}$ .



1: UC, 2: CSH<sup>int</sup>, 3: CH, 4: Outer Product Zone (CSH, AF, CH, Capillary Porosity appearing in black)



1: UC, 2: CSH<sup>int</sup>, 3: CH, 4: CSH<sup>ext</sup>, 5: Capillary Porosity

**Figure I.1: Images of a CEM I 52.5 cement paste with a water to cement ratio (w/c) equal to 0.43 obtained by SEM: A/ representative area of the sample, B/ detailed image of an Outer Product Zone (taken from Béjaoui et al. 2006).**

Depending on the initial sizes of cement grains, an anhydrous part of the cement particles remains after hydration has stopped and constitutes an impermeable core surrounded by these two heterogeneous layers. It is commonly accepted that two different types of porous CSH are associated with each layer. High-density CSH are present inside the inner layer and low-density CSH form inside the outer layer (e.g. Richardson 2000; Tennis and Jennings 2000). Tennis and Jennings (2000) classified them as high-density and low-density, whereas Richardson preferred to call them inner and outer products. In the ensuing, these two types of

CSH are respectively called as internal and external products, denoted  $\text{CSH}^{\text{int}}$  and  $\text{CSH}^{\text{ext}}$ . More precisely, in the inner layer, the  $\text{CSH}^{\text{int}}$  behave as a matrix phase embedding non-diffusive inclusions of CH and AF. Similarly, the external layer has matrix-inclusion type morphology, where CH, AF and some pores play the role of inclusions enclosed in the  $\text{CSH}^{\text{ext}}$ . It is noteworthy that many mineral phases (AF, CH,  $\text{CSH}^{\text{int}}$ ,  $\text{CSH}^{\text{ext}}$ , ...) are involved in the microstructure of HCP and a closer look is given in the next subsection to each one separately.

### 2.1.1.2 Information on the HCP mineral phases

Many phases appear in the mineral composition of HCP and their characteristic sizes can range from the nanometer to micrometer scales. The main solid phases, which volume fractions displayed on Table I.1 in CEM I cement pastes can be estimated by means of the Tennis and Jennings model (2000), are presented in depth below. A particular emphasis is put on the morphology inside the HCP microstructure that is an important aspect for the models developed subsequently.

| W/c  | Anhydrous residuals | $\text{CSH}^{\text{int}}$ | $\text{CSH}^{\text{ext}}$ | CH   | AFt - AFm<br>$\text{C}_4\text{AH}_{13}$ | Hydrogarnet<br>$\text{C}_3(\text{A.F})\text{H}_6$ |
|------|---------------------|---------------------------|---------------------------|------|---|---|
| 0.25 | 19.5                | 38.4                      | 8.7                       | 14.3 | 7.2                                     | 7.3   |
| 0.30 | 13.7                | 37.4                      | 12.0                      | 15.2 | 7.4                                     | 7.2   |
| 0.35 | 9.4                 | 33.9                      | 16.8                      | 15.6 | 7.5                                     | 7.2   |
| 0.38 | 7.5                 | 30.7                      | 20.2                      | 15.6 | 7.3                                     | 7.3   |
| 0.40 | 6.4                 | 28.3                      | 22.6                      | 15.5 | 7.2                                     | 7.3   |
| 0.42 | 5.4                 | 25.7                      | 25.1                      | 15.4 | 7.1                                     | 7.3   |
| 0.45 | 4.3                 | 21.6                      | 28.8                      | 15.1 | 6.9                                     | 7.3   |
| 0.50 | 3.0                 | 14.6                      | 34.8                      | 14.4 | 6.5                                     | 7.5   |
| 0.60 | 1.4                 | 1.0                       | 47.0                      | 13.1 | 5.8                                     | 6.8   |
| 0.65 | 1.0                 | 0.0                       | 47.0                      | 12.5 | 5.5                                     | 6.4   |

**Table I.1: Mineral composition in terms of volume fractions of standard CEM I hydrated pastes obtained by the model of Tennis and Jennings (2000).**

**CSH:** they are formed by hydration of the silicates  $\text{C}_3\text{S}$  and  $\text{C}_2\text{S}$  and represent about half of the paste in terms of volume fractions. The quantity of calcium in the CSH is variable. They are thus characterized by their Calcium over Silicon (C/S) ratio, which can vary from 0.7 in very degraded states to generally about 1.7 in a sound state. At the beginning of the hydration process, a nucleation phase followed by a growing phase of CSH occurs at the surface of cement grains.  $\text{CSH}^{\text{ext}}$  first form a layer around the clinker and hydration process is controlled by diffusion through it. The denser type of CSH, namely  $\text{CSH}^{\text{int}}$ , is then formed inside this

coating. The  $CSH^{int}$  and the  $CSH^{ext}$  have a characteristic size of 10 to 100 nanometres, which makes it very difficult to gain precise information about their geometrical shape. Taylor (1997) describes the  $CSH^{int}$  as a honeycomb or reticular network, while the  $CSH^{ext}$  rather have a foliated structure (Béjaoui et al. 2006), as may be seen on Fig. 1.2.

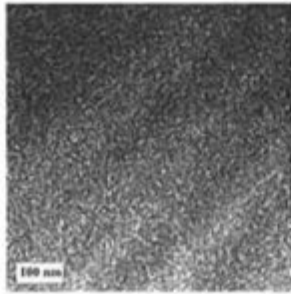
The relative volume fractions of the two types of CSH are computed in this work by means of the Tennis and Jennings model (2000):

$$M_R = 3.017(w/c)\xi - 1.347\xi + 0.538,$$

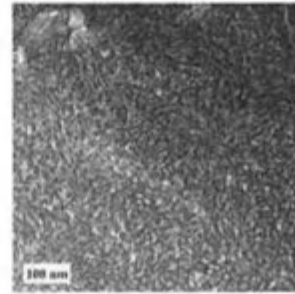
$$c_{CSH^{int}} = \frac{M_t - M_R M_t}{\rho_{CSH^{int}}}, \quad (1.2)$$

$$c_{CSH^{ext}} = \frac{M_R M_t}{\rho_{CSH^{ext}}},$$

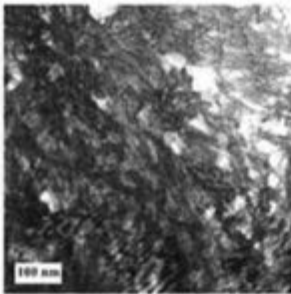
where  $c_{CSH^{int}}$ ,  $c_{CSH^{ext}}$ ,  $\rho_{CSH^{int}}$ ,  $\rho_{CSH^{ext}}$  are respectively the volume fractions and densities of  $CSH^{int}$  and  $CSH^{ext}$ ,  $M_t$  is the total mass of CSH,  $M_R$  is the ratio of the mass of  $CSH^{int}$  to the total mass of CSH,  $\xi$  the hydration rate.



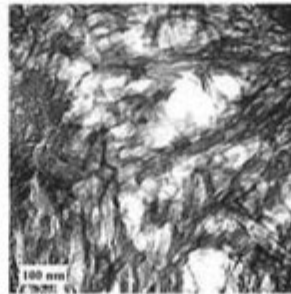
a)  $CSH^{int}$  in a CEM I paste  
with  $w/c = 0.25$



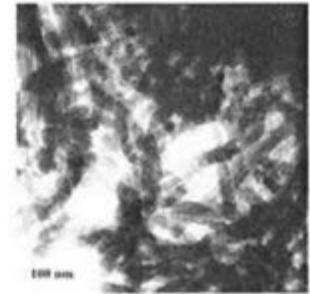
b)  $CSH^{int}$  in a CEM I paste  
with  $w/c = 0.50$



c)  $CSH^{ext}$  in a CEM I paste  
with  $w/c = 0.32$



d)  $CSH^{ext}$  in a CEM I paste  
with  $w/c = 0.43$



e)  $CSH^{ext}$  in a CEM I paste  
with  $w/c = 0.70$

**Figure 1.2: Images of the microstructure of  $CSH^{int}$  and  $CSH^{ext}$  in CEM I 52.5 cement pastes with diverse  $w/c$  ratios obtained by Transmission electron microscopy (TEM) (taken from Béjaoui et al. 2006).**

**CH:** This phase is very important for leaching cases, since it dissolves before any other hydration products. The ordinary Portland cement pastes contain about 15 % in volume of CH but the cement pastes using additives, such as slag or fly ash, generally enclose much less portlandite. CH forms massive crystals, which are often described as platelets or flakes when embedded in HCP (Richardson 2000). Otherwise in non-confined environment, portlandite crystallizes into massive hexagonal plates. Consequently, they are far from being spherical, although information on CH crystals in HCP is insufficient to quantitatively characterize their real shapes inside the microstructure of cement-based materials.

**Aluminates:** The hardened ordinary Portland cement paste contains, in addition to CSH and CH, other major hydration products, produced from reactions involving  $C_3A$ ,  $C_4AF$  and Gypsum: Hydrogarnet, AFm, AFt and Calcium aluminate hydrate ( $C_4AH_{13}$ ). According to Eq. (I.1), AFt, AFm and  $C_4AH_{13}$  are produced by the hydration of  $C_3A$ , whereas Hydrogarnet is produced by the reaction of  $C_4AF$  with portlandite. Though their volume fraction can be rather scarce (about 7 % in volume), those phases have to be accounted for in leaching cases or in sulfatic attacks, since they can be partially or totally dissolved (Adenot 1992). AFt and AFm are usually more abundant in standard cement pastes than Hydrogarnet and  $C_4AH_{13}$  and have received a closer attention from experimentalists. According to Richardson (2000), AFm is present in mature pastes as large irregular plates similar to those of CH and AFt occurs as thin hexagonal prism needles of up to 10  $\mu\text{m}$  in length. AFt is quite easy to observe on the Environmental Scanning Electron Microscopy (ESEM) since they are characterized by long rods when crystallized in non-confined environment. However, according to Tennis and Jennings model, AFt that forms rapidly during the hydration process then react with  $C_3A$  to form AFm and therefore hardly exists in mature cement pastes.

**Unhydrated clinker:** it corresponds to the portion of cement grains that has not reacted with water. The amount of anhydrous residuals present in HCP depends on the w/c ratio and time of hydration. Cement paste micrographs generally tend to show that cement particles do not have spherical shapes. Thanks to very advanced techniques such as X-ray microtomography, cement particles morphology has been rigorously investigated. Garboczi and Bullard (2004), performing recently a spherical harmonic coefficient analysis on microtomographic images of Portland cement grains, managed to characterize quantitatively their real shape (see Fig. I.3). They analyzed about 1200 particles with volume ranging from 1  $\mu\text{m}^3$  to 120000  $\mu\text{m}^3$  and concluded that these particles were definitely non-spherical by plotting their surface area versus their volume. The curve of surface area versus their volume for cement particles was indeed clearly above the spherical one. By fitting their experimental curve, the following result was obtained for the volume  $V$  over surface area  $A$  ratio:

$$\frac{V}{A} = \frac{1}{5.95} V^{1/3}. \quad (\text{I.3})$$

The knowledge of the volume over surface area ratio of real cement particle is a precious piece of information for the modelling of this phase that is further exploited in Part II.

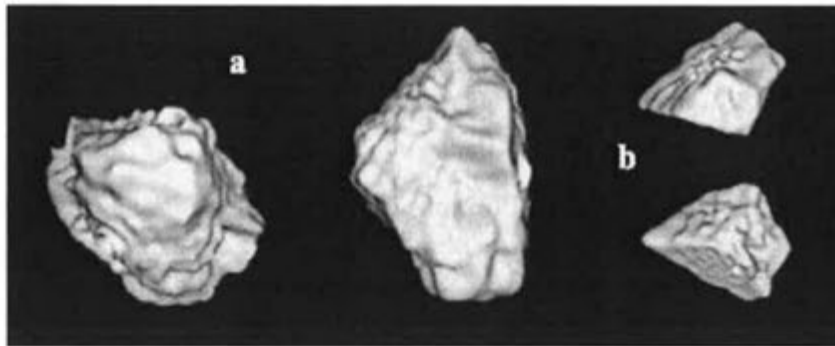


*Figure I.3: Views of cement particles generated from the spherical harmonic expansion (taken from Garboczi and Bullard 2004).*

The previous discussions highlight the complex morphology of all the mineral phases composing HCP. Hence, it is natural to pose the following question: what is the best way to model in a simple and realistic manner these phases? An answer to this question will be provided in Part II.

#### *2.1.1.3 The complex multiscale porosity of HCP*

The HCP described previously (Figs. I.1 and I.2) are complex multi-scale porous media, where the pore size distribution varies by several orders of magnitude (from 1 nm to more than 10  $\mu\text{m}$ ). At the micrometer scale, capillary pores are defined as the remaining space situated between hydrated cement grains. They are originated from the chemical shrinkage of the hydration products or stem from the interstitial space left by water in excess. The CSH, representing about half of the paste in terms of volume fractions, furthermore contain a finer porosity, defined as gel porosity. The  $\text{CSH}^{\text{int}}$  are more porous than  $\text{CSH}^{\text{ext}}$ , the  $\text{CSH}^{\text{int}}$  resulting mainly from higher confinement conditions during hydration reactions. According to the Jennings and Tennis model, the gel porosity comprised in  $\text{CSH}^{\text{int}}$  is about 26 % and the one contained in  $\text{CSH}^{\text{ext}}$  around 36 % in terms of volume fractions. In the present work, the gel pores sizes are assumed to be situated between a few nm and 0.2  $\mu\text{m}$  and the capillary pores ones to range from 0.2  $\mu\text{m}$  and a few  $\mu\text{m}$ , though the definition of these two domains significantly varies in the different classifications for the pore structure of HCP proposed in literature (e.g. Baroghel-Bouny 1994; Daimon et al. 1977; Igarashi et al. 2004; Powers 1948). For example, according to Mindess and Young (1981), the size of the capillary pores may vary from several orders of magnitude (from 10 nm to 10  $\mu\text{m}$ ) and the gel pores from a few

ångströms to 10 nm. It is also noteworthy that some authors differentiate more than two categories of pores in cement pastes (e.g. Daimon et al. 1977) but we limit for simplicity to two main classes of pores.

The pore structure of HCP, especially the capillary porosity, is the subject of many experimental investigations (Taylor 1997). To measure the total porosity of HCP, the simplest technique consists in performing total free water porosity measurements (Gallé 2001). The porosity is practically obtained by measuring the total amount of water removed from saturated pastes after drying them. Other techniques exist but, in the present dissertation, the total porosity is considered to be the value measured by water porosimetry. Two techniques are commonly used to measure the pore size distribution: mercury intrusion porosimetry (MIP) and image analysis on SEM results. In addition, the breakthrough of microtomography and nanotomography could lead to more precise measurements in the oncoming years (Bentz et al. 2002; Burlion et al. 2006; Holzer et al. 2003).

MIP is used to measure the pore size distributions by quantifying mercury able to penetrate the dried material under successively increased pressures. The ability of mercury to pass through pores of a given size depends on the pressure applied. The volume intruded per change in pressure provides the data for calculating the pore size distribution (Gallé 2001). However, Diamond (2000) evidenced the fact that MIP is an inappropriate method for the correct measurement of the pore size distribution in cement-based materials. In particular, he argued that the amount of large pores is underestimated, since most of them are inaccessible to mercury injected at low pressure. In order to attain certain large pores, mercury may indeed be constrained to penetrate through smaller pores. As a consequence, the quantity of small pores is overestimated. Despite these shortcomings, this experimental method gives some insights on the material pore structure in terms of connectivity. Indeed, the measurement of the critical pore or threshold diameter by mercury porosimetry allows for evaluating the largest scale at which percolation, i.e. the formation of a pore cluster connecting one extremity of the material to another, occurs (Diamond 2000). The critical pore diameter is defined as the pore width corresponding to the highest intrusion of mercury per change in pressure, practically determined the maximum of the  $dV/dP$  versus pore diameter curve as plotted in Fig. I.4 (or by the inflection point on the volume intrusion).

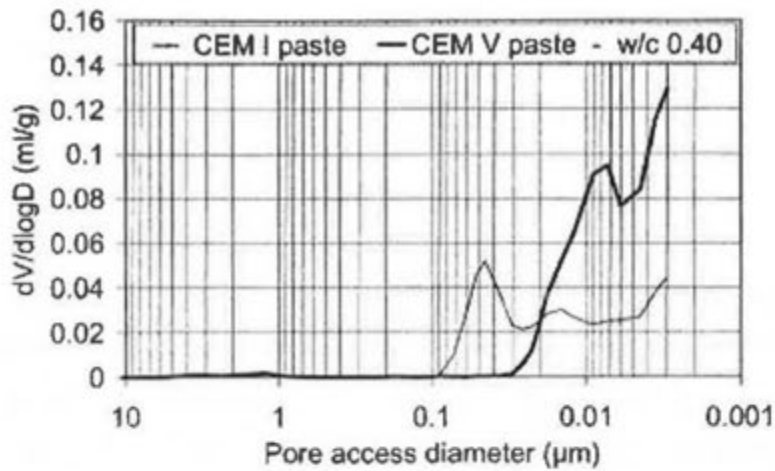


**Figure I.4:** Differential intruded pore volume versus pore diameter curve measured by MIP (taken from Gallé 2001).

According to Katz and Thompson (1987), the threshold diameter permits to identify the less constricted percolating grouping of pores, since this length corresponds to the size of the smallest pore belonging to the percolating ones. It is thus possible to identify the less constricted percolating path in the paste that should logically influence its transport properties (Katz and Thompson 1987). For example, according to the experiments of Gallé et al. (2004), this diameter is about 20 nm for an ordinary CEM I paste with a w/c ratio equal to 0.45. This result shows that the gel pores can percolate through the paste. On the contrary, the larger capillary pores, that are mostly inaccessible to mercury injected at low pressure, may be isolated or connected to each other by a network of gel pores. Values for the threshold diameter can easily be found in the very large data collection of MIP tests available in the open literature (see Table I.2).

Furthermore, other experimental observations confirm the fact that the gel pores should percolate through the paste. Recently, Holzer et al. (2005) asserted that the skeletonization of porosity on 3D-images obtained with the help of nanotomography at resolutions of 20 nm indicated that the pore network is almost completely connected. Béjaoui et al. (2006) also performed an accurate investigation of the pores entrapped in the CSH in CEM I pastes. Their TEM images of CSH<sup>int</sup> show that they keep an invariant morphology characterized by a very finely divided porosity at the nanometre scale. On the contrary, it appears clearly on their TEM observations (see Fig. I.3) that CSH<sup>ext</sup> present diverse morphology depending on the w/c ratio. In particular, the characteristic length of the porosity on their images varies from 10 nm for low w/c pastes to a hundred of nm for high w/c ones. As may be observed on the micrographies of Béjaoui et al. (2006), the gel pores in CSH<sup>ext</sup> are strongly connected for the pastes of medium or high w/c ratios.

The capillary pores can be investigated by image analysis. These techniques have an increasing success in the field of cement-based materials but they are limited by their resolution, generally about  $0.2 \mu\text{m}$  (Scrivener 2004). Nevertheless, they offer the opportunity to measure the size distribution of capillary pores larger than  $0.2 \mu\text{m}$ . Igarashi et al. (2004) measured the volume fraction of capillary pores in different types of cement pastes and mortars by image analysis. The morphology of the capillary pores is very difficult to characterize, though the recent microtomographic images of Rattanasak and Kendall (2005) and of the Visible Cement Data Set (Bentz et al. 2002) could give some insights on their three-dimensional shapes.

| Type of cement paste | w/c  | Sample preparation                | Critical pore diameter |  | Sources                 |
|----------------------|------|-----------------------------------|------------------------|--|-------------------------|
|                      |      |                                   | Sound                  | Leached  |                         |
| CEM I                | 0.45 | Oven-dried at $60^\circ\text{C}$  | 20 nm                  | $0.2 \mu\text{m}$<br>(30 weeks with $\text{NH}_4\text{NO}_3$ ) | (Gallé et al. 2004)     |
| ASTM Type I cement   | 0.45 | Vacuum-dried                      | 40 nm                  |  | (Delagrave et al. 1998) |
| CEM I                | 0.30 | Vacuum-dried                      | 30 nm                  |  | (Richet et al. 1997)    |
| CEM I                | 0.40 | Vacuum-dried                      | 35 - 40 nm             |  | (Richet et al. 1997)    |
| CEM I                | 0.60 | Vacuum-dried                      | 70 - 80 nm             |  | (Richet et al. 1997)    |
| CEM I                | 0.40 | Vacuum-dried                      | 60 nm                  | -  | (Gallé 2001)            |
| CEM I                | 0.40 | Oven-dried at $105^\circ\text{C}$ | 170 nm                 | -  | (Gallé 2001)            |

**Table I.2: Critical pore diameter values measured by MIP tests for various types of cements pastes in sound or leached states issued from diverse sources.**

To summarize, the present subsection pulling together qualitative but also quantitative results obtained on the cement paste porosity with diverse techniques (MIP, SEM, ...) indicates that the percolation of porosity occurs at a scale of several tens of nanometers and that the pore structure of HCP is highly connected at the nanometre scale. It is useful to keep in mind these remarkable insights gained on porosity by experimentalists in the ensuing Parts dedicated to modelling so as to correctly represent the pore structure.

### 2.1.2 *Microstructure of mortars and concretes*

Mortars consist in a mixture of cement pastes and of sand particles, which size ranges from 0.1 mm to 5 mm, in order to improve the packing of these grains. Concretes are obtained by further adding aggregates with sizes varying between 1 mm and about 25 cm. Many studies have evidenced that an interfacial transition zone (ITZ), which thickness ranges from 15 to 40  $\mu\text{m}$  (Hashin and Monteiro 2002), forms between the aggregate particles and the cement. It has been noted that the thickness of the ITZ layers is quite independent from the size of the particle. The ITZ is generally more porous than the cement paste (Lutz and Zimmerman 2005) but is also likely to contain more portlandite and aluminates (Sun et al. 2007) because of the wall effect. The volume fractions occupied by the ITZ is difficult to gain experimentally, because the diverse ITZ layers tend to overlap. But Lu and Torquato (1992) developed a statistical model based on a representation of porosity by a polydispersed system of spheres, which may be employed for estimating the latter quantity. Due to these overlaps, the ITZ is furthermore prone to percolate through the microstructure of mortars or concretes (Scrivener and Nematı 1996) and strongly influences their effective properties (Wang et al. 1988).

## 2.2 **Microscopic and macroscopic properties of cement-based materials**

For their practical use as a construction material, it is necessary to know some basic properties of concrete materials, such as their Young modulus, strength, permeability or diffusivity. These properties may significantly vary from one material to another as will be shown subsequently. Modelling approaches aiming at estimating these characteristics are thus useful to avoid measuring them for each type of cement or concrete. But the development of model for predicting their properties is often constrained by the lack of data concerning the transport and mechanical features of the residual clinker, hydrated phases or aggregates. Therefore this subchapter gathers useful experimental results for the properties of both the cementitious materials and their main constituents at different scales.

### 2.2.1 *Information on the elastic properties of the HCP elementary phases*

At the microscopic scale, the measurements of the elastic properties of the phases composing the microstructure of HCP are mainly carried out by nanoindentation and, at the macroscopic scale, by diverse techniques, such as resonance frequency measurements or by dynamic tests. The nanoindentation tests consist in pushing an indenter with a diamond tip into the specimen. The characteristic length of the indentation area is on the order of  $10^{-6}$  m, and the indentation depth varies in the range of 300–500 nm (Velez et al. 2001). The complete  $F-h$  response is recorded during the test, where  $h$  is the depth of penetration into the specimen and  $F$  is the load applied. The Young modulus can be extracted by analyzing the unloading part of the  $F-h$  curve according to a model for the elastic contact problem. From the measurement of

the effective modulus  $E_t$  of the test area, the elastic modulus  $E_r$  of the phase  $r$  is obtained using the equation (Damidot et al. 2003):

$$\frac{1}{E_t} = \frac{1 - \nu_d^2}{E_d} + \frac{1 - \nu_r^2}{E_r}, \quad (\text{I.4})$$

where  $\nu_d$  and  $E_d$  are the Poisson ratio and the elastic properties of the diamond indenter and  $\nu_r$  is the Poisson ratio of the measured phase. One of the shortcomings from nanoindentation technique is that the Poisson ratio of the material tested is not accessible. The errors of the measures by indentation thus mainly come from the fact that the Poisson ratio elevated to square in the previous formula has to be estimated. Nevertheless, the Young moduli of the HCP elementary phases (see Table I.3) measured by nanoindentation represent crucial pieces of information for the prediction of the mechanical behaviour of cementitious materials.

Different nanoindentation tests measuring the Young moduli of clinker and CH have been performed (e.g. Boumiz et al. 1997; Damidot et al. 2003; Velez et al. 2001) and are furthermore in quite good agreement with each others. The values displayed on Table I.3 are retained as reference values for the micromechanical computations in Part II. The measurements performed on cement pastes exposed to a leaching process, explained in the ensuing chapter, are also displayed. Nevertheless, it is useful to recall that these measures are made by indenting on surfaces representative of the CSH with a minimal area of  $1 \mu\text{m}^2$  and therefore enclose not only the CSH but also some porosity ( $< 1 \mu\text{m}$ ) and probably a certain volume fraction of other hydration products, such as CH or AF phases, that is very difficult to quantify. These two phases of CSH are however considered as homogeneous materials with elastic properties, which may be identified by nanoindentation technique, and aluminates, such as AFt or hydrogarnet, are thus assumed to have similar elastic properties to the ones measured for the two types of CSH (Table I.3). In the ensuing, it is supposed that the entire gel porosity is comprised in the measurements of the  $\text{CSH}^{\text{ext}}$  and  $\text{CSH}^{\text{int}}$  mechanical properties.

| Phases   | SOUND HCP    |              | LEACHED HCP  |              | References   |
|--|--------------|--------------|--------------|--------------|--|
|  | E (GPa)      | $\nu$        | E (GPa)      | $\nu$        |  |
| CH   | <b>42.3</b>  | <b>0.324</b> | <b>0</b>     | <b>0</b>     | Monteiro and Chang (1995)<br>Constantinides and Ulm (2004) |
| Unhydrated clinker                                 | <b>117.6</b> | <b>0.314</b> | <b>117.6</b> | <b>0.314</b> | Boumiz et al. (1997)                                       |
| Capillary Porosity                                 | <b>0</b>     | <b>0</b>     | <b>0</b>     | <b>0</b>     |  |
| Aft, Hydrogarnet, C <sub>4</sub> AH <sub>13</sub>  | <b>22.4</b>  | <b>0.25</b>  | <b>0</b>     | <b>0</b>     | Assumed by Kamali (2003)<br>Haecker et al. (2005)          |
| AFm  | <b>42.3</b>  | <b>0.324</b> | <b>0</b>     | <b>0</b>     | Assumed by Kamali (2003)                                   |
| CSH gel (CSH <sup>ext</sup> + CSH <sup>int</sup> ) | <b>22.4</b>  | <b>0.25</b>  | <b>22.4</b>  | <b>0.25</b>  | Damidot et al. (2003)                                      |
| CSH <sup>ext</sup>                                 | <b>21.7</b>  | <b>0.24</b>  | <b>3</b>     | <b>0.24</b>  | Constantinides and Ulm (2004)                              |
| CSH <sup>int</sup>                                 | <b>29.4</b>  | <b>0.24</b>  | <b>3</b>     | <b>0.24</b>  | Constantinides and Ulm (2004)                              |

\* The numerical values used for the calculations are in bold.

*Table I.3: Elastic properties of the main phases in a sound state present in HCP microstructure, taken from diverse sources in the literature.*

### 2.2.2 Elastic properties of HCP

Diverse experiments have been performed for measuring the macroscopic elastic moduli of HCP, for instance by resonance frequencies techniques (see e.g. Wang et al. 1988; Gallé et al. 2004). This type of measurement is also used for testing mortar and concrete (Sun et al. 2007; Wang et al. 1988). In the resonance method, the test specimen is made to vibrate as a whole in one of its natural frequency modes (transverse, longitudinal, or torsional). The resonance frequency depends on the geometry of the sample, on its density, its pores distribution and on its elastic properties. As an illustration, the Young moduli of different HCP gained by diverse resonance frequency tests are gathered against their total water porosity on Table I.4. The Young moduli are shown to strongly depend on the HCP porosity: the value obtained for HCP with a low porosity paste is about 50 % higher than for a high porosity HCP ( $w/c = 0.50$ ).

| Material                             | E (GPa) | Total water porosity | References                       |
|--------------------------------------|---------|----------------------|----------------------------------|
| CEM I 52.5 paste<br>(w/c = 0.50)     | 15.6    | 0.405                | Carde (1996)                     |
| OPC type I paste<br>(w/c = 0.50)     | 22.8    | 0.328                | Constantinides<br>and Ulm (2004) |
| CEM I 52.5 HTS<br>paste (w/c = 0.45) | 23      | 0.326                | Gallé et al. (2004)              |

*Table I.4: Young moduli measured experimentally of standard cement pastes, taken from diverse sources in the literature.*

A way to increase the stiffness of the cement pastes consists in adding rigid sand particles or aggregates to these materials thus forming mortars and concretes.

### 2.2.3 Elastic properties of mortars and concretes

The sand particles, which Young modulus is measured as 86.7 GPa by Wang et al. (1988), are much stiffer than the cement pastes. One would thus expect that the Young modulus should significantly increase as the volume fractions of sand aggregates augment. But the experiments of Wang et al. (1988) showed only a 25 % increase of the overall Young modulus of the mortars with 40 % of sand aggregates compared to the plain cement paste. This result may be due to a weakening effect of the ITZ that is more porous than the bulk cement paste (Sun et al. 2007). Unfortunately, the elastic moduli of the ITZ layers are very difficult to measure experimentally, since they do not really appear as a homogeneous interface but rather as a graded one. To address this lack of data, many micromechanical approaches modelling the ITZ as a homogeneous phase have been developed to estimate their effective elastic moduli from an inverse approach (see e.g. Hashin and Monteiro 2002). However, Sun et al. (2007) noticed a strong dispersion between the Young modulus of ITZ proposed in literature as the following expression:

$$E_{ITZ} = a E_{HCP}, \quad (I.5)$$

where  $a$  is a constant with a value that is identified between 0.2 and 0.8 depending on the model and on the thickness of the ITZ retained by the authors transition (Hashin and Monteiro 2002; Ramesh et al. 1996; Yang 1998) and  $E_{HCP}$  is the Young modulus of the corresponding plain paste. It is however emphasized that, even though the ITZ is generally modelled as a homogeneous interphase, it would be more realistic to model it as an inhomogeneous one (Lutz and Zimmerman 2005). In the case of concrete, porous ITZ layers still exist but their influence on the physical behaviour of concrete seems less important than in mortars probably because the volume fraction of ITZ is more important in the case of mortars, since the aggregates have much smaller size. That's why these interphases are generally not taken into

account in the models developed to predict the physical properties of concrete (Constantinides and Ulm 2004).

#### *2.2.4 Transport properties of cement-based materials*

The main transport processes in concrete include diffusion, permeation, and convection. Diffusion describes the transport for instance of a particular gas (e.g. CO<sub>2</sub> vapor) in the gaseous phase or dissolved ions as a result of a concentration gradient (Dullien 1992). Permeation describes the flow of a fluid (e.g. water or air) as a result of gravity or a pressure gradient. Convection (or advection) is the process that describes the transport of a solute (e.g. chloride or sulfate ions) as a result of the bulk moving fluid. The transport processes in most concrete structures can be complex and may involve more than one of the referred transport mechanisms. In most of these processes, water is the principal medium by which aggressive agents (such as chloride or sulfate ions) are transported into the concrete.

However, in the context of the long-term behavior of underground concrete facilities, the material is generally assumed to be in saturated conditions in the nominal storage phase so that the chemical species in pore solution are transported by diffusion through the concrete. Convection is neglected, since it is assumed that there is no pressure gradient in water. As may be observed in Fig. I.5, the macroscopic diffusion coefficients of cement pastes strongly vary from one paste to another, with sudden variations occurring for certain w/c ratios. The causes of these variations are discussed in details in Part III.

Concerning the transport properties of mortars and concretes, some authors (Nguyen et al. 2006) argue that the presence of aggregates in a hydrated cement paste matrix probably has two opposite effects that compensate each other. On the one hand, it increases the tortuosity of the matrix and reduces the total space available to diffusion and, on the other hand, the high porosity of ITZ enhances the diffusion process.

As a result of the strong variations between the diffusivities of cement-based material, aggressive agents diffuse more or less rapidly through the material, which is a key issue that influences the long-term degradation of concrete facilities.

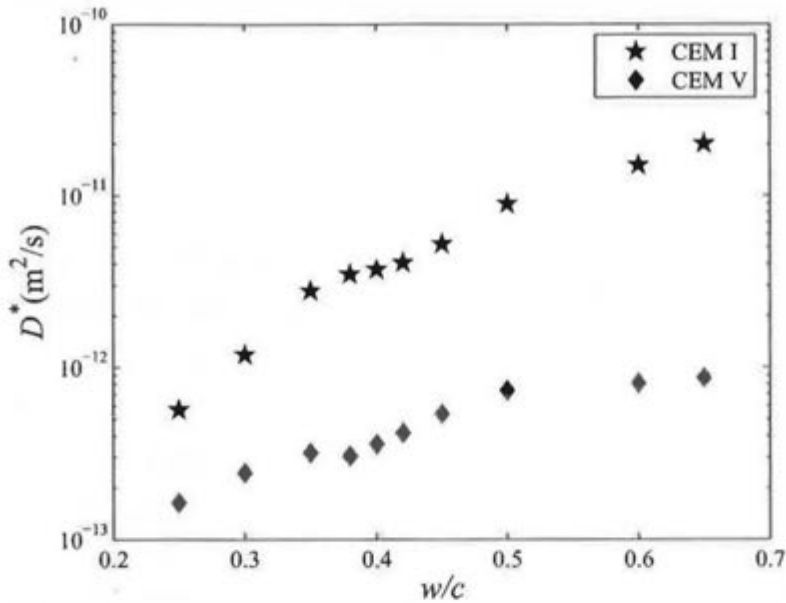


**Figure I.5 (semi-logarithmic scale): Evolution of the macroscopic diffusion coefficients measured experimentally for both sound CEM I and CEM V pastes with their w/c ratio, taken from diverse sources in the literature (adapted from Richet et al. 1997).**

The present chapter has presented some basic features of cementitious materials in a sound state. However, these materials are sensitive to many degradation factors and therefore the evolution with time of their microstructure is strongly conditioned by their environment. The next chapter focuses on some of these deterioration sources that influence the behavior of cementitious materials.

### 3 DEGRADATIONS OF CEMENT-BASED MATERIALS SUBJECTED TO LEACHING

Various degradation mechanisms may affect the concrete materials under service life. They may be altered for instance by: (i) chemical reactions caused by ionic migration between the interstitial solution and ground water; (ii) damage due to external mechanical loadings and to possible precipitation of secondary solid phases generating internal pressures; (iii) thermal expansion due to strong temperature variations; (iv) creep and shrinkage phenomena. The present dissertation only treats the first two deterioration factors that may strongly impact the durability of concrete underground infrastructures, such as the ones for the disposal of long-term nuclear wastes. In these facilities, concrete is for instance employed in the engineering barrier that serves as one of the protections against the propagation of radionuclides. In this context, the chemical degradation mechanisms due to leaching and then the damage

processes, which may alter the diffusive properties of the material, are presented. In both cases, their effects on the microstructure and the overall behaviour of the concrete are pointed out. Finally, the possible interactions between these two degradation processes are investigated.

### 3.1 Chemical deterioration of cementitious materials caused by leaching

The chemical alteration of concrete is a phenomenon that has to be carefully taken into account for predicting the long-term durability of underground structures. In contact with ground water, the material is subjected to chemical reactions originated by the migration of ions, such as calcium or sulfates, caused by concentration gradients between the pore solution and the ground water. The material composed of a solid skeleton and the interstitial solution is initially in a chemical equilibrium state. The concentration of ions in the pore solution is consequently imposed by the mineral composition of the solid part. The movement of ions towards the exterior and inside the material disturbs this equilibrium state and causes dissolution-precipitation reactions in the material to compensate the variation of ions concentrations in the pore solution. This chemical degradation process by contact with pure water is generally called leaching or decalcification, since it principally concerns the calcium ions and the mineral phases containing calcium. However, ground water may contain aggressive chemical species. If the water in contact with the concrete is rich in sulfates or chlorides, we rather speak about external sulfate or chloride attacks but these attacks are out of our scope.

The propagation of the zones affected by leaching is usually very low, since pure water leaches only 4 cm of a concrete structure in roughly 300 years (Adenot 1992), but may reveal detrimental for long-term industrial applications. The development of an accelerating method using ammonium nitrate as aggressive solution (Carde 1996) has significantly enhanced the knowledge about the long-term leaching of cement-based materials. The effects of leaching on the microstructure of HCP are investigated below.

The solid phases containing calcium are the most sensitive to leaching. The CH crystals dissolve before any other hydration products during decalcification process according to the following reaction:



The CSH are then progressively degraded but do not totally dissolve. More precisely, their C/S ratio gradually diminishes from around 1.65 for the intact product to approximately 0.8 during this attack (Heukamp 2002). As the leaching proceeds, the aluminous phases are decalcified and partially dissolved. A picture taken from Adenot (1992) is proposed to

illustrate the progressive degradation of HCP by the stepwise dissolution of its hydration products (see Fig. I.6).

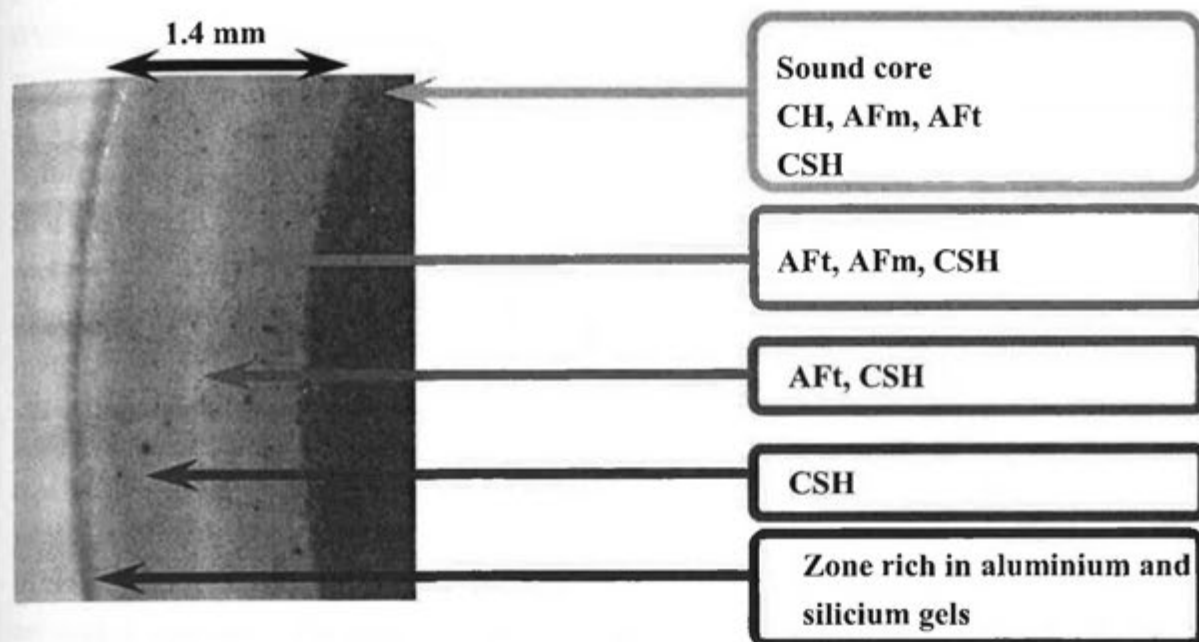


*Figure I.6: Photo of a CEM I 42.5 paste sample with  $w/c = 0.40$  leached during 3 months by pure water (taken from Adenot 1992).*

A convenient variable to describe in good approximation the leaching process is the calcium concentration in the pore solution  $C_{Ca}$ . Fig. I.7, adapted from Bary and Béjaoui (2006), who performed numerical simulations with the chemical equilibrium code CHESS (van der Lee and de Windt 2002), shows the progressive decrease of the calcium concentration in the solid phase  $S_{Ca}$  as a function of  $C_{Ca}$  with the hypothesis that there is no alkalis in solution and that CSH dissolution is discretized by using 3 CSH of diverse C/S ratios. A multi-linear simplification of the CHESS results is also plotted on Fig. I.7 to approximate the progressive decalcification of the hydration products. More precisely, the degradation is supposed to be, in terms of the volume of solid phase replaced by porosity, linearly related to the calcium concentration in pore solution  $C_{Ca}$ : CH dissolves between  $C_{Ca} = 21.54$  and  $C_{Ca} = 20.31$  mol/m<sup>3</sup>, CSH between  $C_{Ca} = 20.31$  and  $C_{Ca} = 1.09$  mol/m<sup>3</sup>, and AF between  $C_{Ca} = 20.31$  and  $C_{Ca} = 3.08$  mol/m<sup>3</sup>.

The porosity measurements with water and MIP for both asymptotically leached and intact pastes allow for a quantitative analysis of the microstructural changes with leaching (see Table I.5). To obtain a homogeneously degraded paste, the latter is exposed to a very aggressive ammonium nitrate solution during a number of weeks that depends on the size of the sample (see e.g. Heukamp 2002). On Table I.5, the total porosity in the material appears almost doubled in the uniformly leached state.

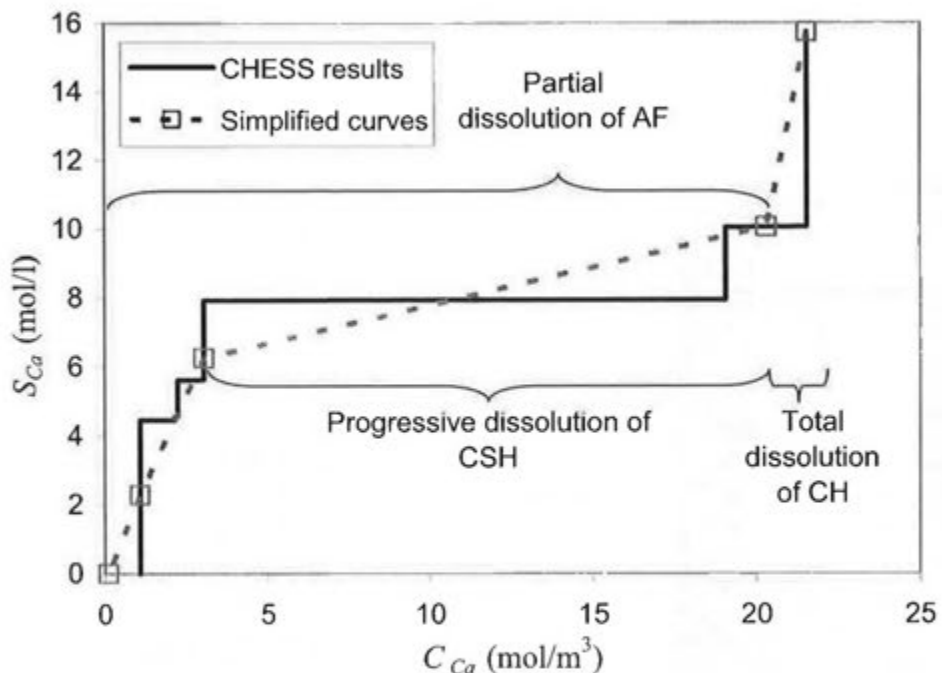


**Figure I.7: Degradation process of the main hydrated phases in terms of calcium concentration in solid phase  $S_{Ca}$  as a function of calcium concentration in solution  $C_{Ca}$  (line = results obtained with the chemical equilibrium code CHES; dotted line = simplified curve) (adapted from Bary and Béjaoui 2006).**

| Phases   | CEM I 52.5 paste of Origny (w/c = 0.40)                 | Lafarge CEM I 52.5 HTS paste (w/c = 0.45)               | CEM I 42.5 paste of Origny (w/c = 0.50)                 | OPC type I paste (w/c = 0.50) |
|--|---|---|---|-------------------------------|
| References   | Moranville et al. (2004)                                | Gallé et al. (2004)                                     | Carde (1996)  | Heukamp (2002)                |
| Estimated hydration rate                           | 0.76  | 0.88  | 0.8   | 0.8                           |
| Initial porosity measured by water                 | 0.39  | 0.326   | 0.405   | 0.397                         |
| Leaching tests                                     | 19 days with 6M of $NH_4NO_3$                           | 16 weeks with 6M of $NH_4NO_3$                          | 1 day with 5.46M of $NH_4NO_3$                          |                               |
| Porosity measured by water on the leached specimen | -   | 0.612   | 0.5098  | 0.632                         |
| Accelerated leaching rate*                         | 1.56 mm d <sup>-0.5</sup> (0.140 mm d <sup>-0.5</sup> ) | 1.74 mm d <sup>-0.5</sup> (0.190 mm d <sup>-0.5</sup> ) | 1.31 mm d <sup>-0.5</sup> (0.125 mm d <sup>-0.5</sup> ) | 2.25 mm d <sup>-0.5</sup>     |

\*Pure water leaching rates are in parenthesis to give a comparison

**Table I.5: Table summarizing some important experimental results of accelerated leaching tests of HCP, taken from diverse sources in the literature.**

Concerning the totally decalcified state, Bary and Béjaoui (2006) assumed that all the CH, half of the AF phases and 5 % of the CSH are dissolved and replaced by additional capillary

pores. Moreover, the internal porosity of CSH is likely to increase because of its degradation (Heukamp 2002). To quantify this porosity, it is proposed to compare the measure of total porosity by MIP with the sum of the initial capillary porosity and the additional one issued from the complete leaching of CH. The difference obtained is then assumed to be attributable to the CSH degradation and the partial one of AF. This empirical method is applied to a CEM I paste with  $w/c = 0.45$  and the values of porosity comprised in the CSH collected in Table I.5 before and after leaching indicate that a total volume fraction of supplementary percolating fine gel porosity of 0.04 appears in the CSH during the decalcification process. In the case of mortar and concrete, the degradation mainly takes place in the cementitious matrix, the aggregates being more resistant to leaching. The kinetics of degradation of mortars is however quite similar to the ones of HCP (Bourdette 1994).

The leaching experiments presented on Table I.5 (e.g. Gallé et al. 2004) reveal that the resistance of cement-based materials to chemical degradation can vary a lot of a material to another. Therefore, modelling approaches aiming at estimating the physical properties of these materials are of high interest to avoid performing degradation tests for each type of cement or concrete. The models existing in literature (Adenot and Buil 1992; Gérard 1996) are treated more in depth in Part V and our own numerical tool will be developed to accurately reproduce the leaching of cementitious materials.

## 3.2 Experimental insights on the chemo-mechanical degradation of leached cement-based materials

### 3.2.1 Impact of leaching on the residual mechanical behaviour

Different experimental works (e.g. Carde 1996; Constantinides and Ulm 2004; Galle et al. 2004; Heukamp et al. 2005; Le Bellégo 2001; Nguyen 2005) have been focused on the effects of decalcification of cementitious materials on their residual mechanical properties. They generally consist in carrying out mechanical tests, such as a uniaxial compression or traction test (e.g. Carde 1996; Heukamp et al. 2005; Nguyen 2005) or 3 points flexion tests (e.g. Le Bellégo 2001), on samples previously subjected to an accelerated leaching process. These experiments, qualified as « residual resistance », systematically evidence a detrimental effect of leaching on the Young modulus and the residual strength of the material.

For instance, a sharp diminution of the HCP elastic properties was measured by Carde (1996), where total dissolution of CH caused a reduction of 63 % in the Young modulus of a CEM I 42.5  $w/c = 0.50$  cylindrical sample with a 30 mm diameter. Gallé et al. (2004) measured a decrease from 23 GPa to 7 GPa (a 71 % reduction) on the dynamic elastic modulus of a cylindrical sample with a 40 mm diameter of a CEM I 52.5 HTS  $w/c = 0.45$  paste subjected to a complete degradation during 30 weeks. Constantinides and Ulm (2004) further measured

that the stiffness modulus of an asymptotically leached OPC type I paste decreased to about 3 GPa representing a 84 % decay. To obtain a uniformly degraded paste, the sample with a diameter of 11.5 mm was attacked by an ammonium nitrate solution during 5 months. The differences between these measurements (Carde 1996; Gallé et al. 2004; Constantinides and Ulm 2004) may be explained by the fact that the pastes are more or less chemically altered, given that the diameters of the samples and the leaching time considered vary from one author to another. However these experiments do not account for the possible effects of damage on the chemical degradation processes that are investigated below.

### ***3.2.2 Influence of damage on the leaching process***

Chemical degradations are potentially influenced by the presence of microcracks because they may provide preferential pathways for fluid or ions to pass through. Many studies have reported that cracks can dramatically influence the transport properties of concrete, in particular its permeability (e.g. Wang et al. 1997). For example, Wang et al. (1997) studied the permeability of cracked concrete and concluded that cracks generally accelerated water permeation in concrete. Jacobsen et al. (1996) investigated the effects of cracking on chloride transport in concrete and found that internal cracking increased the chloride penetration rate 2.5 to 8 times when compared with undamaged specimens.

Tognazzi (1998) carried out an experimental campaign to investigate the effects of damage induced by compressive or tensile loads on mortar effective diffusivity. First, displacement-controlled mechanical tests were performed on mortar specimens so as to generate different states of cracking. A visible impact of the damage created inside the material on its diffusivity increasing by 150-200 % was noticed for samples having attained the post-peak regime of the mechanical test. This influence may be attributed to the coalescence of cracks. On the contrary, load induced damage does not appear to influence the diffusion properties substantially at the peak load due to the discontinuous and localized nature of the crack pattern. Further experimental works confirm the visible effect of damage on the material degradation by putting in evidence the existence of chemically deteriorated zones around artificial cracks (Tognazzi 1998). It is also noteworthy that Yang et al. (2006) draw the same type of conclusions in their work on water absorption and electrical conductivity of concrete damaged by tensile loading and freeze and thaw cycling.

The material diffusivity therefore depends on the characteristics of the crack system, like its connectivity and its distribution. However, it must be emphasized that the influence of cracks on the diffusivity may be less important than the effects of the dissolution due to leaching that may augment the effective diffusivity by a few orders of magnitude (Tognazzi 1998).

### 3.2.3 Fully coupled experiments

The experiments entirely coupling damage and chemical degradation are rare, even though they are useful for assessing the material durability. Le Bellego (2001) and Schneider and Chen (1998; 2005) have conducted such tests, called « life-time » experiments, where a mortar or concrete beam is simultaneously subjected to mechanical solicitations and to a chemical attack by an aggressive solution of ammonium nitrate. More precisely, the inferior part of the beam is simultaneously sollicitated in traction because of the flexural load (Schneider and Chen 1998; 2005) or displacement (Le Bellégo 2001) imposed at the center of the upper face and immersed in an ammonium nitrate solution. These tests present the advantage of sollicitating in traction the most chemically degraded part of the beam and generate in that zone open cracks that are susceptible to enhance the leaching process.

In Schneider and Chen (2005), mortar and concrete samples are subjected to a flexural load such as the macroscopic stress supported by the material varies by 30 to 50 % of its ultimate strength. For a stress equal to 30% of the maximal one, they showed that the influence of creep was low enough to be neglected. These experiments lead to the complete rupture after only a few months.

In Le Bellégo (2001), a displacement is imposed on the center of the upper face of a mortar beam, the lower face being in contact with a 6M  $\text{NH}_4\text{NO}_3$  solution. This flexural displacement is small enough so that no damage should occur in a beam that has not undergone any chemical attack. However, the maximal stresses inside the beam in flexion attain about 80 % of the maximal ultimate strength and, at this level, the creep effects are not negligible. They noticed that a lower strength value of the mortar was obtained in this fully coupled experiments compared with residual mechanical tests. Nevertheless, it is difficult to judge if this decrease is due to the influence of damage on the chemical alteration or rather caused by creep.

## CONCLUSIONS OF PART I

The present Part has collected experimental insights of various types on cement-based materials. First, it was shown that these materials have a complex multi-scale heterogeneous microstructure. The latter is an intricate mixture of different solid phases and porosity. The relative volume fractions of these different components can significantly change from one cement-based material to another, depending for instance on its w/c ratio or its hydration degree. Furthermore, it has been highlighted that strong contrasts may exist between the properties of these diverse phases. As a result, the macroscopic features of the concrete materials vary a lot depending on its composition and its microstructure. Homogenization models based on a simplified representation of the microstructure of cementitious materials

---

will therefore be developed in Parts II and III to predict their effective elastic and diffusive properties.

Some important aspects of the long-term deterioration factors, such as chemical alteration and damage, of HCP have been presented. In particular, their consequences on the microstructure and the material physical properties have been underlined. All the experimental results issued from residual resistance tests (Carde 1996; Gallé et al. 2004; Le Bellégo 2001) and from lifetime experiments (Le Bellégo 2001; Schneider and Chen 1998; 2005) evidence the detrimental interactions between chemical deterioration and damage. It shows the importance to thoroughly account for the couplings between these degradation factors to predict the durability of cement-based materials. These experiments will be discussed more in depth in Part V that is devoted to the chemo-mechanical simulations.

**Part II****PREDICTION OF THE EFFECTIVE ELASTIC PROPERTIES OF CEMENT-BASED MATERIALS**

The purpose of the present Part is to elaborate a realistic homogenization model to predict the effective elastic properties of cement-based materials and their evolution with time. In particular, the model proposed should be capable of correctly estimating the stiffness reduction of these materials due to leaching. The interest of using homogenization techniques is to develop an approach applicable to any cementitious material, provided its composition and the properties of elementary phases are accurately known.

In the first chapter of Part II, diverse analytical homogenization schemes are reviewed so as to find the best suited one for predicting the elastic properties of cementitious materials. Micromechanical models aim at estimating the effective macroscopic properties of a heterogeneous material from the knowledge of the geometric and physical characteristics of its various microstructural components. Due to the plethora of existing micromechanical schemes (e.g. Ma et al. 2004; Milton 2002; Torquato 2001), the review is only limited to matrix-inclusion type schemes with a particular emphasis on the double-inclusion type models that have been the subject of some interesting developments in the last decade. The respective advantages and drawbacks of these homogenization methods presented in a concise way are discussed and the probable connections existing between these different theories are highlighted. Some improvements for the scheme developed by Hori and Nemat-Nasser (1993) are also proposed. The validity range of the reviewed schemes is tested by comparing their predictions with numerical results on well-defined cases. On the basis of this comparative study, the Interaction Direct Derivative (IDD) model due to Zheng and Du (2001) is chosen for it is versatile and simple of use. The Generalized Self-Consistent Scheme (GSCS) is also found to be of interest for composites with coated inclusions.

The second chapter focuses on the effects of particle phase shapes on the effective isotropic linear elastic moduli of hardened cement pastes (HCP). In most micromechanical models applied to cement pastes (e.g. Constantinides and Ulm 2004; Neubauer et al. 1996), particulate phases are modeled as spheres. However, experimental observations clearly show that certain of them are far from being spherical. An attempt to develop a more realistic micromechanical model is proposed by using spheroidal inclusions and including a novel morphological parameter. The latter is identified on the basis of experimental results issued for example from microtomographic images of Portland cement grains and HCP.

In the first Part of the thesis dedicated to the microstructure and the properties of cement-based materials, the main phases composing the microstructure of cement and concrete have been identified as well as their mechanical and diffusive characteristics. On the basis of these results and of the microstructural observations of Part I, the third chapter of the present Part aims at building a multi-scale description with a matrix-inclusion morphology of the microstructure of cement-based materials for predicting the elastic properties of HCP, mortars and concretes, respectively.

## 4 INTRODUCTION TO EFFECTIVE-MEDIUM THEORIES (EMTs)

### 4.1 Fundamental principles of homogenization methods

#### 4.1.1 General principles of homogenization methods

The first step of these methods consists in representing the microstructure of the concerned material by a representative volume element (RVE) composed of a matrix phase, indexed by  $M$ , and of  $P$  particulate phases, which are assumed to be individually homogeneous. Their compliance tensors are respectively denoted by  $\mathbb{S}_M$  and  $\mathbb{S}_r$  ( $r = 1, \dots, P$ ). Fig. II.1 illustrates schematically a RVE.



*Figure II.1: Schematic illustrating the replacement of the heterogeneous RVE by an equivalent homogeneous medium.*

Each particulate phase  $r$  consists of inclusion particles  $V_j^r$  ( $j = 1, \dots, n_r$ ) that are of same shape but can be of different sizes or orientations. Let  $V$  be the domain occupied by the RVE of the heterogeneous material and let  $V^r$  correspond to the sub-domain of inclusion phase  $r$ . In what follows, we designate the boundary surface of  $V$  by  $\partial V$  and the volume fraction of phase  $r$  by  $c_r$ .

The RVE is subjected to uniform boundary tractions over its surface  $\partial V$ :

$$\mathbf{t}_n = \boldsymbol{\sigma}^\infty \cdot \mathbf{n} \text{ on } \partial V, \quad (\text{II.1})$$

where  $\mathbf{t}_n$  denotes the traction vector,  $\mathbf{n}$  designates the outward normal unit vector to the surface  $\partial V$  and  $\boldsymbol{\sigma}^\infty$  is a constant stress tensor. At the scale of the heterogeneities of the RVE, the equilibrium law and Hooke's constitutive one are written in the following manner:

$$\operatorname{div} \boldsymbol{\sigma}(\mathbf{x}) = 0, \quad \forall \mathbf{x} \in V, \quad (\text{II.2})$$

$$\boldsymbol{\varepsilon}(\mathbf{x}) = \mathbb{S}(\mathbf{x}) : \boldsymbol{\sigma}(\mathbf{x}), \quad \forall \mathbf{x} \in V, \quad (\text{II.3})$$

where  $\mathbb{S}(\mathbf{x})$ ,  $\boldsymbol{\sigma}(\mathbf{x})$  and  $\boldsymbol{\varepsilon}(\mathbf{x})$  are respectively the microscopic compliance, stress and strain tensors at a given point  $\mathbf{x}$  of the RVE. The operator ':' indicates a double contraction. The macroscopic stress tensor  $\bar{\boldsymbol{\sigma}}$  is defined as the volume average  $\langle \boldsymbol{\sigma} \rangle_V$  of the microscopic one  $\boldsymbol{\sigma}$  over  $V$  and can be shown to be equal to  $\boldsymbol{\sigma}^\infty$  (e.g. Zaoui 1997):

$$\bar{\boldsymbol{\sigma}} = \frac{1}{V} \int_V \boldsymbol{\sigma}(\mathbf{x}) dV = \boldsymbol{\sigma}^\infty. \quad (\text{II.4})$$

The ensuing relation is also obtained from Eq. (II.3) by performing averaging operations on the entire volume of the RVE:

$$\langle \boldsymbol{\varepsilon} \rangle_V = \mathbb{S}^* : \langle \boldsymbol{\sigma} \rangle_V, \quad (\text{II.5})$$

where  $\langle \boldsymbol{\sigma} \rangle_V$  and  $\langle \boldsymbol{\varepsilon} \rangle_V$  are respectively the averages of the microscopic stress and strain tensors on the volume of the RVE and where  $\mathbb{S}^*$  is the compliance tensor of the equivalent effective medium (Fig. II.1). In the case of a macroscopically isotropic material, the latter tensor may be written in terms of the macroscopic bulk and shear moduli of the heterogeneous material, respectively denoted as  $K^*$  and  $G^*$ :

$$\mathbb{S}^* = (3K^*)^{-1} \mathbb{J} + (2G^*)^{-1} \mathbb{K}, \quad \text{with } \mathbb{J} + \mathbb{K} = \mathbb{I} \quad \text{and} \quad J_{ijkl} = \frac{1}{3} \delta_{ij} \delta_{kl}, \quad (\text{II.6})$$

where  $\mathbb{J}$  and  $\mathbb{K}$  are the hydrostatic and the deviatoric operators and where  $\mathbb{I}$  is the fourth-order identity tensor. The effective Young modulus  $E^*$  and Poisson ratio  $\nu^*$  can simply be deduced from these macroscopic bulk and shear moduli by the intermediary of:

$$E^* = \frac{9K^*G^*}{3K^* + G^*} \quad \text{and} \quad \nu^* = \frac{3K^* - 2G^*}{6K^* + 2G^*}. \quad (\text{II.7})$$

It is easy to show that the macroscopic strain tensor  $\bar{\boldsymbol{\varepsilon}}$  can be expressed in terms of the phase strain averages,  $\bar{\boldsymbol{\varepsilon}}_r$  and  $\bar{\boldsymbol{\varepsilon}}_M$  as:

$$\bar{\boldsymbol{\varepsilon}} = (1 - \sum_r c_r) \bar{\boldsymbol{\varepsilon}}_M + \sum_r c_r \bar{\boldsymbol{\varepsilon}}_r. \quad (\text{II.8})$$

The latter relation may be rewritten as a function of the phase stress averages by the intermediary of Hooke's law:

$$\mathbb{S}^* : \bar{\boldsymbol{\sigma}} = \mathbb{S}_M : \bar{\boldsymbol{\sigma}} + \sum_r c_r (\mathbb{S}_r - \mathbb{S}_M) : \bar{\boldsymbol{\sigma}}_r, \quad (\text{II.9})$$

where  $\bar{\boldsymbol{\sigma}}_r = \langle \boldsymbol{\sigma} \rangle_{V_r}$  denotes the volume average of  $\boldsymbol{\sigma}$  over a particulate phase  $V_r$ . In linear elasticity, this volume average  $\bar{\boldsymbol{\sigma}}_r$  over phase  $r$  and the macroscopic stress tensor  $\bar{\boldsymbol{\sigma}}$  are related by a fourth-order tensor  $\mathbb{B}_r$ , called stress "localization tensor":

$$\bar{\boldsymbol{\sigma}}_r = \mathbb{B}_r : \bar{\boldsymbol{\sigma}}. \quad (\text{II.10})$$

The effective compliance tensor can then be expressed in terms of the compliance tensors of the various phases and of the localization tensors defined by Eq. (II.10) (Hill 1963):

$$\mathbb{S}^* = \mathbb{S}_M + \sum_r c_r (\mathbb{S}_r - \mathbb{S}_M) : \mathbb{B}_r. \quad (\text{II.11})$$

It appears from the latter equation that the knowledge of the localization tensors of inclusion phases  $\mathbb{B}_r$  allows for determining the effective compliance tensor of the heterogeneous material. In the case of random heterogeneous materials, these localization tensors are very difficult to determine and approximations for  $\mathbb{B}_r$  are required. Estimations of these tensors are provided by means of diverse homogenization techniques, some of the widely used ones being presented later. These micromechanical schemes thus permit to predict the effective compliance tensor of the material. The previous equation can be further simplified by introducing the compliance increment tensor  $\mathbb{H}$  and inclusion compliance fluctuations tensor  $\mathbb{H}_r$ , defined as:

$$\mathbb{H} = \mathbb{S}^* - \mathbb{S}_M, \quad \mathbb{H}_r = \mathbb{S}_r - \mathbb{S}_M, \quad (\text{II.12})$$

so that the relation written in Eq. (II.9) results in:

$$\mathbb{H} = \sum_r c_r \mathbb{H}_r : \mathbb{B}_r. \quad (\text{II.13})$$

In order to derive the localization tensors  $\mathbb{B}_r$ , most of the homogenization methods use as a starting point the Eshelby problem (1957) presented below.

#### 4.1.2 Presentation of the Eshelby problem

##### 4.1.2.1 Presentation of the Eshelby theorem

In linear elasticity, the Eshelby theorem constitutes the cornerstone of most of the effective medium theories (EMTs) studied in the present dissertation and is therefore briefly recalled below. A homogeneous elastic ellipsoidal inclusion  $I$ , occupying a domain  $V_I$ , is enclosed in an infinite linear elastic matrix medium, which stiffness tensor is  $\mathbb{C}_M$ . This single inclusion is further subjected to a stress-free strain, or “eigenstrain”  $\boldsymbol{\varepsilon}^*$  that is uniform inside the inclusion and vanishes outside, undergoes a uniform deformation  $\boldsymbol{\varepsilon}_I^U$ :

$$\boldsymbol{\varepsilon}_I^U = \boldsymbol{\Sigma}_I^M : \boldsymbol{\varepsilon}^*, \quad (\text{II.15})$$

where  $\boldsymbol{\Sigma}_I^M$  is called the Eshelby tensor expressed as:

$$\left( \boldsymbol{\Sigma}_I^M \right)_{ijkl} = -\frac{C_{mnlk}}{2} \int_{V_I} [\Gamma_{ij}(\mathbf{y}-\mathbf{x})] dV_y, \quad (\text{II.16})$$

where the operator  $\Gamma_{ij}(\mathbf{y}-\mathbf{x})$  is related to the Green function  $G_{jm,ni}(\mathbf{y}-\mathbf{x})$  by:

$$\Gamma_{ij}(\mathbf{y}-\mathbf{x}) = G_{im,nj}(\mathbf{y}-\mathbf{x}) + G_{jm,ni}(\mathbf{y}-\mathbf{x}). \quad (\text{II.17})$$

The Eshelby tensor thus links the strain inside the homogeneous ellipsoidal inclusion surrounded by an infinite linear elastic medium to its stress-free strain. The main limit of this

fundamental theorem is that it is restricted to ellipsoidal inclusions in its original form (Eshelby 1957). The Eshelby tensor is generally quite difficult to determine analytically but has a very simple expression in the case of spherical homogeneous inclusion embedded in an infinite isotropic matrix (Mura 1987):

$$\Sigma_I^M = \alpha_{Sph} \mathbb{J} + \beta_{Sph} \mathbb{K}, \quad (\text{II.18})$$

with

$$\alpha_{Sph} = \frac{3K_M}{(3K_M + 4G_M)} \quad \text{and} \quad \beta_{Sph} = \frac{6(K_M + 2G_M)}{5(3K_M + 4G_M)}, \quad (\text{II.19})$$

where the subscript 'Sph' refers to the fact that the inclusion is spherical. The Eshelby tensor of a spheroidal inclusion also presents the benefit of being analytically calculable (e.g. Torquato 2001) and its expression for a spheroid with aspect ratio  $r$ , which revolution axis is oriented along the  $\mathbf{e}_3$  axis, is:

$$\begin{aligned} \Sigma_{11} = \Sigma_{22} &= \frac{1}{4(1-\nu)} \left[ \frac{3\alpha}{2(\alpha-1)} + \left( 1-2\nu - \frac{9}{4(\alpha-1)} \right) q \right], \\ \Sigma_{33} &= \frac{1}{2(1-\nu)} \left[ 1-2\nu + \frac{(3\alpha-1)}{(\alpha-1)} - \left( 1-2\nu + \frac{3}{(\alpha-1)} \right) q \right], \\ \Sigma_{12} = \Sigma_{21} &= \frac{1}{4(1-\nu)} \left[ \frac{\alpha}{2(\alpha-1)} - \left( 1-2\nu + \frac{3}{4(\alpha-1)} \right) q \right], \\ \Sigma_{13} = \Sigma_{31} &= \frac{1}{4(1-\nu)} \left[ -\frac{\alpha}{2(\alpha-1)} - \left( 1-2\nu - \frac{3}{(\alpha-1)} \right) q \right], \\ \Sigma_{23} = \Sigma_{32} &= \frac{1}{2(1-\nu)} \left[ -1+2\nu - \frac{\alpha}{(\alpha-1)} + \left( 1-2\nu + \frac{3}{2(\alpha-1)} \right) q \right], \\ \Sigma_{44} = \Sigma_{55} &= \frac{1}{2(1-\nu)} \left[ 1-2\nu - \frac{(\alpha+1)}{(\alpha-1)} - \frac{1}{2} \left( 1-2\nu - \frac{3(\alpha+1)}{(\alpha-1)} \right) q \right], \\ \Sigma_{66} &= \frac{1}{2(1-\nu)} \left[ \frac{\alpha}{2(\alpha-1)} + \left( 1-2\nu - \frac{3}{4(\alpha-1)} \right) q \right], \end{aligned} \quad (\text{II.20})$$

$$\text{where } \alpha = r^2 \text{ and } q = \begin{cases} \frac{r}{(\alpha-1)^{3/2}} \left[ r\sqrt{\alpha-1} - \cosh^{-1}(r) \right], & r \geq 1 \\ \frac{r}{(1-\alpha)^{3/2}} \left[ -r\sqrt{1-\alpha} + \cos^{-1}(r) \right], & r \leq 1 \end{cases},$$

where  $\nu$  is the Poisson ratio of the infinite matrix medium.

#### 4.1.2.2 Extension of the Eshelby tensor to spherical inhomogeneities

Duan et al. (2006) recently derived a generalization of the Eshelby tensor for a spherical inhomogeneity with a graded shell embedded in an infinite matrix. In particular, they gave the following closed-form solution for the volume average of the Eshelby tensor denoted as  $\bar{\Sigma}_I^M$

of a spherical inclusion with a homogeneous interphase enclosed in an infinite matrix, as depicted in Fig. II.2:

$$\tilde{\Sigma}_I^M = (1+3F_I)\mathbb{J} + \left(1 + \frac{63}{5}A_I + 3B_I\right)\mathbb{K}, \quad (\text{II.21})$$

with

$$\begin{aligned} F_I &= -2(1-2\nu_I) \frac{1-\rho^3(1-g_{IM})(1+\nu_I) - 4g_{IM}\nu_I + 2g_{IM}}{3H_I}, \\ A_I &= \frac{2(1-\rho^2)\rho^5(1-g_{IM})}{H_2}, \\ B_I &= \frac{2\rho^3H_{12}}{15H_2(-8-7g_{IM}+5(2+g_{IM})\nu)} - \frac{7-5\nu_I}{45-45\nu_I}, \\ H_1 &= 3(1-\nu_I)(1+2g_{IM}+(1-4g_{IM})\nu_I), \\ H_2 &= 3(1-\nu_I)(7(1+4g_{IM})+5(1-8g_{IM})\nu_I), \\ H_{12} &= (200\nu_I^2-300\nu_I-63\rho^2+175)(7-5\nu)g_{IM}^2 + \\ &\quad 3g_{IM} \left[ 75\nu(7-9\nu_I) - 25\nu_I^2(13-15\nu) - 7(25+3\rho^2-5(5+3\rho^2)\nu) \right] + \\ &\quad (4-5\nu)(25\nu^2+126\rho^2-175), \end{aligned} \quad (\text{II.22})$$

where  $\rho = r_i/r_e$  and  $g_{IM} = G_M/G_I$ . The quantities  $G_I$  and  $G_M$  respectively denote the shear moduli of the inclusion and of the matrix,  $\nu_I$  and  $\nu$  respectively the Poisson ratio of the inclusion and of the matrix,  $r_i$  and  $r_e$  respectively designate the radii of the inclusion and of the domain occupied by the inclusion and the homogeneous interphase. The latter formula is of great utility, since it allows for determining the average strain inside the domain occupied by the spherical inclusion and its homogeneous interphase in response to a prescribed uniform eigenstrain in the inclusion (Fig. II.2):

$$\bar{\epsilon}_I = \tilde{\Sigma}_I^M : \epsilon^*, \quad (\text{II.23})$$

where the average Eshelby tensor  $\tilde{\Sigma}_I^M$  for the spherical inclusion with its homogeneous interphase will be referred to as inhomogeneous Eshelby tensor in the ensuing.

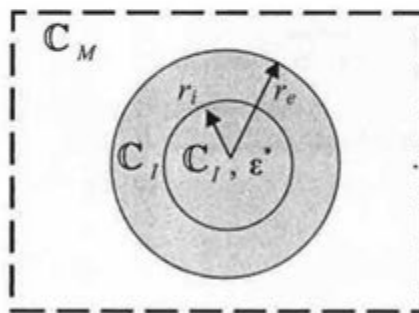


**Figure II.2: Schematic of a spherical inclusion with a homogeneous interphase enclosed in an infinite matrix.**

### 4.1.2.3 Presentation of the equivalent homogeneous inclusion method

First of all, let us consider the situation in which no heterogeneous inclusion is inserted in the infinite linear elastic medium with compliance tensor denoted by  $\mathbb{S}_M$ , which is subjected to a uniform far-field stress  $\sigma^\infty$ . In such case, the stress field is everywhere equal to  $\sigma^\infty$  and the strain field is such as:

$$\epsilon_0 = \mathbb{S}_M : \sigma^\infty. \quad (\text{II.24})$$

A heterogeneous elastic inclusion  $I$  occupying a volume  $V_I$  with elasticity tensor  $\mathbb{C}_I$  is now inserted in this virgin medium and we are interested in calculating the average  $\bar{\epsilon}_I$  of the strain field over  $V_I$ . The microscopic strain tensor decomposes itself into two parts:

$$\epsilon_I(\mathbf{x}) = \epsilon_0 + \epsilon_I'(\mathbf{x}), \quad \forall \mathbf{x}, \quad (\text{II.25})$$

where  $\epsilon_I'(\mathbf{x})$  corresponds to the perturbation strain tensor caused by the insertion of the heterogeneity. In order to apply the Eshelby theorem, the heterogeneous inclusion is assumed to be substituted by a homogeneous fictive inclusion with a stiffness tensor denoted by  $\mathbb{C}_M$  that is subjected to an appropriate uniform eigenstrain  $\epsilon^*$ , as illustrated in Fig. II.3. The latter must be chosen in such a way that the same average stress and strain fields are obtained in the homogeneous fictive inclusion and in the heterogeneous one:

$$\bar{\sigma}_I = \mathbb{C}_I : \bar{\epsilon}_I = \mathbb{C}_M : (\bar{\epsilon}_I - \epsilon^*) \quad \text{and} \quad \bar{\epsilon}_I = \epsilon_0 + \Sigma_I^M : \epsilon^*. \quad (\text{II.26})$$

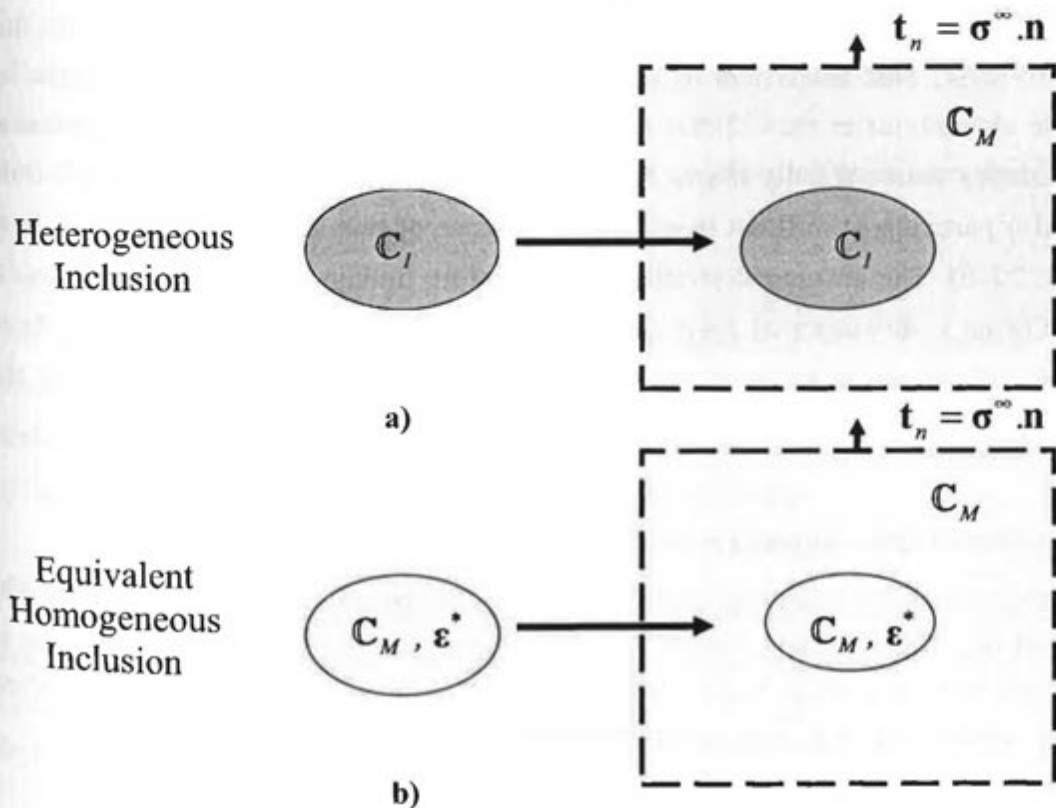


Figure II.3: Schematic picture of the equivalent homogeneous inclusion.

By solving  $\boldsymbol{\varepsilon}^*$  from Eq. (II.26<sub>1</sub>) and substituting its expression in (II.26<sub>2</sub>), the following solution is obtained for  $\bar{\boldsymbol{\varepsilon}}_I$  (Benveniste 1987):

$$\bar{\boldsymbol{\varepsilon}}_I = \left[ \mathbf{I} + \boldsymbol{\Sigma}_I^M : \mathbb{S}_M : (\mathbf{C}_I - \mathbf{C}_M) \right]^{-1} : \boldsymbol{\varepsilon}_0. \quad (\text{II.27})$$

The volume average  $\bar{\boldsymbol{\sigma}}_I$  of the microscopic stress tensor  $\boldsymbol{\sigma}$  over the ellipsoidal inclusion is found as:

$$\bar{\boldsymbol{\sigma}}_I = \mathbf{C}_I : \left[ \mathbf{I} + \boldsymbol{\Sigma}_I^M : \mathbb{S}_M : (\mathbf{C}_I - \mathbf{C}_M) \right]^{-1} : \mathbb{S}_M : \boldsymbol{\sigma}^m, \quad (\text{II.28})$$

which can also be expressed as:

$$\bar{\boldsymbol{\sigma}}_I = \left[ \mathbf{I} + \mathbf{C}_M : (\mathbf{I} - \boldsymbol{\Sigma}_I^M) : (\mathbb{S}_I - \mathbb{S}_M) \right]^{-1} : \boldsymbol{\sigma}^m. \quad (\text{II.29})$$

The average stress tensor over the inclusion can then be written in a compact way (Zheng and Du 2001):

$$\bar{\boldsymbol{\sigma}}_I = \left[ \mathbf{I} + \boldsymbol{\Omega}_I^M : \mathbb{H}_I \right]^{-1} : \boldsymbol{\sigma}^m, \quad (\text{II.30})$$

$$\text{with } \boldsymbol{\Omega}_I^M = \mathbf{C}_M : (\mathbf{I} - \boldsymbol{\Sigma}_I^M), \quad (\text{II.31})$$

where  $\boldsymbol{\Omega}_I^M$  is called eigenstiffness tensor of the single inclusion  $I$  embedded in the matrix (Zheng and Du 2001) and where  $\mathbb{S}_I$  and  $\mathbb{H}_I$  are respectively the compliance and the compliance increment tensors of the inclusion, which can be expressed by means of Eqs. (II.6) and (II.12). The eigenstiffness tensor  $\boldsymbol{\Omega}_I^M$  used by Zheng and Du (2001) has the following mechanical interpretation: the average stress tensor  $\bar{\boldsymbol{\sigma}}_I$  induced by the uniform eigenstrain  $\boldsymbol{\varepsilon}^*$  prescribed over the homogeneous fictive inclusion is linearly related to this eigenstrain by  $\boldsymbol{\Omega}_I^M$ . This tensor can be determined in the case of spheroidal inclusions by means of the expressions of the Eshelby tensor given in Eqs. (II.20). For more complicated cases, the Eshelby tensor usually has to be estimated numerically. The equivalent inclusion method is also particularly difficult to extend to the case of non ellipsoidal inclusions (e.g. Zheng et al. 2006). The ensuing derivations are therefore limited to the case of ellipsoidal inclusions. Owing to fundamental basis of micromechanics collected in the present section, the next one is dedicated to the presentation of EMTs that are of interest for predicting the properties of cement-based materials.

## 4.2 Presentation of some classical matrix-inclusion type EMTs

This presentation does not intend to be exhaustive, since there exist many good monographs on the subject (e.g. Milton 2002; Nemat-Nasser and Hori 1993; Torquato 2001). It aims at providing sufficient theoretical basis for a correct understanding of the homogenization methods that will be applied to cementitious materials subsequently.

### 4.2.1 Dilute approximation

The dilute model provides a simple expression for the localization tensors defined in Eq. (II.10). It considers the ideal situation already illustrated on Fig. II.3 where a single inclusion denoted as  $V_r^r$ , having the same shape as phase  $r$ , is embedded in an infinite matrix medium subjected to a uniform far-field stress. The determination of these dilute localization tensors is thus directly achieved by means of the equivalent homogeneous inclusion method described previously (Eshelby 1957; Mura 1987). According to Eq. (II.30), these tensors can be expressed as follows:

$$\mathbb{B}_r^{dil} = [\mathbb{I} + \mathbf{\Omega}_r^M : \mathbb{H}_r]^{-1}. \quad (\text{II.32})$$

By injecting this expression of the localization tensor in Eq. (II.13), an estimation designated by  $\mathbb{H}^{dil}$  is derived for the compliance increment tensor:

$$\mathbb{H}^{dil} = \sum_r \mathbb{H}_r^{dil}, \quad (\text{II.33})$$

$$\text{with } \mathbb{H}_r^{dil} = c_r \mathbb{H}_r : [\mathbb{I} + \mathbf{\Omega}_r^M : \mathbb{H}_r]^{-1}. \quad (\text{II.34})$$

The validity range of the dilute estimation is very limited, since all the particles are required to be far enough from each other, so as to be regarded as isolated. In other words, the inclusions are supposed to be dispersed in such a dilute manner that there is no interaction with the other inclusions and that they are only subjected to the imposed far-field stress  $\sigma^\infty$ . In addition, it is highlighted that if instead of imposing a uniform stress at infinity, a far-field displacement is applied to the infinite medium, a different estimation is then derived for the compliance increment tensor (Hori and Nemat-Nasser 1993). Consequently, the dilute model is considered as inconsistent by some authors (e.g. Berryman and Berge 1996). More consistent schemes trying to reflect the interaction effects between inclusions are required. Mori-Tanaka (MT) effective medium approximation may be used for this purpose.

### 4.2.2 MT approximation

This scheme was primarily proposed by Mori and Tanaka in 1973. Benveniste (1987) has proposed an elegant reformulation of this estimate, where it can be seen as an improved dilute model. More precisely, the stress applied at infinity is no longer  $\sigma^\infty$  but is replaced by the average  $\bar{\sigma}_M$  of the microscopic stress  $\sigma$  inside the matrix so that:

$$\bar{\sigma}_r = \mathbb{B}_r^{dil} : \bar{\sigma}_M, \quad (\text{II.35})$$

which allows for taking into account the stress perturbation inside the matrix phase due to the presence of the other inclusions. The average of the microscopic stress tensor  $\bar{\sigma}$  on the entire volume of the RVE can be decomposed as a function of microscopic stress tensor on each phase:

$$\bar{\sigma} = (1 - \sum_r c_r) \bar{\sigma}_M + \sum_r c_r \bar{\sigma}_r. \quad (\text{II.36})$$

By combining Eqs. (II.4) and (II.35-36), the localization tensors estimated by the MT model are expressed as (Benveniste 1987):

$$\mathbb{B}_r^{MT} = \mathbb{B}_r^{dil} : \left[ \left( 1 - \sum_r c_r \right) \mathbb{I} + \sum_r c_r \mathbb{B}_r^{dil} \right]^{-1}, \quad (\text{II.37})$$

which may also be expressed as follows:

$$\mathbb{B}_r^{MT} = \mathbb{B}_r^{dil} : \left[ \mathbb{I} - \sum_i c_i \mathbf{\Omega}_i^M : \mathbb{H}_i : \mathbb{B}_i^{dil} \right]^{-1}. \quad (\text{II.38})$$

The effective compliance increment tensor predicted by MT model is then expressed as:

$$\mathbb{H}^{MT} = \mathbb{H}^{dil} : \left[ \mathbb{I} - \sum_i \mathbf{\Omega}_i^M : \mathbb{H}_i^{dil} \right]^{-1}. \quad (\text{II.39})$$

The MT localization tensors are also more realistic than the dilute ones, since they account in a certain manner for the interactions between the inclusions and the matrix. However, Berryman and Berge (1996) asserted by confronting the MT estimations for porous media to experimental data that MT should not be used for inclusion volume fraction superior than 20-30 %. This discrepancy may be due to the fact that the MT localization tensors are not able to accurately take into account the interactions between the inclusions themselves and to incorporate the influence of inclusion spatial distribution.

#### 4.2.3 Generalized self-consistent scheme (GSCS)

The GSCS was originally developed by Christensen and Lo (1979) for estimating the effective elastic properties of a two-phase composite with a matrix-inclusion microstructure. This implicit homogenization method is based on the three-phase model illustrated on Fig. II.4. A spherical core of radius  $r_i$  representing the particle phase and a coating of thickness  $(r_e - r_i)$  occupied by the matrix are immersed in the yet unknown effective medium so as to account for the interactions between inclusions. The radii  $r_i$  and  $r_e$  are chosen so that each coated-sphere has the same composition as the original two-phase material. The rather lengthy derivation of the GSCS is not presently recalled, since it may be found in many articles or manuscripts (e.g. Hervé and Zaoui 1993). The effective bulk modulus predicted by this method for a two-phase isotropic composite reads (e.g. Hashin and Monteiro 2002):

$$K^* = K_M + \frac{c_I}{1/(K_I - K_M) + 3(1 - c_2)/(3K_M + 4G_M)}, \quad (\text{II.40})$$

and coincides with the bulk modulus estimated by the MT scheme. The effective shear modulus is obtained by solving a second order equation:

$$AG^{*2} + BG^* + C = 0, \quad (\text{II.41})$$

where the expressions of the coefficients  $A$ ,  $B$  and  $C$  can be found in Christensen and Lo (1979). The GSCS was extended to the case of composites with multicoated inclusions by

Hervé and Zaoui (1993). The expressions of the shear modulus then become lengthy and the symbolic toolbox of MATLAB has been used to perform the computations of the GSCS.

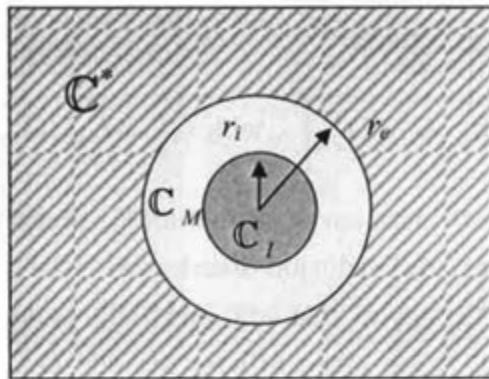


*Figure II.4: Two-dimensional representation illustrating the three-phase model on which is based the GSCS.*

The GSCS in its original form (Christensen and Lo 1979; Hervé and Zaoui 1993) cannot be computed in the case of composites containing multi dispersed particulate phases, even though an empirical method was proposed by Huang et al. (1994) for extending the GSCS to this case. Some attempts have also been proposed in literature to extend the GSCS to the case of non-spherical inclusions (Riccardi and Montheillet 1999) but they appear far too difficult to handle. In the next subsection, another type of models that is more suited for these limiting cases is presented.

### 4.3 Presentation of double-inclusion type models

The basic idea used in the homogenization methods presented below is to model the inclusion spatial distribution by an ellipsoidal cell, called double-inclusion, surrounding the inclusion (e.g. Hori and Nemat-Nasser 1993; Zheng and Du 2001). Its geometry depends on how the inclusions are dispersed through the matrix and thus is representative of the spatial distributions of the particulate phases. As a proof of the popularity of the double-inclusion concept, we have found at least five models using more or less explicitly this idea, such as the ones proposed by Küster-Töksoz (1974), Nemat-Nasser and Hori (1993), Ponte-Castañeda and Willis (1995), Shen and Yi (2001) and Zheng and Du (2001). Hu and Weng (2000) revealed that strong connections exist between the schemes developed by Küster-Töksoz (1974), Nemat-Nasser and Hori (1993) and Ponte-Castañeda and Willis (1995), even though their derivation may radically differ. That's why the notion of double-inclusion type models is introduced in this section to deal with the estimates mentioned. For conciseness, only two of these models, namely the ones of Nemat-Nasser and Hori (1993) and Zheng and Du (2001), are presented in details below.

### 4.3.1 Interaction Direct Derivative (IDD) model

The localization tensors  $\mathbb{B}_r^{IDD}$  for the IDD estimate due to Zheng and Du (2001) can be obtained easily by introducing the eigenstiffness tensors of all double-inclusions and by modifying  $\mathbb{B}_r^{MT}$  in Eq. (II.38) as follows:

$$\mathbb{B}_r^{IDD} = \mathbb{B}_r^{dil} : \left[ \mathbb{I} - \sum_i c_i \mathbb{H}_i : \mathbb{B}_i^{dil} : \Omega_{Di}^M \right]^{-1}, \text{ with } \Omega_{Di}^M = \mathbb{C}_M : (\mathbb{I} - \Sigma_{Di}^M), \quad (\text{II.42})$$

where  $\Omega_{Di}^M$  denotes the eigenstiffness tensor of the double-inclusion of a given phase  $i$ . The subscript 'D' is used here, since the inclusion distribution is involved in these eigenstiffness tensors. Eqs. (II.38) and (II.42) reveal that MT and IDD estimates coincide whenever all inclusion phases  $V_i^r$  have the same eigenstiffness tensors  $\Omega_{Dr}^M = \Omega_r^M$  as their surrounding double-inclusion. It means that every inclusion  $V_i^r$  and its enclosing cell designated by  $V_D^r$  are similar in shape and coaxial in orientation.

In the case of a macroscopically isotropic material, the spatial distribution of inclusions is identical in all directions. A spherical double-inclusion is thus usually adopted to model this distribution (Ponte Castaneda and Willis 1995), since no particular direction in space is then privileged. It implies in particular that IDD and MT models coincide for macroscopically isotropic heterogeneous materials containing only spherical inclusions. However, if the inclusions are spheroids and are isotropically distributed inside the effective material, IDD and MT schemes do not coincide. The substitution of  $\mathbb{B}_r$  in Eq. (II.13) by its expression in Eq. (II.42) yields the following IDD estimate provided that  $\mathbb{H}^{dil}$  is commutative:

$$\mathbb{H}^{IDD} = \left[ \mathbb{I} - \sum_i \mathbb{H}_i^{dil} : \Omega_{Di}^M \right]^{-1} : \mathbb{H}^{dil}, \quad (\text{II.43})$$

where  $\mathbb{H}^{dil}$  and  $\mathbb{H}_i^{dil}$  are expressed in Eqs. (II.33-34), respectively. The tensor  $\mathbb{H}^{dil}$  is generally commutative in the case of a macroscopically isotropic material. The effective stiffness tensor of the material can then be deduced from the knowledge of this increment tensor:

$$\mathbb{C}_{IDD}^* = \mathbb{C}_M : \left[ \mathbb{I} + \mathbb{H}^{IDD} : \mathbb{C}_M \right]^{-1}. \quad (\text{II.44})$$

The demonstration proposed here shows that the IDD scheme can be seen as an improved dilute model (see Fig. II.5) with unbounded matrix material subjected to a modified effective stress  $\sigma_{IDD}^m$  defined as:

$$\sigma_{IDD}^m = \left[ \mathbb{I} - \sum_r c_r \mathbb{H}_r^{dil} : \Omega_{Dr}^M \right]^{-1} : \sigma^m. \quad (\text{II.45})$$

The original deductions of IDD estimate by Zheng and Du (2001) consist in consecutive applications of superposition principles. For more information, the reader should refer to their

original paper. In the present dissertation, we have adopted the philosophy of Benveniste (1987) in order to present the IDD estimate in a simple manner and to put in evidence the strong connection existing between IDD and MT models.

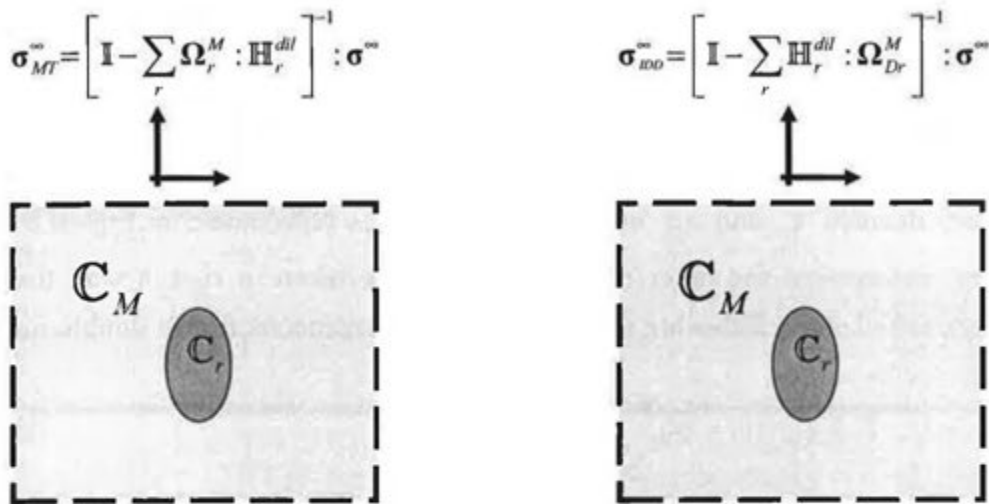


Figure II.5: Derivation of the MT (left) and IDD (right) models for a multi-phase composite from the dilute configuration by modifying the far-field stresses.

Another model derived by Hori and Nemat-Nasser (1993) using the concept of double-inclusion is now presented. Its demonstration is a bit more sophisticated but is useful to understand the physical meaning of the double-inclusion.

### 4.3.2 The Hori and Nemat-Nasser double-inclusion model (DIM)

#### 4.3.2.1 General framework

The DIM developed by Hori and Nemat-Nasser (1993) basically consists in the following three-phase configuration: an ellipsoidal inclusion domain denoted as  $V_{DI}$  that contains an ellipsoidal heterogeneity  $V_I$  is immersed in an infinite homogeneous medium. The latter model is very flexible, since the shape and the orientation of the double-inclusion and of the heterogeneity as well as the elastic properties of the three phases may be chosen. The stiffness tensors of the inclusion, its coating and the embedding infinite medium composing the three-phase representation considered by Hori and Nemat-Nasser (1993) are arbitrary and are respectively designated by  $C_I$ ,  $C_{CI}$  and  $C_0$  (see Fig. II.6). Two parameters are important in this model:

- the double-inclusion geometry that should be representative of the distribution of the inclusions inside the composite;
- the choice of the reference medium that should be representative of the immediate surroundings of the particulate phases.

However, the choice of the reference medium is in reality quite limited, since the three-phase configuration should have a physical interpretation. The most usual choices consist in taking the matrix of the material with stiffness tensor  $\mathbb{C}_M$  or the yet unknown effective material with stiffness tensor  $\mathbb{C}^*$  as the reference medium (Hu and Weng 2000). The main steps necessary for deriving this model are recapitulated below. The detailed demonstration can be found in Hori and Nemat-Nasser (1993). These authors practically apply the concept of the equivalent homogeneous inclusion method (Fig. II.3) to the case of a double-inclusion. Two eigenstrains respectively denoted  $\boldsymbol{\varepsilon}_I^*$  and  $\boldsymbol{\varepsilon}_{CI}^*$  are then necessary, as represented in Fig. II.6. As in Eq. (II.26), the averages of the latter eigenstrains have been taken in such a way that the same average stress and strain fields are obtained in the homogeneous fictive double-inclusion and in the heterogeneous one:

$$\bar{\boldsymbol{\sigma}}_I = \mathbb{C}_I : \bar{\boldsymbol{\varepsilon}}_I = \mathbb{C}_0 : (\bar{\boldsymbol{\varepsilon}}_I - \bar{\boldsymbol{\varepsilon}}_I^*), \quad (\text{II.46})$$

$$\bar{\boldsymbol{\sigma}}_{CI} = \mathbb{C}_{CI} : \bar{\boldsymbol{\varepsilon}}_{CI} = \mathbb{C}_0 : (\bar{\boldsymbol{\varepsilon}}_{CI} - \bar{\boldsymbol{\varepsilon}}_{CI}^*), \quad (\text{II.47})$$

$$\bar{\boldsymbol{\varepsilon}}_I = \boldsymbol{\varepsilon}_0 + \bar{\boldsymbol{\varepsilon}}_I' \quad \text{and} \quad \bar{\boldsymbol{\varepsilon}}_{CI} = \boldsymbol{\varepsilon}_0 + \bar{\boldsymbol{\varepsilon}}_{CI}', \quad (\text{II.48})$$

where  $\bar{\boldsymbol{\varepsilon}}_I'$  and  $\bar{\boldsymbol{\varepsilon}}_{CI}'$  respectively denote the strain perturbation tensors of the inclusion and of its coating. The next step consists in computing respectively the volume averages of the strain tensor  $\bar{\boldsymbol{\varepsilon}}_I$  and  $\bar{\boldsymbol{\varepsilon}}_{CI}$  over the inclusion and its coating. For this purpose, the problem of the homogeneous fictive double-inclusion corresponding to the situation b) depicted in Fig. II.6 is decomposed in three subproblems referred to as c), d) and e) (Shodja and Sarvestani 2001).

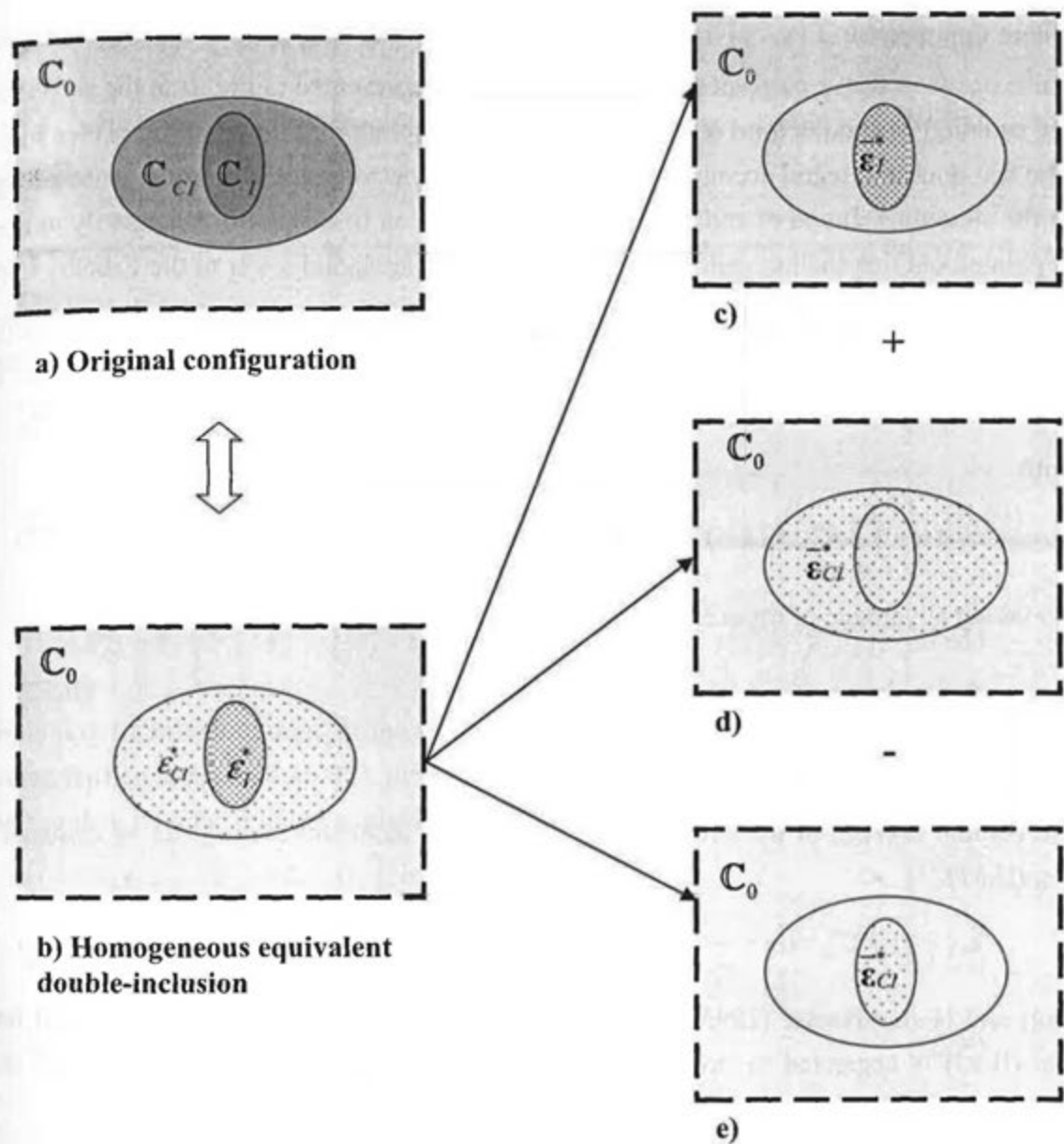


Figure II.6: Schematic of the original three-phase configuration a) used for the derivation of DIM and representation of the different steps b), c), d) and e) employed for its derivation.

In the situation b), the volume average of the perturbation strain tensor  $\bar{\epsilon}_i'$  may be written as:

$$\bar{\epsilon}_i' = \frac{1}{V_I} \int_{V_I} \int_{V_{CI}} \mathbf{C}_0 : \Gamma(\mathbf{x}-\mathbf{y}) : \epsilon^*(\mathbf{y}) dV_y dV_x, \quad (\text{II.49})$$

which can be decomposed as:

$$\bar{\epsilon}_i' = \left\{ \begin{array}{l} \frac{1}{V_I} \int_{V_I} \left( \int_{V_I} \mathbf{C}_0 : \Gamma(\mathbf{x}-\mathbf{y}) dV_y \right) : \bar{\epsilon}_I dV_x + \frac{1}{V_I} \int_{V_I} \left( \int_{V_{CI}} \mathbf{C}_0 : \Gamma(\mathbf{x}-\mathbf{y}) dV_y \right) : \bar{\epsilon}_{CI} dV_x \\ - \frac{1}{V_I} \int_{V_I} \left( \int_{V_I} \mathbf{C}_0 : \Gamma(\mathbf{x}-\mathbf{y}) dV_y \right) : \bar{\epsilon}_{CI} dV_x + \frac{1}{V_I} \int_{V_I} \int_{V_{CI}} \mathbf{C}_0 : \Gamma(\mathbf{x}-\mathbf{y}) : (\epsilon^*(\mathbf{y}) - \bar{\epsilon}_{CI}) dV_y dV_x \end{array} \right\}, (\text{II.50})$$

where the operator  $\Gamma(\mathbf{x}-\mathbf{y})$  is defined in Eq. (II.17). The first term of the right-hand side of the expression above corresponds to the situation c) represented in Fig. II.6, the second one to the situation d) and the third one is issued from the resolution of the situation e) (see Fig. II.6). The last double-integral accounts for the fluctuations between the uniform eigenstrain applied in the situations d) and e) and the actual one in situation b) that is not necessarily uniform. It is pointed out that the integrals between parenthesis correspond either to the Eshelby tensor of the inclusion or of the double-inclusion. Consequently, the expression of the average strain tensor inside the inclusion can be obtained with the aid of these tensors in a compact form:

$$\bar{\boldsymbol{\varepsilon}}_I = \boldsymbol{\varepsilon}_0 + \boldsymbol{\Sigma}_I^0 : \bar{\boldsymbol{\varepsilon}}_I^* + (\boldsymbol{\Sigma}_{DI}^0 - \boldsymbol{\Sigma}_I^0) : \bar{\boldsymbol{\varepsilon}}_{CI}^* + \mathcal{J}, \quad (\text{II.51})$$

with

$$\mathcal{J} = \frac{1}{V_I} \int \int_{V_I, V_{CI}} \mathbf{C}_0 : \Gamma(\mathbf{x}-\mathbf{y}) : (\boldsymbol{\varepsilon}^*(\mathbf{y}) - \bar{\boldsymbol{\varepsilon}}_{CI}^*) dV_y dV_x. \quad (\text{II.52})$$

By taking advantage of these simple relations:

$$\bar{\boldsymbol{\varepsilon}}_{DI}^* = \left(1 - \frac{c_I}{c_{DI}}\right) \bar{\boldsymbol{\varepsilon}}_{CI}^* + \frac{c_I}{c_{DI}} \bar{\boldsymbol{\varepsilon}}_I^*, \quad (\text{II.53})$$

$$\bar{\boldsymbol{\varepsilon}}_{DI}^* = \boldsymbol{\Sigma}_{DI}^0 : \bar{\boldsymbol{\varepsilon}}_{DI}^*, \quad (\text{II.54})$$

the volume average of the strain tensor  $\bar{\boldsymbol{\varepsilon}}_{CI}$  over the inclusion coating can be deduced from Eq. (II.51):

$$\bar{\boldsymbol{\varepsilon}}_{CI} = \boldsymbol{\varepsilon}_0 + \boldsymbol{\Sigma}_{DI}^0 : \bar{\boldsymbol{\varepsilon}}_{CI}^* + \frac{c_I}{c_{DI} - c_I} (\boldsymbol{\Sigma}_{DI}^0 - \boldsymbol{\Sigma}_I^0) : (\bar{\boldsymbol{\varepsilon}}_I^* - \bar{\boldsymbol{\varepsilon}}_{CI}^*) - \frac{c_I}{c_{DI} - c_I} \mathcal{J}. \quad (\text{II.55})$$

Hori and Nemat-Nasser (1993) then make the following approximation: the integral term in Eq. (II.55) is neglected to simplify the ensuing derivations. The relations proposed in Eqs. (II.51) and (II.55) then simply become:

$$\bar{\boldsymbol{\varepsilon}}_I = \boldsymbol{\varepsilon}_0 + \boldsymbol{\Sigma}_I^0 : \bar{\boldsymbol{\varepsilon}}_I^* + (\boldsymbol{\Sigma}_{DI}^0 - \boldsymbol{\Sigma}_I^0) : \bar{\boldsymbol{\varepsilon}}_{CI}^*, \quad (\text{II.56})$$

$$\bar{\boldsymbol{\varepsilon}}_{CI} = \boldsymbol{\varepsilon}_0 + \boldsymbol{\Sigma}_{DI}^0 : \bar{\boldsymbol{\varepsilon}}_{CI}^* + \frac{c_I}{c_{DI} - c_I} (\boldsymbol{\Sigma}_{DI}^0 - \boldsymbol{\Sigma}_I^0) : \Delta \bar{\boldsymbol{\varepsilon}}^*, \quad \text{with} \quad \Delta \bar{\boldsymbol{\varepsilon}}^* = \bar{\boldsymbol{\varepsilon}}_I^* - \bar{\boldsymbol{\varepsilon}}_{CI}^*. \quad (\text{II.57})$$

The effects of this approximation made by Hori and Nemat-Nasser (1993) will be carefully discussed later. The consistency conditions in Eqs. (II.46-48) then imply that (e.g. Hu and Weng 2000):

$$-\left[\boldsymbol{\Sigma}_{DI}^0 + (\mathbf{C}_I - \mathbf{C}_0)^{-1} : \mathbf{C}_0\right] : \bar{\boldsymbol{\varepsilon}}_{CI}^* - \left[\boldsymbol{\Sigma}_I^0 + (\mathbf{C}_I - \mathbf{C}_0)^{-1} : \mathbf{C}_0\right] : \Delta \bar{\boldsymbol{\varepsilon}}^* = \boldsymbol{\varepsilon}_0, \quad (\text{II.58})$$

$$-\left[\boldsymbol{\Sigma}_{DI}^0 + (\mathbf{C}_{CI} - \mathbf{C}_0)^{-1} : \mathbf{C}_0\right] : \bar{\boldsymbol{\varepsilon}}_{CI}^* - \frac{c_I}{c_{DI} - c_I} (\boldsymbol{\Sigma}_{DI}^0 - \boldsymbol{\Sigma}_I^0) : \Delta \bar{\boldsymbol{\varepsilon}}^* = \boldsymbol{\varepsilon}_0, \quad (\text{II.59})$$

which can be re-arranged by using the fact that  $\boldsymbol{\Sigma}_I^0 = \mathbb{I} - \mathbb{S}_0 : \boldsymbol{\Omega}_I^0$  and  $(\mathbf{C}_I - \mathbf{C}_0)^{-1} : \mathbf{C}_0 = -\mathbb{S}_I : \mathbb{H}_I^{-1}$  into:

$$\mathbb{F}_{DI}^{\prime -1} : \bar{\boldsymbol{\varepsilon}}_{CI}^* + \mathbb{F}_I^{\prime -1} : \Delta \bar{\boldsymbol{\varepsilon}}^* = \boldsymbol{\sigma}^\infty, \quad (\text{II.60})$$

$$\mathbb{F}_{DI}^{CI -1} : \bar{\boldsymbol{\varepsilon}}_{CI}^* - \frac{c_I}{c_{DI} - c_I} (\boldsymbol{\Omega}_I^0 - \boldsymbol{\Omega}_{DI}^0) : \Delta \bar{\boldsymbol{\varepsilon}}^* = \boldsymbol{\sigma}^\infty, \quad (\text{II.61})$$

where

$$\mathbb{F}_k^j = - \left[ \boldsymbol{\Sigma}_k^0 + (\mathbb{C}_j - \mathbb{C}_0)^{-1} : \mathbb{C}_0 \right]^{-1} : \mathbb{S}_0 = \left[ \mathbb{H}_j^{-1} + \boldsymbol{\Omega}_k^0 \right]^{-1}, \quad \text{with } j = [I, CI] \text{ and } k = [I, DI]. \quad (\text{II.62})$$

By solving this system of two equations, the averages of the two eigenstrains can be related to the far field-stress by:

$$\bar{\boldsymbol{\varepsilon}}_{CI}^* = \mathbb{U}_{CI} : \boldsymbol{\sigma}^\infty \quad \text{and} \quad \Delta \bar{\boldsymbol{\varepsilon}}^* = \mathbb{U}_I : \boldsymbol{\sigma}^\infty, \quad \text{with} \quad (\text{II.63})$$

$$\mathbb{U}_{CI} = \mathbb{F}_{DI}^{\prime} : \left[ \mathbb{I} - \mathbb{F}_I^{\prime -1} : \left[ \mathbb{F}_{DI}^{\prime} : \mathbb{F}_I^{\prime -1} + \frac{c_I}{(c_{DI} - c_I)} \mathbb{F}_{DI}^{CI} : (\boldsymbol{\Omega}_I^0 - \boldsymbol{\Omega}_{DI}^0) \right] \right]^{-1} : (\mathbb{F}_{DI}^{\prime} - \mathbb{F}_{DI}^{CI}), \quad (\text{II.64})$$

$$\mathbb{U}_I = \mathbb{F}_{DI}^{\prime} : \left[ \mathbb{I} - \left[ \mathbb{F}_{DI}^{\prime} : \mathbb{F}_I^{\prime -1} : (\boldsymbol{\Omega}_I^0 - \boldsymbol{\Omega}_{DI}^0)^{-1} + \frac{c_I}{(c_{DI} - c_I)} \mathbb{F}_{DI}^{CI} \right] \right]^{-1} : (\mathbb{F}_{DI}^{\prime} - \mathbb{F}_{DI}^{CI}). \quad (\text{II.65})$$

By combining these expressions of the eigenstrains with Eqs. (II.56-57) and the consistency conditions written in Eqs. (II.46-48), the average strain and stress inside the inclusion and its coating can then be related to the applied far-field stress as:

$$\bar{\boldsymbol{\varepsilon}}_I = \left[ \mathbb{S}_0 + \boldsymbol{\Sigma}_{DI}^0 : \mathbb{U}_{CI} + \boldsymbol{\Sigma}_I^0 : \mathbb{U}_I \right] : \boldsymbol{\sigma}^\infty, \quad (\text{II.66})$$

$$\bar{\boldsymbol{\varepsilon}}_{CI} = \left[ \mathbb{S}_0 + \boldsymbol{\Sigma}_{DI}^0 : \mathbb{U}_{CI} + \frac{c_I}{c_{DI} - c_I} (\boldsymbol{\Sigma}_{DI}^0 - \boldsymbol{\Sigma}_I^0) : \mathbb{U}_I \right] : \boldsymbol{\sigma}^\infty, \quad (\text{II.67})$$

$$\bar{\boldsymbol{\sigma}}_I = \left[ \mathbb{I} - \boldsymbol{\Omega}_{DI}^0 : \mathbb{U}_{CI} - \boldsymbol{\Omega}_I^0 : \mathbb{U}_I \right] : \boldsymbol{\sigma}^\infty, \quad (\text{II.68})$$

$$\bar{\boldsymbol{\sigma}}_{CI} = \left[ \mathbb{I} - \boldsymbol{\Omega}_{DI}^0 : \mathbb{U}_{CI} - \frac{c_I}{c_{DI} - c_I} (\boldsymbol{\Omega}_{DI}^0 - \boldsymbol{\Omega}_I^0) : \mathbb{U}_I \right] : \boldsymbol{\sigma}^\infty. \quad (\text{II.69})$$

From the knowledge of these average strains and stresses inside the inclusion and its coating, the volume averages of the strain and stress tensors inside the double-inclusion can finally be computed:

$$\bar{\boldsymbol{\varepsilon}}_{DI} = \left[ \mathbb{S}_0 + \boldsymbol{\Sigma}_{DI}^0 : (\mathbb{U}_{CI} + c_I \mathbb{U}_I) \right] : \boldsymbol{\sigma}^\infty, \quad (\text{II.70})$$

$$\bar{\boldsymbol{\sigma}}_{DI} = \left[ \mathbb{I} - \boldsymbol{\Omega}_{DI}^0 : (\mathbb{U}_{CI} + c_I \mathbb{U}_I) \right] : \boldsymbol{\sigma}^\infty. \quad (\text{II.71})$$

Now that the average strain and stress inside the double-inclusion are known, different estimates can be developed by making particular choices of the elastic properties of the coatings and of the shapes of the ellipsoids. In the case of a two-phase composite with a particulate phase *I* with a volume fraction designated by  $c_I$ , the double-inclusion is considered as a RVE so that  $c_{DI} = 1$ . In such occurrence, the effective compliance tensor of the material can be estimated by eliminating  $\boldsymbol{\sigma}^\infty$  in the last two equations:

$$\mathbf{S}^* = \left[ \mathbf{S}_0 - \boldsymbol{\Sigma}_{DI}^0 : (\mathbf{U}_{CI} + c_I \mathbf{U}_I) \right] : \left[ \mathbf{I} - \boldsymbol{\Omega}_{DI}^0 : (\mathbf{U}_{CI} + c_I \mathbf{U}_I) \right]^{-1}, \quad (\text{II.72})$$

where the tensors  $\mathbf{S}_0$  and  $\boldsymbol{\Sigma}_{DI}^0$  may be chosen in diverse ways (Hu and Weng 2000). Given the different possibilities offered by DIM, we only focus below on its application to composites having matrix-inclusion morphology. The simplest choice to obtain an estimation for such materials then consists in letting the reference infinite medium in the three-phase configuration represented in Fig. II.7 be the matrix of the material, i.e.  $\mathbf{C}_0 = \mathbf{C}_M$ .

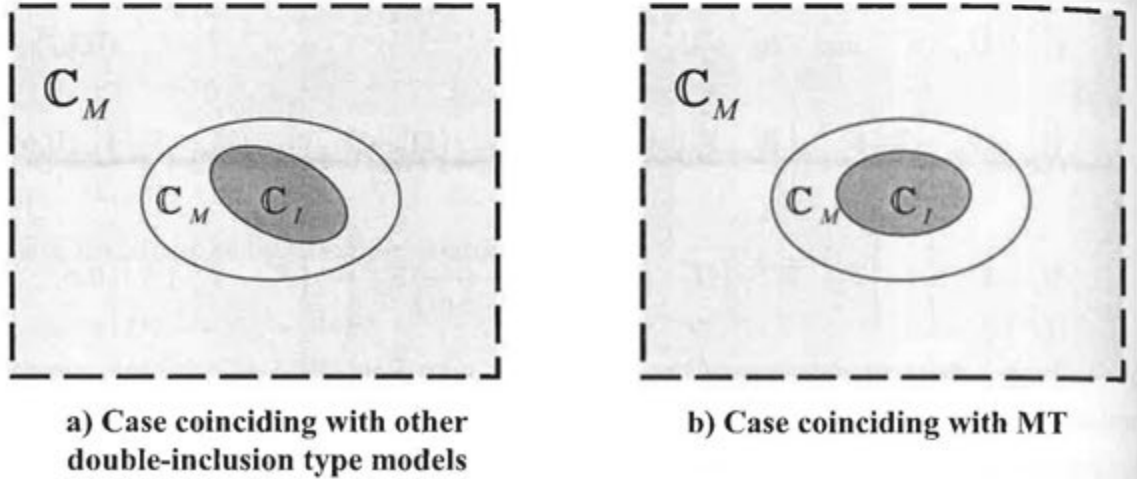


Figure II.7: Schematic illustrating the link between the Hori and Nemat-Nasser DIM and other micromechanical schemes (Hu and Weng 2000).

#### 4.3.2.2 Application of DIM to two-phase composites

In the case of a two-phase composite, let the coating of the inclusion be filled by the matrix of the material so that  $\mathbf{C}_{CI} = \mathbf{C}_M$  and  $c_{DI} = 1$ . Noticing that  $\mathbf{H}_I^{dil} = c_I \mathbf{F}_I'$  for a two-phase composite, Eqs. (II.63) and (II.70-71) respectively reduce to:

$$\Delta \bar{\boldsymbol{\varepsilon}}^* = \mathbf{F}_I' \quad \text{and} \quad \bar{\boldsymbol{\varepsilon}}_{CI}^* = 0, \quad (\text{II.73})$$

$$\bar{\boldsymbol{\varepsilon}} = \left[ \mathbf{S}_M + \boldsymbol{\Sigma}_{DI}^M : \mathbf{H}_I^{dil} \right] : \boldsymbol{\sigma}^\infty, \quad (\text{II.74})$$

$$\bar{\boldsymbol{\sigma}} = \left[ \mathbf{I} - \boldsymbol{\Omega}_{DI}^M : \mathbf{H}_I^{dil} \right] : \boldsymbol{\sigma}^\infty. \quad (\text{II.75})$$

It is interesting to observe from the last equation that, if the modified far-field stress written in Eq. (II.45) is applied instead of  $\boldsymbol{\sigma}^\infty$ , the average of the stress tensor inside the double-inclusion is then simply equal to  $\boldsymbol{\sigma}^\infty$ . By combining the last two equations, the following estimation can be obtained for the effective compliance tensor:

$$\mathbf{S}^{DIM} = \left[ \mathbf{S}_M + \boldsymbol{\Sigma}_{DI}^M : \mathbf{H}_I^{dil} \right] : \left[ \mathbf{I} - \boldsymbol{\Omega}_{DI}^M : \mathbf{H}_I^{dil} \right]^{-1}, \quad (\text{II.76})$$

which is recast in the simplified form:

$$\mathbf{H}^{DIM} = \mathbf{H}_I^{dil} : \left[ \mathbf{I} - \boldsymbol{\Omega}_{DI}^M : \mathbf{H}_I^{dil} \right]^{-1}. \quad (\text{II.77})$$

The expression of the DIM estimate for the effective increment compliance tensor is very close to the one given by the IDD estimate in Eq. (II.43). More precisely, the two estimates coincide whenever  $\mathbb{H}_I^{dil}$  is invertible, which is true in the case of a macroscopically isotropic composite. Hu and Weng (2000) have investigated DIM in some special cases and shown theoretical connections with other micromechanical schemes. They have already demonstrated that, in the case of two-phase composites, DIM leads to the same results as the Kuster-Tökösz (KT), and Ponte-Castañeda and Willis (PCW) models but, to our knowledge, this connection between DIM and the IDD model has not yet been evidenced. It also appears by comparing Eqs. (II.38) and (II.77) that, if the inclusion and its enclosing cell have the same shape and orientation, DIM yields exactly the same predictions as the MT model, as illustrated in Fig. II.7 (Hu and Weng 2000). Hori and Nemat-Nasser (1993) generalized their DIM to composites containing inclusions with  $n$  layers. In the next subsection, the extension of DIM to inclusions with one layer is treated.

#### 4.3.2.3 Application of DIM to coated inclusions

For the oncoming application of DIM to cement-based materials, we are interested in finding its estimation for the particular pattern illustrated on the right-hand side of Fig. II.8. On this figure, DIM is constituted of four regions: the ellipsoidal inclusion  $I$  with a volume fraction  $c_I$  representing a particulate phase with a stiffness tensor denoted as  $\mathbb{C}_I$  is enclosed in a confocal ellipsoidal coating with a volume fraction  $c_{CI}$  occupied by a phase having its stiffness tensor designated by  $\mathbb{C}_{CI}$ . The double-inclusion thus obtained is in turn embedded in another confocal ellipsoidal coating with a volume fraction  $c_M = 1 - c_I - c_{CI}$  filled by the matrix phase having for stiffness tensor  $\mathbb{C}_M$  immersed in an infinitely large matrix medium with stiffness tensor  $\mathbb{C}_M$ .

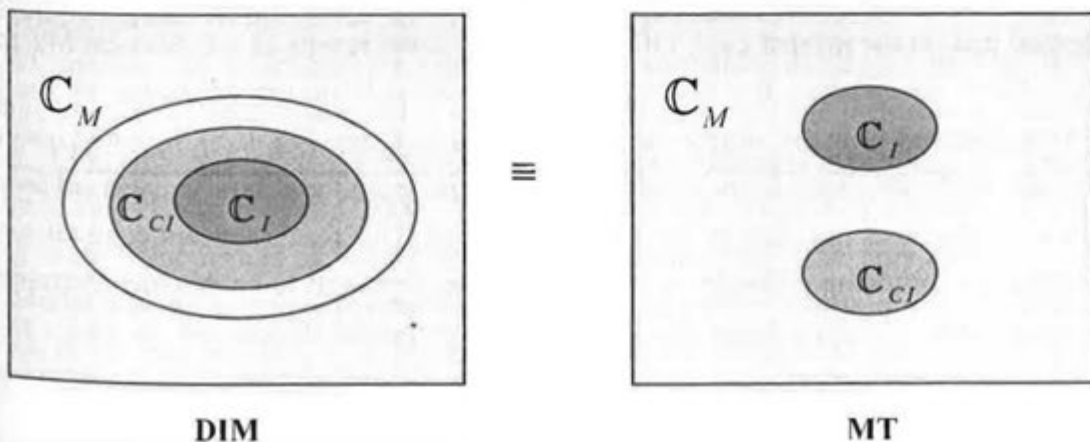


Figure II.8: Schematic illustrating the discrepancies of the Hori and Nemat-Nasser DIM.

The latter representation is of great interest for mortars for example, where an ITZ forms between the sand aggregates and the cement paste. In order to derive an estimate for this configuration, it is necessary to compute the averages of the strain and stress fields inside the domain occupied by the double-inclusion and its matrix coating that may be decomposed as follows:

$$\bar{\boldsymbol{\varepsilon}} = (1 - c_{DI}) \bar{\boldsymbol{\varepsilon}}_M + c_{DI} \bar{\boldsymbol{\varepsilon}}_{DI} \quad \text{and} \quad \bar{\boldsymbol{\sigma}} = (1 - c_{DI}) \bar{\boldsymbol{\sigma}}_M + c_{DI} \bar{\boldsymbol{\sigma}}_{DI}, \quad (\text{II.78})$$

where  $\bar{\boldsymbol{\varepsilon}}_{DI}$  and  $\bar{\boldsymbol{\sigma}}_{DI}$  are given by Eqs. (II.70-71) and the averages of the strain  $\bar{\boldsymbol{\varepsilon}}_M$  and stress  $\bar{\boldsymbol{\sigma}}_M$  inside the matrix outer layer are still to be determined. Hori and Nemat-Nasser (1993) showed that in the case of layered inclusions:

$$\bar{\boldsymbol{\varepsilon}}_M = \boldsymbol{\varepsilon}_0 + (\boldsymbol{\Sigma}_{CDI}^M - \boldsymbol{\Sigma}_{DI}^M) : \left( \frac{c_I}{1 - c_{DI}} \bar{\boldsymbol{\varepsilon}}_I^* + \frac{c_{CI}}{1 - c_{DI}} \bar{\boldsymbol{\varepsilon}}_{CI}^* \right), \quad (\text{II.79})$$

where  $\boldsymbol{\Sigma}_{CDI}^M$  designates the Eshelby tensor of the coating of the double-inclusion and where  $\bar{\boldsymbol{\varepsilon}}_I^*$  and  $\bar{\boldsymbol{\varepsilon}}_{CI}^*$  are provided by Eq. (II.63). The coating of the double-inclusion having the same shape and orientation of the double-inclusion, the latter equation reduces to  $\bar{\boldsymbol{\varepsilon}}_M = \boldsymbol{\varepsilon}_0$ . Furthermore, the coating of the double-inclusion having the same properties as the unbounded matrix medium, the average stress inside the coating of the double-inclusion simply writes as:

$$\bar{\boldsymbol{\sigma}}_M = \mathbf{C}_M : \boldsymbol{\varepsilon}_0. \quad (\text{II.80})$$

By combining the last three equations, it comes that:

$$\bar{\boldsymbol{\sigma}} = \left[ \mathbf{I} - \boldsymbol{\Omega}_{DI}^M : (\mathbb{H}_{CI}^{dil} + \mathbb{H}_I^{dil}) \right] : \boldsymbol{\sigma}^\infty \quad \text{and} \quad \bar{\boldsymbol{\varepsilon}} = \left[ \mathbf{S}_M - \boldsymbol{\Sigma}_{DI}^M : (\mathbb{H}_{CI}^{dil} + \mathbb{H}_I^{dil}) \right] : \boldsymbol{\sigma}^\infty. \quad (\text{II.81})$$

By eliminating  $\boldsymbol{\sigma}^\infty$  in the equations just above and using the fact that  $\boldsymbol{\Omega}_{DI}^M = \boldsymbol{\Omega}_I^M$ , the following expression can be obtained for the effective increment compliance tensor:

$$\mathbb{H}^{DIM} = (\mathbb{H}_I^{dil} + \mathbb{H}_{CI}^{dil}) : \left[ \mathbf{I} - \boldsymbol{\Omega}_I^M : (\mathbb{H}_I^{dil} + \mathbb{H}_{CI}^{dil}) \right]^{-1}, \quad (\text{II.82})$$

which coincides with the MT estimate written in Eq. (II.38) for three-phase composites. To our knowledge, this connection with the MT scheme has not yet been noticed. It is however unexpected that, in the present case, DIM leads to the same results as the classical MT model for three-phase composites, the microgeometry considered for the derivation of the DIM being very different from the simple one employed by MT (see Fig. II.5). It would mean that whether one inclusion phase is enclosed in the other one or on the contrary dispersed far away one from another does not change the elastic properties. This result appears contradictory by considering the following example. A stiff inclusion is supposed to be completely trapped in water constituting a coating layer due for instance to a partial dissolution. In such case, the stiff inclusion should logically not be able to reinforce the material, whereas according to the DIM estimate it does.

This discrepancy is symptomatic of the fact that DIM as proposed by Hori and Nemat-Nasser (1993) fails to accurately account for the interactions between the inclusion and its coating.

Hu and Weng (2000) furthermore noticed other shortcomings of DIM for the cases in which the infinite reference medium is chosen as the yet unknown effective material, i.e.  $C_0 = C^*$ . The only approximation used for the derivation of DIM (Hori and Nemat-Nasser 1993) consists in disregarding the integral term in Eq. (II.52) and is thus likely to be the cause to these anomalies. This integral term neglected practically means that the eigenstrain is supposed uniform inside the coating of the inclusion. This approximation of a uniform eigenstrain field inside the coating is strong, whenever the coating and the infinite reference medium do not have the same elastic properties, and may lead to significant shortcomings such as the ones described on Fig. II.8. Nevertheless, this integral term vanishes whenever the eigenstrain is uniform inside the coating of the inclusion. This practically means that, for the particular case represented in Fig. II.7 for which the coating has the same stiffness tensor as the infinite matrix, the DIM of Hori and Nemat-Nasser is exact, since the eigenstrain is equal to zero everywhere inside the coating of the inclusion.

### 4.3.3 Other double-inclusion type models

#### 4.3.3.1 The Kuster-Toksöz (1974) model

The latter model is popular among geophysicians. Berryman and Berge (1996) have confronted this method with different experimental data and concluded that it should not be used for volume fractions of inclusions higher than 30 %. Analogously to the Hori and Nemat-Nasser DIM, the starting point of the Kuster-Toksöz (KT) model consists in embedding the different inclusions modelling the  $P$  particulate phases inside a matrix coating with ellipsoidal form and in turn in inserting this pattern, designated as composite inclusion (e.g. Hu and Weng 2000), inside an infinite matrix medium. The external geometry of this composite inclusion depends on the spatial distribution of the particulate phases. In the case of two-phase composites, the KT model is based on the same pattern as DIM (Fig. II.7 left) and, as shown by Hu and Weng (2000), the two estimates coincide.

The KT model was developed by comparing two situations illustrated in Fig. II.9 and asserting that the average strain field is identical inside the composite inclusion represented at the top of Fig. II.9 and inside the homogeneous effective inclusion depicted at the bottom of the figure (e.g. Hu and Weng 2000). Recently, Shen and Yi (2001) derived an estimate leading to the same results as KT by using the same philosophy. The only difference is that they assume that the elastic strain energy changes in the infinite matrix due to the respective insertion of the two previous types of double-inclusion are identical in both cases (Fig. II.9). The demonstration proposed by Shen and Yi (2001) seems more rigorous than the KT original one and is briefly recalled below.

The elastic strain energy perturbations of the infinite matrix, caused respectively by the insertion of the composite inclusion and of the equivalent homogeneous inclusion (Fig. II.9),

are denoted  $\Delta U_{micro}$  and  $\Delta U^*$ . It is assumed that these two elastic strain energy changes are identical (Shen and Yi 2001). The quantity  $\Delta U^*$  can be determined from the results of the Eshelby problem (1957):

$$\Delta U^* = -\frac{1}{2}V_{DI}\sigma^\infty : \left[ \mathbf{C}_M : (\mathbf{C}^* - \mathbf{C}_M) : \mathbf{C}_M + \mathbf{C}_M : \boldsymbol{\Sigma}_{DI}^M \right] : \sigma^\infty, \quad (\text{II.83})$$

where the subscript  $DI$  designates the homogeneous effective inclusion (Fig. II.9) that is analogous to a double-inclusion. The elastic strain energy  $\Delta U_{micro}$  can be directly related to the average eigenstrains over the different particulate phases, denoted as  $\bar{\boldsymbol{\epsilon}}_r$  ( $r \in [1, P]$ ) (e.g. Mura 1987):

$$\Delta U_{micro} = \frac{1}{2}V_{DI}\sigma^\infty : \left( \sum_{r=1}^P \bar{\boldsymbol{\epsilon}}_r \right), \quad (\text{II.84})$$

where  $\bar{\boldsymbol{\epsilon}}_r$  can be expressed by means of Eq. (II.73) if the interactions between the particulate phases are neglected.

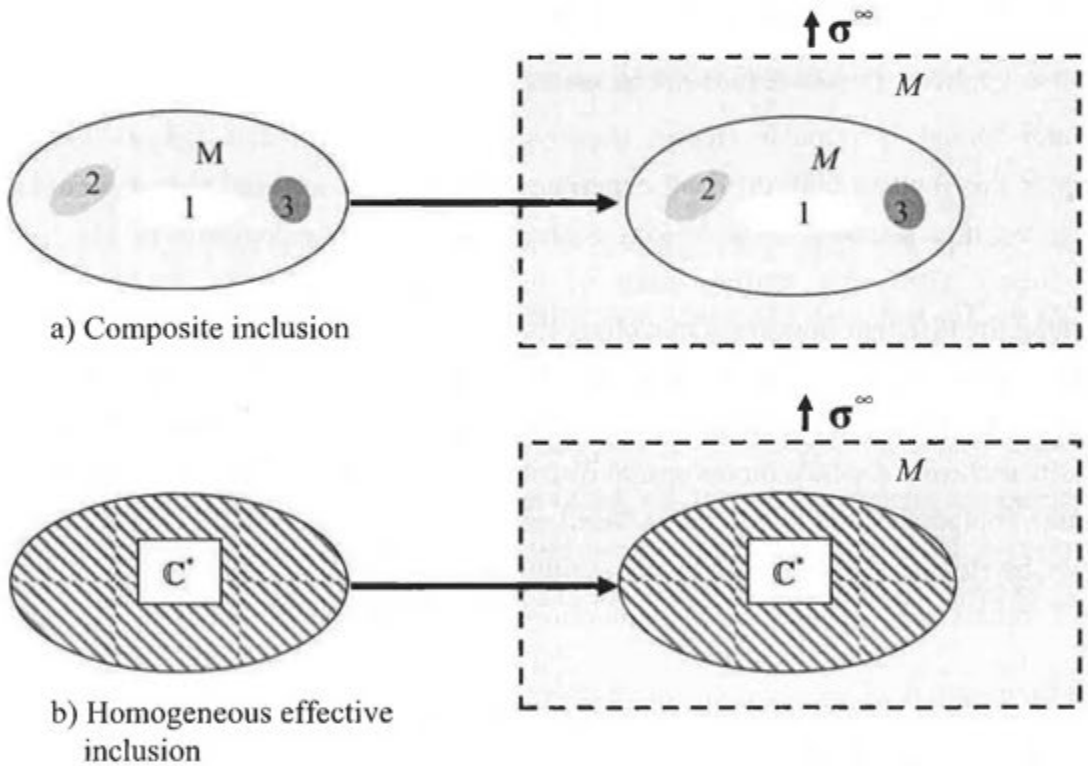


**Figure II.9: Schematic illustrating the effective inclusion concept employed by Kuster-Toksöz (1974) and Shen and Yi (2001).**

An estimation for the effective stiffness tensor can then be derived by assuming the equality between the last two equations (Shen and Yi 2001):

$$\mathbf{C}^* = \left[ \mathbf{I} - \left( \mathbf{S}_M + \sum_r \mathbf{H}_r^{dil} : \mathbf{C}_M : \boldsymbol{\Sigma}_{DI}^M : \mathbf{S}_M \right)^{-1} : \mathbf{H}^{dil} \right] : \mathbf{C}_M, \quad (\text{II.85})$$

which leads to the following expression for the compliance increment tensor after a few manipulations:

$$\begin{aligned}
 \mathbf{H} &= \left[ \mathbf{C}_M - \mathbf{C}_M : (\mathbf{I} + \mathbf{H}^{dil} : \mathbf{C}_M : \boldsymbol{\Sigma}_{DI}^M)^{-1} : \mathbf{H}^{dil} : \mathbf{C}_M \right]^{-1} : \mathbf{S}_M, \\
 &= \left[ \mathbf{C}_M : (\mathbf{I} + \mathbf{H}^{dil} : \mathbf{C}_M : \boldsymbol{\Sigma}_{DI}^M) : \mathbf{S}_M - \mathbf{H}^{dil} : \mathbf{C}_M \right]^{-1} (\mathbf{I} + \mathbf{H}^{dil} : \mathbf{C}_M : \boldsymbol{\Sigma}_{DI}^M) : \mathbf{S}_M - \mathbf{S}_M, \\
 &= \left[ \mathbf{I} - \mathbf{H}^{dil} : (-\mathbf{C}_M : \boldsymbol{\Sigma}_{DI}^M + \mathbf{C}_M) \right]^{-1} : (\mathbf{I} + \mathbf{H}^{dil} : \mathbf{C}_M : \boldsymbol{\Sigma}_{DI}^M) : \mathbf{S}_M - \mathbf{S}_M, \\
 &= \left[ \mathbf{I} - \mathbf{H}^{dil} : \boldsymbol{\Omega}_{DI}^M \right]^{-1} : (\mathbf{H}^{dil} : \mathbf{C}_M : \boldsymbol{\Sigma}_{DI}^M + \mathbf{H}^{dil} : \boldsymbol{\Omega}_{DI}^M) : \mathbf{S}_M, \\
 &= \left[ \mathbf{I} - \mathbf{H}^{dil} : \boldsymbol{\Omega}_{DI}^M \right]^{-1} : \mathbf{H}^{dil}.
 \end{aligned} \tag{II.86}$$

The latter combinations are valid provided that  $\mathbf{H}^{dil}$  is commutative with  $\mathbf{C}_M$ , which is true in the case of a macroscopically isotropic composite. The last equation coincides with the IDD formula in Eq. (II.43), whenever all double-inclusions have an identical shape.

#### 4.3.3.2 The Ponte-Castañeda and Willis (PCW) model

The demonstration of the PCW model (1995) based on the Hashin and Shtrikman (1962) variational principles is not recalled here, since their rigorous derivation is quite lengthy and requires notions of statistics. Nonetheless, the comparison of the previous double-inclusion type models with the PCW approach is instructive because it enables us to understand better the double inclusion role. In fact, it geometrically characterizes the cumulative density function for the distribution of inclusions introduced by Ponte-Castañeda and Willis (1995). It is defined from a conditional probability density function that represents the probability density for finding an inclusion centred at one point given that there is an inclusion centred at another point  $\mathbf{x}$ . Imagine that we randomly toss a segment from the centre  $\mathbf{x}$  of length  $R$  with a specified orientation and count the fraction of times the end point coincides with the centre of another inclusion. With the above interpretation, it becomes obvious that for macroscopically isotropic composites, such as cement-based materials, this probability is the same in all the directions. Consequently, the double-inclusion will be taken as spherical for these materials.

According to Zheng and Du (2001), explicit expressions are difficult to obtain with the PCW scheme if the different particulate phases do not have the same distribution. When one cumulative density function is enough for characterizing the distribution of all the inclusions, the PCW estimate coincides with the formula of the KT model and with the predictions of DIM and IDD. Another consequence of the similarities of these double-inclusion type models with PCW is that these estimates may be interpreted as rigorous bounds, provided that the inclusion distribution is accurately known.

In the next subsection, a new estimate based on the recent works of Duan et al. (2006) is proposed to remedy the shortcomings of DIM for composites with coated inclusions.

#### 4.3.4 Development of a modified DIM for composites with coated spherical inclusions

The scope of this subsection is to develop a double-inclusion type estimate that remedies some of the shortcomings of DIM noticed previously. Several attempts (Shodja and Roumi 2005; Shodja and Sarvestani 2001) to improve the scheme of Hori and Nemat-Nasser (1993) exist in the literature but most of these models requires numerical computations. For instance, Shodja and Sarvestani (2001) applied polynomial eigenstrains instead of uniform ones to the Hori and Nemat-Nasser DIM. However, closed-form solutions are difficult to reach with their theory. It is now proposed to derive differently DIM by employing the inhomogeneous Eshelby tensor in Eq. (II.21) derived by Duan et al. (2006). The configuration considered for the present derivation consists in a composite pattern embedded in an infinite matrix medium and subjected to a far-field stress  $\sigma^\infty$ . This composite pattern comprises various double-inclusions denoted as  $D_r$ , with  $r \in [1, P]$ , enclosed in a matrix region, each of them being constituted of a spherical inclusion with stiffness tensor  $\mathbb{C}_r$ , surrounded by a spherical coating with elasticity tensor  $\mathbb{C}_{Cr}$ . DIM was proved to lead to unexpected results for this type of microgeometry that is commonly encountered in cement-based materials, as will be shown in chapter 6.

The present derivation comprises two main steps. The effective stiffness tensors of the different double-inclusions are first estimated with the aid of the work of Duan et al. (2006). The particular configuration described on Fig. II.10a) is thus approximated by a simpler one described on Fig. II.10b). The effective elastic properties of the multiphase composite are then computed using the energy balance employed by Shen and Yi (2001). To achieve the computation of the effective stiffness of the double-inclusions, eigenstrain fields are introduced inside the inclusion domain so that each inclusion has the same elastic properties as its coating.

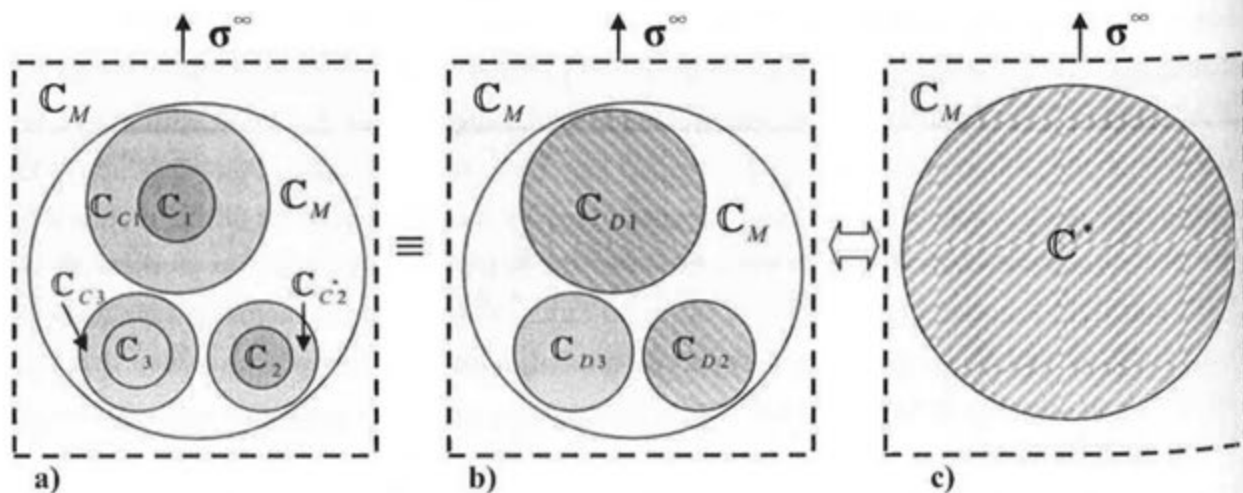


Figure II.10: Schematic illustrating the main steps employed to derive the modified DIM.

The average perturbation strain tensor inside an inclusion representing phase  $r$  and having the same stiffness tensor as its coating can be related to the volume average  $\bar{\boldsymbol{\varepsilon}}_r^*$  of the prescribed eigenstrain by means of the inhomogeneous Eshelby tensor defined by Duan et al. (2006):

$$\bar{\boldsymbol{\varepsilon}}_r' = \tilde{\boldsymbol{\Sigma}}_r^M : \bar{\boldsymbol{\varepsilon}}_r^*, \quad (\text{II.87})$$

where the expression of  $\tilde{\boldsymbol{\Sigma}}_r^M$  is given in Eq. (II.21). By neglecting the interactions between the double-inclusions, the average strain tensor inside the inclusion corresponding to a given particulate phase  $r$  takes the form:

$$\bar{\boldsymbol{\varepsilon}}_r = \mathbf{W}_{Dr}^M : \mathbf{S}_M : \boldsymbol{\sigma}^m + \bar{\boldsymbol{\varepsilon}}_r', \quad (\text{II.88})$$

with

$$\mathbf{W}_{Dr}^M = \left[ \mathbf{I} + \boldsymbol{\Sigma}_{Dr}^M : \mathbf{S}_M : (\mathbf{C}_{Cr} - \mathbf{C}_M)^{-1} \right]^{-1}, \quad (\text{II.89})$$

where  $\mathbf{W}_{Dr}^M$  designates the dilute strain localization tensor, also called the Wu tensor (Wu 1966) of the double-inclusion  $D_r$ , with  $r \in [1, P]$ , and  $\boldsymbol{\Sigma}_{Dr}^M$  denotes its Eshelby tensor. The Wu tensor practically links the volume average of the strain tensor inside an ellipsoidal inclusion to the far-field strain. The consistency condition written in an average sense:

$$\mathbf{C}_r : \bar{\boldsymbol{\varepsilon}}_r = \mathbf{C}_{Cr} : (\bar{\boldsymbol{\varepsilon}}_r - \bar{\boldsymbol{\varepsilon}}_r'), \quad (\text{II.90})$$

provides the following relation for the average eigenstrain  $\bar{\boldsymbol{\varepsilon}}_r^*$  in the inclusion:

$$\bar{\boldsymbol{\varepsilon}}_r^* = - \left[ (\mathbf{C}_r - \mathbf{C}_{Cr})^{-1} : \mathbf{C}_{Cr} + \tilde{\boldsymbol{\Sigma}}_r^M \right]^{-1} : \mathbf{W}_{Dr}^M : \mathbf{S}_M : \boldsymbol{\sigma}^m. \quad (\text{II.91})$$

The average perturbation strain tensor inside the inclusion  $\bar{\boldsymbol{\varepsilon}}_r'$  can then be deduced from Eq. (II.87). Using Eqs. (II.53-54) and (II.91), the mean perturbation strain tensor inside the inclusion coating  $\bar{\boldsymbol{\varepsilon}}_{Cr}'$  is obtained as:

$$\bar{\boldsymbol{\varepsilon}}_{Cr}' = - \frac{c_r}{c_{Dr} - c_r} \left( \tilde{\boldsymbol{\Sigma}}_{Dr}^M - \tilde{\boldsymbol{\Sigma}}_r^M \right) : \left[ (\mathbf{C}_r - \mathbf{C}_{Cr})^{-1} : \mathbf{C}_{Cr} + \tilde{\boldsymbol{\Sigma}}_r^M \right]^{-1} : \mathbf{W}_{Dr}^M : \mathbf{S}_M : \boldsymbol{\sigma}^m, \quad (\text{II.92})$$

where  $\tilde{\boldsymbol{\Sigma}}_{Dr}^M$  is the inhomogeneous Eshelby tensor of the double-inclusion  $D_r$  derived by Duan et al. (2006) and expressed in Eq. (II.21). It is emphasized that even though the inclusion and double-inclusion both have a spherical shape, their inhomogeneous Eshelby tensors are not identical, since their expressions given in Eq. (II.21) also depend on their relative size characterized by the parameter  $\rho$ . The mean strain and stress tensors inside the double-inclusion are further expressed with the help of Eqs. (II.53-54):

$$\bar{\boldsymbol{\varepsilon}}_{Dr} = \left[ \mathbf{I} - \frac{c_r}{c_{Dr}} \tilde{\boldsymbol{\Sigma}}_{Dr}^M : \left[ (\mathbf{C}_r - \mathbf{C}_{Cr})^{-1} : \mathbf{C}_{Cr} + \tilde{\boldsymbol{\Sigma}}_r^M \right]^{-1} \right] : \mathbf{W}_{Dr}^M : \mathbf{S}_M : \boldsymbol{\sigma}^m, \quad (\text{II.93})$$

$$\bar{\sigma}_{Dr} = \mathbf{C}_{Cr} : \left[ \mathbf{W}_{Dr}^M + \frac{c_r}{c_{Dr}} \mathbf{S}_M : \tilde{\Omega}_{Dr}^M : \left[ (\mathbf{C}_r - \mathbf{C}_{Cr})^{-1} : \mathbf{C}_{Cr} + \tilde{\Sigma}_r^M \right]^{-1} : \mathbf{W}_{Dr}^M \right] : \mathbf{S}_M : \sigma^\infty, \quad (\text{II.94})$$

where  $\tilde{\Omega}_{Dr}^M = \mathbf{C}_M : (\mathbf{I} - \tilde{\Sigma}_{Dr}^M)$  is called the inhomogeneous eigenstiffness of the double-inclusion  $D_r$ . By eliminating  $\sigma^\infty$  in the last two relations, the following expression can be obtained for the effective stiffness tensor of this double-inclusion:

$$\mathbf{C}_{Dr} = \left\{ \begin{array}{l} \mathbf{C}_{Cr} : \left[ \mathbf{I} + \frac{c_r}{c_{Dr}} \mathbf{S}_M : \tilde{\Omega}_{Dr}^M : \left[ (\mathbf{C}_r - \mathbf{C}_{Cr})^{-1} : \mathbf{C}_{Cr} + \tilde{\Sigma}_r^M \right]^{-1} \right] \\ \left[ \mathbf{I} - \frac{c_r}{c_{Dr}} \tilde{\Sigma}_{Dr}^M : \left[ (\mathbf{C}_r - \mathbf{C}_{Cr})^{-1} : \mathbf{C}_{Cr} + \tilde{\Sigma}_r^M \right]^{-1} \right]^{-1} \end{array} \right\}, \quad (\text{II.95})$$

By carrying out exactly the same reasoning as in Eqs. (II.83-85) (see subsection 4.3.3.1), an explicit estimation can then be achieved for the effective stiffness tensor of the composite with coated inclusions:

$$\mathbf{C}^* = \left[ \mathbf{I} - \left( \mathbf{S}_M + \sum_r \mathbf{H}_{Dr}^{dil} : \mathbf{C}_M : \Sigma_{CDI}^M : \mathbf{S}_M \right)^{-1} : \left( \sum_r \mathbf{H}_{Dr}^{dil} \right) \right] : \mathbf{C}_M, \quad (\text{II.96})$$

where  $\Sigma_{CDI}^M$  is the Eshelby tensor of the equivalent composite pattern depicted on Fig. II.10c) and the stiffness tensor  $\mathbf{C}_{Dr}$  can be predicted by Eq. (II.95). In the ensuing, this estimation will be referred to as the modified DIM.

#### 4.4 Accuracy of EMTs

The actual capacity of predictions of the different schemes in literature has been a subject of extensive debate (Christensen 1990). The precise knowledge of the accuracy of each scheme is a crucial issue of micromechanics, since it would allow for determining the cases for which an EMT can be preferentially employed or not.

##### 4.4.1 Review on the accuracy of EMTs

Testing the accuracy of an EMT is not a trivial matter, since their predictions highly depend on the way the microstructure is represented. The two best methods for performing such tests consist in comparing estimations of micromechanical schemes with FE simulations of simple microgeometries (Segurado and Llorca 2002; Zheng and Du 2001) or in confronting them with experimental data on materials having a simple and well-defined microstructure (e.g. Berryman and Berge 1996). Cement-based materials with their complex microstructure are not suited for performing such experimental comparisons.

For instance, Segurado and Llorca (2002) performed 3D numerical simulations of materials reinforced by rigid spheres or weakened by spherical voids. The simulated materials contain different volume fractions (up to 50 %) of spherical inclusions that are monodisperse and randomly distributed. They concluded that GSCS provided estimations close to the FE results

even for 50 % of spheres, while the MT estimate visibly differs from the elastic and shear moduli obtained numerically for volume fractions higher than 30 %. Another instructive comparative study has been carried out by Zheng and Du (2001) on a 2D matrix weakened by isotropically distributed circular voids. On the contrary to Segurado and Llorca (2002), they noticed that the MT and double-inclusion type schemes provide better estimations than the GSCS.

Berryman and Berge (1996) have compared both KT and MT estimates with experimental data on porous materials, such as sintered glass beads, and have noticed that the prediction of the KT or MT estimate with spherical inclusions was only in acceptable agreement with the experimental measurements for volume fractions of pores less than 20 %. Berryman and Berge (1996) managed to obtain some slight improvement by using needled-shaped inclusions but concluded that KT or MT schemes should not be used when the inclusion volume fraction is greater than 20-30 %. These results seem to be coherent with the analysis of Segurado and Llorca (2002). These errors may be due to the fact that over a certain volume fraction of inclusions, MT and double-inclusion type estimates do not manage to accurately take into account the interactions between inclusions. It appears however intricate from these diverse results found in literature to affirm which one of the presently reviewed models is the most accurate. Therefore, it is useful to further compare these estimations with recent numerical simulations performed on cementitious materials.

#### *4.4.2 Comparison with numerical simulations on cement-based materials*

Owing to progress in the computer modelling of cement microstructure, many three-dimensional numerical simulations have been carried out for computing the macroscopic elastic properties of cement-based materials and constitute good comparison points. By confronting the predictions of the different EMTs presented previously with different types of simulations, we try to determine which scheme is the best suited for three well-defined cases:

- a concrete composed of a mortar matrix and aggregates modeled as spherical inclusions (Wriggers and Moftah 2006);
- a mortar consisting in a cement matrix rigidified by spherical coated inclusions representing the sand grains surrounding by ITZ (Garboczi and Berryman 2001);
- a porous medium that can be assimilated to a cement paste comprising a rigid solid phase and spheroidal porous inclusions (Roberts and Garboczi 2000).

The input elastic parameters for the different simulations and micromechanical estimations are gathered in Appendix II.A. The three materials treated are simulated as macroscopically isotropic and the inclusions are supposed to be isotropically distributed. Therefore, a spherical double-inclusion is adopted for the computations of the double-inclusion type schemes.

#### 4.4.2.1 Comparison with the simulations of Wriggers and Moftah (2006)

Wriggers and Moftah (2006) performed advanced FE simulations on geometrical models of concrete generated with the Monte-Carlo's method to compute its mechanical properties. The aggregates are modeled as spheres of different sizes, so as to accurately reproduce the material granulometry.

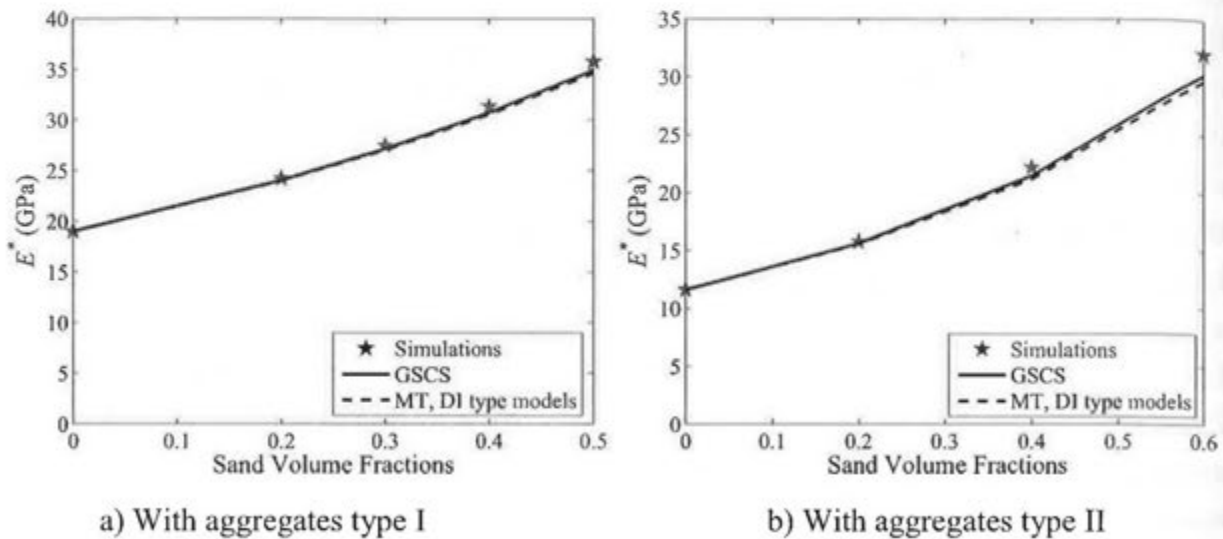


**Figure II.11: Evolutions of the effective Young moduli estimated by different micromechanical schemes and by FE simulations (Wriggers and Moftah 2006) for two types of concretes as functions of the volume fractions of aggregates a) type I and b) type II.**

All the micromechanical estimations appear to be relatively close the numerical results plotted on Fig. II.11, the GSCS of Christensen and Lo (1979) giving slightly better predictions than the other models. For spherical cases, the GSCS should thus be preferred to MT and double-inclusion type models. If all the inclusions are approximated by spheres, the other matrix-inclusion type estimates (see Eqs. (II.38) and (II.43)) lead exactly to the same results for a macroscopically isotropic material. A frequent problem with using spherical inclusions is that too many EMTs give exactly the same result even if certain ones may be much more evolved and efficient. The case of non-spherical inclusions will therefore be treated later. The mortar matrix considered as a homogeneous phase in the Wriggers and Moftah (2006) is in fact a heterogeneous material that has been the subject of advanced numerical simulations by Garboczi and Berryman (2001).

#### 4.4.2.2 Comparison with the simulations of Garboczi and Berryman (2001)

Garboczi and Berryman (2001) performed simulations on a material model composed of a matrix reinforced by spherical coated inclusions. They made the elastic properties of the inclusion coating vary and investigated numerically the effects on the material effective elastic properties. Their tests are very instructive for the case of mortars, where the

characteristics of ITZ forming a layer around the sand grains strongly influence their mechanical behaviour, as already explained in Part I. It has been asserted by diverse authors (e.g. Hashin and Monteiro 2002) that ITZ that is more porous than HCP (Lutz and Zimmerman 2005) should have a lower Young modulus than the cement matrix (see Eq. (I.5)). The numerical results obtained by Garboczi and Berryman (2001) for diverse values of the parameter  $e$  characterizing the ratio of the Young modulus of ITZ on the one of HCP are plotted in Fig. II.12 and serve as comparison points for the predictions of different EMTs. The closest estimations are provided as previously by GSCS, even though the modified DIM is also in good agreement with the numerical results. However, despite its good accuracy on the examples treated, the GSCS is more complicated to compute than the other schemes and may appear less suited for the case presented below of an elastic body containing non-spherical inclusions.

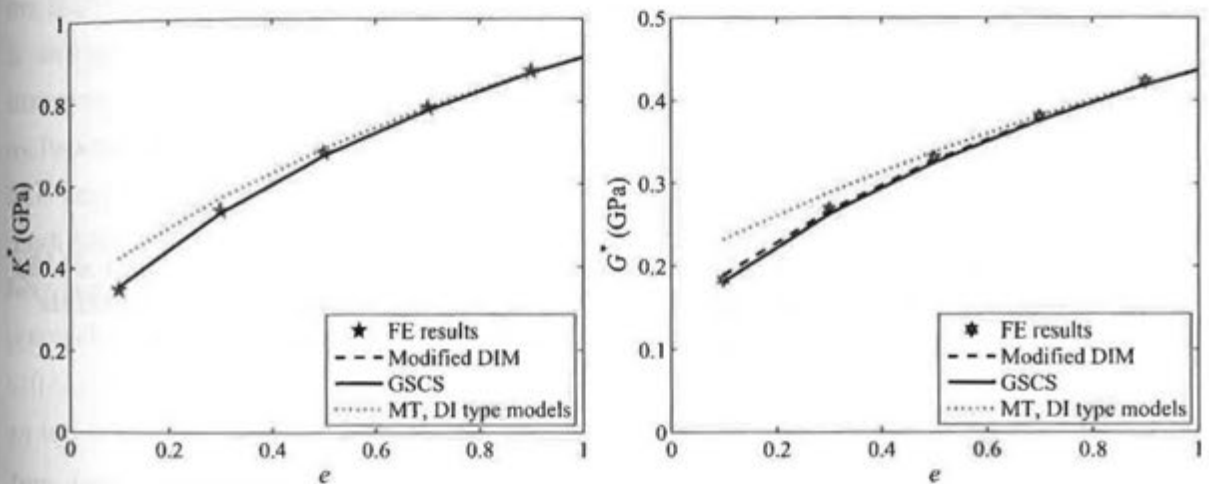


**Figure II.12: Evolutions of the effective elastic bulk (left) and shear (right) moduli estimated by different EMTs and by FE simulations (Garboczi and Berryman 2001) for both sound and degraded HCP as a function of  $e = E_{ITZ} / E_{HCP}$ .**

#### 4.4.2.3 Comparison with the simulations of Roberts and Garboczi (2000)

The case of an elastic body weakened by spheroidal voids is now studied, in order to further compare the concerned EMTs. The GSCS and modified DIM presently developed are not considered for this study, since closed-form expressions are too difficult to reach for such cases. Roberts and Garboczi (2000) conducted series of simulations with porous inclusions of diverse shapes. The elastic moduli of pores are considered to vanish. In particular, numerical tests were performed with oblate spheroidal voids that are randomly distributed in a rigid solid matrix and are allowed to overlap. The model of microstructure thus obtained is well suited for representing a porous material such as a HCP and is furthermore very similar to the micromechanical model of Zimmerman (1986), in which HCP is represented by a solid matrix weakened by spheroidal pores. The FE results of Roberts and Garboczi (2000) for the simulated porous material are plotted on Fig. II.13 and compared with the predictions of

EMTs, even though the latter are not capable to account for the overlappings between these cavities. The double-inclusion type estimates are seen to give the closest estimations and should consequently be preferentially used in the case of non-spherical inclusions.

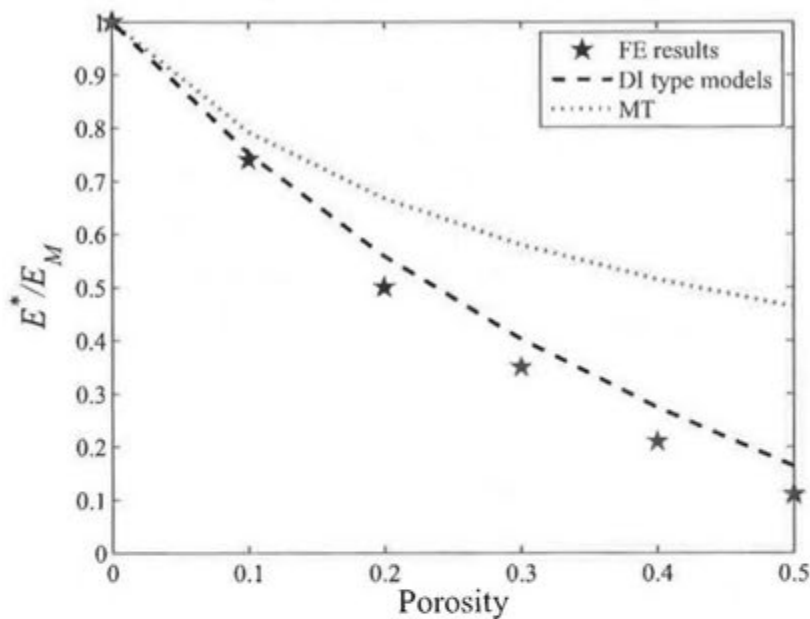


*Figure II.13: Evolutions of the effective Young moduli estimated by different EMTs and by FE simulations (Roberts and Garboczi 2000) for an elastic body weakened by oblate spheroidal voids with aspect ratio  $r = 0.25$ , as a function of porosity.*

#### 4.5 Conclusion of chapter 4

Different analytical homogenization schemes from literature have been presented and examined in a critical way. The respective benefits and drawbacks of these methods are now recapitulated on the basis of well-defined criteria. In order to choose the best suited scheme for the estimations of the elastic properties of cement-based materials, the following criteria are adopted:

- (i) simplicity of computation and versatility;
- (ii) respect of the rigorous bounds;
- (iii) accuracy.

By versatility, it is intended that we assess if the model can be extended to the cases of multiphase composites, non-spherical inclusions or diverse distributions of inclusion. The IDD scheme is the most versatile one, since it is the only model that is valid for multiphase composites with various inclusion geometries and that can properly take into account the influence of various inclusion distributions. It should furthermore be theoretically applicable for non-ellipsoidal inclusions, according to Zheng and Du (2001). In addition, it has a simple and explicit structure, as well as MT and other double-inclusion type models.

Many authors (e.g. Berryman 2006) argue that a consistent EMT should respect rigorous bounds such as the Hashin-Shtrikman (HS) or the Willis bounds that have been proved to be

rigorous. Norris (1989) found a simple three-phase example with disk-shaped particles for which the effective thermal conductivity estimated by MT violates HS bounds. It may thus be hazardous to apply MT to multiphase composites containing more than two phases. Conversely, Ponte-Castaneda and Willis (1995) proved that their estimate may be interpreted as rigorous bounds. The other double-inclusion type schemes that coincide in most cases with the PCW model are also likely to respect rigorous bounds.

The confrontation of the different schemes with diverse numerical simulations has revealed that the GSCS is generally more accurate than MT and double-inclusion type estimates in the case of spherical inclusions. In addition, the GSCS and modified DIM are the only two models that do not lead to unexpected results for the case of coated spherical inclusions that is of practical importance for cement-based materials. However, the double-inclusion type models provide the closest estimations to the FE results of Roberts and Garboczi (2000) for the important case of an elastic body weakened by spheroidal voids. The accuracy of an EMT is strongly conditioned by the way in which the phase interactions are accounted for. For instance, the dilute scheme does not take into consideration any interaction between inclusions and frequently appears to be inaccurate in the present study. As already mentioned, MT and double-inclusion type estimates can also be seen as dilute models improved by modifying the far-field stress (see Eq. (II.45)). They only incorporate indirectly the interaction between inclusions and their immediately surrounding region. The GSCS integrates more precisely these interactions by embedding matrix and inclusions in the yet unknown effective infinite medium. Table II.1 aims at weighing the pros and the cons of the various theories in an informal way.

| Micromechanical scheme           | Simplicity of use and versatility | Respects rigorous bounds | Accuracy for non-spherical inclusions | Accuracy for coated inclusions |
|----------------------------------|-----------------------------------|--------------------------|---------------------------------------|--------------------------------|
| Dilute (e.g. Eshelby 1957)       | **                                | *                        | *                                     | *                              |
| MT (Mori and Tanaka 1973)        | **                                | *                        | **                                    | *                              |
| IDD (Zheng and Du 2001)          | ***                               | ***                      | ***                                   | *                              |
| DIM (Hori and Nemat-Nasser 1993) | **                                | ***                      | ***                                   | *                              |
| Modified DIM                     | **                                | ***                      | *                                     | ***                            |
| GSCS (Christensen and Lo 1979)   | *                                 | ***                      | *                                     | ***                            |

\*: Insufficient, \*\*: Moderate, \*\*\*: Good

*Table II.1: Table confronting the merits of the different EMTs presently reviewed.*

Even though, the GSCS and modified DIM are more appropriate for materials with coated spherical inclusions, the IDD scheme seems to present the best compromise otherwise. It is emphasized that this approach is more accessible and versatile than other double-inclusion type models (Ponte-Castañeda and Willis 1995). The IDD estimate shows in particular its efficiency in the cases of macroscopically isotropic materials containing non-spherical inclusions and therefore constitutes a suitable tool for the next chapter dedicated to the influence of inclusion shape on the elastic effective properties of cement pastes.

## 5 INFLUENCE OF INCLUSION SHAPE ON THE LINEAR ELASTIC EFFECTIVE PROPERTIES OF HCP (STORA ET AL. 2006a)

In most micromechanical models applied to HCP in literature, all inclusion phases are approximated by spheres for simplicity, though cement paste micrographs indicate that none of these phases is really spherical. The present chapter assesses how the predictions of the effective linear elastic properties of HCP change with the inclusion geometry. In particular, it is useful to detect the cases, for which these properties vary significantly and for which more realistic geometric forms should be applied. The determination of the Eshelby tensor  $\Sigma_r^M$  of the inclusion phases is usually quite complicated for non-spherical inclusions and it generally has to be estimated numerically except for some simple cases. In particular, the Eshelby

tensor of spheroids presents the benefit of being analytically calculable (see Eq. (II.20)). That's why all inclusion phases are approximated by spheroids with different aspect ratios in order to scrutinize the influence of inclusion shapes on the linear elastic effective properties of cement pastes. The IDD scheme that has been previously identified to be suited for accounting for the effects of non-spherical morphologies of inclusions is chosen for computing these macroscopic properties.

The chapter is organized as follows. First, a dimensionless morphological parameter is introduced to characterize the inclusion shape. Then, the cases for which this parameter actually plays a significant role on HCP elastic macroscopic properties are investigated by successively modeling each particulate phase as spheroids, which shape ranges from needle-like to disk-like. Finally, an attempt is made to approximate the morphological parameter on the basis of experimental results. The spheroids representing the particulate phases in the micromechanical approach are then determined through this parameter. The estimations thus obtained for the effective Young modulus are compared with the results respectively predicted by a homogenization model with spherical inclusions and by FE simulations.

### 5.1 Definition of a shape parameter for the inclusions

In the micromechanical schemes presented in the previous chapter, none of the basic input parameters, i.e. the phase volume fractions and elastic properties, takes into consideration the morphology of the particulate phases. The aim of this section is to introduce a relevant parameter approximating the real shapes of inclusions.

We propose to analyze the geometry of an inclusion  $I$  by considering the ratio of its volume  $V_I$  over surface area  $A_I$ . For example, this ratio for an arbitrary spheroid can be written as:

$$\frac{V_I}{A_I} = f\left(\frac{b}{a}\right)a, \quad (\text{II.97})$$

where  $a$  is the radius of the circular base of the spheroid and  $b$  is either the minor axis for oblate spheroids or the major one for prolate ones. The aspect ratio of the spheroid is designated by  $r_I = b/a$ . The most natural way to normalize  $V_I/A_I$  is to divide this ratio by one third of the radius  $R_{eq}$  of the equivalent sphere having the same volume  $V_I$ :

$$\zeta = \frac{3V_I}{A_I R_{eq}} \quad \text{with} \quad \begin{cases} \zeta_{sph} = 1 \\ \zeta_{disk} = \zeta_{needle} = 0 \end{cases} \quad (\text{II.98})$$

This shape or morphological parameter  $\zeta$  has the interesting property that it varies between 0 and 1. This comes from the fact that, among all shapes, the sphere is the one that maximizes the inner volume for a given surface area according to an isoperimetric theorem (Pólya and Szegő 1951). The less spherical the inclusion is the lower  $\zeta$  becomes. Therefore the value of  $\zeta$  allows for quantifying the asphericity of a particle.

In order to assess the reliability of  $\zeta$ , it is interesting to study if oblate and prolate spheroidal inclusions with the same shape parameter and volume fraction actually have similar effects on macroscopic elastic moduli. Hence, computations are performed in which an arbitrary particulate phase  $r$  of HCP is approximated respectively by prolate and oblate spheroids while the other inclusion phases are represented by spheres. The evolution of the effective elastic moduli is examined with these two types of spheroids as their parameter  $\zeta$  decreases from 1 to 0. Fig. II.14 schematically represents the randomly oriented spheroids corresponding to an identical particulate phase  $r$  and their surrounding double-inclusions inside the RVE. For simplicity these spheroids are assumed to have the same size. The number of spheroids per unit volume is denoted by  $N_r$ . The volume fraction  $c_r$  of phase  $r$  can thus be written as:

$$c_r = N_r V_{\text{spheroid}} = \begin{cases} \frac{4}{3} N_r \pi a^3 r_f & \text{for oblate spheroids} \\ \frac{4}{3} N_r \pi \frac{b^3}{r_f^2} & \text{for prolate ones} \end{cases} \quad (\text{II.99})$$

According to this equation, the variation of the aspect ratio  $r_f$ , and consequently of the shape parameter  $\zeta$ , of the spheroids can be performed in two different ways:

- The maximum axis of the spheroid (=  $a$  for an oblate one and  $b$  for a prolate one) varies and  $c_r$  is kept constant, as illustrated on Fig. II.14 (bottom left).
- The maximum axis of the spheroid remains constant and  $c_r$  changes, as illustrated on Fig. II.14 (bottom right).

For the present application, the first possibility seems more appropriate because it keeps a constant volume fraction. But it presents the following deficiency: the spheroid maximum axis appearing on the equation just above has to augment, as  $\zeta$  decreases, and in particular tends to infinity, as  $\zeta$  goes to 0. The second possibility is more adapted for inclusion forms tending to cracks, but we prefer the first option, since the inclusion phases present inside the HCP are far from being crack-like.

Two examples on ordinary Portland cement pastes (CEM I) are considered to verify the efficiency of the shape parameter  $\zeta$ . These CEM I pastes with  $w/c = 0.25, 0.40$  and  $0.50$  used for this study are defined in Tables II.2 and I.3 in terms of volume fractions and mechanical properties of their constituent phases. The following representation of the microstructure is adopted to compute the HCP effective elastic properties: the CSH gel acts as a matrix in which the main particulate phases presented in Part I, namely Aft, AFm, CH, CP and UC, are embedded and play the role of inclusion (Fig. II.15). This representation is close to the one of the Constantinides and Ulm model (2004), except that a homogenized CSH gel is used instead of the two CSH considered in their description.

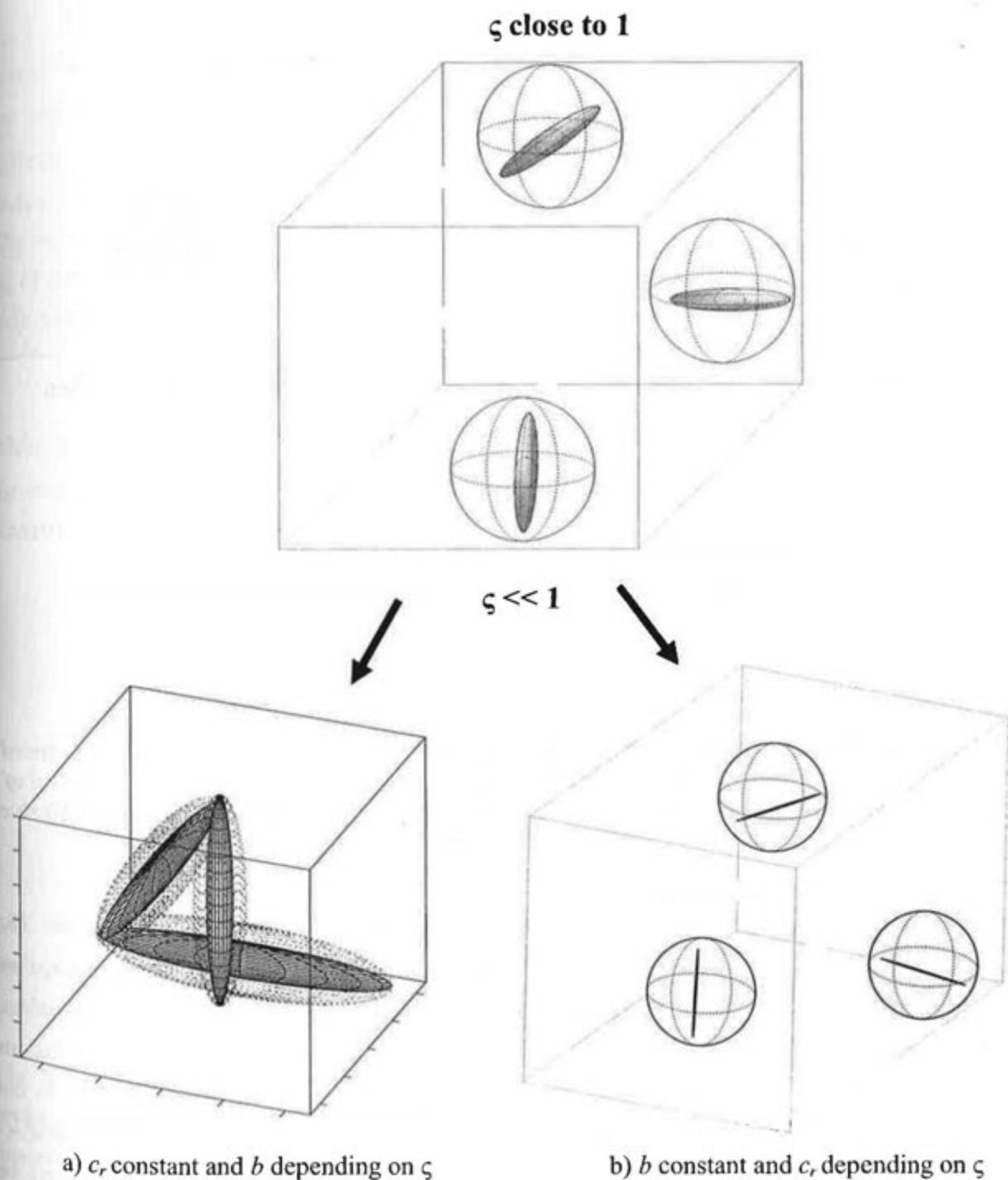


**Figure II.14:** schematic representation of the evolution of the dimensions of prolate spheroids corresponding to an inclusion phase  $r$  with the shape parameter  $\zeta$ :  
 a)  $c_r$  constant; b)  $b$  constant (Stora et al. 2006a).

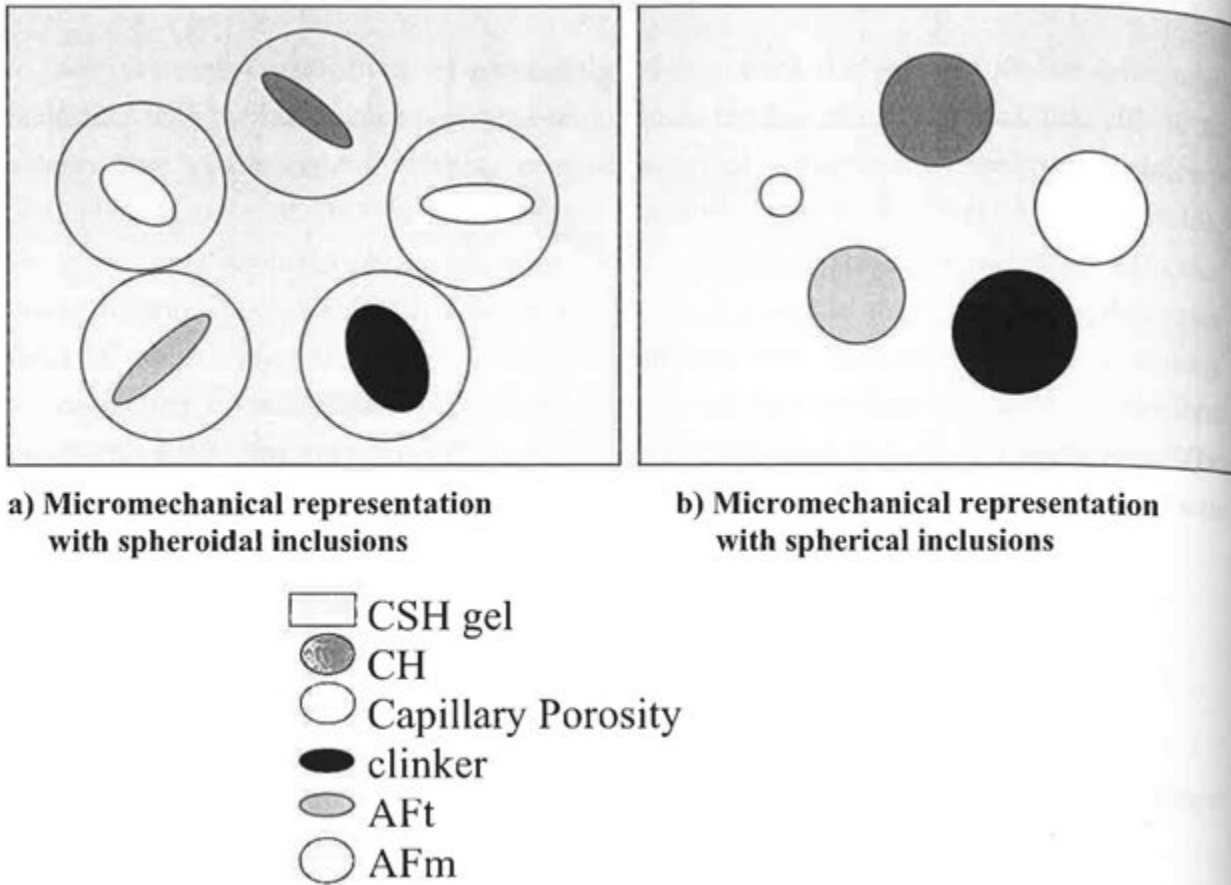


**Figure II.15:** a) Two-dimensional representation of HCP with spheroidal inclusions based on MT and double-inclusion type schemes (left); b) Two-dimensional representation of HCP with spherical inclusions based on MT and double-inclusion type schemes (Stora et al. 2006a).

The effective elastic properties of HCP are estimated by means of the IDD estimate. The cement pastes are considered as macroscopically isotropic. Consequently, for each particulate phase of HCP, the corresponding double-inclusion should be taken as spherical. Nevertheless, for a spherical distribution of randomly oriented spheroids, highly-concentrated inclusions may overlap. The maximum volume fraction for which these spheroidal inclusions do not overlap is calculated in Appendix II.B. For higher volume fractions, a non-spherical double-inclusion must be adopted and a volume average over all possible orientations must be performed. Once its exact shape has been determined for each particulate phase  $r$ , the eigenstiffness tensors of the various double-inclusions denoted by  $\Omega_{Dr}^M$  enclosing the inclusions  $V_i^r$  are calculated from Eq. (II.30). The IDD estimate of the compliance increment tensor  $\mathbb{H}_{HCP}^{IDD}$  applied to this representation of HCP microstructure with spheroidal inclusions (Fig. II.15) then results in:

$$\mathbb{H}_{HCP}^{IDD} = \left[ \mathbb{I} - \left\{ \mathbb{H}_{HCP}^{dil} : \Omega_{Dr}^{CSH} \right\} \right]^{-1} : \left\{ \mathbb{H}_{HCP}^{dil} \right\}, \quad (\text{II.100})$$

with

$$\{\mathbb{H}_{HCP}^{dil}\} = \text{tr}(\mathbb{H}_{HCP}^{dil} : \mathbb{J})\mathbb{J} + \frac{1}{5} \text{tr}(\mathbb{H}_{HCP}^{dil} : \mathbb{K})\mathbb{K}, \quad (\text{II.101})$$

where the curly brackets denote the average over all possible orientations, where  $\text{tr}$  denotes the trace operator and where  $r = \text{CH, CP, UC, AFt or AFm}$ . The tensors  $\Omega_{Dr}^{CSH}$  and  $\mathbb{H}_{HCP}^{dil}$  are defined in Eqs. (II.31) and (II.33). The macroscopic Young moduli of the HCP can be deduced from the latter expression by using Eqs. (II.6-7) and (II.12-13).

The input data required for the micromechanical estimations are the volume fractions  $c_r$  and  $c_M$  of each phase that can be found respectively on Table II.2 for the six HCP samples and the bulk and shear moduli, respectively denoted as  $K_i$  and  $G_i$ , reading as follows:

$$K_i = \frac{E_i}{3(1-2\nu_i)} \quad \text{and} \quad G_i = \frac{E_i}{2(1+\nu_i)} \quad \text{with } i \in \{\text{AFt, AFm, CP, CH, CSH, UC}\}, \quad (\text{II.102})$$

where the Young modulus  $E_i$  and the Poisson ratio  $\nu_i$  of each phases are given in Table I.3. for sound and degraded HCP. The present input values are the same as those employed by Kamali (2003) in her simulations.

| Volume fractions in % |             |       |      |                |      |      |
|-----------------------|-------------|-------|------|----------------|------|------|
|                       | CEM I paste |       |      | CEM II/A paste |      |      |
| w/c =                 | 0.5         | 0.4   | 0.25 | 0.5            | 0.4  | 0.25 |
| CH                    | 16.4        | 16.9  | 15.7 | 10.5           | 10.8 | 8.5  |
| CSH                   | 47.3        | 47.4  | 42.1 | 49.4           | 49.7 | 45.1 |
| UC                    | 10.04       | 14.46 | 28   | 13             | 18.4 | 31.4 |
| AFt                   | 2.4         | 2.8   | 2.9  | 2.7            | 2.3  | 2.9  |
| AFm                   | 0.16        | 0.14  | 0.3  | 0.4            | 0.4  | 1    |
| Porosity (%)          | 23.7        | 18.3  | 11.0 | 24.0           | 18.4 | 11.1 |

**Table II.2: Input volume fractions of principal hydrates, unhydrated clinker and capillary porosity for six different HCP (Kamali 2003).**

The first example consists in approximating the initial capillary porosity respectively as prolate and oblate spheroids with varying shapes, while the other particulate phases are modeled as spherical inclusions. The different volume fractions of these initial capillary pores are  $c_{CP} = 11\%$ ,  $18.3\%$  and  $23.7\%$  in the CEM I pastes with  $w/c = 0.25, 0.40$  and  $0.50$ , respectively. The effects of both types of porous spheroids on the effective Young modulus are plotted on Fig. II.16 for the three CEM I pastes. It is worth noting that for this case of porous inclusions the spherical shape optimizes the Young modulus. This can be understood intuitively considering the fact that for a given area the spherical surface maximizes the inner volume (e.g. Polya and Szego 1951). The curves on Fig. II.16 show that prolate and oblate porous spheroids with an identical value for the morphological parameter do not have the same effects on Young modulus except for  $\zeta$  close to 1. The weakening effects of prolate

porous spheroids compared to the spherical case are quite negligible, whereas oblate ones have a much more pronounced impact. These tendencies are even more marked for high volume fractions of initial capillary pores. In this condition, the parameter seems not to be well appropriate except for values higher than 0.80. But it should be underlined that this example corresponds to an extreme case, since the contrast between the elastic properties of matrix and inclusion is infinite.

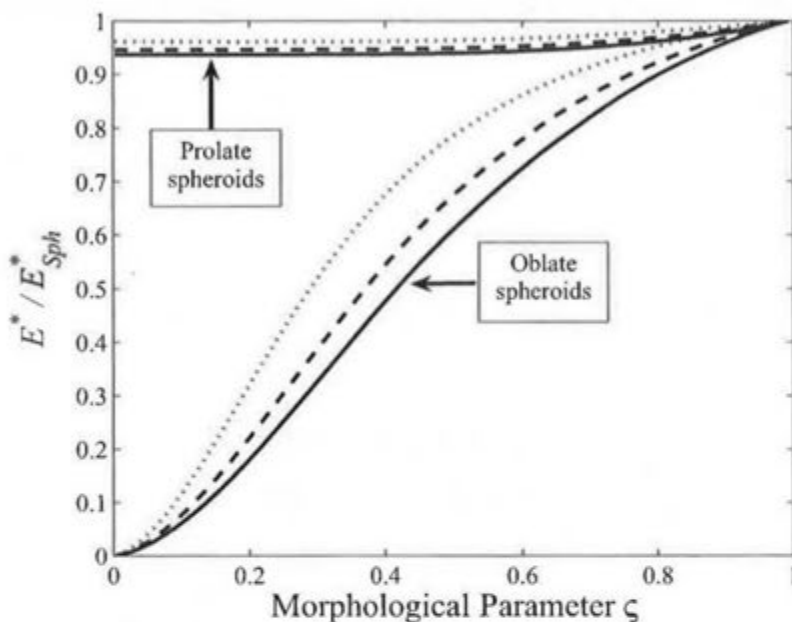


**Figure II.16: Evolutions of the normalized effective Young modulus for sound CEM I pastes with capillary pores as a function of the shape parameter  $\zeta$  for different volume fractions. Solid lines:  $w/c = 0.50$  ( $c_{CP} = 23.7\%$ ), dashed lines:  $w/c = 0.40$  ( $c_{CP} = 18.3\%$ ), dotted lines:  $w/c = 0.25$  ( $c_{CP} = 11\%$ ) (Stora et al. 2006a). The subscript *Sph* means that the modulus has been estimated using the spherical particle approximation.**

The second example illustrates the case of finite contrast by focusing on unhydrated clinker inclusions, which are stiffer than the CSH matrix. Their volume fractions in the three CEM I pastes are  $c_{UC} = 10.04\%$ ,  $14.46\%$  and  $28\%$  respectively. The curves obtained when  $\zeta$  varies from 0 to 1 for both types of spheroids are presented on Fig. II.17; they are relatively close and, for  $\zeta$  higher than 0.5, the Young moduli estimated with oblate and prolate spheroids are almost confounded. For lower values, oblate spheroids produce a stronger stiffening effect. This result is not surprising in view of the evolution of the spheroids with  $\zeta$ : as the latter goes to 0, oblate spheroids tend to infinite disks whereas prolate ones tend to infinite needles, as may be observed on Fig. II.14. Both types of spheroids thus tend to radically different geometries. For this particular example,  $\zeta$  turns out to be relevant on a limited range, where it is useful for approaching real inclusion shapes. For inclusions whose geometrical shape is very far from spherical,  $\zeta$  is small and other parameters are required to precisely characterize the effects of morphology on elastic moduli. This remark applies particularly when the

contrast between matrix and inclusion elastic properties is high, as in the first example presented above.

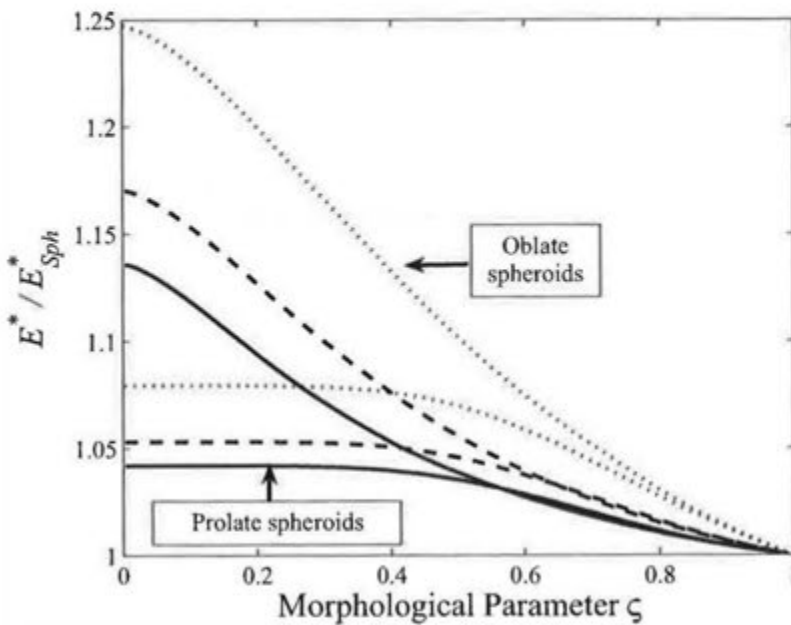


Figure II.17: Evolutions of normalized effective Young modulus for sound CEM I pastes with unhydrated clinker respectively represented by oblate and prolate spheroids, as a function of the shape parameter  $\zeta$ . Solid lines:  $w/c = 0.50$ ; dashed lines:  $w/c = 0.40$ ; dotted lines:  $w/c = 0.25$  (Stora et al. 2006a).

## 5.2 Significance of the shape parameter for HCP elastic properties

The purpose of this section is to determine the particulate phases whose shape parameter may become significant for the estimation of HCP elastic properties. We now make the shape parameter vary individually for each inclusion phase, while  $\zeta$  is kept fixed and equal to 1 for the other particulate phases. The dependence of the elastic properties on  $\zeta$  is thus investigated successively for all inclusion phases composing HCP in both sound and degraded pastes defined in Table II.2.

From the microstructural description detailed in Part I, it appears that needle-like ettringite should rather be characterized by prolate shapes and disk-like portlandite by oblate morphologies. Concerning unhydrated clinker, AFm and initial capillary pores, no evidence indicates whether to preferentially use oblate or prolate spheroids for characterizing their shape. Thus, they are represented by 50 % of both oblate and prolate spheroids in this work.

The influence of the shape of aluminates and portlandite on effective elastic properties of unleached HCP is negligible as shown on Fig. II.18. On the contrary, the morphology of initial capillary pores clearly plays a significant role due to the infinite contrast between matrix and porous inclusions, as already highlighted in the preceding subsection. The relative

significance of this porous phase depends on its volume fraction ( $c_{CP} = 11\%$ ,  $18.3\%$  and  $23.7\%$  for  $w/c = 0.25$ ,  $0.40$  and  $0.50$  respectively). The shape of unhydrated clinker may also have a non negligible effect, since an increase of  $25\%$  can be obtained as  $\zeta$  goes to  $0$  (see Fig. II.17).

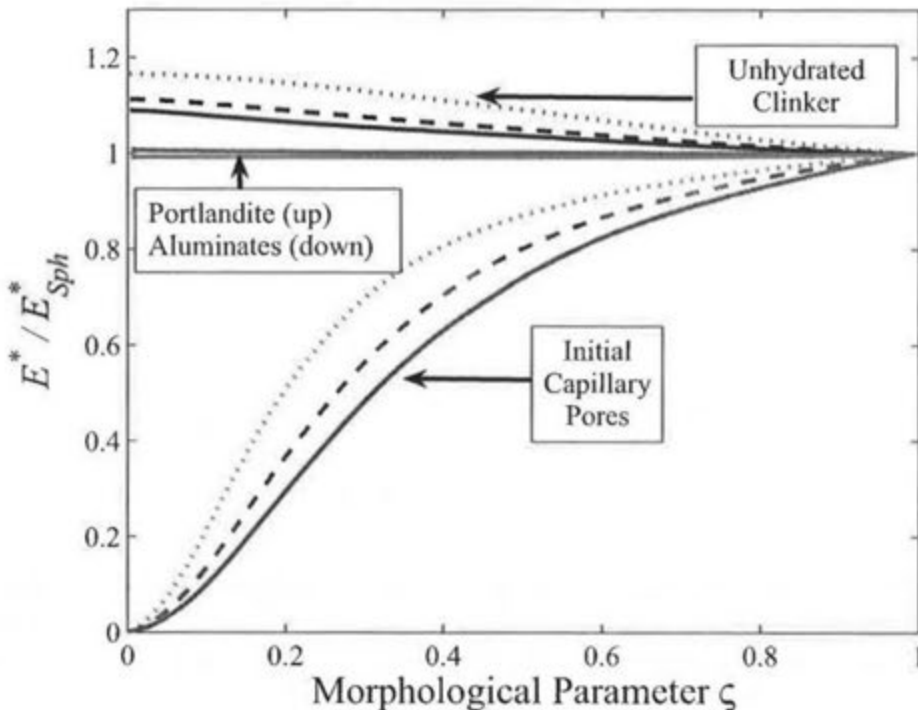


**Figure II.18:** Evolutions of the normalized effective Young modulus for sound CEM I pastes, as a function of the morphological parameter  $\zeta$ . Solid lines:  $w/c = 0.50$ ; dashed lines:  $w/c = 0.40$ ; dotted lines:  $w/c = 0.25$  (Stora et al. 2006a).

We now focus on the degraded state. On Fig. II.19 are presented the evolutions of the Young modulus as a function of  $\zeta$  for the three CEM I pastes when CH, AFt and AFm are degraded successively. For  $\zeta$  higher than  $0.1$ , the influence of dissolved ettringite and AFm shapes remains negligible because of their scarce volume fractions (see Table II.2). Conversely, the influence of leached portlandite morphology increases considerably compared to the sound state. This is partly due to its high volume fractions ( $> 15\%$ ) but it should also be emphasized that its effects are even more significant than the initial capillary pores one, although some of their concentrations are higher ( $c_{CP} = 11\%$ ,  $18.3\%$  and  $23.7\%$ ). As may be observed on Fig. II.19, the decrease of the effective Young modulus is much more pronounced for oblate spheroids than for prolate ones. Consequently, the elastic properties are more sensitive to the flattened morphology of CH than to the initial capillary pores one, represented not only by oblate spheroids but also by prolate ones (see Fig. II.19).

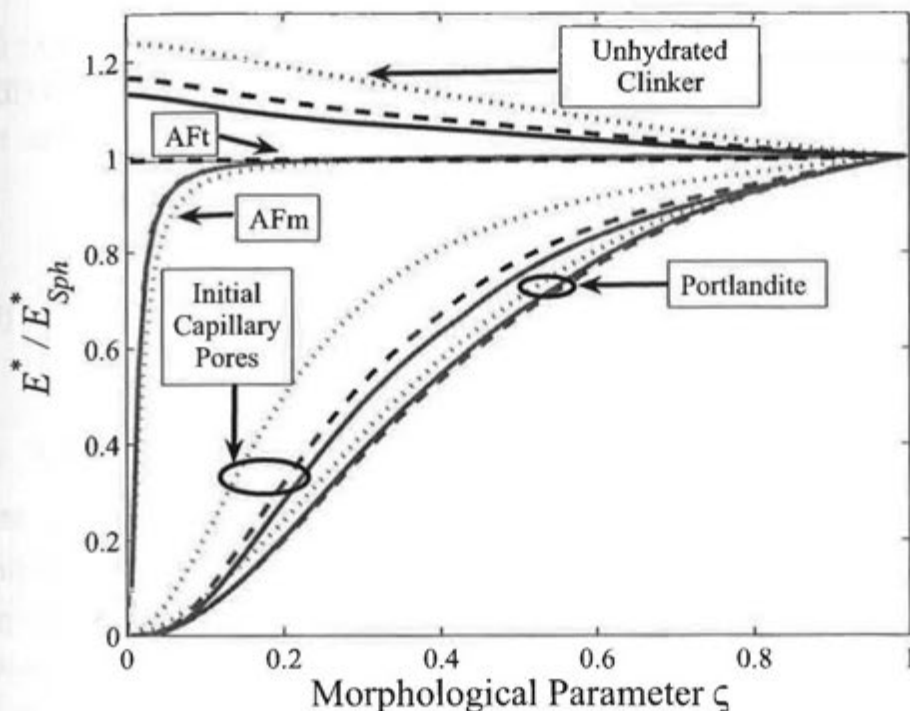


**Figure II.19:** Evolutions of the normalized effective Young modulus for leached CEM I pastes, as a function of the morphological parameter  $\zeta$ . Solid lines:  $w/c = 0.50$ ; dashed lines:  $w/c = 0.40$ ; dotted lines:  $w/c = 0.25$  (Stora et al. 2006a).

Because of the straightforward calculation of the Eshelby tensor for spherical inclusions (see Eq. (II.18)), the spherical assumption is easy to use provided that morphology has a negligible effect. In this section, the influence of inclusion shapes on the effective mechanical properties is shown to highly depend on the contrast between matrix and inclusion elastic parameters, on the volume fractions and on the flattening of the particles. In particular, the morphology of a completely dissolved phase such as portlandite can severely affect the effective properties of leached HCP. Consequently, it is quite natural to wonder if the sphere really constitutes a reasonable approximation. The next section assesses the validity range of this spherical shape assumption and investigates the possibility of improving the micromechanical predictions by integrating some significant information about the shapes of HCP particulate phases.

### 5.3 Approximation of the particulate phases by spheroidal inclusions

The discussions on the morphology of the phase composing HCP microstructure in Part I have highlighted the asphericity of all the hydrated phases and unhydrated clinker. Hence, it is natural to pose the following questions: what is the error induced by the spherical shape approximation of the inclusions of HCP with respect to the homogenized isotropic elastic properties? Is it possible to improve the micromechanical predictions by adopting non-spherical inclusions?

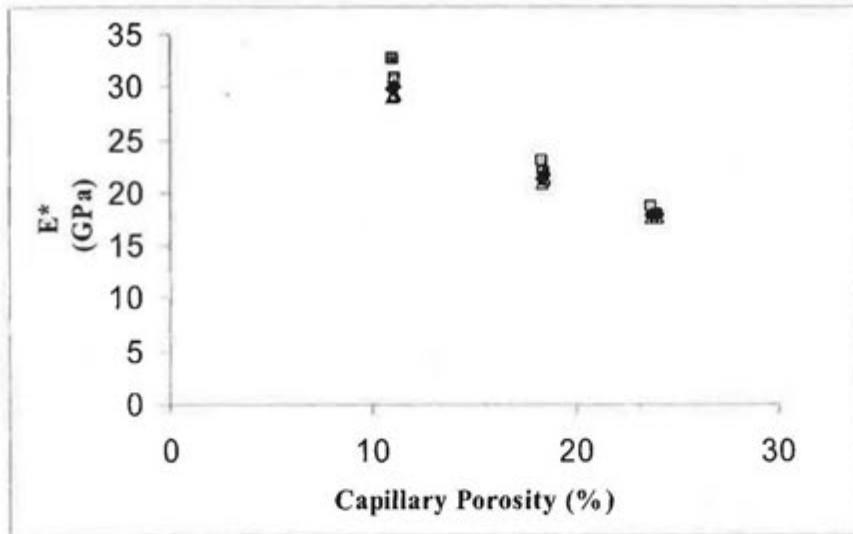
### 5.3.1 Assessment of the spherical particle assumption

All the particulate phases are approximated as spherical inclusions for simplicity, as depicted on the right-hand side of Fig. II.15. By combining Eqs. (II.6), (II.12), (II.18) and (II.43-44), the estimations of the effective bulk and shear moduli by the IDD model thus take the following form:

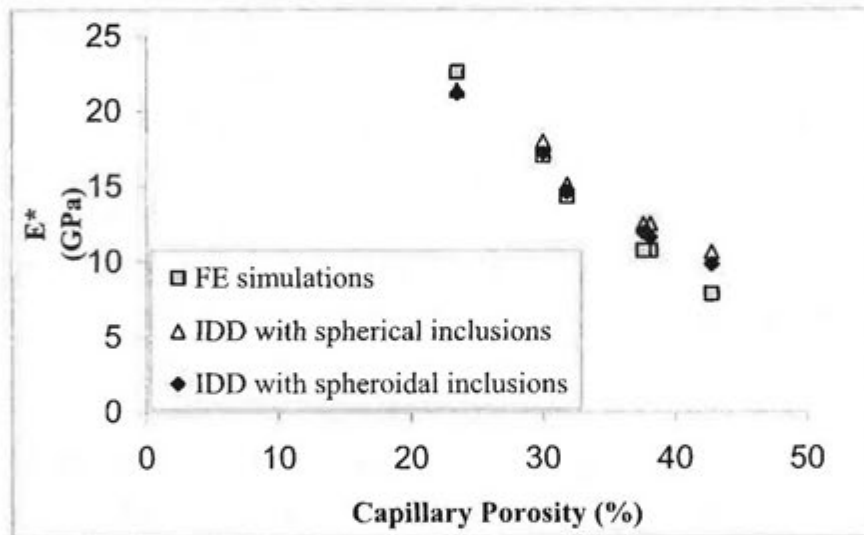
$$K_{Sph}^{MT} = K_{CSH} \left[ \frac{1 + \sum_r c_r \left( \frac{K_r}{K_{CSH}} \alpha_r - 1 \right)}{1 + \sum_r c_r (\alpha_r - 1)} \right] \quad \text{and} \quad G_{Sph}^{MT} = G_{CSH} \left[ \frac{1 + \sum_r c_r \left( \frac{G_r}{G_{CSH}} \beta_r - 1 \right)}{1 + \sum_r c_r (\beta_r - 1)} \right], \quad (\text{II.103})$$

where  $r \in \{AFt, AFm, CP, CH, UC\}$ , where  $\alpha_r$  and  $\beta_r$  are given in Eq. (II.19),  $K_r$  and  $G_r$  respectively denote the bulk and shear moduli of inclusion phase  $r$  and where  $K_{CSH}$  and  $G_{CSH}$  respectively designate the bulk and shear moduli of CSH matrix. To check the validity range of the spherical shape approximation, the micromechanical estimations given by the previous equation are compared with the simulations of Kamali (2003) applied to a representative panel of sound and degraded HCP. Two NIST models are used for the FE simulations: CEMHYD3D and ELAS3D (Bentz 1997; Bohn and Garboczi 2003; Garboczi 1998). The first one is a three-dimensional cement hydration and microstructure development modeling package. The second one is a linear elastic FE program developed for computing the linear elastic properties of random materials whose microstructure has been stored in a 2D or 3D digital image. CEMHYD3D is probably the most well-known and efficient hydration model. A unit cell of 100  $\mu\text{m}$  in size was used for all the simulations. The limitations of these simulations come from the size of the voxels being only of 1  $\mu\text{m}^3$ . For further details, the reader should refer to the article of Haecker et al. (2005). Three CEM I and three blended Portland cement pastes with 7.7 % silica fume content (CEM II/A) with various w/c ratios (0.25, 0.40, 0.50) are considered. The estimations provided by Eq. (II.103) are plotted on Fig. II.20 as a function of capillary porosity and are compared to the FE results of Kamali (2003).

For all sound pastes, the results of the micromechanical model are in good agreement with the FE values, since the deviation compared to numerical simulations is always lower than 12 %. In view of the fact that FE simulations are more difficult to perform than the present homogenization method, the latter provides an efficient analytical tool for the prediction of sound HCP elastic properties.



a) Sound HCP



b) Partially leached HCP

**Figure II.20: Evolutions of the effective Young moduli estimated respectively by the IDD model with spherical and spheroidal inclusions and by FE simulations (Kamali 2003) for both a) sound and b) partially degraded HCP as a function of capillary porosity volume fraction (Stora et al. 2006a).**

Concerning the partially degraded pastes, the FE simulations of Kamali (2003) assume the complete leaching of CH and aluminates but do not incorporate the degradation of CSH; we have then adopted the same leaching scenario to be able to compare the different results. The difference between the results in the sound and the degraded pastes suggest a few general comments. The detrimental effect of leaching on Young modulus is significant, though the elastic properties of CSH are kept constant during the degradation process. Kamali (2003) predicted a reduction of 58 % for the CEM I 42.5 paste with  $w/c = 0.50$  and obtained good agreement with experimental results (Carde 1996), where total dissolution of CH caused a reduction of 63 % in the Young modulus of this cement paste. The numerical results of

Kamali (2003) agree quite well with their measures considering the fact that the paste appears more degraded in the experiments than in the simulations. The decrease of the Young modulus is lower for CEM II/A pastes, varying between 25 % and 40 %. The blended cement pastes show better mechanical properties after degradation process than CEM I because of their smaller content of portlandite. This phase appears then to be predominant for leaching problems.

For the leached HCP, the IDD estimations computed with spherical inclusions diverge significantly from the numerical results for volume fractions of capillary porosity higher than 35 %. It is striking to notice that the predictions follow the same trend as in Berryman and Berge (1996) and in Segurado and Llorca (2002): the more porous the material becomes, the more the homogenization models overestimates the elastic properties.

Though volume fractions and mechanical data of the main phases composing HCP can be determined in a relatively precise way, less is known concerning their morphology. Based on relevant experimental results, an attempt to approach the components real shapes by means of a morphological parameter is made. Although the breakthrough of three-dimensional analysis techniques provides some interesting data, the introduction of realistic particle shapes in homogenization models is still a difficult task. Due to the difficulty of computing the Eshelby problem in the case of non-ellipsoidal shapes, it is generally impossible to incorporate the phase real morphologies directly in micromechanical methods and approximations of these shapes by simpler geometrical forms are necessary. The dilemma is to integrate the most realistic shapes possible and at the same time conserve a calculable model. An analytical solution is proposed in the present homogenization approach by introducing spheroids adequately chosen with the help of the previously mentioned morphological parameter. Therefore this section aims at finding some approximate values for  $\zeta$  on the basis of experimental observations.

As an example, the morphological parameter  $\zeta$  of Portland cement particles is calculated with the aid of the results of Garboczi and Bullard (2004). If use is made of their fit function  $A = 8V^{0.64}$ ,  $\zeta$  is not dimensionless. Consequently, we perform a new fitting of their results with a fixed exponent of 2/3 and obtain:

$$A = 5.95V^{2/3}. \quad (\text{II.104})$$

The dimensionless morphological parameter  $\zeta$  is easily calculable from this new fit function:

$$\zeta_{\text{cement particles}} \cong 0.81. \quad (\text{II.105})$$

This value agrees with the analysis of Garboczi and Bullard (2004) concluding that cement grains are not spherical. By approximating the particle shape,  $\zeta$  introduces some important information on material microstructure in the elastic moduli estimate, and may be regarded as the most significant microstructural parameter after volume fractions.

A value of  $\zeta$  for unhydrated clinker can be proposed by assuming that these clinker residuals inherit from a shape similar to the initial cement particle one. The argument for such an assumption is that the reaction of cement particles with water initially taking place at the particle surface, the morphology of their unhydrated core should not change significantly during the hydration process. The microtomographic pictures of the evolution of cement particles morphology issued from the Visual Cement Database (Bentz et al. 2002) during hydration permit to properly assess this assumption and show that the latter may be too idealistic. Nevertheless, this approximation is maintained, since the residual clinker seems to inherit from a shape closer to unhydrated cement particles than spheres. Under this hypothesis, the unhydrated clinker keeps the same shape parameter value as the initial cement grains:  $\zeta_{UC} = \zeta_{\text{cement particles}} \cong 0.81$ . As illustrated on Fig. II.21, this particulate phase is then approximated by equivalent oblate and prolate spheroids of respective aspect ratios of  $r_{UC} = 0.35$  and  $r_{UC} = 3.5$ . However, the difference between HCP effective Young moduli estimated by means of clinker spheroidal inclusions having a shape parameter of  $\zeta_{UC} = 0.81$  with respect to the spherical case remains quite negligible except for high volume fractions of clinker. This statement leads to the remarkable consequence that, though the shape of anhydrous residuals is noticeably non-spherical, it may not affect importantly the elastic properties.

Furthermore, some approximate values may be found for CH and AFt shape parameters. By examining carefully micrographs of Brown and Hooton (2002), ettringite is characterized by long cylinders, whose height is at least ten times bigger than its diameter, as represented in Fig. II.21. These rather empirical dimensions provide a morphological parameter  $\zeta_{AFt} = 0.69$ , having an insignificant influence according to Fig. II.18. portlandite is further assumed to inherit from a similar shape inside the HCP as in non-confined environments, where it crystallizes in massive hexagonal plates (Richardson 2000). Considering such a plate, whose thickness is four times smaller than the maximum length of the regular hexagonal base,  $\zeta_{CH} = 0.70$  is obtained (see Fig. II.21). This value leads to a relative variation of Young modulus comprised between 0.75 and 0.90 for the three HCP, which is not negligible.

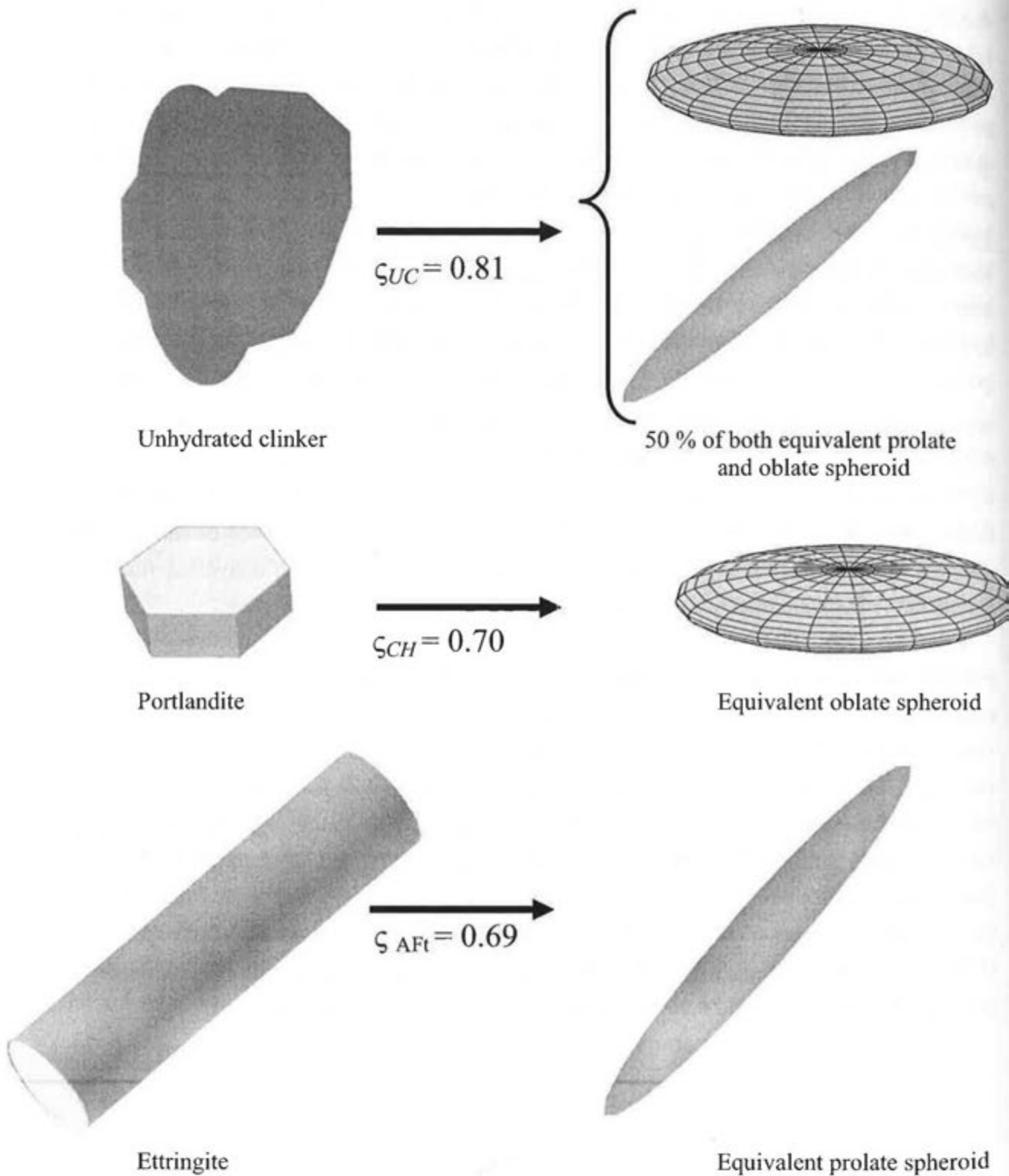


**Figure II.21: Approximation of realistic HCP particulate phases shapes by equivalent spheroids (Stora et al. 2006a).**

The spheroids (see Fig. II.21) chosen from experimentally based approximate values for the shape parameter of clinker, ettringite and portlandite (respectively with  $\zeta = 0.81$ ,  $0.69$  and  $0.70$ ) may improve on the spherical assumption. The first value is based on the hypothesis that

the residual clinker inherits from a shape similar to the unhydrated cement particles and the last two shape parameter values are equivalent to considering the shape of CH and AFt inside the HCP identical to their well-crystallized geometry in non-confined environment. These approximations appear quite idealized in comparison with the images of Bentz et al. (2002) but they are probably more realistic than the spherical hypothesis. For the remaining phases, namely initial capillary pores and AFm, the default value taken for  $\zeta$  is the spherical one:  $\zeta_{Sph} = 1$ . The schematic micromechanical representation obtained with the equivalent spheroids deduced from these novel approximations is illustrated on the left-hand side of Fig. II.15.

Fig. II.20 recapitulates the different results obtained by the micromechanical models and numerical simulations. In the sound case, the model with spheroidal inclusions does only improve modestly on the model with spherical ones except when the concentration of unhydrated clinker is high. These results confirm the previous curve on Fig. II.18 showing that the morphologies of UC, CH and AFt do not strongly affect the effective properties of sound HCP. The present estimate becomes of higher interest for early-age cement pastes where the amount of clinker is particularly high. Otherwise, it is perhaps not worthy to take spheroidal shapes for clinker, ettringite and portlandite, the spherical assumption already giving satisfactory results.

For the leached cases, the present estimations with spheroidal inclusions are closer to the FE simulations than the ones with the spherical particle approximation except for the CEM II/A w/c = 0.25 paste but both diverge significantly from the numerical results for volume fractions of capillary porosity higher than 35%. This improvement tends to prove that the proposed approximations constitute a better alternative to the spherical assumption. More precisely, in the micromechanical representation illustrated on Fig. II.15a), portlandite, ettringite and clinker are no longer idealized by spheres but are presently approximated by spheroids with an estimated shape parameter. Compared to the spherical case, the elongated spheroids of ettringite and the flattened ones of portlandite weaken the leached cement pastes, while those of unhydrated clinker tend to stiffen the effective material. Fig. II.19 reveals that the detrimental impact due to the oblate shape of portlandite prevails on the stiffening effects due to the asphericity of unhydrated clinker and leached AFt. Therefore the variations between the two micromechanical estimations are mainly due to the strong influence of leached portlandite shape. It should be underlined that, though its shape is negligible in sound HCP, it becomes a significant data for leached ones.

However, the present model is still insufficient to predict correctly the effective elastic properties of leached HCP with high volume fractions of capillary porosity. As the material degrades, this porous phase is not only composed of the initial capillary pores but also of the space left by dissolved hydrates such as CH and AFt, whose shapes inside the HCP microstructure are difficult to describe. The shape parameter may not incorporate sufficient information on the inclusion morphology. In addition, the values of  $\zeta$  estimated for UC, CH

and Aft in the previous section are perhaps too approximate, even though they provide better results than the spherical one. The latter values were introduced in order to give an example illustrating the limits of the spherical particulate assumption and more precise quantitative data for the morphological parameter are necessary to build a sound homogenization model. There is presently a lack of quantitative data concerning the hydrate shapes but better estimations could be obtained by characterizing more accurately their morphologies, for example with the help of the Visual Cement Database and the shape analysis techniques developed recently (Bentz et al. 2002; Garboczi 2002). It constitutes a promising field of investigation for future improvement of the homogenization processes.

Nevertheless, even if it were ideally possible to directly integrate the exact shapes of all elementary phases in the homogenization process, it is not guaranteed that micromechanical estimations of the effective elastic properties would be fully accurate. Indeed, the IDD effective medium approximations may fail to adequately account for interactions between highly-concentrated porous inclusions (e.g. Berryman and Berge 1996).

#### 5.4 Conclusions of chapter 5

In the present chapter, the influence of inclusion shapes on the effective elastic properties of HCP has been examined by successively modeling each particulate phase as spheroids, whose shape ranges from needle-like to disk-like. The validity range of the spherical inclusion approximation in the homogenization process applied to both sound and leached HCP has also been assessed. For this purpose, the estimations obtained with both spherical and spheroidal inclusions are compared to the results of Kamali (2003) by FE simulations. On the one hand, the spherical particle simplification turns out to be suitable for sound pastes. On the other hand, our work evidences the limits of the spherical assumption for leached pastes. The significant effects observed for the additional capillary porosity formed by leaching of hydrated products shows the necessity of better approaching the morphologies of dissolved phases such as portlandite.

Furthermore, an analytical way has been proposed to integrate more realistic inclusion morphologies in homogenization estimates. The key point of this method is the introduction of the morphological parameter  $\zeta$ , which corresponds to the normalized characterizations of the ratios between the volume and surface of inclusions. This parameter appears as the most important one after volume fractions. Approximate values of  $\zeta$  for particulate phases such as clinker, portlandite and ettringite are proposed on the basis of experimental results. These phases are then represented by equivalent spheroids. This procedure allows for conveniently coupling experimental observations and micromechanical modeling. The explicit micromechanical estimations thus obtained for the effective elastic properties of HCP are

shown to give better results than those performed with the spherical approximation. However, they are still insufficient for degraded cement pastes with capillary porosity higher than 40%. Three reasons are possible for these shortcomings. It could first be due to intrinsic insufficiencies of the IDD micromechanical estimate. The latter might fail to properly account for interactions between highly-concentrated inclusions. The application of a generally more accurate scheme, like GSCS, may be of interest. Secondly, the convenient use of spheroids determined by means of the morphological parameter presents the considerable advantage of providing an analytical model but it may have its limits to approach fairly complex shapes. Moreover, the values proposed for this parameter are very approximate due to the lack of complete morphological information on hydration products. The further development of three-dimensional image analysis methods (Garboczi 2002) should give the opportunity to better characterize the morphology of inclusion phases, in particular for portlandite, and might lead to improvement of homogenization methods in the field of cementitious materials durability.

The third reason is that the one-scale representations depicted in Fig. II.15 may be too simple to correctly describe the complex microstructure of HCP, which heterogeneities manifest themselves at different scales. Therefore, the next chapter aims at building a more realistic multi-scale homogenization model for cement-based materials and in particular for HCP.

## **6 CONSTRUCTION OF A MULTI-SCALE HOMOGENIZATION MODEL FOR ESTIMATING THE ELASTIC PROPERTIES OF CEMENT-BASED MATERIALS**

As already pointed out in Part I, the characteristic sizes of the phases composing HCP range from the nanometer to micrometer scales. The scope of the present chapter is to investigate the possibility of improving the micromechanical estimations of elastic properties of HCP by integrating some significant information about the different sizes of its particulate phases. For this purpose, the different micromechanical descriptions of cement pastes proposed in literature are first reviewed.

### **6.1 A multi-scale approach for estimating the elastic effective properties of HCP**

#### ***6.1.1 Review of the existing micromechanical models for cement pastes***

To our knowledge, the application of micromechanics for estimating the isotropic linear elastic effective properties of cement pastes dates back to Zimmerman (1986). They modeled HCP as a two-phase composite consisting in a solid matrix weakened by spheroidal pores and employed the KT estimate to compute its elastic properties. A homogenization attempt for  $C_3S$  pastes was also performed by Neubauer et al. (1997) using the differential scheme (e.g. Norris 1989) but mechanical input values for the CSH phase were lacking. Owing to progress

in experimental mechanics, elastic properties of all the main phases present in HCP are nowadays measurable by nanoindentation techniques and many data may be found in the literature (see Table I.3). Benefiting from these recent nanoindentation measures, a two-step homogenization procedure for HCP on the basis of the MT model has been developed by Constantinides and Ulm (2004). Their Young modulus estimations for both sound and leached OPC type I pastes with  $w/c = 0.50$  showed good agreement with experimental results. Bernard et al. (2003) used the same two-scale description of microstructure and the self-consistent scheme to study early-age cement pastes and predict the solid phase percolation during hydration process. They also obtained results consistent with experimental values.

Constantinides and Ulm (2004) distinguish two microstructural levels respecting the scales separation condition: the first one denoted as I and ranging from 10 nanometers to 0.1 micrometer is characteristic of the two types of CSH, while the second designated by II and varying from 1 micrometer to 100 micrometers corresponds to the scale where CSH can be regarded as a homogeneous matrix with CH crystals, capillary pores, anhydrous residuals and aluminates as inclusions. The first step consists in calculating CSH matrix effective properties from  $CSH^{int}$  and  $CSH^{ext}$  intrinsic values and the second one is to determine HCP effective properties with the aid of the previous result for CSH matrix.

At level I, the CSH matrix behaves as a heterogeneous material with an inclusion-matrix type microstructure. The  $CSH^{ext}$  play the role of a matrix phase, surrounding the  $CSH^{int}$  as inclusion. According to Constantinides and Ulm (2004), the latter phase modeled as spherical inclusions has a characteristic size of  $10^{-8}$  to  $10^{-7}$  m. However, according to some authors (Taylor 1997; Richardson 2000; Bary and Béjaoui 2006), the distinction between  $CSH^{int}$  and  $CSH^{ext}$  should be done only at a higher scale since these phases form successively from cement grain surfaces, the  $CSH^{int}$  resulting mainly from higher confinement conditions and from water accessibility during hydration reactions. At level II, the main phases are the homogenized CSH, capillary pores, clinker residuals, and hydrated phases such as CH crystals, AFt and AFm. Precisely, the CSH act as a matrix phase in which the other phases are embedded and play the role of inclusion. The next section is devoted to the construction of another multi-scale model that aims at representing more faithfully the microstructure of cement pastes.

### ***6.1.2 Construction of a multi-scale homogenization model for HCP***

The proposed two-scale description of HCP is inspired by the one developed by Bary and Béjaoui (2006) for diffusion. Two microstructural levels respecting the scales separation condition are presently distinguished: the first ranging from a few tens of  $\mu\text{m}$  to about 100  $\mu\text{m}$  is typical of the sizes of hydrated cement grains, while the second one ranging from 0.2  $\mu\text{m}$  to a few tens of  $\mu\text{m}$  corresponds to the scale of hydration products, such as CH or AF, and of capillary pores. These two scales are respectively denoted as I and II.

The level I corresponding to the biggest scale of HCP is described first. This level depicted in Fig. II.22 represents the hydrated cement grains. During the hydration of cement particles, two layers presently defined as inner and outer layers form successively from cement grains surface. The inner layer is less porous than the outer one, since the first one results from higher confinement conditions and from poorer water accessibility during hydration process. Generally, an anhydrous part of the cement particles remains after hydration has stopped and constitutes a rigid core surrounded by these two heterogeneous layers. The GSCS and modified DIM derived in the present manuscript are the two most suited effective medium schemes for estimating the elastic properties of composite with layered inclusions, as evidenced in subsection 4.4.2.2, and are thus employed to compute such a model of microstructure. The present description is based on the assumption that the cement grains supposed initially spherical hydrate forming doubly-coated spheres that fill the HCP microstructure. The spherical particle approximation was shown to be reasonable for modelling unhydrated clinker in the previous chapter.

The level II also depicted in Fig. II.22 corresponds to the scale of the heterogeneities of the two layers. It is commonly accepted that two different types of porous CSH are associated with each layer. In the inner layer, the  $\text{CSH}^{\text{int}}$  behave as a matrix phase embedding inclusions of CH and aluminates. Similarly, the external layer has matrix-inclusion type morphology, where CH, the aluminates and the capillary pores play the role of inclusions enclosed in the  $\text{CSH}^{\text{ext}}$ . During hydration, the outer coatings of the hydrated cement grains expand so that they get in contact with each other and we can assume that the capillary pores get entrapped in the outer coatings. The two layers, schematically illustrated on Fig. II.22, are estimated by means of the IDD estimate that is appropriate for materials with matrix-inclusion morphology.

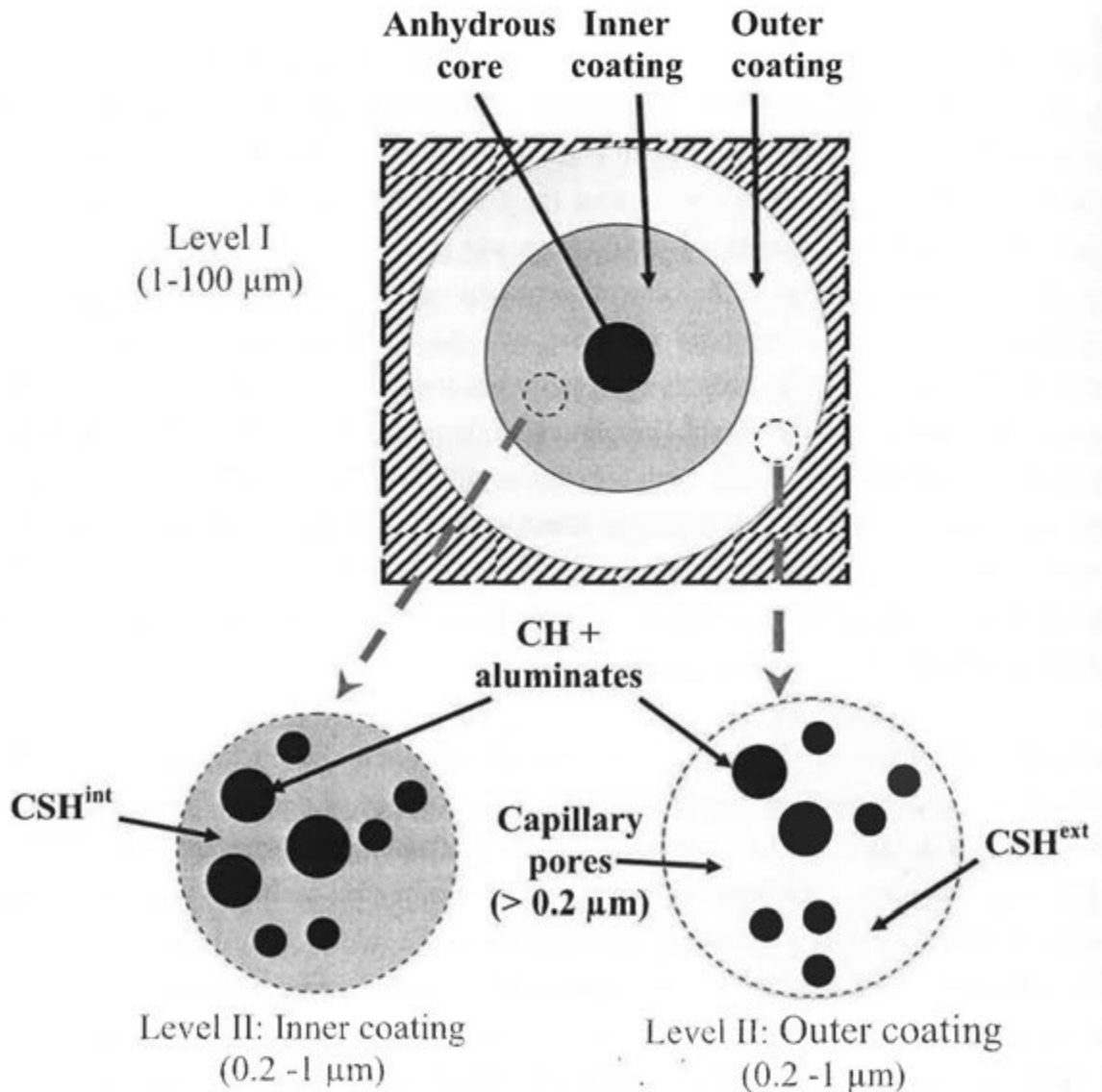


**Figure II.22:** Schematic of the levels I and II of the two-scale representation used for the estimation of the effective elastic properties of HCP.

### 6.1.3 Predictions of the elastic properties of sound and leached HCP

The estimations of the elastic moduli of HCP by the present multi-scale homogenization model are validated by respectively comparing with the numerical results from Kamali (2003), two experimental results on sound pastes (Constantinides and Ulm 2004; Gallé et al. 2004) and one on uniformly leached ones (Constantinides and Ulm 2004). Other experiments conducted by Carde (1996) and Gallé et al. (2004) have measured the stiffness reduction of HCP due to leaching. However, their results are not used for the present validation, because the degradation state of the CSH inside their chemically altered samples may not be uniform. The volume fractions of the HCP elementary phases collected in Table II.3 are computed by means of the Jennings model (see Eq. (I.1)), the total porosity being adjusted with the total water porosity measured experimentally. The volume fraction of capillary porosity is taken from the experimental results of Igarashi et al. (2004).

| Volume fractions in % |                                   |   |
|-----------------------|-----------------------------------|---|
|                       | CEM I 52.5<br>(Gallé et al. 2004) | OPC type I paste<br>(Constantinides and Ulm 2004) |
| w/c =                 | 0.45                              | 0.50  |
| Hydration rate        | 0.87                              | 0.77  |
| CH                    | 15.1                              | 11.3  |
| CSH <sup>int</sup>    | 21.6                              | 15.6  |
| CSH <sup>ext</sup>    | 28.8                              | 42.8  |
| UC                    | 4.3                               | 5.0   |
| Aluminates            | 14.2                              | 6.3   |
| CP                    | 3.6                               | 6.0   |
| Porosity (%)          | 31.9                              | 38.5  |
| Water porosity (%)    | 32.6                              | 39.7  |

**Table II.3: Input volume fractions of principal hydrates, unhydrated clinker and capillary porosity for two different HCP.**

Constantinides and Ulm (2004) measured that the stiffness modulus of a uniformly leached OPC type I paste decreased to about 3 GPa representing a 84 % decay. To obtain a uniformly degraded paste, the sample with a diameter of 11.5 mm was attacked by an ammonium nitrate solution during 5 months. Inside this leached sample, Constantinides and Ulm (2004) furthermore asserted that even the CSH<sup>int</sup> and CSH<sup>ext</sup> reach a uniform degraded state and measured by nanoindentation that their Young moduli diminish from 21.7 GPa to 3 GPa and from 29.4 GPa to 12 GPa, respectively. Their bulk and shear moduli, designated by  $K_{CSH_{int}}$ ,  $G_{CSH_{int}}$  for CSH<sup>int</sup> and by  $K_{CSH_{ext}}$ ,  $G_{CSH_{ext}}$  for CSH<sup>ext</sup>, are immediately deduced from Eq. (II.102). The input elastic parameters for the two sound phases are then equal to  $K_{CSH_{int}} = 18.8$  GPa,  $G_{CSH_{int}} = 11.9$  GPa and  $K_{CSH_{ext}} = 13.9$  GPa,  $G_{CSH_{ext}} = 8.8$  GPa, while their degraded elastic properties decrease to  $K_{CSH_{int}}^l = 7.7$  GPa,  $G_{CSH_{int}}^l = 4.8$  GPa and  $K_{CSH_{ext}}^l = 1.9$  GPa,  $G_{CSH_{ext}}^l = 1.2$  GPa (the subscript  $l$  stands for leached state). All these moduli are calculated supposing that the Poisson ratio of both phases is not sensitive to leaching and remains equal to 0.24 (Constantinides and Ulm 2004). This approximation is made due to the lack of experimental data on the Poisson ratio.

Fig. II.23 displays the effective Young moduli estimated for sound pastes and a uniformly leached one and shows that they are in good agreement with the experimental data from Constantinides and Ulm (2004) and from Gallé et al. (2004). It is worth noting that the estimations of the multi-scale model computed respectively with modified DIM and GSCS at level II (Fig. II.23) are presently almost confounded due to the scarce volume fractions of clinker residuals. Experimental data on elastic properties of uniformly degraded pastes are

difficult to find, since these experiments cost a lot of time. To further validate the multi-scale homogenization model, it is now proposed to confront its predictions with the numerical results of Kamali (2003).

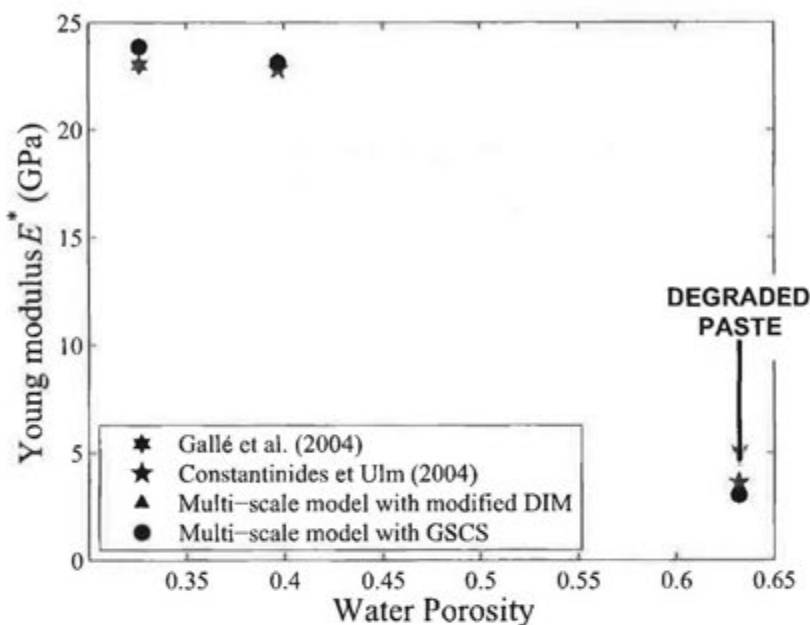


**Figure II.23: Comparison between the effective Young moduli estimated by the multi-scale model with experimental measurements (Constantinides and Ulm 2004; Gallé et al. 2004) on both sound and degraded HCP.**

The input mechanical data required for computing the multi-scale model are the same as those employed by Kamali (see Table I.3) except that in the micromechanical model the CSH gel is modelled as two phases,  $\text{CSH}^{\text{int}}$  and  $\text{CSH}^{\text{ext}}$ , which elastic moduli are given just above. In addition, the relative volume fractions of these two types of CSH are computed by means of Eq. (I.2) with a hydration rate assumed equal to 0.60. The predictions of the multi-scale model for the macroscopic Young modulus of undecalcified pastes are plotted in Fig. II.24 and are very close to the numerical results. Two different schemes, namely modified DIM and GSCS, have been employed to compute the elastic properties of level II of the model. The GSCS provides the closest estimations to the FE results. The mean deviation between the results obtained with the modified DIM and with the GSCS and the numerical ones are about 3 % and 7 %, respectively.

In order to compute the multi-scale model for the case of partially leached pastes simulated by Kamali (2003), it is necessary to know the volume fractions and the elastic properties of degraded  $\text{CSH}^{\text{int}}$  and  $\text{CSH}^{\text{ext}}$ . It has been observed that the relative amount of both CSH types seems not to change when leaching occurs (Constantinides and Ulm 2004; Thomas et al. 2004). It is furthermore assumed that the CSH elastic moduli are not affected by decalcification as in the simulations of Kamali (2003). This approximation may be justified

by the fact that the progressive evolution of their elastic properties during the leaching process is difficult to characterize experimentally. Velez et al. (2001) showed by means of nanoindentation tests that the Young moduli of the partially decalcified CSH do not significantly change especially if their C/S ratio is superior to 1.

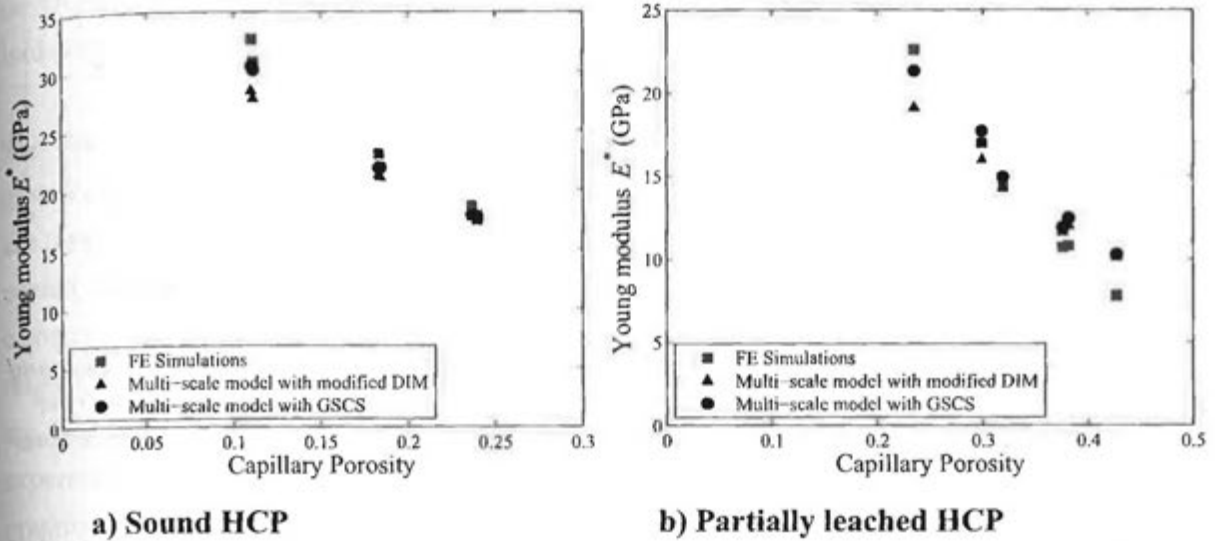


**Figure II.24: Evolutions of the effective Young moduli estimated by the multi-scale model and by FE simulations (Kamali 2003) for both a) sound and b) partially degraded HCP as a function of capillary porosity volume fraction.**

The mean deviation with respect to the numerical simulations is about 12 % for both estimates. However, the estimations computed with the modified DIM can deviate by more than 30 %, whereas those computed with GSCS do not. Therefore GSCS that is a little more accurate than the modified DIM is chosen in the ensuing computations of the multi-scale homogenization model.

Better predictions plotted in Fig. II.25 can furthermore be obtained by adopting spheroidal inclusions with aspect ratio  $r = 0.25$  to represent CH phase, the mean deviation then becomes about 7 % for the estimations obtained with GSCS. By confronting Figs. II.20, II.24 and II.25, it seems that the shape of the inclusion modelling portlandite has a moderate influence on the micromechanical predictions except in the particular case of leached pastes with a capillary porosity higher than 30 %. The use of oblate spheroidal inclusions instead of spherical ones in the multi-scale homogenization model then leads to a visible improvement of the estimations for the Young moduli of such porous pastes. However, CH will be modeled in the ensuing as a spherical inclusion for simplicity but also because of the difficulty to characterize the real shape of portlandite crystals present in HCP microstructure.

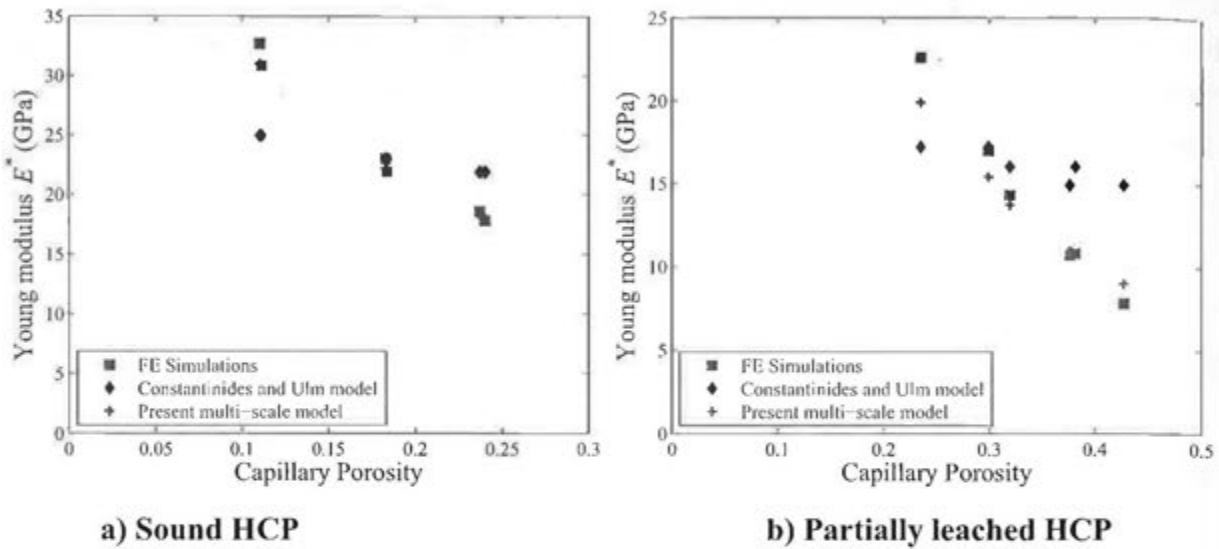


**Figure II.25:** Evolutions of the effective Young moduli estimated by the Constantinides and Ulm model, by the present multi-scale one and by FE simulations (Kamali 2003) for both a) sound and b) partially degraded HCP as a function of capillary porosity volume fraction.

By further comparing Figs. II.24 and II.25, the estimations of the proposed multi-scale models obtained either with spherical or spheroidal CH inclusions can both be seen to significantly improve on the predictions of the Constantinides and Ulm model (Fig. II.25). Two main reasons may explain these improvements achieved with the present multi-scale model in comparison with the Constantinides and Ulm one. First, the effective elastic properties are computed with GSCS at level I and the IDD estimate at level II, which have both been shown precedently to be more accurate than the MT model usually employed (see Figs. II.13). Second, the present two-scale description of HCP microstructure may be more realistic than the representation proposed by Constantinides and Ulm (2004).

## 6.2 A multi-scale approach for estimating the macroscopic elastic properties of mortars

The application of homogenization methods to mortars is complicated by the lack of experimental data on ITZ elastic properties. To circumvent this difficulty, many authors have estimated these characteristics of ITZ from experimental values of mortars by inverse analysis employing for instance GSCS (e.g. Ramesh et al. 1996; Hashin and Monteiro 2002) or DIM (Yang 1998) as upscaling methods. Unfortunately, very different values have been identified for the Young modulus of ITZ from one author to another, as pointed out in Eq. (I.5). An alternative multi-scale homogenization approach based on the modified DIM presented previously is proposed to predict the elastic properties of mortars without having to estimate the elastic moduli of ITZ by inverse analysis.

In addition, the total volume fraction occupied by this zone is also difficult to gain experimentally and also has to be estimated. The predictions for the volume fraction of ITZ

fluctuate from one author to another depending for instance on the method employed and on the thickness retained for ITZ. As an illustration, the values estimated can vary from about 8 % (Sun et al. 2007) to 30 % (Heukamp 2002). The use of statistical models (e.g. Lu and Torquato 1992) taking into account the overlapping between these transition zones is generally required to compute accurately this volume fraction. The multi-scale model developed below furthermore presents the salient feature to be computable without having to look after the volume fraction of ITZ.

The use of GSCS represented in Fig. II.4 is widespread to predict the elastic properties of mortars (e.g. Ramesh et al. 1996; Hashin and Monteiro 2002). In the present work, mortars are represented as a more detailed multi-scale microgeometry depicted on Fig. II.26. Diverse coated spheres having different sizes are nested inside a matrix region filled by the bulk cement paste. The coated-spheres are defined as follows: the core and the outer layer are respectively occupied by sand particles and ITZ. A few representative grains of different sizes are chosen to discretize the wide size distribution of sand particles with the aid of experimental data on the mortar grading. The grading curve of the mortar characterizing the granulometry of its sand particles is generally provided by the producer. As an example, the mortar with fine Nevada sand particles employed by Heukamp (2002) is chosen for the present study. Three representative sizes of sand particles, with radii  $R_1 = 0.085$  mm,  $R_2 = 0.20$  mm and  $R_3 = 0.315$  mm, are adopted to represent the sand aggregates of this mortar, on the basis of the grading data of Heukamp (2002) collected in Table II.4. The total volume fraction occupied by sand is about 50 % (Heukamp 2002).

| Size of sand particles | Relative proportion |
|------------------------|---------------------|
| 0- 0.17 mm             | 30 %                |
| 0.17 - 0.23 mm         | 30 %                |
| 0.23 - 0.50 mm         | 40 %                |

*Table II.4: Grading of the fine Nevada sand used for mortars by Heukamp (2002).*

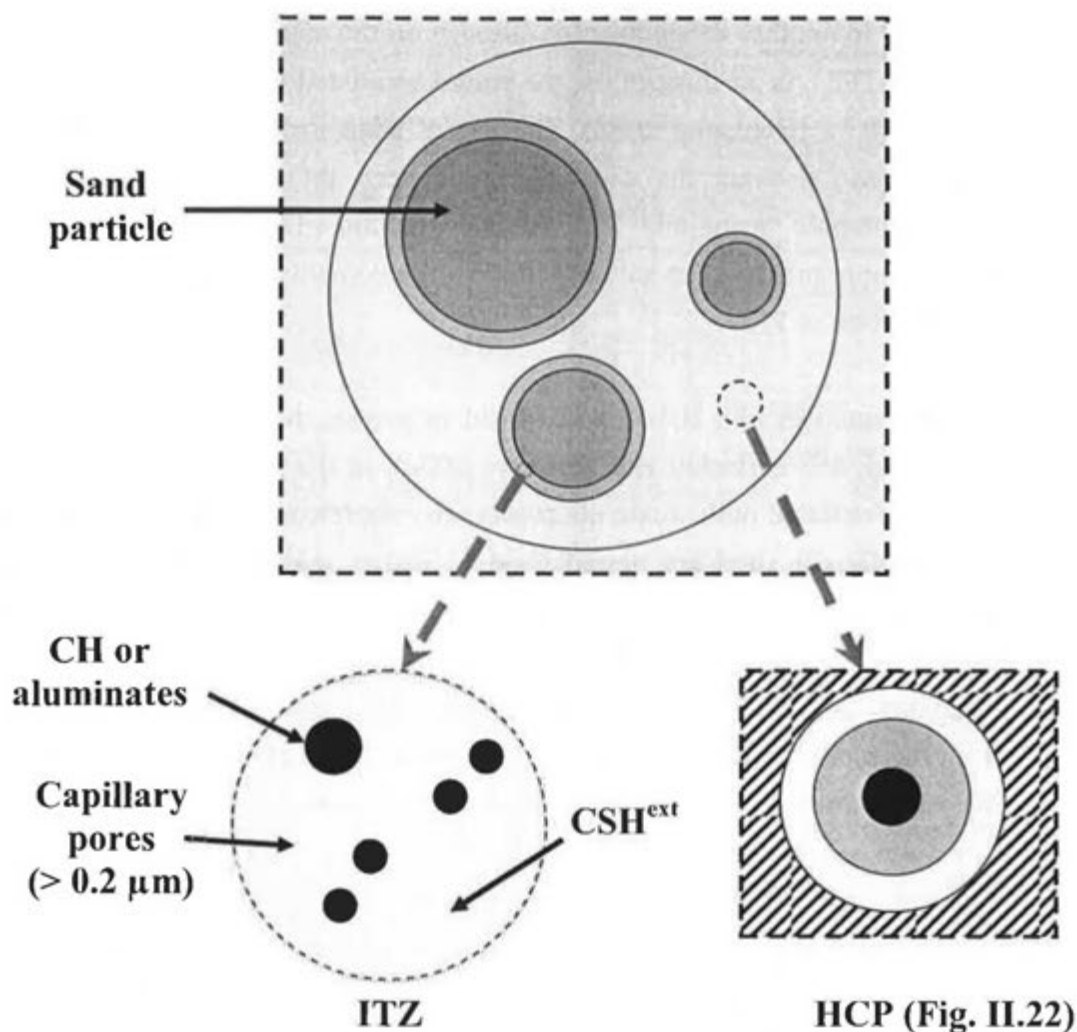


*Figure II.26: Schematic of the representation used for the estimation of the effective elastic properties of mortars.*

The thickness of ITZ inside a given mortar is generally observed to remain constant regardless of the aggregate sizes, according to diverse experimental observations (Heukamp 2002; Monteiro and Ostertag 1989). In the present description, this thickness is consequently assumed to be constant and equal to  $20\ \mu\text{m}$  (Heukamp 2002). The volume fractions occupied by ITZ obtained with the present representation is 21.7 %.

The Young modulus and Poisson ratio of sand aggregates are respectively equal to 62.5 GPa and 0.21 (Heukamp 2002). The elastic properties of ITZ and HCP can be computed by means of the previous two-scale model depicted in Fig. II.22. However, a few assumptions on how the diverse phases are dispersed in ITZ and HCP are necessary. Heukamp (2002) measured that the water porosities of plain cement paste and mortar were equal to 39.7 % and 27.5%, respectively. For simplicity, the cement matrix in mortar is supposed to have exactly the same composition as the plain cement paste, which composition is given in Table II.4. As a consequence, only 11.2 % of the mortar porosity is entrapped inside the cement matrix representing 28.7 % of the mortar in terms of volume fractions, the rest of the porosity being

scattered in ITZ. The porosity thus obtained inside ITZ is about 75 %. Because of this high porosity, dense phases like  $\text{CSH}^{\text{int}}$  and UC are not likely to be present in ITZ. Therefore, the only solid phases inside ITZ are assumed to be CH, aluminates and  $\text{CSH}^{\text{ext}}$  that act as a matrix (Fig. II.26) and contain about 36 % of gel pores (Jennings et al. 2007). The respective volume fractions of CH and aluminates in ITZ are considered to be identical to the ones in HCP. The respective volume fractions of capillary pores,  $\text{CSH}^{\text{ext}}$ , CH and aluminates inside ITZ are thus equal to 70.7 %, 11.6 %, 11.3 % and 6.3 %. The elastic properties of ITZ are computed by means of the IDD estimate in Eqs. (II.43-44) and the HCP elastic moduli are estimated by the multi-scale model developed in the precedent section. The elastic properties of the mortar are then predicted from Eqs. (II.95-96) with the aid of the previous results for ITZ and HCP. For the sake of comparison between GSCS and modified DIM, the GSCS with one size of aggregates is also employed to compute the elastic properties of the mortar. The different estimations thus obtained for the Young modulus of these different composites are collected in Table II.5 and compared with experimental data (Heukamp 2002).

| Phases | Young modulus predicted (GPa) with 3 sizes of aggregates |         | Young modulus predicted (GPa) with 1 size of aggregates |         | Experimental Measures (GPa) |         |
|--------|--|---------|---|---------|-----------------------------|---------|
|        | Sound  | Leached | Sound   | Leached | Sound                       | Leached |
| ITZ    | 4.6  | 2.8     | 4.6   | 2.8     | -                           | -       |
| HCP    | 23.1   | 3.0     | 23.1  | 3.0     | 22.8                        | 3.5     |
| Mortar | 25.1   | 3.7     | 27.4  | 5.3     | 25.1                        | 4.8     |

*Table II.5: Comparison of the micromechanical estimations with experimental data on cement pastes and mortars (Heukamp 2002).*

Good agreement is found for the different micromechanical predictions with the experimental measurements but the Young modulus of the uniformly leached mortar is somehow underestimated by the various models. This may be due to an excessive porosity inside ITZ attaining more than 90 % in the present representation. The modified DIM with three different types of aggregates gives the closest estimation to the experimental result on sound mortar, while GSCS is the most accurate in the case of uniformly leached mortar. Despite the fact that the modified DIM with three diverse sizes of aggregates provides the best predictions of the Young modulus of the sound mortar, the GSCS will be employed in the ensuing Parts for computing the elastic moduli of mortars for two motives. First, it is more coherent to adopt the same scheme for estimating both the effective properties of HCP and mortars. Second, the grading of the involved mortars may not always be known precisely, so that it is not possible to use the modified DIM with diverse sizes of sand grains.

## CONCLUSIONS OF PART II

The first goal of the present Part is to expose some of the fundamental aspects of homogenization techniques and review in a non exhaustive manner some EMTs that may be of interest for predicting the linear elastic properties of cement-based materials. By assessing these methods using different criteria and by testing their accuracy on particular cases that have computed numerically, a small set of EMTs, like IDD, GSCS and the modified DIM, are outlined to present valuable features for estimating with a good precision the elastic moduli of cement-based materials and are retained for the construction of a homogenization model specifically suited for these composites. According to the authors' knowledge, the modified DIM proposed in the present manuscript by revisiting the double-inclusion scheme of Hori and Nemat-Nasser (1993) has not been derived elsewhere.

The influence of inclusion shapes on the micromechanical estimations of the effective elastic properties of HCP has then been investigated. This study puts in evidence the fact that the inclusion shapes of phases such as portlandite have a visible impact on the predictions of the macroscopic Young moduli of leached pastes. However, it also appears possible in most cases to approximate the particle phases of HCP as spherical inclusions, even though their real shape inside the microstructure of cement pastes (see Figs. I.2 and I.3) are far from being spherical.

On the basis of the set of EMTs retained from the preceding review, a two-step homogenization model is finally developed for the prediction of the macroscopic elastic properties of HCP and mortars and validated by confronting with experimental measurements performed on standard pastes and mortars. The developed model is furthermore applied to cement pastes and mortars submitted to leaching.

### Appendix A: Input data for the comparison between EMTs and numerical simulations

The basic input data of the simulations of Garboczi and Berryman (2001) and of Wriggers and Moftah (2006) are gathered below.

| Phases            | Elastic properties |       |
|-------------------|--------------------|-------|
|                   | $E$ (GPa)          | $\nu$ |
| Type I aggregate  | 62.0               | 0.2   |
| Type II aggregate | 74.5               | 0.2   |
| Mortar            | 11.6               | 0.2   |

*Table II.A.1: Basic input data for the simulations of Wriggers and Moftah (2006).*

| Phases          | Volume fractions | Elastic properties |       |
|-----------------|------------------|--------------------|-------|
|                 |                  | $E$ (GPa)          | $\nu$ |
| Sand aggregates | 0.091            | 5                  | 0.2   |
| ITZ             | 0.392            | -                  | 0.3   |
| HCP             | 0.517            | 1                  | 0.3   |

*Table II.A.2: Basic input data for the simulations of Garboczi and Berryman (2001).*

### Appendix II.B: Non-overlapping condition and determination of the double-inclusion geometry for highly concentrated spheroidal inclusions

If an inclusion overlaps its double-inclusion, the homogenization calculations fail to work. The inclusion volume fraction  $c_I$  is represented by the ratio of inclusion volume on the double-inclusion one. When  $r_I \neq 1$ , the condition on volume fractions which has to be respected in order to avoid overlapping of inclusions reads (Ponte-Castaneda and Willis 1995):

$$\begin{cases} c_{I+} = \frac{V_I}{V_{DI}} = r_I & (r_I < 1) \\ c_{I+} = \frac{V_I}{V_{DI}} = \left(\frac{1}{r_I}\right)^2 & (r_I > 1) \end{cases} \quad (\text{II.B1})$$

These equations express the condition for the spheroidal inclusion not to overlap the double-inclusion (see Fig. II.B.1). The use of a spherical double-inclusion enclosing spheroids has the consequence that  $c_I \leq c_{I+}$ . Note that this condition is even more restrictive for prolate spheroids than for oblate ones due to the presence of the square in the expression (II.B1<sub>2</sub>) of  $c_{I+}$ .

For concentrations higher than  $c_{I+}$ , the double-inclusion can no longer be taken as spherical. To avoid any risk of overlap, it is sufficient to adapt its geometry to the inclusion one (see Fig. II.B.1). Its aspect ratio  $r_{DI}$  is suitably chosen so that the IDD remains valid for any concentration as illustrated on Fig. II.B.1.

In other words, the determination of the double-inclusion geometry is now linked to the choice of inclusion shape. The IDD estimate taken with such a shape for the double-inclusion works for any concentration and is called the full-range IDD (Zheng and Du 2001).

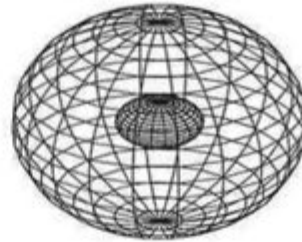
- **Oblate spheroids:**

$$c_f \geq r_f$$



$$r_{DI} = \frac{r_f}{c_f}$$

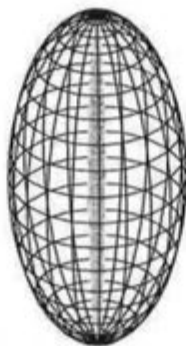
$$c_f \leq r_f \quad (r_f < 1)$$



$$r_{DI} = 1$$

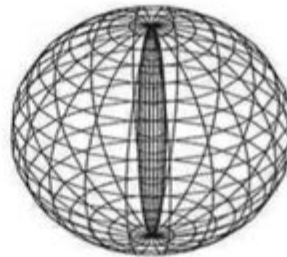
- **Prolate spheroids:**

$$c_f \geq \left(\frac{1}{r_f}\right)^2$$



$$r_{DI} = r_f \sqrt{c_f}$$

$$c_f \leq \left(\frac{1}{r_f}\right)^2 \quad (r_f > 1)$$



$$r_{DI} = 1$$

**Figure II.B.1:** Schematic illustrating the non-overlapping condition and the variation of the double-inclusion geometry with the volume fraction of a particulate phase represented respectively by oblate and prolate spheroids.

### Part III

## PREDICTION OF THE MACROSCOPIC DIFFUSIVITIES OF CEMENTITIOUS MATERIALS

The macroscopic diffusion coefficients of dissolved chemical species such as chlorides or sulfates in saturated cementitious materials control the degradation process of these materials. Therefore they represent important data for predicting the service life of cement-based materials, which can serve as engineering barriers for the disposal of nuclear waste. Homogenization models aim at estimating the macroscopic diffusion coefficients of cementitious materials from their microstructure and their phase diffusive properties. The present Part is concerned with the construction of a homogenization model for predicting the effective diffusivities of cement-based materials. As already mentioned in Part I, these materials are complex multi-scale porous media, where the pore size distribution varies by several orders of magnitude (from 1 nm to more than 10  $\mu\text{m}$ ). On the basis of these observations, a multi-scale approach is adopted to deal with such a porous medium as in linear elasticity (e.g. Constantinides and Ulm 2004).

Some theoretical connections exist between elasticity and diffusivity. An elasticity problem can be decomposed in three diffusion problems (Milton 2002). Hence, the derivations exhibited in the present Part are generally much simpler than the ones presented in the previous Part. Nevertheless, it does not mean that the development of a homogenization model for predicting the effective diffusive properties of cement-based materials is a simple task, since the fact that the derivations in diffusion are easier than in linear elasticity is compensated by other difficulties. Indeed, much less information seems to be available on the phase diffusivities than on their elastic properties in particular for the CSH. Another difficulty for building a suited homogenization model for concrete materials consists in reproducing the highly non linear changes of their transport properties measured experimentally as their total porosity varies (e.g. Oh and Jang 2004).

The present Part is organized as follows. The first chapter assesses the capacity of matrix-inclusion type methods that have been focused on in linear elasticity to face this aspect. In the second one, other theories (Bergman 1976; Bruggeman 1935; Kirkpatrick 1971; 1973) more adequate for predicting these non-linear effects are discussed. A novel estimate for the transport properties of random heterogeneous media, such as conductivity and diffusivity, is then proposed by exploiting the main ideas underlying a celebrated exactly solvable assemblage of Hashin and Shtrikman (1962). For random heterogeneous media consisting of high contrast phases, the derived estimate is apt to capture the sudden variations of the effective diffusivity of HCP generally observed experimentally (Fig. 1.5). The third chapter

presents the multi-scale homogenization approach incorporating the latter estimate developed for predicting the macroscopic diffusion coefficients of HCP and mortars. The model developed will then be implemented into the ALLIANCES platform (Montarnal et al. 2006; 2007) so as to perform simulations of chemical degradations of cement-based materials presented in Part V.

By diffusion, we mean mass transfer generated by concentration gradients of aqueous species through saturated materials. The results obtained for diffusion are directly transposable to other transport properties such as electrical or thermal conductivity.

## 7 REVIEW OF MATRIX-INCLUSION TYPE EMTs FOR PREDICTING THE DIFFUSIVITIES OF POROUS MEDIA

This chapter aims at assessing if the matrix-inclusion type EMTs, already presented in Part II, are suited for estimating the macroscopic diffusive properties of porous media. The equations necessary for deriving these EMTs in the case of diffusion are quite alike the ones presented in the previous Part except that second-order tensors are now involved instead of fourth-order ones (Milton 2002), so that only the most basic or important ones are presently recalled.

### 7.1 Fundamental principles of matrix-inclusion type EMTs

The computations presented are analogous to the one performed in linear elasticity. However, the basic formulae necessary for applying homogenization methods are recalled for clarity.

#### 7.1.1 General principles of homogenization methods

The first step of these methods consists in representing the microstructure of the concerned material by a RVE, such as the one depicted in Fig. II.1, composed of a matrix phase, indexed by  $M$ , and of  $P$  particulate phases, which are assumed to be individually homogeneous (Fig. II.1). Their diffusion tensors are respectively denoted as  $\mathbf{D}_r$  ( $r = 1, \dots, P$ ). The same notations are used as in the previous Part.

The RVE is subjected to uniform ions flux vector over its surface  $\partial V$ :

$$\mathbf{J}_n(\mathbf{x}) = \mathbf{J}^\infty \cdot \mathbf{n}, \quad \forall \mathbf{x} \in \partial V, \quad (\text{III.1})$$

where  $\mathbf{J}_n(\mathbf{x})$  denotes the ions flux vector at a given point  $\mathbf{x}$  of the surface and  $\mathbf{J}^\infty$  is a uniform flux vector. The operator ‘.’ indicates a simple contraction. At the scale of the heterogeneities of the RVE, the equilibrium law and Fick’s constitutive one take the form:

$$\text{div}(\mathbf{J}(\mathbf{x})) = 0, \quad \forall \mathbf{x} \in V, \quad (\text{III.2})$$

$$\mathbf{J}(\mathbf{x}) = -\mathbf{D}(\mathbf{x}) \cdot \mathbf{g}(\mathbf{x}), \quad \forall \mathbf{x} \in V, \quad (\text{III.3})$$

where  $\mathbf{J}(\mathbf{x})$ ,  $\mathbf{D}(\mathbf{x})$  and  $\mathbf{g}(\mathbf{x})$  designate the microscopic flux vector, diffusivity tensor and concentration gradient of ions at a given point  $\mathbf{x}$  of the RVE, respectively. The macroscopic flux tensor  $\bar{\mathbf{J}}$  is defined as the volume average  $\langle \mathbf{J} \rangle_V$  of the microscopic one  $\mathbf{J}$  over  $V$  and can be shown to be equal to  $\mathbf{J}^\infty$ :

$$\bar{\mathbf{J}} = \frac{1}{V} \int_V \mathbf{J}(\mathbf{x}) dV = \mathbf{J}^\infty. \quad (\text{III.4})$$

The ensuing relation is also obtained from Eq. (III.3) by performing averaging operations on the entire volume of the RVE:

$$\bar{\mathbf{g}} = -\mathbf{D}^* \bar{\mathbf{J}}, \quad (\text{III.5})$$

where  $\bar{\mathbf{J}}$  and  $\bar{\mathbf{g}}$  are respectively the averages of the microscopic flux and concentration gradient tensors on the total volume of the RVE. Estimations of these averages by means of the diverse homogenization techniques presented before then allows for predicting the effective diffusivity tensor  $\mathbf{D}^*$  of the material. In the case of a macroscopically isotropic composite, the latter tensor may be written as:

$$\mathbf{D}^* = \frac{1}{3} D^* \mathbf{1}, \quad (\text{III.6})$$

where  $\mathbf{1}$  is recalled to be the second order identity tensor and  $D^*$  is a scalar.

## 7.1.2 Presentation of the Eshelby problem

### 7.1.2.1 Presentation of the Eshelby theorem

The Eshelby theorem presented in subsection 4.1.2 is also applicable in diffusion and is therefore briefly recalled below. A homogeneous ellipsoidal inclusion  $I$ , occupying a domain  $V_I$  and having for diffusivity tensor  $\mathbf{D}_I$ , is enclosed in an infinite matrix, which diffusivity tensor is denoted as  $\mathbf{D}_M$ . The concentration gradient through this single inclusion subjected to a fictive concentration gradient  $\mathbf{g}^*$ , which is uniform inside the inclusion and vanishes outside, is uniform:

$$\mathbf{g}_I^U = \mathbf{A}_I \cdot \mathbf{g}^*, \quad (\text{III.7})$$

where  $\mathbf{A}_I$  is called the Eshelby or the depolarization tensor (e.g. Torquato 2001) of the inclusion  $I$  expressed as:

$$(\mathbf{A}_I)_{ij} = \int_{V_I} \Gamma_{ij}(\mathbf{y} - \mathbf{x}) dV_y, \quad (\text{III.8})$$

where the operator  $\Gamma_{ij}(\mathbf{y} - \mathbf{x})$  is related to the Green function  $G_{ij}(\mathbf{y} - \mathbf{x})$  by:

$$\Gamma_{ij}(\mathbf{y} - \mathbf{x}) = G_{ij}(\mathbf{y} - \mathbf{x}). \quad (\text{III.9})$$

The Eshelby tensor thus links the concentration gradient inside the homogeneous ellipsoidal inclusion surrounded by an infinite medium to its fictive concentration gradient. The main limit of this fundamental theorem is that it is restricted to ellipsoidal inclusions in its original form (Eshelby 1957). The Eshelby tensor is generally quite difficult to determine analytically but has a very simple expression in the spherical homogeneous inclusion immersed in an infinitely large isotropic matrix (e.g. Torquato 2001; Milton 2002):

$$\mathbf{A}_I = \frac{1}{3} \mathbf{1}. \quad (\text{III.10})$$

The Eshelby tensor of a spheroidal homogeneous inclusion also presents the benefit of being analytically calculable (e.g. Torquato 2001) and its expression for a spheroid with aspect ratio  $r$ , which revolution axis is oriented along the  $\mathbf{e}_3$  axis, is:

$$\mathbf{A}_I = \begin{bmatrix} Q & 0 & 0 \\ 0 & Q & 0 \\ 0 & 0 & 1-2Q \end{bmatrix}, \quad (\text{III.11})$$

$$\text{with } Q = \begin{cases} \frac{1}{2} \left[ 1 + \frac{1}{r^2-1} \left[ 1 - \frac{r}{2\sqrt{r^2-1}} \ln \left( \frac{r+\sqrt{r^2-1}}{r-\sqrt{r^2-1}} \right) \right] \right], & r \geq 1; \\ \frac{1}{2} \left[ 1 + \frac{1}{r^2-1} \left[ 1 - \frac{r}{\sqrt{1-r^2}} \tan^{-1} \left( \frac{r}{\sqrt{1-r^2}} \right) \right] \right], & r \leq 1. \end{cases}$$

#### 7.1.2.2 Extension of the Eshelby tensor to spherical isotropic inhomogeneities

On the basis of the work of Duan et al. (2006) in linear elasticity, the Eshelby tensor in diffusion for a spherical isotropic inhomogeneity with a homogeneous shell (see Fig II.2) embedded in an infinite matrix is derived in Appendix III.A. By introducing the quantity  $\beta_i^j$  called "polarizability" by analogy with dipoles in electricity defined as (e.g. Torquato 2001):

$$\beta_i^j = \frac{D_i - D_j}{D_i + 2D_j}, \quad (\text{III.12})$$

a simple closed-form solution is found for the Eshelby tensor denoted as  $\tilde{\mathbf{A}}_I^M$  of a spherical isotropic inhomogeneity with a homogeneous interphase enclosed in an infinite matrix, as depicted in Fig. II.2:

$$\tilde{\mathbf{A}}_I^M = \left( \frac{1}{3} + 2\beta_i^M \rho^3 \right) \mathbf{1}, \quad (\text{III.13})$$

with  $\rho = r_i/r_e$ , where the radii  $r_i$  and  $r_e$  have been defined in Part II (see Fig. II.2). The polarizability  $\beta_i^j$  practically links the perturbation of the concentration gradient due to the insertion of a fictive concentration gradient. Its use will be very practical to lighten the diverse EMTs presented in the ensuing. The latter formula is of great utility, since it allows for

determining the average concentration gradient inside the domain occupied by the spherical inhomogeneity and its homogeneous interphase in response to a prescribed uniform fictive concentration gradient in the inclusion (Fig. II.2):

$$\bar{\mathbf{g}}_I = \tilde{\mathbf{A}}_I^M \cdot \mathbf{g}^*, \quad (\text{III.14})$$

where the Eshelby tensor  $\tilde{\mathbf{A}}_I^M$  for the spherical inhomogeneity with its homogeneous interphase will be referred to as inhomogeneous Eshelby tensor in the ensuing (Duan et al. 2006).

### 7.1.2.3 Presentation of the equivalent homogeneous inclusion method

First of all, let us consider the situation in which no heterogeneous inclusion is inserted in the infinite matrix with diffusivity tensor  $\mathbf{D}_M$ , which is subjected to a uniform far-field flux  $\mathbf{J}^\infty$ . In such case, the flux field is everywhere equal to  $\mathbf{J}^\infty$  and the concentration gradient field is such as:

$$\mathbf{g}_0 = \mathbf{D}_M^{-1} \cdot \mathbf{J}^\infty. \quad (\text{III.15})$$

A heterogeneous inclusion  $I$  occupying a volume  $V_I$  with diffusivity tensor  $\mathbf{D}_I$  is now inserted in this virgin medium and we are interested in calculating the average  $\bar{\mathbf{g}}_I$  of the concentration gradient field over  $V_I$ . The microscopic concentration gradient decomposes itself into two parts:

$$\mathbf{g}_I(\mathbf{x}) = \mathbf{g}_0 + \mathbf{g}_I'(\mathbf{x}), \quad \forall \mathbf{x}, \quad (\text{III.16})$$

where  $\mathbf{g}_I'(\mathbf{x})$  corresponds to the perturbation of the concentration gradient caused by the insertion of the heterogeneity. In order to apply the Eshelby theorem, the heterogeneous inclusion is assumed to be substituted by a homogeneous fictive inclusion with a diffusivity tensor denoted as  $\mathbf{D}_M$  that is subjected to an appropriate uniform fictive concentration gradient  $\mathbf{g}^*$ . The latter must be chosen in such a way that the same average flux and concentration gradient fields are obtained in the homogeneous fictive inclusion and in the heterogeneous one:

$$-\bar{\mathbf{J}}_I = \mathbf{D}_I \cdot \bar{\mathbf{g}}_I = \mathbf{D}_M \cdot (\bar{\mathbf{g}}_I - \mathbf{g}^*) \quad \text{and} \quad \bar{\mathbf{g}}_I = \mathbf{g}_0 + \mathbf{A}_I \cdot \mathbf{g}^*. \quad (\text{III.17})$$

By solving  $\mathbf{g}^*$  in (III.17<sub>2</sub>) and substituting its expression in (III.17<sub>1</sub>) the following solution is obtained for  $\bar{\mathbf{g}}_I$ :

$$\bar{\mathbf{g}}_I = [\mathbf{1} + \mathbf{A}_I \cdot \mathbf{D}_M^{-1} \cdot (\mathbf{D}_I - \mathbf{D}_M)]^{-1} \cdot \mathbf{g}_0. \quad (\text{III.18})$$

By carrying out an analogous reasoning as in Eqs. (II.28-30), the volume average  $\bar{\mathbf{J}}_I$  of the microscopic flux can be expressed as:

$$\bar{\mathbf{J}}_I = [\mathbf{1} + \Theta_I^M \cdot \mathbf{H}_I]^{-1} \cdot \mathbf{J}^\infty, \quad \text{with} \quad \Theta_I^M = \mathbf{D}_M \cdot (\mathbf{1} - \mathbf{A}_I) \quad \text{and} \quad \mathbf{H}_I = \mathbf{D}_I^{-1} - \mathbf{D}_M^{-1}, \quad (\text{III.19})$$

where  $\Theta_I^M$  is called the eigendiffusivity tensor of the single inclusion  $I$  embedded in the infinite reference medium by analogy with the eigenstiffness tensor in linear elasticity (Zheng and Du 2001) and where  $\mathbf{H}_I$  is the resistivity increment tensor of the inclusion. The eigendiffusivity tensor  $\Theta_I^M$  can be determined in the case of spheroidal inclusions by means of the expressions of the Eshelby tensor given in Eq. (III.11). For more complicated cases, the Eshelby tensor usually has to be estimated numerically (Douglas and Garboczi 1995). The ensuing derivations are therefore limited to the case of spheroidal inclusions. The next section gathers the basic expressions for the effective diffusive properties predicted by the EMTs presented in Part II.

## 7.2 Basic expressions of EMTs for estimating macroscopic diffusivities

Various EMTs have been presented in depth in the previous section. The derivations of these methods for predicting the material effective diffusivity that are very similar to the ones written previously are not recalled for concision. However, their final expressions are enlisted below.

### 7.2.1 Classical matrix-inclusion type estimates

In such type of EMTs, a matrix phase designated by the letter  $M$  is supposed to enclose the other phases modelled as inclusions. As in Part II, the effective resistivity increment tensor  $\mathbf{H}$  of the heterogeneous material defined as follows is introduced:

$$\mathbf{H} = \mathbf{D}^{*-1} - \mathbf{D}_M^{-1}. \quad (\text{III.20})$$

The effective diffusivity tensor of the material can be immediately deduced from the knowledge of this resistivity increment tensor:

$$\mathbf{D}^* = [\mathbf{1} + \mathbf{D}_M \cdot \mathbf{H}]^{-1} \cdot \mathbf{D}_M. \quad (\text{III.21})$$

By performing the same reasoning as in Eqs. (II.32-34), the dilute model provides a simple expression for estimating this effective resistivity increment tensor:

$$\mathbf{H}^{dil} = \sum_r \mathbf{H}_r^{dil}, \quad \text{with} \quad \mathbf{H}_r^{dil} = c_r \mathbf{H}_r \cdot [\mathbf{1} + \Theta_r^M \cdot \mathbf{H}_r]^{-1}. \quad (\text{III.22})$$

It is recalled that the validity range of the dilute estimation is very limited, since all the particles are required to be far enough from each other, so as to be regarded as isolated. More consistent schemes trying to reflect the interaction effects between inclusions are required. MT effective medium approximation may be used for this purpose. Following the same path as in Eqs. (II.35-39), the MT estimate of the resistivity increment tensor takes the form:

$$\mathbf{H}^{MT} = \mathbf{H}_r^{dil} \cdot \left[ \mathbf{1} - \sum_i \Theta_i^M \cdot \mathbf{H}_i^{dil} \right]^{-1}. \quad (\text{III.23})$$

However, as pointed out in the previous Part, the latter equation leads exactly to the same predictions as Eq. (III.22) derived with the dilute model and yields the following expression for the effective diffusivity of a macroscopically isotropic material:

$$D_{MT}^* = D_M \left( \frac{1 + 2 \sum_r c_r \beta_r^M}{1 - \sum_r c_r \beta_r^M} \right). \quad (\text{III.24})$$

The GSCS has been applied previously to estimate with a good accuracy the linear effective elastic properties of HCP and mortars modeled as composites with coated spherical inclusions such as the one depicted in Fig. III.1. On this figure, a spherical inclusion  $I$  with a volume fraction  $c_I$  and with a diffusion tensor denoted as  $\mathbf{D}_I$  is enclosed in a coating with a volume fraction  $c_{CI}$  occupied by a phase having its diffusion tensor designated by  $\mathbf{D}_{CI}$ . The double-inclusion thus obtained is in turn embedded in another coating with a volume fraction  $c_M = 1 - c_I - c_{CI}$  filled by the matrix phase having for diffusion tensor  $\mathbf{D}_M$  immersed in an infinitely large effective medium with diffusion tensor  $\mathbf{D}^*$ .

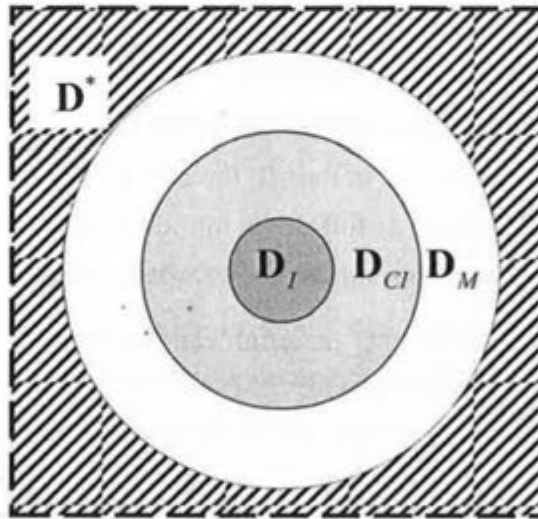


**Figure III.1:** Two-dimensional representation illustrating the application of the GSCS for computing the diffusive properties of a composite with coated spherical inclusions.

If all these phases are assumed to be isotropic, the estimation of the effective diffusivity by GSCS can then be computed by means of this formula (e.g. Hervé 2002):

$$D_{GSCS}^* = D_{DI} \left( \frac{1 + 2c_{DI} \beta_{DI}^M}{1 - c_{DI} \beta_{DI}^M} \right), \text{ with } D_{DI} = D_I \left( \frac{c_{DI} + 2c_I \beta_I^{CI}}{c_{DI} - c_I \beta_I^{CI}} \right). \quad (\text{III.25})$$

The MT estimate and GSCS are seen by comparing the last two equations to provide identical expressions for the effective diffusivity of an isotropic two-phase composite with spherical inclusions. It was shown in section 4.4. that GSCS is more accurate than MT in linear

elasticity, even though the first one is more intricate to compute. Nevertheless, these two models appear to be quite similar in the case of diffusion.

### 7.2.2 Double-inclusion type schemes

These methods have been preferred to compute the linear elastic properties of cement-based composites to the classical MT scheme, because of their better accuracy, versatility and their capacity of accounting for the spatial distributions of particulate phases (e.g. Hori and Nemat-Nasser 1993; Shen and Yi 2001; Zheng and Du 2001). Since the derivations are very similar as in Part II (Eqs. (II.42-80)), only the final expressions of these different estimates are recalled below. For a multiphase composite, the estimations provided by IDD and KT schemes are respectively:

$$\mathbf{H}^{IDD} = \mathbf{H}_r^{dil} \cdot \left[ \mathbf{1} - \sum_i \mathbf{H}_i^{dil} \cdot \boldsymbol{\Theta}_{Di}^M \right]^{-1}, \quad (\text{III.26})$$

$$\mathbf{H}^{KT} = \mathbf{H}_r^{dil} \cdot \left[ \mathbf{1} - \boldsymbol{\Theta}_D^M \cdot \mathbf{H}^{dil} \right]^{-1}, \quad (\text{III.27})$$

where  $\boldsymbol{\Theta}_{Dr}^M$  designates the eigendiffusivity tensor of the double-inclusion embedding the inclusion phase  $r$  and  $\boldsymbol{\Theta}_D^M$  denotes the eigendiffusivity tensor of the homogeneous effective inclusion (Fig. II.9). In the case of macroscopically isotropic materials with spherical inclusions, the tensors  $\mathbf{H}_r^{dil}$  are invertible provided that the phase diffusivities are not infinite. These last two equations then exactly coincide and furthermore yield a simple expression for the effective diffusivity of such materials:

$$D_{IDD,KT}^* = D_M \left( \frac{1 + 2 \sum_r c_r \beta_r^M}{1 - \sum_r c_r \beta_r^M} \right), \quad (\text{III.28})$$

which exactly coincides with the MT predictions in Eq. (III.24). The expression of DIM was derived in Part II for the particular cases of a two-phase material (Eq. (II.77)) and of a composite with coated inclusions (Eq. (II.82)) depicted respectively on the left-hand sides of Figs. II.7 and II.8. The two respective Eqs. (II.77) and (II.82) take an analogous form in diffusion:

$$\mathbf{H}^{DIM} = \mathbf{H}_I^{dil} \cdot \left[ \mathbf{1} - \boldsymbol{\Theta}_{DI}^M \cdot \mathbf{H}_I^{dil} \right]^{-1}, \quad (\text{III.29})$$

$$\mathbf{H}^{DIM} = \left( \mathbf{H}_I^{dil} + \mathbf{H}_{CI}^{dil} \right) \cdot \left[ \mathbf{1} - \boldsymbol{\Theta}_I^M \cdot \left( \mathbf{H}_I^{dil} + \mathbf{H}_{CI}^{dil} \right) \right]^{-1}. \quad (\text{III.30})$$

As in linear elasticity, the last formula leads to the same estimations as the MT scheme (Eq. III.23) for a composite with dispersed inclusions, as illustrated in Fig. II.8. To avoid this unexpected result, a modified version of DIM has been proposed in Part II. Its derivation in the case of diffusion is proposed below by employing the inhomogeneous Eshelby tensor in Eq. (III.13) derived in Appendix III.A. The configuration considered for the present

derivation consists in a composite pattern embedded in an infinite matrix medium and subjected to a far-field flux  $\mathbf{J}^\infty$ . This composite pattern comprises various double-inclusions denoted as  $D_r$  ( $r \in [1, P]$ ) enclosed in a matrix region, each of them being constituted of a spherical inclusion with diffusivity tensor  $\mathbf{D}_r$  surrounded by a spherical coating with diffusivity tensor  $\mathbf{D}_{Cr}$ .

The effective diffusion tensors of the different double-inclusions are first estimated with the aid of the work of Duan et al. (2006). The particular configuration described on Fig. III.2a) is thus approximated by a simpler one described on Fig. III.2b). The effective diffusive properties of the multiphase composite are then computed using the energy balance employed by Shen and Yi (2001). To achieve the computation of the effective diffusion tensor of the double-inclusions, fictive concentration gradients are introduced inside the inclusion domain so that each inclusion has the same diffusive properties as its coating.

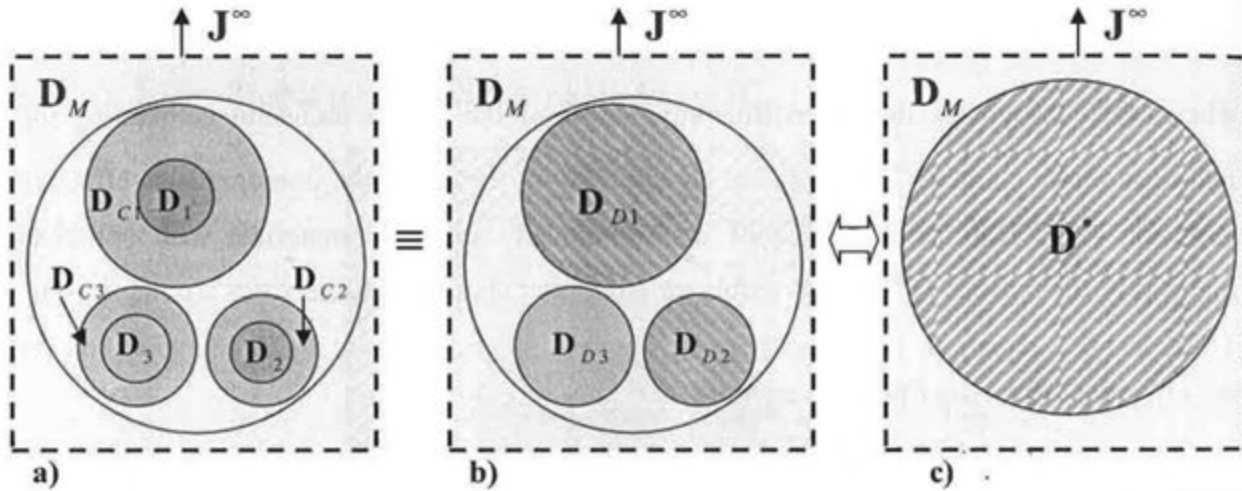


**Figure III.2: Schematic illustrating the main steps employed to derive the modified DIM.**

The average perturbation of the concentration gradient inside an inclusion representing phase  $r$  and having the same diffusion tensor as its coating can be related to the volume average  $\bar{\mathbf{g}}_r^*$  of the prescribed fictive concentration gradient by means of the inhomogeneous Eshelby tensor defined by Duan et al. (2006):

$$\bar{\mathbf{g}}_r^* = \tilde{\mathbf{A}}_r^M \cdot \mathbf{g}_r^*, \quad (\text{III.31})$$

where the expression of  $\tilde{\mathbf{A}}_r^M$  is given in Eq. (III.13) for the particular configuration of a spherical isotropic inhomogeneity embedded in an infinite isotropic matrix. By neglecting the interactions between the double-inclusions, the average concentration gradient inside the inclusion corresponding to a given particulate phase  $r$  takes the form:

$$\bar{\mathbf{g}}_r = \left[ \mathbf{D}_M + \mathbf{A}_{Dr} \cdot (\mathbf{D}_r - \mathbf{D}_M) \right]^{-1} \cdot \mathbf{J}^\infty + \bar{\mathbf{g}}_r^*, \quad (\text{III.32})$$

where  $\mathbf{A}_{Dr}$  denotes the homogeneous Eshelby tensor (Eq. (III.11)) of the spherical double-inclusion  $D_r$  ( $r \in [1, P]$ ). The consistency condition written in an average sense:

$$\mathbf{D}_r \cdot \bar{\mathbf{g}}_r = \mathbf{D}_{Cr} \cdot (\bar{\mathbf{g}}_r - \mathbf{g}_r^*), \quad (\text{III.33})$$

provides the following relation for the fictive concentration gradient  $\mathbf{g}_r^*$  in the inclusion:

$$\mathbf{g}_r^* = - \left[ (\mathbf{D}_r - \mathbf{D}_{Cr})^{-1} \cdot \mathbf{D}_{Cr} + \tilde{\mathbf{A}}_r^M \right]^{-1} \cdot \left[ \mathbf{D}_M + \mathbf{A}_{Dr} \cdot (\mathbf{D}_r - \mathbf{D}_M) \right]^{-1} \cdot \mathbf{J}^{\infty}. \quad (\text{III.34})$$

The average perturbation of the concentration gradient inside the inclusion  $\bar{\mathbf{g}}_r'$  can then be deduced from Eq. (III.31). Using the fact that:

$$\bar{\mathbf{g}}_{Dr}' = \left( 1 - \frac{c_r}{c_{Dr}} \right) \bar{\mathbf{g}}_{Cr}' + \frac{c_r}{c_{Dr}} \bar{\mathbf{g}}_r', \quad (\text{III.35})$$

$$\bar{\mathbf{g}}_{Dr}' = \mathbf{A}_{Dr} : \bar{\mathbf{g}}_{Dr}^*, \quad (\text{III.36})$$

the mean perturbation of the concentration gradient inside the inclusion coating  $\bar{\mathbf{g}}_{Cr}'$  is obtained as:

$$\bar{\mathbf{g}}_{Cr}' = - \frac{c_r}{c_{Dr} - c_r} \left( \tilde{\mathbf{A}}_{Dr}^M - \tilde{\mathbf{A}}_r^M \right) \cdot \left[ (\mathbf{D}_r - \mathbf{D}_{Cr})^{-1} \cdot \mathbf{D}_{Cr} + \tilde{\mathbf{A}}_r^M \right]^{-1} \cdot \left[ \mathbf{D}_M + \mathbf{A}_{Dr} \cdot (\mathbf{D}_r - \mathbf{D}_M) \right]^{-1} \cdot \mathbf{J}^{\infty}, \quad (\text{III.37})$$

where  $\tilde{\mathbf{A}}_{Dr}^M$  is the inhomogeneous Eshelby tensor of the double-inclusion  $D_r$  expressed in Eq. (III.13). The mean concentration gradients and flux inside the double-inclusion are further expressed with the help of Eqs. (III.35-36):

$$\bar{\mathbf{g}}_{Dr} = \left[ \mathbf{1} + \frac{c_r}{c_{Dr}} \tilde{\mathbf{A}}_{Dr}^M \cdot \left[ (\mathbf{D}_r - \mathbf{D}_{Cr})^{-1} \cdot \mathbf{D}_{Cr} + \tilde{\mathbf{A}}_r^M \right]^{-1} \right] \cdot \left[ \mathbf{D}_M + \mathbf{A}_{Dr} \cdot (\mathbf{D}_r - \mathbf{D}_M) \right]^{-1} \cdot \mathbf{J}^{\infty}, \quad (\text{III.38})$$

$$\bar{\mathbf{J}}_{Dr} = \mathbf{D}_{Cr} \cdot \left[ \mathbf{1} + \frac{c_r}{c_{Dr}} \left( \mathbf{1} - \tilde{\mathbf{A}}_{Dr}^M \right) \cdot \left[ (\mathbf{D}_r - \mathbf{D}_{Cr})^{-1} \cdot \mathbf{D}_{Cr} + \tilde{\mathbf{A}}_r^M \right]^{-1} \right] \cdot \left[ \mathbf{D}_M + \mathbf{A}_{Dr} \cdot (\mathbf{D}_r - \mathbf{D}_M) \right]^{-1} \cdot \mathbf{J}^{\infty}, \quad (\text{III.39})$$

By eliminating  $\mathbf{J}^{\infty}$  in the last two relations, the following expression can finally be obtained for the effective diffusion tensor of this double-inclusion:

$$\mathbf{D}_{Dr} = \left\{ \begin{array}{l} \mathbf{D}_{Cr} \cdot \left[ \mathbf{1} + \frac{c_r}{c_{Dr}} \left( \mathbf{1} - \tilde{\mathbf{A}}_{Dr}^M \right) \cdot \left[ (\mathbf{D}_r - \mathbf{D}_{Cr})^{-1} \cdot \mathbf{D}_{Cr} + \tilde{\mathbf{A}}_r^M \right]^{-1} \right] \cdot \\ \left[ \mathbf{1} - \frac{c_r}{c_{Dr}} \tilde{\mathbf{A}}_{Dr}^M : \left[ (\mathbf{D}_r - \mathbf{D}_{Cr})^{-1} \cdot \mathbf{D}_{Cr} + \tilde{\mathbf{A}}_r^M \right]^{-1} \right]^{-1} \end{array} \right\}, \quad (\text{III.40})$$

By carrying out exactly the same reasoning as in Eqs. (II.83-85) (see subsection 4.3.3.1), an explicit estimation can then be achieved for the effective diffusion tensor of the composite with coated inclusions:

$$\mathbf{D}^* = \mathbf{D}_M - \left[ \left( \sum_r c_r \left( \mathbf{A}_{Dr} + (\mathbf{D}_r - \mathbf{D}_M)^{-1} \cdot \mathbf{D}_M \right)^{-1} \right) + \mathbf{A}_{CDI}^M \right]^{-1} \cdot \mathbf{D}_M, \quad (\text{III.41})$$

where  $\mathbf{A}_{CDI}^M$  is the Eshelby tensor of the equivalent composite pattern (see Fig. III.2c) and where the diffusion tensor  $\mathbf{D}_{Dr}$  can be predicted by the preceding equation. In the ensuing, this estimation will be referred to as the modified DIM.

If all the involved phases are assumed to be isotropic, simple expressions are provided for the homogeneous and inhomogeneous Eshelby tensors by Eqs. (III.10) and (III.13), respectively. In the particular case where only one double-inclusion is considered, the effective diffusion coefficients for this double-inclusion and the composite respectively simplify into:

$$D_{DI} = D_I \left( \frac{c_{DI} + 2c_I \beta_I^{CI}}{c_{DI} - c_I \beta_I^{CI}} \right) \text{ and } D^* = D_{DI} \left( \frac{1 + 2c_{DI} \beta_{DI}^M}{1 - c_{DI} \beta_{DI}^M} \right), \quad (\text{III.42})$$

which exactly coincide with GSCS formula written in Eq. (III.25). A good number of homogenization methods have been presented in this section but it is now necessary to test their relevance for predicting the macroscopic diffusivities of porous media. For this purpose, attention should be primarily focused on the principal effects acting on the material effective transport properties. It is pointed out in the next section that these properties are strongly dependent on certain microstructural factors that have to be taken into consideration in the computation by homogenization.

### 7.3 Significant microstructural parameters from the viewpoint of diffusion

Porous media are generally regarded as a mixture of a solid phase, denoted as  $D_1$ , considered non-diffusive and a diffusive porous phase designated by  $D_2$ . A very strong contrast exists between the transport properties of these two phases so that it is frequently assumed that  $D_1 / D_2 \rightarrow 0$  in porous media.

#### 7.3.1 Importance of the percolation of the diffusive phase

In cases of infinite contrasts such as  $D_1 / D_2 \rightarrow 0$ , many authors (e.g. Kirkpatrick 1971; Torquato 2001) assert by means of numerical simulations that the effective diffusivity or conductivity of the medium tends to obey the scaling law:

$$\begin{cases} \frac{D^*}{D_2} \rightarrow 0, & \text{for } c_2 \leq c_2^{th}, \\ \frac{D^*}{D_2} \sim (c_2 - c_2^{th})^t, & \text{for } c_2 \geq c_2^{th}, \end{cases} \quad (\text{III.43})$$

where  $c_2^{th}$  is called percolation threshold and  $t$  varies between 1 and 2 (e.g. Torquato 2001). This percolation threshold physically corresponds to the critical volume fraction at which a

cluster of the diffusive phase first connects one extremity of the microstructure to another. According to the scaling law above, the formation of this cluster spanning the entire microstructure induces sudden variations of diffusivity, which may be denominated as percolation effects.

As was already observed in Fig. I.5, the macroscopic diffusivities of HCP strongly vary from one paste to another. Many authors attribute these significant changes to the geometrical percolation of capillary porosity, defined as the remaining space situated between hydrated cement grains (e.g. Richardson 2000). It physically corresponds to the formation of a cluster composed of pores that first spans the material. It appears consequently necessary to assess the ability of the homogenization schemes introduced previously to account for such phenomenon.

At this point, an important clarification is necessary about the differences between linear elasticity and diffusion in cement-based materials. According to the previous remarks, the percolation of pores is suspected to have a very strong impact on the macroscopic diffusive properties of porous materials. This phenomenon has not been discussed in the previous Part dedicated to linear elasticity but it seems to have less influence on the material effective elastic properties as illustrated by the subsequent example. Let a standard CEM I paste with  $w/c = 0.45$ , which effective elastic properties and diffusivity have both been measured experimentally (Richet et al. 1997; Gallé et al. 2004), be perforated by infinitely long cylindrical water-filled tunnels isotropically distributed. The diffusivity of these idealistic porous percolating paths is assumed to be equal to the diffusion coefficient  $D_{\text{H}_2\text{O}} = 2.2 \times 10^{-9} \text{ m}^2/\text{s}$  of tritiated water in bulk water at  $23^\circ\text{C}$  (Bary and Béjaoui 2006), while their bulk and shear moduli are respectively equal to 2.2 GPa and 0 GPa. The size of the RVE of the perforated paste is taken large enough so that the original cement paste can be regarded as homogeneous. Its macroscopic diffusivity is measured to be  $D_{\text{HCP}}^*(w/c = 0.45) = 5.21 \times 10^{-12} \text{ m}^2/\text{s}$  (Richet et al. 1997), whereas its effective Young modulus and its Poisson ratio are taken equal to 23 GPa and 0.25 (Gallé et al. 2004), respectively. The total volume fraction of these tunnels spanning over the whole paste is assumed to vary between 0 and 0.25 and we are interested in estimating their effects on the material elastic and diffusive properties by means of the full-range IDD scheme (Zheng and Du 2001). On Fig. III.3, the material effective diffusivity appears to be much more affected by the tunnels than its effective elastic moduli. A major difference between diffusion and elasticity is that the macroscopic elastic properties of a material such as concrete may be more influenced by the formation of the solid skeleton (Bernard et al. 2003) than by the percolation of pores, whereas this percolation of porosity is crucial for the effective diffusive properties. According to this example, the pore percolation has to be carefully taken into consideration in diffusion, despite the fact that it has a secondary importance in linear elasticity.

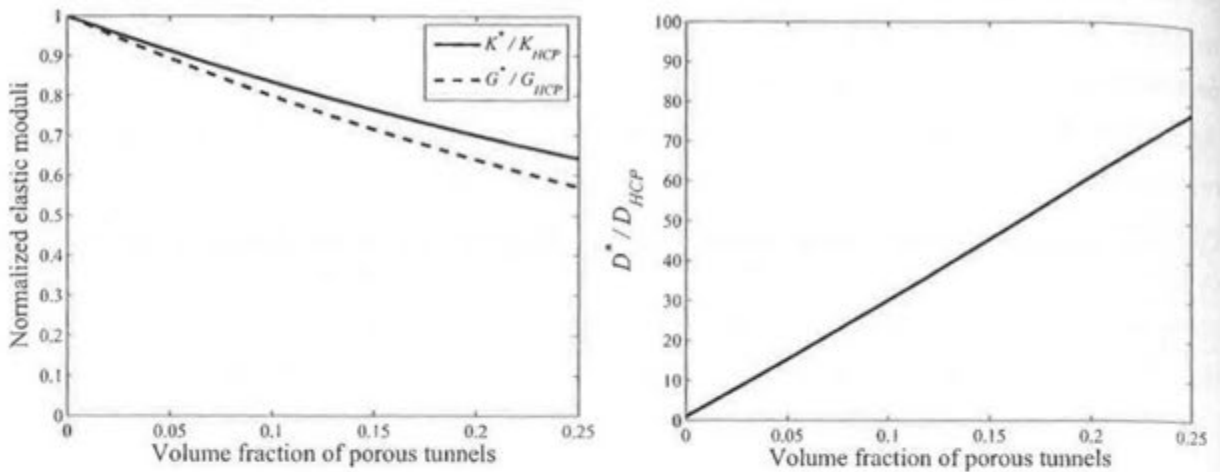


**Figure III.3: Evolution of the normalized effective elastic properties a) and of the diffusivity b) of the perforated cement paste with the volume fraction of porous cylindrical tunnels.**

### 7.3.2 Importance of other microstructural indicators

In linear isotropic porous media, the following equation is generally employed to compute the macroscopic diffusion coefficient denoted as  $D^*$  (e.g. Bear and Bachmat 1991; Dullien 1992):

$$D^* = \tau c_2 D_2, \quad (\text{III.44})$$

where  $\tau$  is called the tortuosity and  $c_2$  corresponds to the volume fraction of porous phase. The tortuosity can geometrically be interpreted in terms of the ratio of the length of the material over the distance covered by the ions or the fluid to get through the sample (Dullien 1992). Practically, the closer to 1 the tortuosity is, the straighter the percolating paths are. It also gives some information in terms of pore connectivity and percolation. For the extreme case where  $\tau = 0$ , the distance that the ions should cover to get through the sample becomes infinite, which means that the porous phase does not percolate. In addition, the material effective diffusion  $D^*$  goes to 0, since the porous phase remains occluded. This shows the primary importance of the percolation of the porous phase on the diffusive properties of porous media.

The macroscopic diffusivity can also be related to the formation factors, which constitute precious microstructural indicators and are defined as (Berryman 2005):

$$\lim_{D_1 \rightarrow \infty} \frac{D^*}{D_1} = \frac{1}{F_1}; \quad \lim_{D_2 \rightarrow \infty} \frac{D^*}{D_2} = \frac{1}{F_2}. \quad (\text{III.45})$$

The formation factors are usually measured from electrical resistance data (Dullien 1992). Geometrical properties of the constituent phases, such as their tortuosity (e.g. Bear and Bachmat 1991), are closely related to these formation factors. Given the fact that

$D^*(D_1, D_2)/D_2 = D^*(D_1/D_2, 1)$  (Milton 2002), a comparison of the two previous equations gives the relation  $\tau c_2 = 1/F_2$  for such materials. The latter indicates that the formation factor of a given phase incorporates information on both the tortuosity and the volume fraction of this phase.

#### 7.4 Review of matrix-inclusion type EMTs from the viewpoint of connectivity and percolation

A brief review of the capacity of the main existing analytical homogenization schemes to accurately model actual percolating paths of pores and capture strong variations due to the creation or annihilation of percolating paths in random heterogeneous media is proposed.

The matrix-inclusion type EMTs, such as GSCS, DIM, MT, KT and IDD, studied in this manuscript all present the considerable advantage of being explicit in diffusion. However, all these approaches except the GSCS are obtained by embedding one single isolate homogeneous or composite inclusion into a supposed infinite matrix phase, as pointed out by Ma et al. (2004). They consequently fail to take into account the connectivity of the particulate phase and appear hardly compatible with the percolation theory, since a single inhomogeneity cannot percolate except if it degenerates into an infinite disk or cylinder. However, though appearing inadequate to percolation problems, these models have up to now not been shown to be unable to mimic the effects due to the transition from a microstructure comprising no or few tortuous percolating clusters of a high-diffusive phase to one where significant paths of this phase have formed.

The 3D simulations of Garboczi et al. (1995) demonstrated that the aspect ratio of spheroidal inclusions denoted by  $r = b/a$  (where  $a$  designates the radius of the circular basis of the spheroid and  $b$  corresponds to its revolution axis) influences significantly their percolation threshold and consequently their connectivity. For example, the percolation threshold of spherical inclusions corresponds to a critical volume fraction  $c_2^{th} \approx 0.29$  (Rintoul and Torquato 1997), whereas for spheroidal inclusions with  $r = 100$  this threshold decreases to  $c_2^{th} = 0.01$  (Garboczi et al. 1995). The shape of the spheroidal inclusion should be in average representative of the diverse pore clusters, since the pore structure is simultaneously composed of isolated pores assumed quasi-spherical and of very connected pores forming elongated clusters. In other words, the better the pores connect to each other, the more the spheroids representing the porous phase should be elongated. Thus the connectivity could indirectly be taken into account by using adequately chosen spheroids.

As an example, an attempt is now made to reproduce percolation effects in a macroscopically isotropic material composed of two isotropic phases by modelling the most diffusive phase, called 2, as a randomly oriented prolate spheroid embedded in the other phase, called 1. In the ensuing, the number 1 will always refer to the phase less diffusive and 2 to the most diffusive one so that  $D_2 > D_1$ . The volume fractions of the two phases are respectively denoted by  $c_1$  and  $c_2$  with  $c_1 + c_2 = 1$ . Two cases, one of high contrast and another one of infinite contrast, can be considered in order to test the reliability of EMTs for predicting percolation effects. The diffusion coefficients,  $D_1$  and  $D_2$ , are supposed to be respectively such as  $D_2 / D_1 = 10^3$  in the high-contrast case and  $D_1 / D_2 \rightarrow 0$  in the infinite contrast one. The overall shape of the curves presented on Fig. III.4 in the case of high-contrast is not adapted to correctly predict the effects due to changes in the volume fraction of a high-diffusive phase percolating through the microstructure. Indeed, these variations generally have a sigmoidal shape for the curve of the effective transport coefficients plotted against the volume fractions of the high-diffusive phase, reflecting the transition from a macroscopically low-diffusive material to a high-diffusive one.

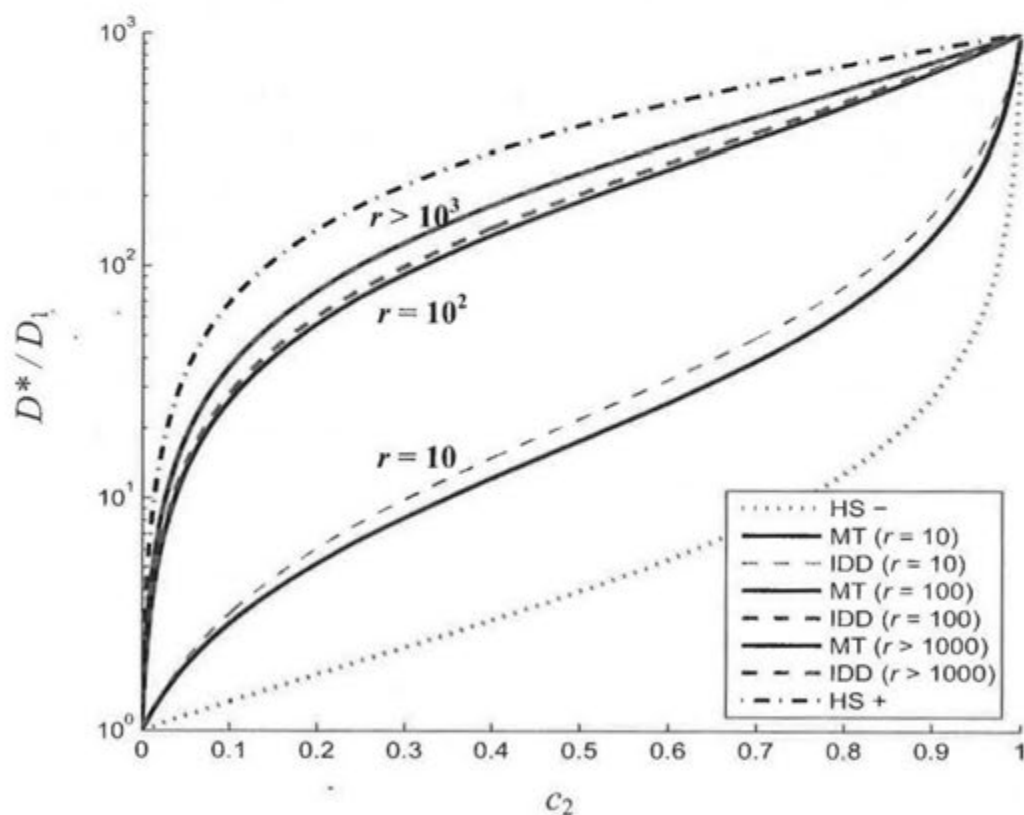


**Figure III.4 (logarithmic scale): Evolution of the effective diffusion coefficient of a macroscopically isotropic two-phase material with  $D_2 / D_1 = 10^3$  respectively estimated by the MT (Mori and Tanaka 1973) and the IDD (Zheng and Du 2001) schemes as a function of the volume fraction of the diffusive phase. The latter phase is modeled as prolate spheroids with diverse aspect ratios  $r$ .**

The Hashin and Shtrikman (HS) bounds that are presented in the chapter just after are also plotted on Fig. III.4 for the sake of comparison. In the infinite contrast case, the effective diffusivities predicted by MT and IDD schemes both go to zero except for the case of an infinite cylinder. Matrix-inclusion type schemes, such as MT or IDD, are consequently not well suited for physically reproducing percolation effects and should not be employed whenever the particulate phase percolates in the real microstructure. Besides, the GSCS (Hervé 2002) used for estimating the diffusion properties of mortars by Caré and Hervé (2004) does not seem to be adequate either, since only the outer matrix shell can percolate with this method (see Fig. II.1). Recently, Mélé et al. (2005) proposed quite an empirical method involving numerous parameters so as to artificially incorporate the percolation effects into the GSCS. However, more reliable EMTs from the percolation viewpoint exist in literature and are discussed in the next chapter.

## 8 REVIEW AND DEVELOPMENT OF OTHER HOMOGENIZATION THEORIES FOR PREDICTING THE DIFFUSIVITIES OF POROUS MEDIA

It was shown in the previous chapter that matrix-inclusion type EMTs are not suited for predicting percolation phenomena and reproduce the rapid variations of diffusivity observed experimentally on cement-based materials (Fig. I.5). Still, other theories of homogenization have been developed to address this issue. Some of them deriving from the self-consistency principles (Bruggeman 1935; Landauer 1952) or from the variational ones (Hashin and Shtrikman 1962) are therefore presently reviewed. By focusing on some classical exactly solvable microstructures (Hashin and Shtrikman 1962), a novel estimate based on a simple exactly solvable assemblage is also proposed to predict the macroscopic diffusivities of porous media.

In the present chapter, only macroscopically isotropic two-phase materials are considered. The volume fractions of the two phases respectively called 1 and 2 are denoted by  $c_1$  and  $c_2$ . The diffusion coefficients of the two isotropic phases,  $D_1$  and  $D_2$ , are taken such as  $D_2 > D_1$ .

### 8.1 Review of bounding approaches

The HS bounds for a macroscopically isotropic two-phase material are given by:

$$D_{HS}^- = D_1 \left( 1 + c_2 \frac{3\beta_2^1}{1 - c_2\beta_2^1} \right), \quad D_{HS}^+ = D_2 \left( 1 + c_1 \frac{3\beta_1^2}{1 - c_1\beta_1^2} \right), \quad (\text{III.46})$$

with  $\beta_i^j$  defined in Eq. (III.12). The latter formula was derived by means of variational principles (Hashin and Shtrikman 1962) that are explained in many monographs (e.g. Milton 2002; Torquato 2001) and are thus not presently recalled. The application of the HS bounds to composite materials with high contrasts is problematic, since the bounds are not tight enough to bind the effective transport coefficients, as may be seen on Fig. III.4. It is possible to improve the HS bounds if more information, in the form of correlation functions (Beran 1965), formation factors (Berryman 2005) or experimental measurements (Bergman 1976), is available for the composite. On the basis of these pieces of information, a good number of tighter bounds (e.g. Beran 1965; Bergman 1976; Torquato 2001; Milton 2002) have been derived from the variational principles of Hashin and Shtrikman (1962).

The form and the derivation of these bounds (Beran 1965) in their original form can be quite complex but Berryman introduced a convenient canonical function that enables to express the main bounds within a unified framework:

$$\Lambda(y) \equiv \left[ \frac{c_1}{D_1 + 2y} + \frac{c_2}{D_2 + 2y} \right]^{-1} - 2y, \quad (\text{III.47})$$

This function depends monotonically on  $y$ , which has the dimension of diffusivity and is referred to as a transformation parameter. Berryman (2005) evidenced that most of the known bounds, such as Reuss and Voigt, HS or Beran bounds, can be gained from the latter equation for simple values of  $y$ . If the parameter  $y$  is equal to  $D_1$  or  $D_2$ , the lower and upper HS bounds are respectively retrieved. If the parameter  $y$  is equal to  $\zeta_1 D_1 + \zeta_2 D_2$  or  $(\zeta_1 / D_1 + \zeta_2 / D_2)^{-1}$ , the lower and upper Beran bounds are respectively retrieved (Berryman 2005). The microstructural parameters  $\zeta_1$  and  $\zeta_2 = 1 - \zeta_1$  are known as three-point parameters and are related to the three-point spatial correlation functions (e.g. Torquato 2001) of the composite microstructure.

Let us assume that an experimental value for the material effective diffusivity, denoted as  $D'$ , is available at a given volume fraction of porosity. Bergman (1976) then derived improved bounds incorporating this piece of information and taking the following form:

$$D_{B-} = \Lambda(y_{B-}) \text{ and } D_{B+} = \Lambda(y_{B+}), \quad (\text{III.48})$$

where

$$y_{B-} = \left( \frac{u}{D_1} + \frac{1-u}{D_2} \right)^{-1}, \quad \text{with } u = \frac{(\Lambda^{-1}(D'))^{-1} - D_2^{-1}}{D_1^{-1} - D_2^{-1}}, \text{ and}$$

$$y_{B+} = (vD_1 + (1-v)D_2) \quad \text{with } v = \frac{(\Lambda^{-1}(D')) - D_2}{D_1 - D_2}. \quad (\text{III.49})$$

These Bergman bounds have been recently argued as being adequate to deal with the cases of high contrasts (Berryman 2005). To give an example of the curves predicted by Bergman

bounds, it is presently supposed that  $D^*/D_2 = 0.1$ . The HS, Beran and Bergman bounds for the effective diffusivity of random heterogeneous media with phase diffusivities such as  $D_1/D_2 \rightarrow 0$  and  $D_2/D_1 = 10^3$  are plotted in Figs. III.5 and III.6, respectively. The bounds plotted on Fig. III.5 appear to have similar shape as the curves on Fig. III.4, which may not be suited for capturing percolation effects.

In the case of infinite contrasts (Fig. III.6), the lower bounds all tend to zero and are therefore not represented. Moreover, no percolation threshold appears on the upper bounds. None of the bounds reviewed consequently seems to be apt to account for percolation effects. That's why self-consistent (SC) EMTs that present valuable features for the prediction of the diffusivity of porous media are discussed hereafter.

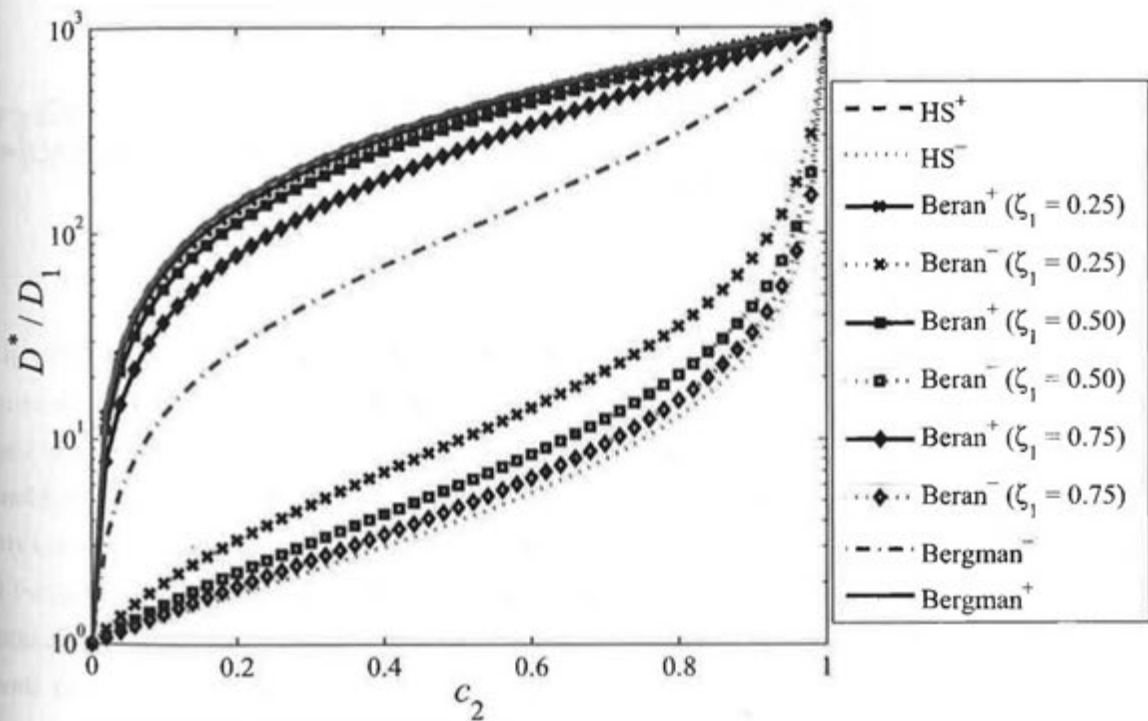
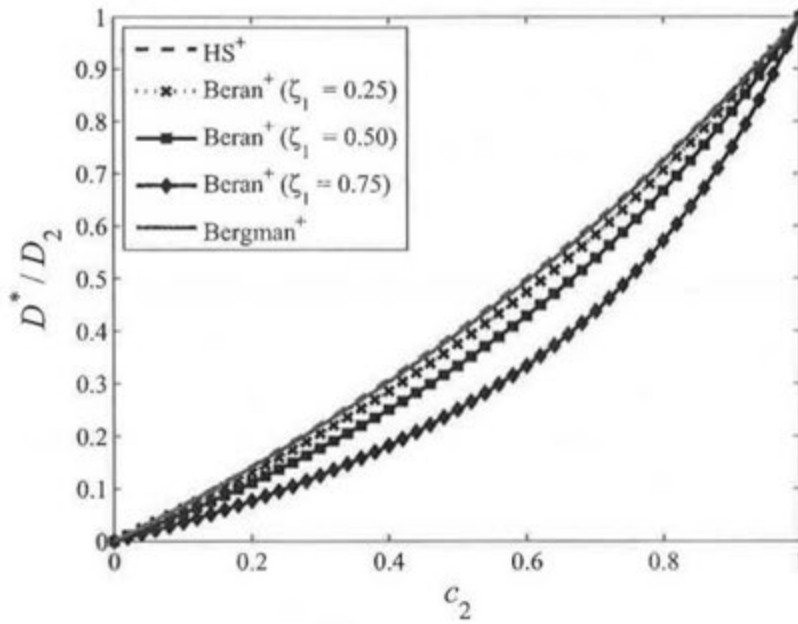


Figure III.5 (semi-logarithmic scale): Evolutions of HS, Beran and Bergman bounds for a macroscopically isotropic two-phase material with  $D_2/D_1 = 10^3$  as a function of the volume fraction of the high diffusive phase.



**Figure III.6: Evolutions of HS, Beran and Bergman bounds for a macroscopically isotropic two-phase material with  $D_1 / D_2 \rightarrow 0$  as a function of the volume fraction of the high diffusive phase.**

## 8.2 Review of SC type schemes

The SC scheme (Bruggeman 1935; Landauer 1952) counts among the most popular homogenization models in diffusion (e.g. Oh and Jang 2004; Bary and Béjaoui 2006) because of its capacity of capturing sudden variation of diffusivity. That's why many commonly used EMTs (Kirkpatrick 1971; 1973; McLachlan 1987) for dealing with homogenization problems in diffusion or conduction directly derive from the SC scheme. On the contrary to matrix-inclusion type models where the particulate phases are represented as inclusions embedded in a supposed infinite matrix phase, in the SC ones all the phases are modelled as inclusions enclosed in a yet unknown effective medium supposed infinite. The SC estimate in three dimensions can be obtained by solving the following equation (Torquato 2001):

$$c_1 \beta_1^* + c_2 \beta_2^* = 0, \quad (\text{III.50})$$

where  $\beta_1^*$  and  $\beta_2^*$  are defined in Eq. (III.12). The SC predictions for the effective diffusivity of random heterogeneous media with phase diffusivities such as  $D_1 / D_2 \rightarrow 0$  and  $D_2 / D_1 = 10^3$  are plotted in Figs. III.7 and III.8, respectively. The two curves on these figures provided by the SC estimate exhibit drastic changes of curvatures. These effects are induced by the percolation of the high-diffusive phase, i.e. the formation of a cluster of this phase spanning the entire microstructure.

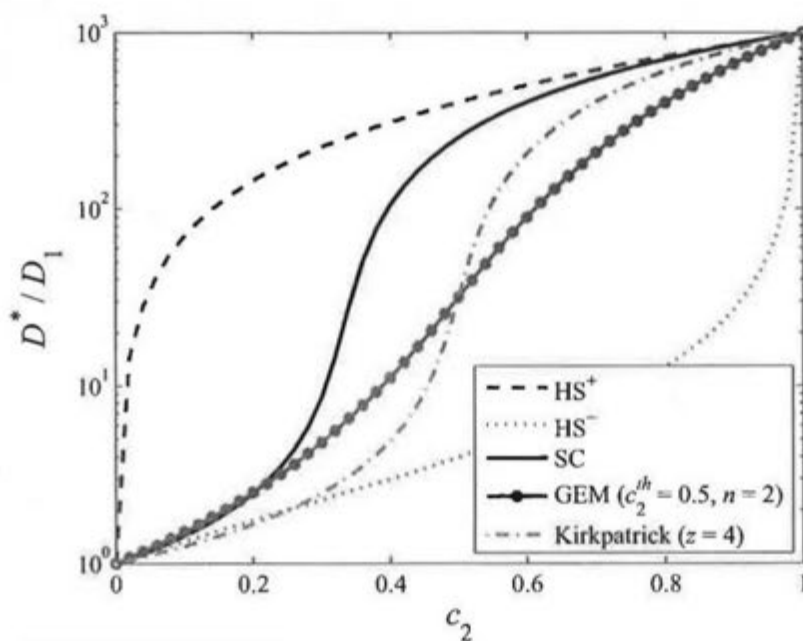


**Figure III.7 (semi-logarithmic scale): Evolutions of the effective diffusion coefficient of a macroscopically isotropic two-phase material with  $D_2 / D_1 = 10^3$  estimated by SC type schemes as a function of the volume fraction of the high diffusive phase.**

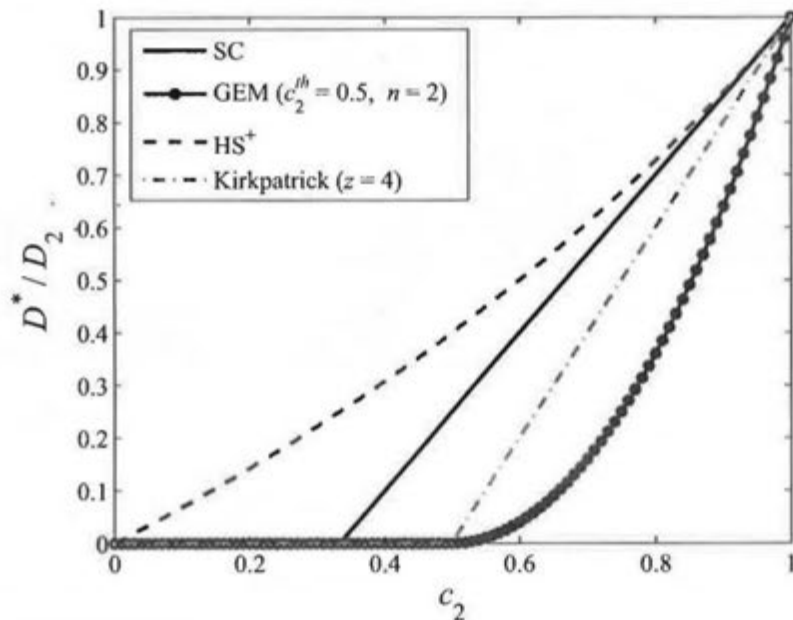


**Figure III.8: Evolutions of the effective diffusion coefficient of a macroscopically isotropic two-phase material with  $D_1 / D_2 \rightarrow 0$  estimated by SC type schemes as a function of the volume fraction of the diffusive phase.**

Moreover, these jumps observed for the SC estimations on the figures just above occur at a particular volume fraction or percolation threshold of the high-diffusive phase. The SC model

thus presents the notorious advantage compared to the matrix-inclusion type EMTs to predict a nontrivial percolation threshold but it occurs systematically at a volume fraction of  $c_2^{th} = 1/d$  for a two-phase composite composed of spherical inclusions, where  $d$  is the space dimension, regardless of the microstructure. However, it is clear that the microstructure strongly affects the percolation threshold. For example, if a matrix encloses monodisperse overlapping spherical inclusions (Fig. III.9), a volume fraction of 0.03 is sufficient to ensure that it percolates (Torquato 2001), whereas 0.29 are required for the particulate phase. Accordingly, the two phases composing the latter material percolate at volume fractions different from those predicted by the SC model. The choice of spheroidal particles instead of spherical ones may partly overcome this shortcoming, since with the percolation threshold then given by the SC scheme changes with the aspect ratio of the spheroid, but the SC predictions generally violate the HS bounds for non negligible range of volume fractions of the high-diffusive phase.

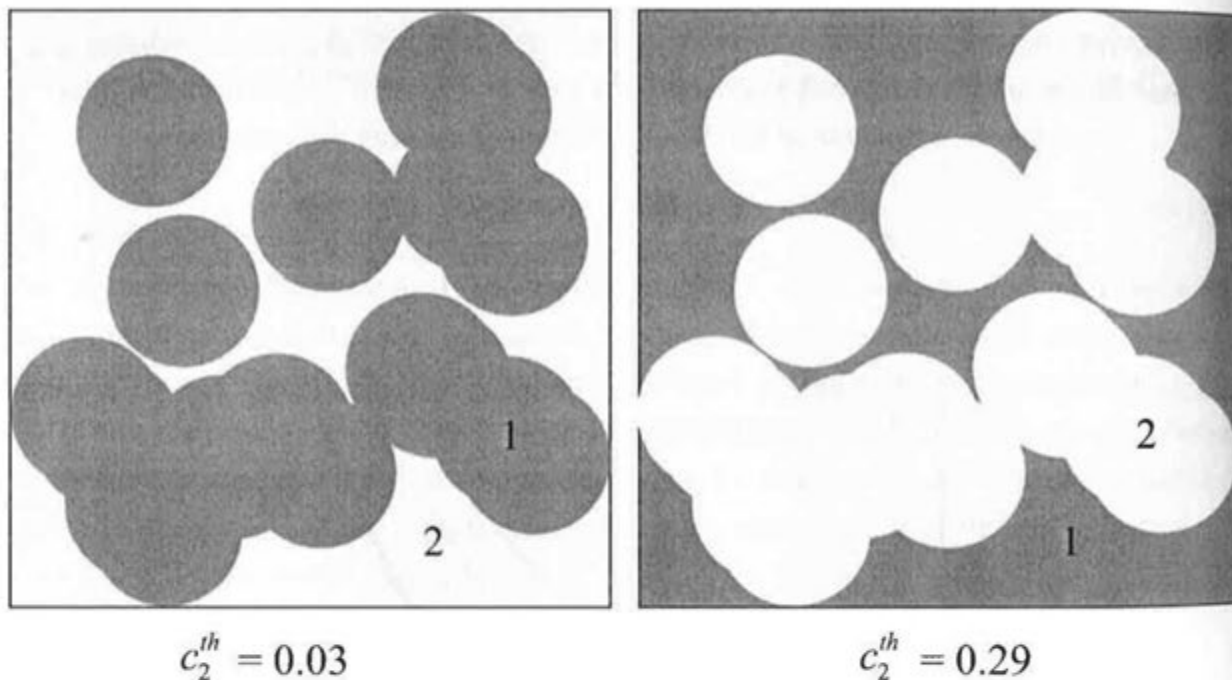


**Figure III.9:** Two-dimensional representations of monodisperse overlapping spherical inclusions that are randomly distributed in space. The percolation thresholds of the clusters formed by these spherical inclusions and of the remaining space differ significantly.

Kirkpatrick (1971; 1973) developed an EMT combining the discrete percolation theory (e.g. Shante and Kirkpatrick 1971) and the self-consistency principle. For more information concerning the discrete or lattice percolation one, which dates back to the fifties (Broadbent and Hammersley 1957), the reader should refer to Shante and Kirkpatrick (1971). The microstructure in the Kirkpatrick model is represented as a resistor network and the percolation threshold predicted by the latter scheme no longer depends on the dimensionality

but on the coordination number designated by  $z$ . This quantity is defined as the number of bonds connected at the same node and thus allows for taking into account the connectivity of particles. The second-order equation provided by the Kirkpatrick estimate (1971; 1973) is strongly similar to the one given by the SC scheme:

$$c_1 \beta_1^*(z) + c_2 \beta_2^*(z) = 0, \quad \text{with} \quad \beta_i^*(z) = \frac{(D_i - D_j)}{\left( D_i + \left( \frac{z}{2} - 1 \right) D_j \right)}. \quad (\text{III.51})$$

It is straightforward that Eq. (III.50) obtained with the classical SC scheme is a particular case of Eq. (III.51) for  $z = 6$ . Supposing that  $D_2$  is infinitely bigger than  $D_1$  in the equation above, the percolation threshold appears to be inversely proportional to the coordination number:  $c_2^{th} = 2/z$ . The latter equation has only one positive root corresponding to the Kirkpatrick estimate:

$$D^* = \frac{\alpha + \sqrt{\alpha^2 + 2(z-2)D_1D_2}}{(z-2)} \quad \text{with} \quad \alpha = D_2 \left( \left( \frac{z}{2} - 1 \right) c_2 - 1 \right) - D_1 \left( \left( \frac{z}{2} - 1 \right) c_1 - 1 \right). \quad (\text{III.52})$$

The Kirkpatrick model uses the concept of coordination number that allows for taking into account the connectivity of particles. This scheme is based upon resistor networks constituting an idealistic discrete representation of the microstructure of ordered heterogeneous materials. They are very practical of use in the case of crystalline materials, where the coordination number is exactly known. Nevertheless, this number is very difficult to estimate in random heterogeneous materials containing particles that can be of very different sizes and the discrete resistor network on which the SC estimates of Kirkpatrick (1971; 1973) are based seems quite far from the actual continuous microstructures of disordered materials. In addition, though the Kirkpatrick estimate may provide more realistic thresholds than the original SC model, they violate HS bounds for non negligible ranges of volume fractions, as may be seen in Fig. III.7. More precisely, it is seen on this figure that the Kirkpatrick estimate obtained for  $z = 4$  violates them for the ranges of volume fractions  $c_2 < 0.25$ . On the contrary, the classical SC estimate, corresponding to a coordination number of  $z = 6$  (Kirkpatrick 1971; 1973), always satisfies HS bounds.

A model called the general effective media (GEM), used for instance by Oh and Jang (2004) to predict the diffusion coefficients of HCP, has been proposed by McLachlan (1987):

$$c_1 \frac{(D_1^{1/p} - D^{*1/p})}{\left( D_1^{1/p} + \left( \frac{1}{c_2^{th}} - 1 \right) D^{*1/p} \right)} + c_2 \frac{(D_2^{1/p} - D^{*1/p})}{\left( D_2^{1/p} + \left( \frac{1}{c_2^{th}} - 1 \right) D^{*1/p} \right)} = 0, \quad (\text{III.53})$$

where  $c_2^{th}$  is recalled to be the percolation threshold and  $p$  is a parameter identified as the critical exponent. The McLachlan model is quite similar to the Kirkpatrick one but involves two parameters instead of one. It is noteworthy that for  $p = 1$ , GEM coincides with the

Kirkpatrick estimate. Consequently, the McLachlan scheme can also violate HS bounds for certain values of the parameter  $p$ . Another method that is capable to predict different percolation thresholds consists in deriving the SC scheme by adopting spheroidal inclusions instead of spherical ones, as is generally the case. The percolation threshold estimated with this approach then varies with the aspect ratio of the spheroid. Nevertheless, the respect of HS bounds is not necessarily guaranteed with this methodology.

To summarize the discussions made in this section, a comparative table recapitulating the merits of the presently reviewed EMTs is proposed (Table III.1). It appears that none of them is really capable of both reproducing percolation effects in random heterogeneous materials and respecting HS bounds. The next section is therefore devoted to the presentation of a recent estimate based on a well-defined continuous microgeometry satisfying these two conditions.

|                              | Capacity to capture sudden variations of diffusivity | Respect of HS bounds | Number of extra parameters involved | References  |
|------------------------------|--|----------------------|-------------------------------------|---|
| Matrix-inclusion type models | No   | Yes                  | 0                                   | Maxwell (1873), Mori-Tanaka (1973), Küster-Toksoz (1974), ... |
| SC scheme                    | Only for $c_2^{th} = 1/3$ for spherical inclusions   | Yes                  | 0                                   | Bruggeman (1935), Landauer (1952), ...                        |
| Kirkpatrick scheme           | Yes  | No                   | 1                                   | Kirkpatrick (1971; 1973)                                      |
| GEM                          | Yes  | No                   | 2                                   | McLachlan (1987)  |
| GSCS                         | No   | Yes                  | 0                                   | Hervé (2002)  |

*Table III.1: Comparative table aiming at testing homogenization models on three simple criteria.*

### 8.3 Mixed composite spheres assemblage (MCSA) estimate (Stora et al. 2006b)

#### 8.3.1 Presentation of the estimate

Hashin and Shtrikman (1962) proved that their bounds written in Eq. (III.46) are realized by two composite spheres assemblages (CSAs) corresponding to idealized microstructures, where the space is entirely filled by coated-spheres of sizes ranging from finite down to infinitesimal. Neither the size nor the spatial distribution of the coated-spheres is specified in CSA. However, all the composite spheres are homothetic and consist of a spherical core of radius  $r_i$  and a coating of thickness  $(r_e - r_i)$ . The radii  $r_i$  and  $r_e$  are chosen so that each coated-sphere has the same composition as the original two-phase material. Though the opportunities

offered by the self-consistency principles (Bruggeman 1935; Landauer 1952) or the variational ones (Hashin and Shtrikman 1962) for estimating the transport properties of random heterogeneous media with high contrasts have been thoroughly investigated, the possibilities given by the celebrated CSA of Hashin and Shtrikman (1962) may conversely not have been studied sufficiently for such media. This exactly solvable microstructure was initially established to materialize HS bounds and thus prove their optimality. In the present section, by exploiting the idea underlying the original CSA, an assemblage mixing two types of composite sphere is proposed to obtain an estimation model capable of remedying the shortcomings of HS bounds.

The construction of Hashin and Shtrikman (1962) relies on the fact that the concentration field in a homogeneous medium characterized by a diffusion coefficient  $D_0$ , subjected to a uniform concentration gradient on its boundary, is not disturbed by the insertion of a spherical composite inclusion which overall diffusion coefficient is equal to  $D_0$ . In particular, any previously defined coated-sphere, which core and shell are respectively occupied by phases 2 and 1, embedded in a homogeneous medium with  $D_0 = D_{HS}^-$  does not perturb the concentration field outside the composite element in question. Consequently, an assemblage exclusively composed of these particular composite spheres realizes the lower bound. The upper one can in turn be attained by a similar construction, where the roles of the two phases inside the composite sphere are switched and the radii are taken such as  $(r_i/r_e)^3 = c_1$ .

CSAs are widely used, because they provide exact and straightforward analytical results. Nevertheless, the two CSAs materializing HS bounds correspond to extreme matrix/inclusion morphology (Fig. III.10). In the assemblage achieving the HS lower bound, the low-diffusive phase 1 is fully connected and plays the role of matrix, while the high-diffusive phase 2 occupying the cores of the coated-spheres is entirely disconnected and distant from each other due to the systematic presence of coatings made of phase 1. The exact opposite situation occurs in the assemblage attaining the HS upper bound. As a matter of fact, this characteristic can even be regarded as an advantage for some special design problems (Torquato et al. 2005). Nevertheless, actual microstructures having such an extreme morphology do not abound in Nature. To obtain a more realistic and more versatile microstructure, it would be desirable to use for instance different types of composite spheres. That's why another microgeometry, called MCSA, is presented below.

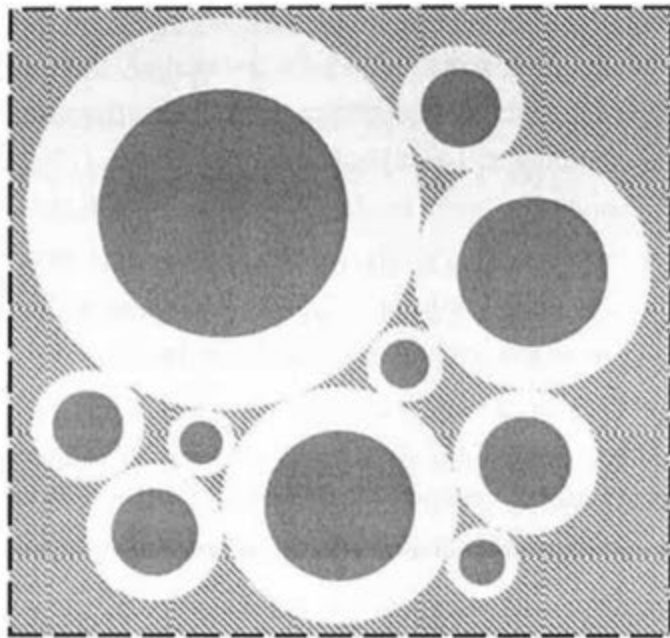


*Figure III.10: Two-dimensional representation of the CSA developed by Hashin and Shtrikman (1962).*

The MCSA follows the same construction rule as CSA but two types of composite spheres are involved in MCSA instead of one type in CSA. The idea of using assemblages mixing two types of composite spheres is not new. Pham (1997) proposed an estimate on the basis of a MCSA, where the volume fractions of the phases in the composite spheres are fixed but the embedding orders of the two phases can be interchanged. However, this assemblage is not exactly solvable, since the two types of coated-spheres generally do not have the same effective diffusivity and the diverse perturbations they induce on the concentration fields are tremendously difficult to calculate. Gilormini (2001) evidenced that a simple MCSA can be constructed so as to realize any compressibility or conductivity of isotropic two-phase materials comprised between HS bounds. Analogously, it is possible to build a MCSA that achieves any macroscopic diffusion coefficient  $D^*$  of an isotropic two-phase material verifying the condition  $D_{HS}^- \leq D^* \leq D_{HS}^+$ , as shown below.

The macroscopic diffusion coefficient  $D^*$  of the material and the phase volume fractions  $c_1$  and  $c_2$  are assumed given; the particular example of the diffusion through a porous material with high contrast between the phase diffusivities is considered for the present demonstration:  $c_1 = 0.56$ ,  $c_2 = 0.44$ ,  $D_2/D_1 = 10^3$  and  $D^*/D_1 = 20$ , where  $D_1$  and  $D_2$  are recalled to designate the diffusivities of the solid and porous phases, respectively. The lower and upper HS bounds for this material are plotted on Fig. III.11.

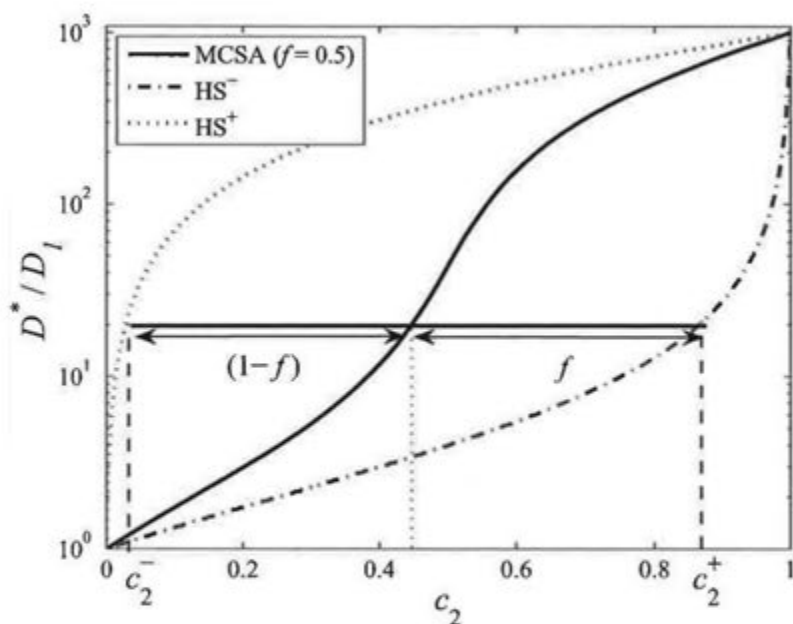


**Figure III.11 (semi-logarithmic scale): Evolution of HS bounds as a function of the porous phase volume fraction and graphical representation of the geometric parameter  $f$  of MCSA (Stora et al. 2006b).**

The condition  $D_{HS}^- \leq D^* \leq D_{HS}^+$  ensures that two CSAs corresponding to the lower and upper HS bounds, with the respective porous phase volume fractions  $c_2^+ (\geq c_2)$  and  $c_2^- (\leq c_2)$ , can realize the effective coefficient  $D^*$ . In the coated-sphere with the volume fraction  $c_2^-$ , the core is occupied by phase 1 and the shell by phase 2, whereas the roles of the two phases are exchanged in the coated-sphere with the volume fraction  $c_2^+$ . These volume fractions are deduced from Eq. (III.46):

$$c_2^+ = \frac{\beta_1^1}{\beta_2^1}, \quad c_2^- = 1 - \frac{\beta_2^2}{\beta_1^2}. \quad (\text{III.54})$$

In the present assemblages, the macroscopic diffusion coefficients of the two types of coated-spheres, whose compositions defined by the equation just above may be very different, are both equal to  $D^*$ . No perturbation in the concentration fields is then induced if any of these two types of composite spheres is inserted in the homogeneous material whose effective diffusion coefficient is  $D^*$ . It is consequently feasible to establish an exactly solvable microstructure as a hybrid assemblage of these two types of composite spheres, filling together the entire space (Fig. III.12). An interesting characteristic of the MCSA thus obtained is that both phases are simultaneously present in the cores and shells. In the ensuing, the coated-spheres with phase 2 as external coating are denoted by C1, and those which core is occupied by phase 2 are designated by C2. The density  $f$  of C1 spheres in MCSA is chosen so that the total volume fraction of phase 2 in this assemblage is equal to  $c_2$ :

$$c_2 = f c_2^- + (1-f) c_2^+. \quad (\text{III.55})$$

This condition permits to determine the geometric parameter  $f$  as a function of  $c_2$  and  $D^*$ :

$$f = \frac{-1}{2\beta_2^2} \left( \frac{1}{\beta_2^1} - \frac{1}{\beta_2^1} c_2 \right). \quad (\text{III.56})$$

The resulting microstructure illustrated on Fig. III.12, that can materialize any macroscopic diffusion coefficient  $D^*$  of an isotropic two-phase material verifying HS bounds, does not seem to correspond to any known EMT but can give rise to physically sound estimates, as shown below.

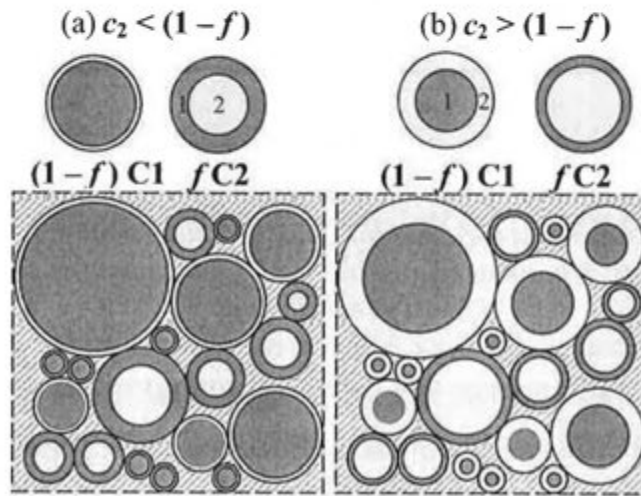


**Figure III.12:** Two-dimensional representation of an assemblage mixing two types of composite spheres (Stora et al. 2006b).

The MCSA with a given effective diffusion coefficient  $D^*$  is determined through a unique parameter  $f$  specified in Eq. (III.56). Inversely, by considering the macroscopic diffusion coefficient  $D^*$  as unknown and the parameter  $f$  as given, we can establish the quadratic equation:

$$aD^{*2} + bD^* + c = 0, \quad (\text{III.57})$$

where

$$\begin{aligned} a &= 1 + (2f - c_2)\beta_2^1, \\ b &= 2D_2[1 - (f + c_2)\beta_2^1] - D_1[1 + 2(f + c_2)\beta_2^1], \\ c &= 2D_1D_2[(f - 2c_2)\beta_2^1 - 1]. \end{aligned}$$

The solution of this equation provides only one positive root that constitutes an estimate for the effective diffusion coefficient of the material:

$$D^* = \frac{-b + \sqrt{b^2 - 4ac}}{2a}. \quad (\text{III.58})$$

According as  $f = 0$  or  $1$ , the previous equation yields the  $HS^-$  or  $HS^+$  bound. Furthermore,  $D^*$  given above varies monotonically with  $f$ . The MCSA estimate can consequently attain any value comprised between HS bounds.

The derivation of a MCSA estimate for the effective elastic moduli could also be of interest but is not a simple matter. Whereas the effective diffusivity and bulk modulus of CSA presents the benefit of being exactly solvable, the effective shear modulus of this microgeometry is not exactly computable (e.g. Milton 2002). Consequently, an exactly realizable MCSA estimate can be obtained in linear elasticity for the effective bulk modulus, but not for the shear modulus.

It is insightful to see how the MCSA estimate in Eq. (III.58) can be recast by means of the canonical function proposed by Berryman (2006) in Eq. (III.47). In two-phase materials, the relation linking  $f$  to the transformation parameter  $y$  can be derived from Eqs. (III.47) and (III.56-57) (Stora et al. 2006b):

$$f = \left[ \frac{1}{\beta_1^2} + 2c_2 \left( \frac{D_2 - y}{D_2 + 2y} \right) \right] \left( \frac{D_1 - y}{D_1 + 2y} \right). \quad (\text{III.59})$$

The inverse relation requires solving a quadratic equation with only one positive root which takes the form:

$$y = \frac{-e + \sqrt{e^2 - 4dg}}{2d}. \quad (\text{III.60})$$

where

$$\begin{aligned} d &= 2 + 2(2f - c_2)\beta_1^2, \\ e &= -2D_1 + D_2 + 2\beta_1^2(f + c_2)(D_1 + D_2), \\ g &= D_1 D_2 [(f - 2c_2)\beta_1^2 - 1]. \end{aligned}$$

This function providing the transformation parameter  $y$  is also monotonic with respect to  $f$ . Eqs. (III.59-60) show that a one-to-one correspondence exists between  $f$  and  $y$ . So, the geometric parameter  $f$  in the MCSA model can be taken as equivalent to the transformation parameter entering the canonical function defined in Eq. (III.47). At the same time, since the properties of the canonical function are such that it leads to excellent estimates even with rough estimates of the transformation parameter (Berryman 2006), we can expect that Eq. (III.58) produces good estimates when  $f$  is evaluated from relevant experimental data. It is emphasized that, by construction, these estimates always comply with HS bounds. Besides, the parameter  $f$  has a simple geometric signification and can easily be related to physical factors that are primordial for transport phenomena, as will be shown in the next section.

### 8.3.2 Signification and interpretation of the MCSA parameter

Given the phase volume fractions of a random heterogeneous material, the estimate derived from MCSA for the effective diffusivity depends only on one geometric parameter  $f$  reflecting the relative proportion of the two types of composite spheres in the assemblage. The purpose of the present section is to highlight the connections existing between the parameter  $f$  characterizing MCSA and important physical concepts, such as connectivity and tortuosity.

#### 8.3.2.1 A parameter for connectedness

The estimate given by Eq. (III.58) is mathematically quite similar to the SC model of Kirkpatrick (1971; 1973). They are both analytical and each of them only depends on one clearly identified parameter, respectively the coordination number  $z$  in the Kirkpatrick approach and the geometric parameter  $f$  in the MCSA model. In the Kirkpatrick theory (1971, 1973), the microstructure is considered as a resistor network and the coordination number  $z$  is defined as the number of bonds connected at the same node. In the actual microstructure, this quantity is practically identified to the number of contacting neighbors to a given particle. This parameter thus allows for taking into account the connectedness of the diverse phases. Analogously, the geometric parameter  $f$  can be interpreted as a parameter for connectedness in the MCSA model. As illustrated in Figs. III.12, each phase inside the assemblage can be broken into two parts: the first one contained in the cores of the composite spheres is completely isolated, while the second one present in the coatings is well connected, since a given coated-sphere is in contact with infinity of neighbors. In practice, the volume fraction of the phase 2 dispersed in the outer layers of the C1 spheres, denoted by  $c_2^{out}$ , can be identified to the experimental measurement of the connected volume fraction of phase 2, once such measure is available. After some calculations detailed in Appendix III.B, the geometric parameter  $f$  can be expressed as a function of this volume fraction  $c_2^{out}$ :

$$f = c_2^{out} \left( \frac{1 + 2\beta_1^2 \beta_2^1 (c_2 - c_2^{out})}{c_2 + 2\beta_1^2 \beta_2^1 (c_2 - c_2^{out})} \right). \quad (\text{III.61})$$

According to this equation, it is possible in the case of porous media to gain information for  $f$  from the knowledge of the percentage of connected pores, which may be accessible via various experimental procedures such as MIP. On the opposite, the coordination number  $z$  is far more difficult to estimate for such materials generally containing pores that can be of very different sizes.

#### 8.3.2.2 Link with the formation factors

The measurement of one of these formation factors allows for calculating the value of the geometric parameter  $f$  when the volume fractions are also known. Indeed, the parameter  $f$  is related to the formation factors  $F_1$  and  $F_2$  in the following manner:

$$f = c_1 \left( \frac{2F_2 + 1}{2F_2 - 2} \right) = 1 - c_2 \left( \frac{2F_1 + 1}{2F_1 - 2} \right). \quad (\text{III.62})$$

Nevertheless, the demonstration detailed in Appendix III.C of the previous equation is valid only if both formation factors are finite. This fact clearly defines the situations for which MCSA are of interest: they are useful provided that both formation factors are finite, i.e. the two phases percolate. When one of the formation factors is infinite, MCSA degenerates into a simple CSA.

In this section, some connections have been established between the geometric parameter characterizing MCSA and crucial microstructural parameters, such as the connected volume fractions and the formation factors. A detailed comparison with the SC type estimates is carried out in the subsequent section to show the original features of the MCSA estimate and discuss its potential application fields.

### 8.3.3 Comparisons with other EMTs

The predictions by the MCSA of the effective diffusivity of a porous medium, with phase diffusivities such as  $D_2/D_1 = 10^3$  and  $D_2/D_1 \longrightarrow 0$ , are plotted against the volume fraction  $c_2$  of the pore phase on Figs. III.13 and III.14. On these figures, the MCSA model is seen to always satisfy HS bounds. As illustrated on Fig. III.13, the latter model is even able to sweep all the values comprised between these rigorous bounds, as  $f$  varies from 0 to 1, which is not the case of the classical SC estimate. On Fig. III.14, the lower HS bound tends to zero and is consequently not represented.

The consistency of the MCSA and classical SC estimates with HS bounds is a direct consequence of their realizability (Gilormini 2001; Milton 1985). The realizability conditions are necessary for testing the merits of EMTs but may reveal insufficient, since it is also desirable to ensure that the microstructures materializing EMTs are realistic from the point of view of connectivity. The real connectedness of the diverse phases cannot be correctly modeled by the CSA realizing HS bounds except if they are fully connected or disconnected. Conversely, as pointed out previously, both the SC estimate of Kirkpatrick and the MCSA model provide quite simple means to approach the actual connectivity of the different phases.

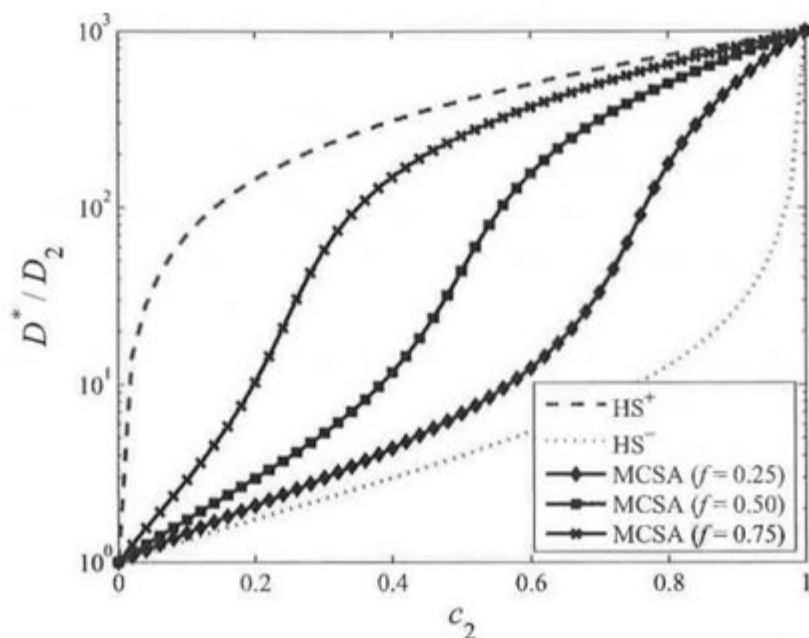


**Figure III.13:** Evolutions of the effective diffusion coefficient of a macroscopically isotropic two-phase material with  $D_2 / D_1 = 10^3$  estimated by the MCSA scheme as functions of the high-diffusive phase volume fraction for diverse values of the parameter  $f$ .

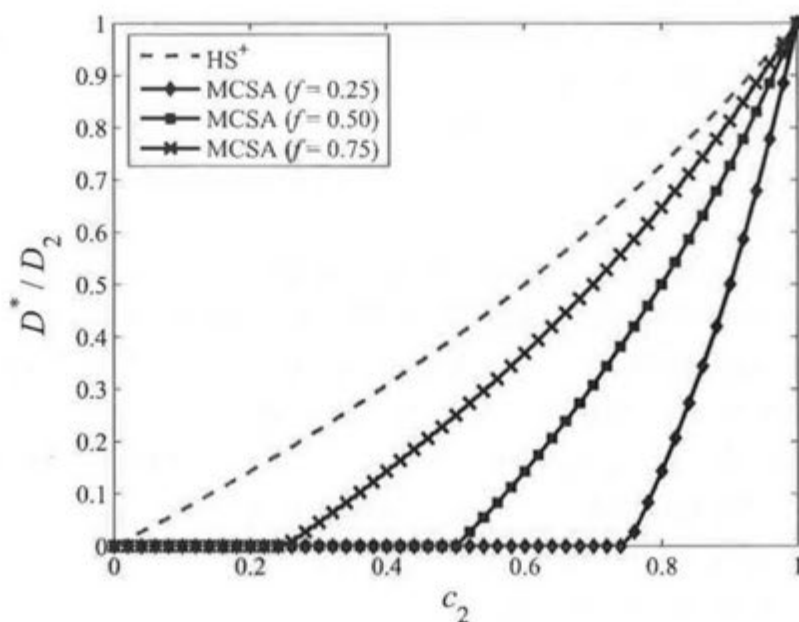


**Figure III.14:** Evolutions of the effective diffusion coefficient of a macroscopically isotropic two-phase material with  $D_1 / D_2 \rightarrow 0$  estimated by the MCSA scheme as functions of the high-diffusive phase volume fraction for diverse values of the parameter  $f$ .

All the MCSA curves on Fig. III.13 exhibit strong changes of curvatures for  $c_2 = (1-f)$  that are quite similar to those observed on the SC curves. A natural question thus arises: are these

significant changes of the effective diffusivity of the MCSA also provoked by the percolation of the high-diffusive phase? The following reasoning could help in answering to this interrogation. The volume fraction of the high-diffusive phase 2 is taken initially small so that the effective diffusivity  $D^*$  of MCSA is low and is then assumed to increase progressively, while the parameter  $f$  remains fixed. Thus, in order to conserve a low effective diffusivity, the coating of C1 spheres occupied by phase 2 is maintained as thin as possible, as can be seen in Fig. III.15a, and the major part of phase 2 is dispersed in the cores of C2 spheres (see Fig. III.15b). The effective diffusion coefficient of such an assemblage is low, since the high diffusive phase present in the cores of C2 spheres is isolated due to the coatings made of the low-diffusive phase (see Fig. III.12a). However, when the volume fraction of the high-diffusive phase exceeds the density  $(1-f)$  of C2 spheres, this phase can no longer be massively trapped in C2 spheres (see Fig. III.15b) and the connected part distributed in the coatings of C1 spheres inevitably augments, as may be seen on the right-hand half part of Fig. III.15. The apparently similar radical changes of the macroscopic diffusivities estimated respectively by SC and MCSA models are consequently originated by two different physical transitions: the jumps of SC estimations are provoked by the percolation of the high-diffusive phase, while the changes of the effective diffusivity of MCSA are caused by a transition from tortuous percolating clusters only composed of a small part of the high-diffusive phase to less sinuous paths gathering the major part of this phase, as illustrated on Figs. III.12.

The latter transition may be quite alike the ones inducing the pronounced increase of diffusivity observed in cementitious materials (Fig. I.5) as the porosity augments (e.g. Cui and Cahyadi 2001; Oh and Jang 2004), since percolating paths of pores can systematically be found regardless of their volume fraction in the material by considering very fine scales. This assertion is experimentally sustained by numerous MIP tests (e.g. Gallé 2001), where the liquid injected at high pressure manages to pass through any cement paste, mortar or concrete by porous paths less constricted than 3 nm. It is worth saying that there are a large number of other materials, such as for example porous media having a multi-scale pore structure like rocks or sandstones, where this highly diffusive phase always percolates.

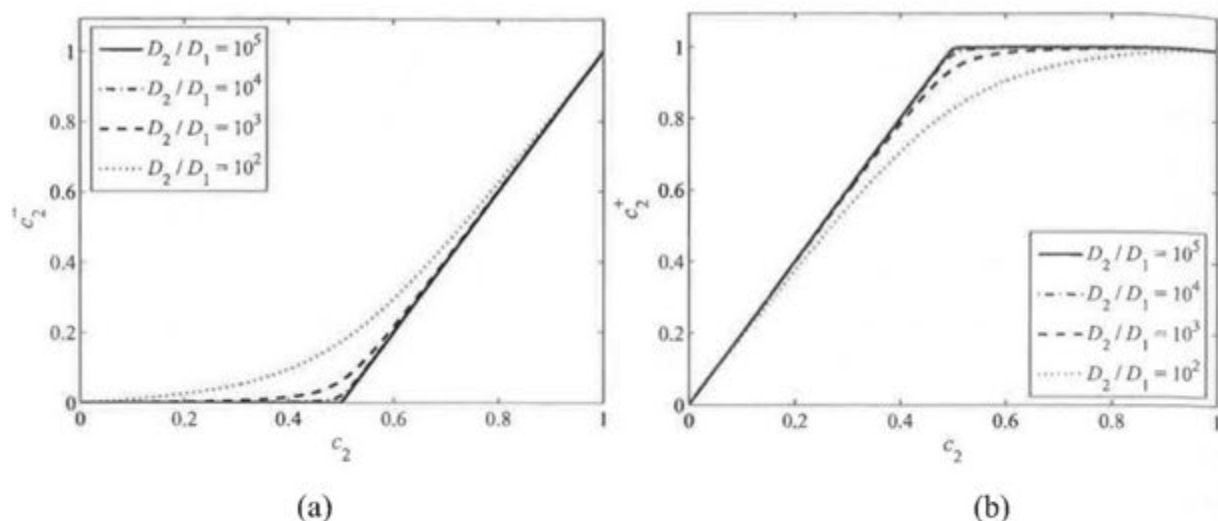


**Figure III.15:** Evolution of the volume fractions of the high-diffusive phase respectively dispersed in the shells of C1 spheres (a) and in the cores of C2 spheres (b) as functions of the total volume fraction of the high-diffusive phase for diverse contrasts between phase diffusivities, the geometric parameter  $f$  being equal to 0.5.

#### 8.4 Conclusions of chapter 8

The success of models developed for engineering applications depends to a large extent on their simplicity and, in particular, on the easiness with which the parameters involved in the models can be physically interpreted. Based on simple space filling assemblages composed of two types of composite spheres, the MCSA estimate presently developed needs only one geometric parameter, in addition to the phase volume fractions and diffusivities. This parameter can take into account the phase connectivity and is in direct relation with the formation factors (Eq. (III.62)).

Original features of the MCSA, such as its capacity to describe tortuous percolating paths, have been outlined and could be of particular interest for multi-scale random porous media. The MCSA estimate is also capable of capturing pronounced variations of the material diffusivity, while respecting rigorous bounds. It thus appears suited for predicting the macroscopic diffusive properties of porous media or more generally of random heterogeneous media with high contrasts. Therefore the multi-scale homogenization approach developed in the ensuing chapter to predict the macroscopic diffusion coefficients of cementitious materials incorporates the MCSA model.

## 9 CONSTRUCTION OF A MULTI-SCALE HOMOGENIZATION MODEL FOR ESTIMATING THE EFFECTIVE DIFFUSIVITIES OF CEMENT-BASED MATERIALS

As already argued previously, cement-based materials have complex microstructure with a multi-scale porosity. It is consequently quite natural to adopt multi-scale approaches to deal with such media. In the present chapter, a multi-scale homogenization model is first developed for HCP that constitutes the matrix of concrete materials, and is then extended to mortars. The main difficulty for building a suited homogenization model for HCP consists in correctly representing their multifaceted porosity and in reproducing the highly non linear changes of their diffusive properties measured experimentally (Fig. I.5). Several homogenization models developed for predicting the transport properties of cement-based materials (e.g. Oh and Jang 2004; Bary and Béjaoui 2006) attribute these significant changes to the geometrical percolation of capillary porosity. However, this explanation may not really be in accordance with the critical pore diameters measured by MIP, as shown below.

As already mentioned in Part I, gel pores sizes are assumed to be situated between a few nm and  $0.2 \mu\text{m}$  and capillary pores ones to range from  $0.2 \mu\text{m}$  and a few  $\mu\text{m}$ , even though the size range of capillary pores varies in the different classifications for the pore structure of HCP proposed in literature (e.g. Powers and Brownyard 1948). Diamond (2000) evidenced that the critical pore diameter, defined as the pore width corresponding to the highest rate of mercury intrusion per change in pressure, allows for assessing the largest scale at which pores percolate. The values obtained from diverse MIP tests reported in the literature (see Table I.5) are much smaller than the capillary porosity size range ( $> 0.2 \mu\text{m}$ ). This means that the capillary pores, that are mostly inaccessible to mercury injected at low pressure, should not percolate through the paste. Conversely, it is possible to find percolating paths of gel pores regardless of the volume fraction of total porosity in HCP, as already asserted previously.

On the basis of these indications given by MIP results, the present chapter proposes an approach focusing on the percolating gel pores located in the CSH. The strategy adopted for building a multi-scale homogenization model capable of reproducing strong variations of the diffusivities of HCP is thus the following:

- (i) Development of an appropriate description of HCP, where percolation occurs in the porous CSH in accordance with experimental results from MIP;
- (ii) Prediction of the effective diffusivity of CSH by a suited homogenization scheme;
- (iii) Validation of the multi-scale homogenization model on cement pastes with different porosities.

Once validated, the developed model is applied to predict the evolutions of the macroscopic diffusivities of degraded pastes subjected to a chemical degradation. In the previous chapter (Stora et al. 2006a), a simple estimate has been developed for modeling sudden variations of

diffusivities of heterogeneous materials with high contrasts. In the present one, a realistic three-scale homogenization model based on the latter estimate is proposed for HCP and mortars in order to provide accurate predictions of their effective diffusivities.

The chapter is organized as follows. The first section presents the multi-scale description of HCP based on the investigation of its microstructure proposed in Part I. The second one details the three-step homogenization process specifically developed for HCP and the estimations thus obtained are compared to experimental results obtained on diverse cement pastes. The approach is then applied to leached pastes in the third section by adopting a simplified scenario of the decalcification process. In the fourth one, the homogenization model is extended to mortars.

### 9.1 Multi-scale description of HCP microstructure

The experimental results collected in Part I about the critical pore diameter indicate that the highest scale at which porosity percolates through HCP is about tens of nanometres depending on the type of pastes. Benefiting from this precious information, a three-scale representation of HCP microstructure is now proposed for estimating the material diffusive properties focusing on the highest scale at which percolation of porosity occurs. This three-scale description is similar to the one exposed previously in linear elasticity. Indeed, the first two microstructural levels respecting the scales separation condition are identical to the ones depicted in Fig. II.22: the first level varying from 0.2  $\mu\text{m}$  to a few tens of  $\mu\text{m}$  corresponds to the scale of the non-diffusive hydration products and of capillary pores, while the second one ranging from a few tens of  $\mu\text{m}$  to about 100  $\mu\text{m}$  is typical of the sizes of hydrated cement grains. These two scales are respectively denoted as I and II.

The level I corresponding to the biggest scale of HCP is described first. This level depicted in Fig. II.22 represents the hydrated cement grains. During the hydration of cement particles, two diffusive layers presently defined as inner and outer layers form successively from cement grains surface. The inner layer is less porous than the outer one, since the first one results from higher confinement conditions and from poorer water accessibility during hydration process. Generally, an anhydrous part of the cement particles remains after hydration has stopped and constitutes an impermeable core surrounded by these two heterogeneous layers. As in linear elasticity, the GSCS is employed to model such a microstructure at the micrometer scale.

The level II also depicted in Fig. II.22 corresponds to the scale of the heterogeneities of the two layers. It is commonly accepted that two different types of porous CSH are associated with each layer. In the inner layer, the  $\text{CSH}^{\text{int}}$  behave as a matrix phase embedding non-diffusive inclusions of CH and AF. Similarly, the external layer has matrix-inclusion type morphology, where CH, AF and capillary pores play the role of inclusions enclosed in the  $\text{CSH}^{\text{ext}}$ . Furthermore, according to the critical pore diameters measured by MIP (Table I.5),

the capillary pores should not percolate and it is consequently appropriate to model them as isolated inclusions. The two layers can then be estimated by means of matrix-inclusion type schemes, such as the IDD one (Zheng and Du 2001).

Nevertheless, the macroscopic diffusivities of porous  $CSH^{int}$  and  $CSH^{ext}$  also have to be estimated by homogenization techniques for example, since they are difficult to gain experimentally and have not yet been measured to the authors' knowledge. In the case of elasticity, it is not necessary to estimate the effective properties of  $CSH^{int}$  and  $CSH^{ext}$ , since their macroscopic Young moduli have been measured by nanoindentation (Constantinides and Ulm 2004).

As already emphasized in Part I, CSH are generally described as an intricate mixture of a solid compound and gel porosity. In the present representation, both  $CSH^{int}$  and  $CSH^{ext}$  are supposed to be only composed of gel pores and of an impermeable solid phase. A detailed assessment of the connectivity of their gel pores constitutes a key point for estimating their effective diffusion properties. It appears in Table I.5, gathering some values of the critical pore diameter of CEM I cement pastes taken from the large data collection of MIP tests available in literature, that these diameters vary from a few tens of nm to less than one hundred of nms for CEM I pastes depending on the w/c ratio and on the sample preparation. It signifies that a significant amount of gel pores can percolate through the paste. The insulating solid phase and the gel pores composing the microstructure of  $CSH^{int}$  and  $CSH^{ext}$  are assumed in both cases to form together a MCSA, as depicted in Fig. III.16, in order to account for the fact that gel pores which size can go down to 1 nm are very likely to percolate. Using the latter scheme to estimate the effective diffusivities of the CSH, the stepwise homogenization process based on the three-scale description of HCP proposed above is presented in the following section and applied to predict the macroscopic diffusion coefficients of sound and leached HCP.

## 9.2 Three-step homogenization process

Cement pastes are assumed to be macroscopically isotropic so that the effective diffusion tensor  $\mathbf{D}_{HCP}^*$  of HCP is simplified into  $D_{HCP}^* \mathbf{1}$ , where  $D_{HCP}^*$  is a scalar diffusion coefficient. All the main phases constituting HCP microstructure, namely CH, AF,  $CSH^{int}$ ,  $CSH^{ext}$ , UC, capillary pores (CP) and gel pores (GP), are all supposed to be isotropic and their total volume fractions and diffusivities are respectively designated by  $c_i$  and  $D_i$ , with  $i \in \{CH, AF, CSH^{int}, CSH^{ext}, UC, CP, GP\}$ .

The first step of the process consists in estimating the effective diffusivities of  $CSH^{int}$  and  $CSH^{ext}$  represented by means of a MCSA (see Fig. III.16). The effective diffusivity of the solid phase denoted  $D_S$  is taken such as  $D_S/D_{GP} \rightarrow 0$ . The diffusion coefficients  $D_{CSH^{int}}^*$  and  $D_{CSH^{ext}}^*$  of the two types of CSH are then obtained from Eq. (III.58) that simplifies into:

$$D_i^* = \frac{-1 + (f + c_{GP}^i) + |1 - (f + c_{GP}^i)|}{1 + (2f - c_{GP}^i)}, \quad i \in \{CSH^{int}, CSH^{ext}\}, \quad (III.63)$$

where  $c_{GP}^{int}$  and  $c_{GP}^{ext}$  designate the relative volume fractions of the gel pores in  $CSH^{int}$  and  $CSH^{ext}$ , respectively.

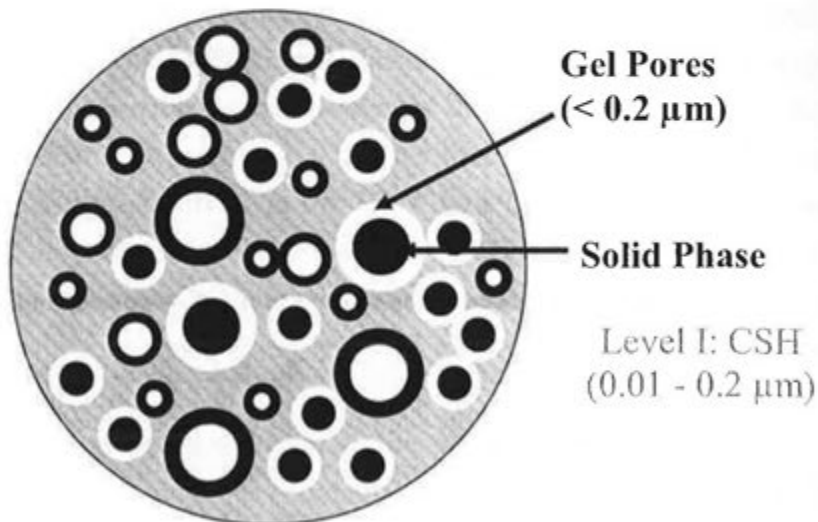


**Figure III.16:** Two-dimensional representation of the assemblages mixing two types of composite spheres used for representing the microstructures of  $CSH^{int}$  and  $CSH^{ext}$ .

At the second step, the inner and outer layers composing the assemblage of doubly-coated spheres have matrix-inclusion type morphology, as already mentioned in Part II. More precisely, the impermeable mineral phases CH, AF and/or the capillary pores play the role of inclusion enclosed in a matrix of  $CSH^{int}$  or  $CSH^{ext}$ . Each layer is supposed isotropic so that the diffusion coefficients of the inner and external layers are simply denoted by the scalars  $D_{inn}^*$  and  $D_{out}^*$ , respectively. In the micromechanical model developed to estimate the elastic properties of cement pastes by Zimmerman et al. (1986) and Stora et al. (2006b), spheroidal shapes are used to model certain particulate phases but it is presently preferred for simplicity to adopt spherical inclusions for representing all these phases. The effective diffusion coefficients  $D_{inn}^*$  and  $D_{out}^*$  of the inner and outer layers are estimated by the IDD scheme (Eq. III.28):

$$D_{inn}^* = 2D_{CSH^{int}}^* \left( \frac{1 - c_{CH}^{inn} - c_{AF}^{inn}}{2 + c_{CH}^{inn} + c_{AF}^{inn}} \right)$$

$$D_{out}^* = 2D_{CSH^{ext}}^* \left( \frac{1 - c_{CH}^{out} - c_{AF}^{out} + 2c_{CP}^{out} \beta_{CP}^{CSH^{ext}}}{2 + c_{CH}^{out} + c_{AF}^{out} - c_{CP}^{out} \beta_{CP}^{CSH^{ext}}} \right), \quad (III.64)$$

where the superscripts 'inn' and 'out' indicate that the volume fractions are relative to the total volume fraction of the inner and outer layers in the doubly coated spheres model

respectively. The IDD estimate was outlined to be valid provided that the most diffusive phase does not percolate but it can be applied for the outer layer, since the capillary pores should not percolate or only through a network of smaller gel pores, according to the MIP tests performed on sound pastes.

The third and last step of the homogenization process consists in computing the effective diffusivity of HCP represented by a doubly coated spheres model, which can be computed with Eq. (III.26). The anhydrous core being impermeable to diffusion, the effective diffusivity of HCP can thus be simply expressed as follows:

$$D_{HCP}^* = 2D_{out}^* \left( \frac{3}{2 + c_{UC} - 2c_{inn} \beta_{inn}^{out}} - 1 \right) \quad (III.65)$$

### 9.3 Estimations of the effective diffusivities of HCP

#### 9.3.1.1 Evaluation of the macroscopic diffusion coefficients of sound HCP

The three-step homogenization model described in the previous section is now applied to diverse CEM I standard pastes, which total porosity vary from about 20 % to 45 %. The basic input parameters required for the calculations of the effective diffusivity of these pastes are the diffusion coefficient and total volume fraction of every phase. The numerical values retained for the diffusivities of the gel and capillary pores are:  $D_{CP} = 2.2 \times 10^{-9} \text{ m}^2/\text{s}$  and  $D_{GP} = 2 \times 10^{-10} \text{ m}^2/\text{s}$  (Bary and Béjaoui 2006). More precisely,  $D_{CP}$  is obtained by simply assuming it equal to the diffusion coefficient  $D_{HTO}$  of tritiated water in bulk water at 23 °C and  $D_{GP}$  is supposed to be one order of magnitude lower than  $D_{CP}$  because of the constrictivity effects. The mineral compositions in terms of volume fractions, evaluated from the hydration model developed in Jennings (2000) and Tennis and Jennings (2000) of ordinary (CEM I) cement pastes with different w/c ratios, are taken from Béjaoui and Bary (2007). The volume fractions of total porosity obtained with the Jennings and Tennis model are in very good agreement with total water porosity measured on the same cement pastes (Bejaoui and Bary 2007). The volume fraction of capillary porosity is difficult to quantify precisely due to the fact that they are mostly inaccessible by mercury injected at low pressure. For the present work, the latter quantity is supposed to be equal to the value  $c_{CP} = 0.036$  measured with the help of BSE by Igarashi et al. (2004) in ordinary Portland cement pastes of w/c = 0.25 and w/c = 0.40 with the help of image analysis. Still, this approximation introduced because of a lack of experimental results may require further investigation. The total amount of gel pores are then calculated by subtracting the volume fractions of capillary pores to the total porosity ones. The repartition of the gel porosity between the two types of CSH is performed in the following manner: the CSH<sup>int</sup> that appear to keep an invariant morphology on the micrographies of Béjaoui et al. (2006) always contain about 20% of gel

porosity (Tennis and Jennings 2000), while the gel porosity comprised in the  $CSH^{ext}$  increases with the w/c ratio of the paste. The volume fractions of the mineral phases and of the different types of porosity present inside CEM I pastes are listed in Table III.2.

| w/c  | Anhydrous residuals | $CSH^{int}$<br>(percentage of gel pores) | $CSH^{ext}$<br>(percentage of gel pores) | Capillary porosity<br>(assumed from Igarashi et al. 2004) | CH + AF |
|------|---------------------|--|--|---|---------|
| 0.30 | 0.137               | 0.374 (20 %)                             | 0.155 (46.6 %)                           | 0.036   | 0.298   |
| 0.35 | 0.094               | 0.339 ("")                               | 0.229 (49.4 %)                           | 0.036   | 0.303   |
| 0.38 | 0.075               | 0.307 ("")                               | 0.281 (50.4 %)                           | 0.036   | 0.302   |
| 0.40 | 0.064               | 0.283 ("")                               | 0.317 (50.8 %)                           | 0.036   | 0.300   |
| 0.42 | 0.054               | 0.257 ("")                               | 0.361 (50.9 %)                           | 0.036   | 0.298   |
| 0.45 | 0.043               | 0.216 ("")                               | 0.411 (51.7 %)                           | 0.036   | 0.293   |
| 0.50 | 0.03                | 0.146 ("")                               | 0.504 (52.4 %)                           | 0.036   | 0.284   |
| 0.60 | 0.014               | 0.010 ("")                               | 0.684 (52.6 %)                           | 0.036   | 0.257   |
| 0.65 | 0.010               | 0.000                                    | 0.711 (54.4 %)                           | 0.036   | 0.244   |

**Table III.2: Composition in terms of volume fractions of hydrated CEM I pastes obtained by combining the mineral compositions given in Béjaoui and Bary (2007) computed with the hydration model of Jennings (2000) and Tennis and Jennings (2000) and the experimental measurements of capillary pores (Igarashi et al. 2004).**

Two additional parameters, namely the densities  $f^{int}$  and  $f^{ext}$  of composite spheres with low porosity in the MCSA representing the  $CSH^{int}$  and  $CSH^{ext}$  respectively, still need to be determined. Bary and Bejaoui (2006) assumed that only a very small volume fraction of 0.01 percolates through the  $CSH^{int}$ . Using this value, Eq. (III.56) yields  $f^{int} = 0.805$ . The effective diffusivity of  $CSH^{int}$  is then estimated from Eq. (III.63):  $D_{CSH^{int}}^* = 8.30 \times 10^{-13} \text{ m}^2/\text{s}$ . The geometric parameter of the MCSA representing  $CSH^{ext}$  is identified from an experimental value of the macroscopic diffusion coefficient of tritiated water in CEM I paste with w/c = 0.50 (Richet et al. 1997):  $D_{HCP}^*(w/c = 0.50) = 8.91 \times 10^{-12} \text{ m}^2/\text{s}$ . The value thus obtained for the density  $f$  of low-porosity composite spheres is  $f^{ext} = 0.546$ . Eq. (III.63) provides estimations of  $D_{CSH^{ext}}^*$  that vary from  $D_{CSH^{ext}}^*(w/c = 0.30) = 7.17 \times 10^{-11} \text{ m}^2/\text{s}$  to  $D_{CSH^{ext}}^*(w/c = 0.65) = 1.04 \times 10^{-10} \text{ m}^2/\text{s}$  depending on its gel porosity. It is noteworthy that the high-density  $CSH^{int}$  that are much less diffusive than  $CSH^{ext}$  could be approximated as a non-diffusive phase without strongly influencing the final results. However, it seems more consistent to model this porous phase as diffusive, since the  $CSH^{int}$  contain a significant

amount of gel pores. Then, Eqs. (III.64-65) are computed, the relative volume fractions of CH and AF distributed in the inner and outer layers being taken proportional to the relative percentage of  $\text{CSH}^{\text{int}}$  and  $\text{CSH}^{\text{ext}}$  in CSH.

The predictions, resulting from the three-step homogenization process, of the effective diffusivities of tritiated water in sound CEM I pastes with diverse w/c ratios are plotted on Fig. III.17 and are confronted to experimental results issued from Richet et al. (1997). It is recalled that a HCP becomes more porous as its w/c ratio increases. They are in quite good agreement with the values measured, since the mean relative error is about 16 %. It is outlined that the results can be notably improved by taking  $f$  as a linear function instead of a constant. Furthermore, using the identical three-step homogenization model, the predictions obtained by employing MT with the gel pores embedding solid spherical inclusions instead of the MCSA for the effective diffusivities of the  $\text{CSH}^{\text{ext}}$  are provided in Fig. III.17 and highly overestimate the experimental results thus confirming the inadequacy of this matrix-inclusion type scheme in the particular mentioned configuration for predicting their effective diffusivities.

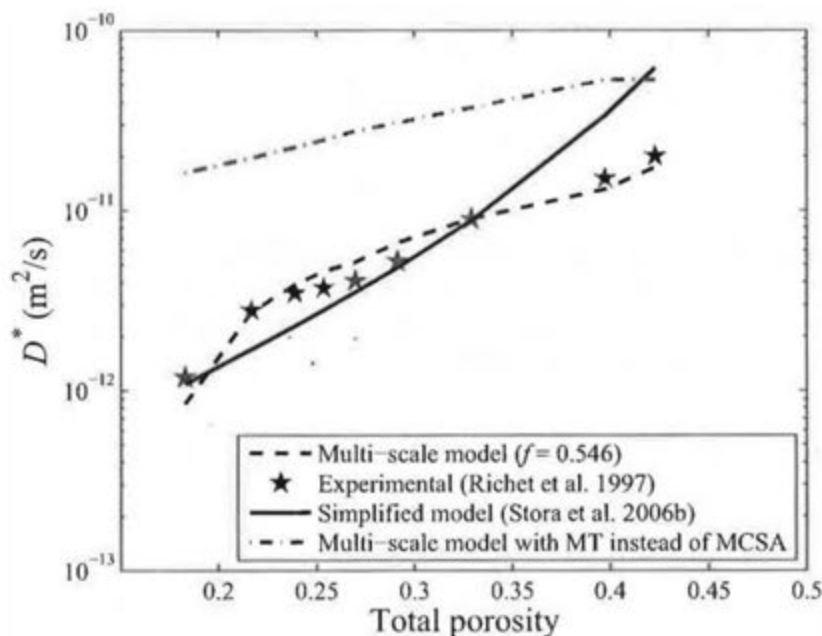


**Figure III.17 (semi-logarithmic scale): Evolutions of the diffusivities of CEM I pastes measured experimentally (Richet et al. 1997) and predicted respectively by the multi-scale model with  $f = 0.546$  and by the simplified model in Stora et al. (2006b), as a function of their total porosity.**

For the sake of comparison, the results obtained with the two-step representation proposed in Stora et al. (2006b) and briefly recalled below are also displayed in Fig. III.17. At the first step, by taking all the little or non diffusive phases as spherical inclusions embedded in a solid diffusive  $\text{CSH}^{\text{ext}}$  matrix, we obtain a two-phase material composed of a low diffusive

homogenized solid phase, which diffusivity results from the first step, and of porosity (Fig. III.18). At the second step, this two-phase material representing HCP is modelled as a MCSA. According to Fig. III.17, the three-step homogenization model leads to a significant improvement compared to this two-scale approach, since it proposes a more precise description of HCP microstructure and of its porosity.

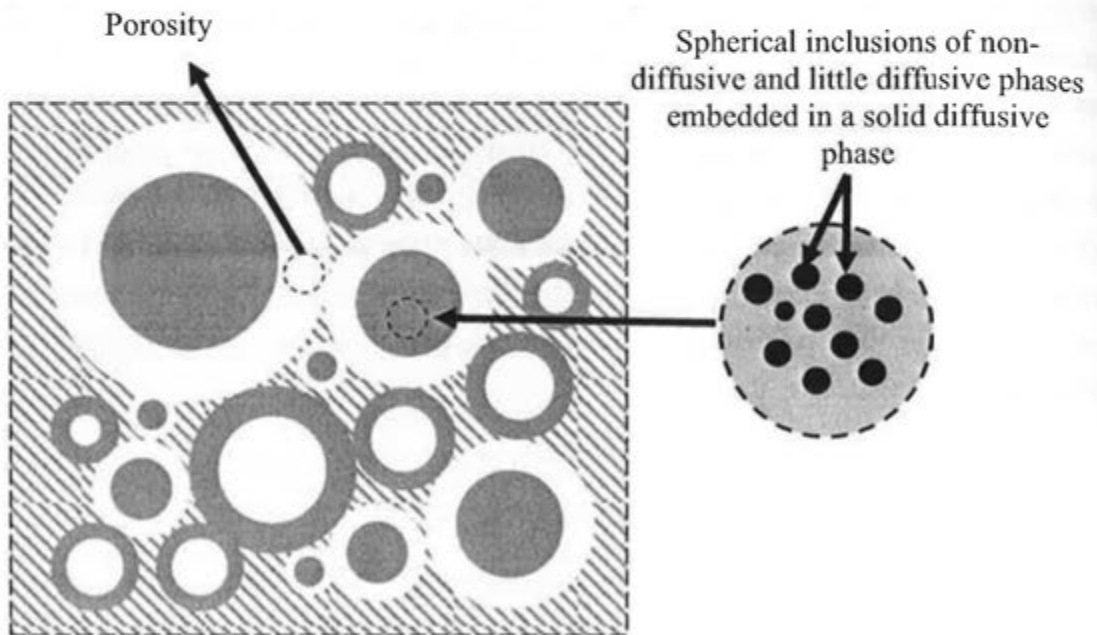


**Figure III.18:** Two-dimensional representation of HCP using two scales: at the first scale, non-diffusive and little diffusive phases are modeled as spherical inclusions embedded in a solid diffusive phase; at the second scale, the homogenized solid phase and the porous one are modeled as a MCSA (Stora et al. 2006b).

The present multi-scale representation of the pore structure is still very simplified in comparison with the real pore network. Nevertheless, it reproduces some of its important characteristics. First, the proposed description represents in a simple manner the percolating gel pores, which is consistent with the critical pore diameters measured by MIP. Furthermore, the gel porosity of  $\text{CSH}^{\text{ext}}$  in the present model augments with the w/c ratio, while  $f$  is kept constant. Under these conditions, it can be seen from Eq. (III.56) that the quantity of percolating gel pores also increases in the MCSA. This is in good agreement with the micrographies of Béjaoui et al. (2006), in which the gel porosity of  $\text{CSH}^{\text{ext}}$  appears to be of greater size and to be more connected in high w/c pastes than in low w/c ones (Fig I.2).

The present homogenization model is quite similar to the one proposed by Bary and Béjaoui (2006). The main difference lies in the modeling of the external coating, since in the present representation gel pores percolate instead of capillary ones. It should be emphasized that most of the homogenization methods existing in literature focus on the percolation of capillary

porosity and require the knowledge of its percolation threshold. But as outlined by Béjaoui and Bary (2007), no consensus exists concerning its actual value because the definition of capillary porosity and the method for computing its percolation threshold vary from one author to another. The percolation thresholds of capillary pores in HCP are often estimated with the help of advanced cement simulation tools (Garboczi and Bentz 2001; Ye 2005). Nevertheless, the diverse values proposed by these simulation tools, globally ranging from 0.03 to 0.2, vary significantly from one author to the other (Garboczi and Bentz 2001; Ye 2005) and some of these estimations appear to be in contradiction with the critical pore thresholds measured by MIP. The present model proposes an alternative approach rather focusing on the percolating gel pores located in CSH. In the present description, the capillary pores only percolate through a network of smaller pores and the sudden variations of HCP diffusivity are caused by the change in connectivity of gel porosity.

### 9.3.2 Evaluation of the macroscopic diffusion coefficients of leached HCP

The model is now applied to the case of a hydrated CEM I paste subjected to leaching by pure water. The degradation scenario retained here is exactly the same as in Bary and Béjaoui (2006). The reader should refer to this paper for more details. The decalcification is supposed to be, in term of the volume of solid phase replaced by porosity, linearly related to the decreasing calcium concentration in the pore solution  $C_a$ : CH totally dissolves before any other hydration products between  $C_a = 21.54$  and  $C_a = 20.31$  mol/m<sup>3</sup>, then half of AF dissolve between  $C_a = 20.31$  and  $C_a = 3.08$  mol/m<sup>3</sup> and the CSH are progressively degraded between  $C_a = 20.31$  and  $C_a = 1.09$  mol/m<sup>3</sup>. More precisely, only 5 % of the CSH are dissolved and replaced by additional capillary pores in the most decalcified state but their internal porosity significantly increases during degradation (Gallé et al. 2004; Heukamp 2002). Their gel porosity is quantified by subtracting the sum of the initial capillary pores and the additional ones, issued from the dissolution of hydration products, from the measure of total porosity by MIP. This method is applied to a CEM I paste with w/c = 0.45 and the values of porosity comprised in the CSH before and after leaching indicate that a total volume fraction of supplementary percolating gel porosity of 0.04 appears in the CSH during degradation. The effective diffusivities of CSH<sup>int</sup> and CSH<sup>ext</sup>, which are updated from Eq. (III.63) and from these higher values of gel porosity, significantly increase when decalcification occurs.

An important issue for the application of the present model to the case of degraded cement pastes is the possible formation of percolating paths composed of capillary pores due to the dissolution of hydration products. Nevertheless, the critical pore diameter measured by MIP for leached pastes (Gallé et al. 2004) remains inferior to the typical sizes of dissolved hydration products (CH, AF) situated at the micrometer scale, though it increases by an order of magnitude (Table I.4). This result suggests that the additional capillary pores formed during the leaching process do not percolate or only through smaller pores. It is consequently

sound to use a matrix-inclusion type scheme for estimating the effective properties of the layers of the doubly coated spheres during leaching. The effective diffusion coefficients thus obtained versus calcium concentration for CEM I pastes with different  $w/c$  ratios are shown on Figure III.19. Two principal domains are observed on the curves displayed on this figure. Looking at these curves from the right to the left, the macroscopic diffusivities of the pastes appear to first increase suddenly. This augmentation is caused by the dissolution of all the portlandite, while the other hydration products (AF, CSH) are still intact. These solid phases then progressively dissolve as the calcium concentration decreases and the effective diffusivities continue to augment but less rapidly. At the end of the leaching process, the increase of the effective diffusion coefficient is about one order of magnitude for the totally leached cement pastes with low  $w/c$  ratio (0.30 - 0.40) and a factor of 6 to 9 for the ones with higher  $w/c$ . Both initial and final values obtained for  $w/c = 0.40$  are consistent with the ones reported by Planel (2002) for a similar material.

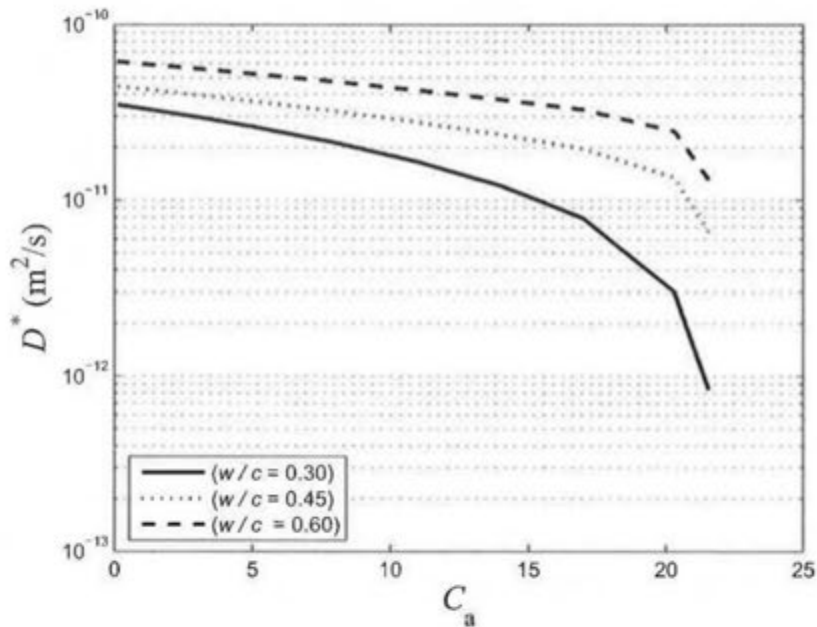


**Figure III.19: Evolutions of the effective diffusion coefficients of CEM I pastes with different  $w/c$  ratios as a function of calcium concentration in pore solution (Stora et al. 2006b).**

The present predictions are also close to the results of Bary and Béjaoui (2006) obtained with a comparable assemblage, where the same degradation scenario was adopted. But the advantage of the present model compared to the previous one is that the MCSA allows for representing in a more simple and convenient manner the percolating porosity than the SC scheme, that can be realized only by a complex microgeometry (Milton 1985).

#### 9.4 Estimations of the macroscopic diffusive properties of mortars

Many models already exist to deal with such applications (e.g. Caré and Hervé 2004; Garboczi and Bentz 1997). It is worth saying that the effective diffusivity of a mortar is approximatively of the same order as the diffusivity of its cement matrix. Some authors (Nguyen 2005) argue that it is due to the fact that the presence of aggregates in a hydrate cement paste matrix probably has two opposite effects on the transport properties that compensate each other. On the one hand, it increases the tortuosity of the matrix and reduces the total space available to diffusion and, on the other hand, the presence of porous ITZ enhances the diffusion process.

The homogenization model presented below is based on a few assumptions. First, the macroscopic diffusion coefficient of the cement matrix of mortar will be supposed equal to the one of the bulk cement paste. In addition, the ITZ is supposed to be a homogeneous interphase, even though it would be more realistic to model it as an inhomogeneous one (Lutz and Zimmerman 2005). A doubly coated-spheres model is adopted to represent mortars (Fig. III.20). Precisely, the core, the intermediary layer and the external one are respectively occupied by sand particles, ITZ and HCP, which diffusive properties result from the previous step. The sand aggregates are non-diffusive and, as in linear elasticity, the diffusivity of ITZ is computed by means of a simplified model (Caré and Hervé 2004). The macroscopic diffusivity of mortar can then be estimated by the GSCS or modified DIM (Eq. (III.25)). This homogenization approach for computing the diffusivity of mortars will be applied and validated in Part V, which proposes simulations of the chemical degradation of mortar samples.

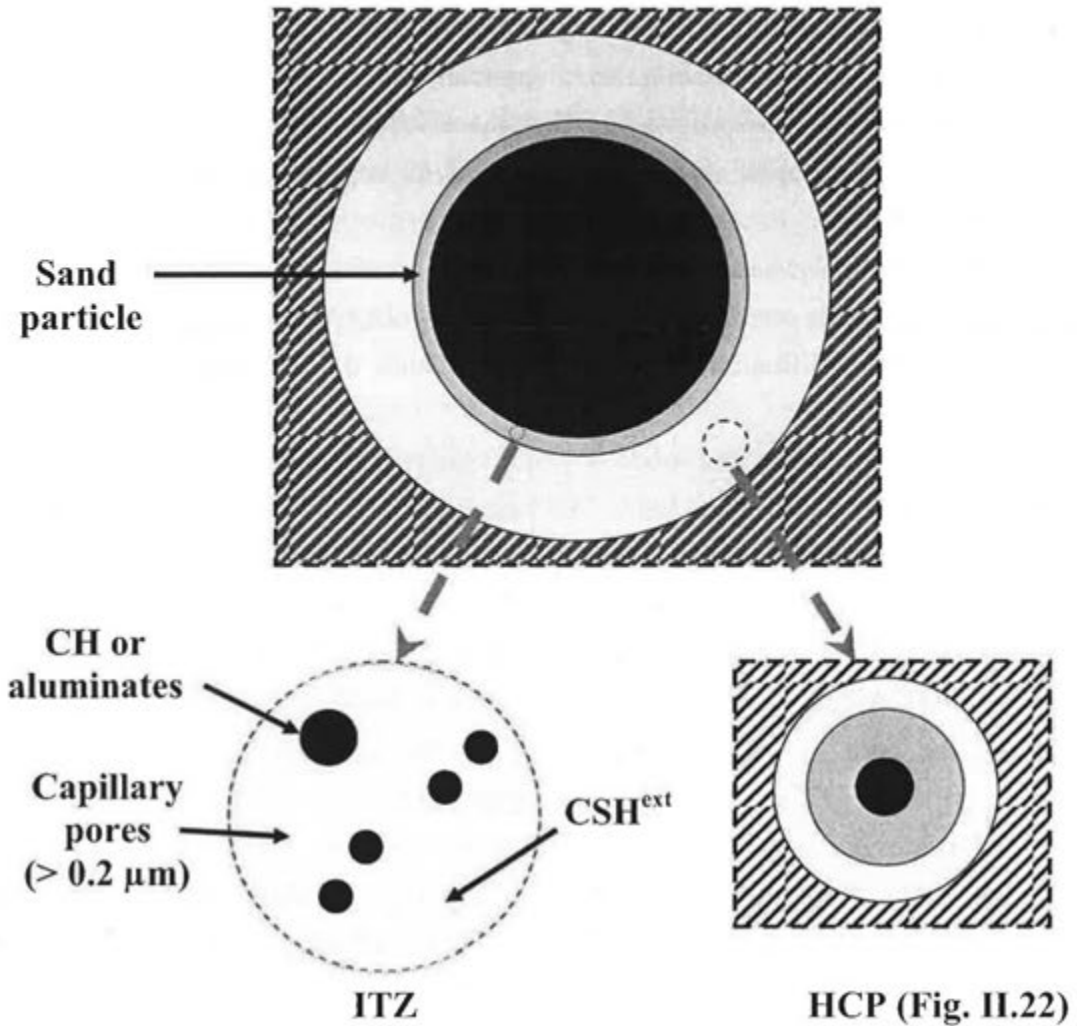


*Figure III.20: Schematic of the representation used for the estimation of the effective diffusive and elastic properties of mortars.*

### CONCLUSIONS OF PART III

The contributions of this Part are both theoretical and practical. The estimations of the macroscopic transport properties of porous media such as concrete materials represent a challenging issue for homogenization theories because of the difficulty of reproducing the highly non linear changes of these properties observed experimentally (e.g. Oh and Jang 2004). The brief review performed reveals that only a small group of commonly used EMTs, like GEM or Kirkpatrick models, exhibits the capacity to model the sudden variation of the effective diffusion coefficient of porous media due to a critical microstructure change. It is in particular pointed out that commonly used matrix-inclusion type EMTs are to be excluded for predicting such rapid changes of diffusivity, since they are inadequate for modelling percolating pores.

A novel estimate associated to a MCSA apt to account for pore connectivity has thus been developed. By construction, this MCSA scheme automatically respects the HS rigorous bounds. Another salient feature of this estimate is its capacity to model connected phases forming tortuous paths in a geometrically simple and clear way, which is essential for the prediction of effective diffusion properties of porous media. In this sense, as an estimation model, it provides a real improvement on HS bounds and other EMTs and it is expected to be applicable for a large class of porous materials, such as cementitious ones, granular media and rocks.

From a practical standpoint, a three-step homogenization model, where the two types of CSH containing connected gel porosity are modelled as a MCSA, is specifically developed for the prediction of the macroscopic diffusivities of HCP and validated by confronting with experimental measurements performed on CEM I pastes. But the success of models developed for engineering applications also depends on their simplicity of use and on the number of parameters it involves. The present model well complies with these criteria. Apart from the usual intrinsic parameters, such as phase volume fractions and diffusivities, it depends only on two geometrical parameters that allow for characterizing the connectivity of gel pores in the CSH<sup>int</sup> and in the CSH<sup>ext</sup>. The model distinguishes itself from already existing approaches in the sense that it does not require the knowledge of the percolation threshold of capillary porosity. The multi-scale homogenization model is furthermore applied to cement pastes submitted to leaching. The significant increase of cement paste diffusivities predicted highlights the highly detrimental influence of the dissolution of hydration products.

### Appendix III.A: Derivation of the inhomogeneous Eshelby tensor for a spherical isotropic inclusion

We are presently interested in solving the boundary value problem depicted below (Fig. III.A.1) so as to derive an analytic expression for the inhomogeneous Eshelby tensor of a spherical isotropic inclusion. All phases are supposed isotropic so that it is possible formulate the reasoning with scalars instead of second-order tensors.

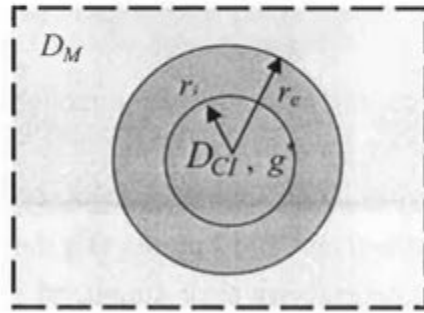


*Figure III.A.1: Schematic of a spherical isotropic inclusion with a homogeneous interphase enclosed in an infinite matrix.*

The general solution for this problem can be expressed in the following way:

$$\begin{cases} c_I = B_1 r + \frac{B_2}{r^2}, \\ J_I = -D_{Cl} \left( B_1 - \frac{2B_2}{r^3} - g^* \right), \end{cases} \quad (\text{III.A1})$$

$$\begin{cases} c_{Cl} = B_3 r + \frac{B_4}{r^2}, \\ J_{Cl} = -D_{Cl} \left( B_3 - \frac{2B_4}{r^3} \right), \end{cases} \quad (\text{III.A2})$$

$$\begin{cases} c_M = B_5 r + \frac{B_6}{r^2}, \\ J_M = -D_M \left( B_5 - \frac{2B_6}{r^3} \right), \end{cases} \quad (\text{III.A3})$$

where  $B_i (i \in [1,6])$  are constants that can be determined from the interfaces and boundary conditions. It is straightforward that  $B_2 = B_5 = 0$ . It furthermore comes from the definition of the inhomogeneous Eshelby tensor in Eq. (III.13) that  $B_1 \mathbf{1} = \tilde{\mathcal{A}}_I \cdot g^* \mathbf{1}$  (Duan et al. 2006). The interfaces conditions at  $r = r_i$  and  $r = r_e$  respectively read:

$$\begin{cases} (\tilde{\mathcal{A}}_I^M - 1) g^* = B_3 r_i + \frac{B_4}{r_i^2}, \\ -D_{Cl} (\tilde{\mathcal{A}}_I^M - 1) g^* = -D_{Cl} \left( B_3 - \frac{2B_4}{r_i^3} \right), \end{cases} \quad (\text{III.A4})$$

$$\begin{cases} B_3 r_e + \frac{B_4}{r_e^2} = \frac{B_6}{r_e^2}, \\ -D_{Cl} \left( B_3 - \frac{2B_4}{r_e^3} \right) = D_M \frac{2B_6}{r_e^3}, \end{cases} \quad (\text{III.A5})$$

From the interface conditions written in Eq. (III.A4), it comes that:

$$B_3 = \left( \tilde{A}_i^M - \frac{1}{3} \right) g^* \quad \text{and} \quad B_4 = \frac{g^* r_i^3}{3}. \quad (\text{III.A6})$$

The unknown constant  $B_6$  is then gained from Eqs. (III.A5-A6):

$$B_6 = \left[ \left( \tilde{A}_i - \frac{1}{3} \right) r_e^3 + \frac{1}{3} r_i^3 \right] g^*. \quad (\text{III.A7})$$

By injecting the expressions of Eqs. (III.A6-A7) into (III.A5), the following expression is finally obtained for  $\tilde{A}_i^M$ :

$$\tilde{A}_i^M = \left( \frac{1}{3} + 2\beta_i^M \rho^3 \right). \quad (\text{III.A8})$$

**Appendix III.B: Derivation of Eq. (III.61)**

This Appendix details the calculations required to obtain Eq. (III.61). To begin with, Eq. (III.54) is rewritten as:

$$\beta_*^1 = \beta_2^1 c_2^+, \quad \beta_*^2 = \beta_1^2 (1 - c_2^-). \quad (\text{III.B1})$$

Using Eq. (III.55),  $\beta_*^1$  can also be expressed as a function of  $c_2^-$ :

$$\beta_*^1 = \beta_2^1 \frac{c_2 - f c_2^-}{1 - f}. \quad (\text{III.B2})$$

By recalling that the connected volume fraction  $c_2^{out}$  of phase 2 verifies  $c_2^{out} = f c_2^-$ , Eqs. (III.B1-B2) become:

$$\beta_*^1 = \beta_2^1 \frac{c_2 - c_2^{out}}{1 - f}, \quad \beta_*^2 = \beta_1^2 \left( 1 - \frac{c_2^{out}}{f} \right). \quad (\text{III.B3})$$

Substituting the expressions (III.B3) of  $\beta_*^1$  and  $\beta_*^2$  in Eq. (III.56) yields Eq. (III.61).

### Appendix III.C: Link between $f$ and the formation factors

This Appendix aims at establishing the links between the geometric parameter  $f$  of MCSA and the formation factors defined in Eq. (III.45). For this purpose, the quadratic equation (III.57) is first divided by  $D_2^2$ :

$$a \left( \frac{D^*}{D_2} \right)^2 + \frac{bD^*}{D_2^2} + \frac{c}{D_2^2} = 0. \quad (\text{III.C1})$$

We next consider the limit of (III.C1) when  $D_2 \rightarrow \infty$ , in order to make the formation factor  $F_2$  appear. Noticing that  $\beta_2^1$  tends to one when  $D_2 \rightarrow \infty$ , Eq. (III.C1) simplifies into:

$$\frac{1}{F_2} \left[ (1+2f-c_2) \frac{1}{F_2} + 2(1-f-c_2) \right] = 0. \quad (\text{III.C2})$$

Two cases are to be treated. If  $F_2 \rightarrow \infty$  (i.e.  $D^*/D_2 \rightarrow 0$ ), no relation can be established between  $f$  and  $F_2$ . This case corresponds to the situation in which the phase 2 does not percolate. Consequently the lower HS bound, also obtained by taking  $f = 0$  in the MCSA estimate, should be applied. If  $F_2$  is finite, Eq. (III.C2) yields:

$$f = c_1 \left( \frac{2F_2 + 1}{2F_2 - 2} \right). \quad (\text{III.C3})$$

Analogously, it is possible to express  $f$  as a function of  $F_1$  by inverting the indexes 1 and 2 and substituting  $f$  by  $(1-f)$ :

$$f = 1 - c_2 \left( \frac{2F_1 + 1}{2F_1 - 2} \right). \quad (\text{III.C4})$$

Conversely, the formations factors can be expressed in terms of  $f$ :

$$F_2 = \frac{2f + c_1}{2f - 2c_1} \quad \text{and} \quad F_1 = \frac{2(1-f) + c_2}{2(1-f) - 2c_2}. \quad (\text{III.C5})$$

## Part IV

### MODELLING OF DAMAGE OF CEMENTITIOUS MATERIALS

The damage of heterogeneous materials such as concrete is a complex nonlinear dissipative phenomenon, which has been the subject of extensive researches (e.g. Krajcinovic 1996). Damage in cement-based materials is generally qualified as quasi-brittle and is caused by the nucleation, growth and coalescence of microcracks. These cracks grow preferentially in certain directions depending on the loads applied thus inducing an anisotropy of the damaged material. Many models, which are more or less phenomenological, have been proposed for treating damage in concrete (e.g. Mazars 1984; 1985). But some phenomena such as the unilateral effects of the opening and closing of microcracks represent challenging issues for researchers (e.g. Cormery and Welemane 2002). Aiming at proposing a damage model that can be incorporated into a FE code, the present Part adopts a hybrid approach using homogenization techniques to determine the number and nature of damage variables and the free energy for a given damage state but also revisits the main ideas underlying the most popular models in concrete (e.g. Mazars 1984; 1985).

The framework of continuum damage mechanics presently employed to develop a physically sound model is usually associated with the thermodynamics of irreversible processes with internal variables (e.g. Nguyen 2000). As noticed by He and Curnier (1995), a damage model within this framework is generally composed of three parts. First, the damage variables are adequately chosen to characterize as accurately as possible the damaged state of the concerned material. Second, the material behaviour is formulated for a given damage state. For this purpose, homogenization techniques are employed to remedy the lack of uniformity and rigor in formulating the free energy function. The evolution laws of the damage variables for a loading history are then established. The damage model presently developed does not claim to tackle complicated issues of damage, such as unilateral effects or complex loading. In the manuscript, the model is only applied in tension but could be extended to the case of compression with the aid of the work of Deudé et al. (2002).

The present work first assesses the capacity of prominent homogenization schemes to predict the mechanical effective properties for a given damage state. Then different evolution laws for the damage variables are discussed and a strain-based criterion is established. The damage model developed is then applied in uniaxial and biaxial tension tests. It is outlined that we aim at building a relatively simple model based on the ensuing simplifying assumptions. The undamaged material is considered to be isotropic. The assumptions of small strains and of isothermal conditions are adopted. Damage in cement-based materials being quasi-brittle,

plasticity may be neglected for simplicity at least in tension. In addition, the unilateral effects due to the opening or closure of microcracks and the frictional effects are neglected.

## 10 DEFINITION OF STATE VARIABLES

The state variables are defined as the group of variables which current values characterize the physical state of a system at equilibrium. Only mechanical state variables are presently considered. The state variables are constituted of the macroscopic strain  $\bar{\epsilon}$  associated with the stress  $\bar{\sigma}$  and of parameters chosen to characterize the damaged state of the material. Two main categories of damage models based on different definitions of the damage parameters may be distinguished: the phenomenological models (e.g. Ladevèze 1983) focusing on the damage effects at the macroscopic level and micromechanical approaches (e.g. Dormieux et al. 2006; Pensée and Kondo 2003) linking the macro-response of the material to microscopic parameters characterizing its microdefects (Budiansky and O'Connell 1976).

Many anisotropic damage models use a second-order damage tensor (e.g. Ladevèze 1983), although such choice may lead to strong shortcomings (Krajcinovic 1996). Among them, Cormery and Welemane (2002) evidenced that the spectral decompositions of these second-order damage tensors may lead to certain inconsistencies, for example the non uniqueness of the thermodynamic potential. Micromechanical approaches (e.g. Kachanov 1992) are more recent than phenomenological models but may reveal very difficult to implement in a FE code.

The basic idea used by the micromechanical models for dealing with damage consists in representing the microcracks as degenerated ellipsoidal voids. By degenerated it is meant that the lengths of one or two of its axis are reduced to zero. In the present part, only penny-shaped spheroids are considered. Damage variables that characterize material microdefects are the crack density parameters  $d_i$  characterizing a family  $i$  of cracks having the same normal vector  $e_i$  associated with the driving forces  $Y_{di}$  defined in the ensuing. More precisely, these crack density parameters introduced by Budiansky and O'Connell (1976) are defined as  $d_i = N_i a_i^3$ , where  $N_i$  is the volume density of the family  $i$  of microcracks and where  $a_i$  is the maximum axis of the degenerated spheroid representing the microcracks of type  $i$ . The damaged material is then viewed as a homogeneous matrix of cement-based material in which the microcracks are distributed. The idea of modelling these cracks as penny-shaped spheroids permits to account in an intuitive manner for the anisotropy caused by loads. In the ensuing, the presently defined crack density parameters  $d_i$  are chosen as damage parameters. The total number  $n_c$  of families of cracks necessary to correctly model the damaged material is discussed later.

## 11 MICROMECHANICAL ESTIMATIONS OF THE DAMAGED MATERIAL BEHAVIOR

In the case of a strain formulation, the Helmholtz free energy practically corresponding to the energy stocked by elastic strains is written as:

$$\Phi = \frac{1}{2} \bar{\boldsymbol{\varepsilon}} : \mathbb{C}^*(d_i) : \bar{\boldsymbol{\varepsilon}}, \quad (\text{IV.1})$$

where the effective damaged stiffness tensor  $\mathbb{C}^*$  depends on the homogenization scheme adopted. The scope of the next part consists in finding a relevant one providing accurate estimations for the effective damaged stiffness tensor  $\mathbb{C}^*$ . Different micromechanical schemes are presently reviewed to find which ones provide the best estimations. However, the present review is only focused on explicit schemes, that can easily be implemented in a FE code and do not require any numerical resolution to obtain the effective damaged stiffness tensor  $\mathbb{C}^*$ .

### 11.1 General presentation

A brief review of the micromechanical schemes, that cannot pretend in any case as being exhaustive, is presented, starting obviously from the rudimentary dilute model (e.g. Eshelby 1957) to more recent ones. To simplify the ensuing calculations, the following two tensors, which are both linked to the Eshelby tensor  $\Sigma_i^M$  of the penny-shaped inclusion representing the type  $i$  family of cracks embedded in the sound material, are introduced:

$$\mathbb{T}_i = \lim_{r_i \rightarrow 0} r_i \left( \mathbb{I} - \Sigma_i^M \right)^{-1}, \quad \mathbb{H}_i^{dil} = \frac{4}{3} \pi d_i \mathbb{T}_i : \mathbb{S}_M, \quad (\text{IV.2})$$

where  $r_i$  is the aspect ratio of the penny-shaped inclusion representing the type  $i$  family of cracks and  $\mathbb{H}_i^{dil}$  defined in Eq. (II.34) is called the dilute compliance increment tensor of type  $i$  microcracks. It is recalled that  $\mathbb{I}$  and  $\mathbb{S}_M$  designate the fourth order identity tensor and the compliance tensor of the undamaged material behaving as a matrix entrapping the penny-shaped crack, respectively. The tensor  $\mathbb{H}_i^{dil}$  has got a simple expression, since the only non vanishing terms are (Mura 1987):

$$H_{iii}^{dil} = \frac{16(1-\nu^2)}{3E_M} d_i; \quad H_{jjj}^{dil} = \frac{8(1-\nu^2)}{3(2-\nu)E_M} d_i \quad (j \neq i), \quad (\text{IV.3})$$

where  $E_M$  and  $\nu$  respectively designate the Young modulus and the Poisson ratio of the undamaged material. Using the tensorial operators, the tensor  $\mathbb{H}_i^{dil}$  can also be written as:

$$\mathbb{H}_i^{dil} = \sum_i \frac{16(1-\nu^2)}{3E_M(2-\nu)} d_i \left[ \mathbf{1} \otimes \underline{\underline{\Delta}}_i + \underline{\underline{\Delta}}_i \otimes \mathbf{1} - \nu \underline{\underline{\Delta}}_i \otimes \underline{\underline{\Delta}}_i \right], \quad (\text{IV.4})$$

where  $\mathbf{\Lambda}_i = \mathbf{e}_i \otimes \mathbf{e}_i$ , and where it is recalled that  $\mathbf{1}$  is the second order identity tensor. It is noteworthy that, if all the cracks are aligned, the tensor  $\mathbb{H}_i^{dil}$  is then singular.

The estimation for the effective stiffness tensor in Eq. (IV.1) by the dilute model computed with homogeneous displacements applied at infinity (e.g. Eshelby 1957) varies linearly with the crack density parameters:

$$\mathbf{C}_{dil}^* = \mathbf{C}_M : (\mathbf{1} - p_i \mathbf{T}_i), \quad \text{with} \quad p_i = \frac{4}{3} \pi d_i. \quad (\text{IV.5})$$

It is however well-known that the dilute model does not account for the interactions between microcracks. The MT model capable of accounting for interactions in a certain manner between the cracks and the matrix, gives the following expression of the damaged effective stiffness tensor (e.g. Benveniste 1987):

$$\mathbf{C}_{MT}^* = (\mathbf{S}_M + \mathbb{H}^{MT})^{-1} \quad \text{with} \quad \mathbb{H}^{MT} = \mathbb{H}^{dil} : \left( \mathbf{1} - \sum_i \mathbf{\Omega}_{Di}^M : \mathbb{H}_i^{dil} \right)^{-1}, \quad (\text{IV.6})$$

where  $\mathbb{H}^{dil}$  defined in Eq. (II.33) is the dilute compliance increment tensor of the damaged body. As already mentioned in Part II, different double-inclusion schemes providing quite similar predictions have been developed to account for the cracks spatial distribution (e.g. Küster-Toksöz 1974; Hori and Nemat-Nasser 1993; Ponte-Castaneda Willis 1995; Shen and Yi 2001; Zheng and Du 2001). In the case of an isotropic distribution of cracks, identical estimations can thus be obtained from the IDD model (Zheng and Du 2001), PCW one (Ponte-Castaneda Willis 1995) or DIM (e.g. Hori and Nemat-Nasser 1993):

$$\mathbf{C}_{PCW}^* = \mathbf{C}_{IDD}^* = (\mathbf{S}_M + \mathbb{H}^{IDD})^{-1} \quad \text{with} \quad \mathbb{H}^{IDD} = \left( \mathbf{1} - \sum_i \mathbb{H}_i^{dil} : \mathbf{\Omega}_{Di}^M \right)^{-1} : \mathbb{H}^{dil}, \quad (\text{IV.7})$$

where  $\mathbf{\Omega}_{Di}^M = \mathbf{C}_M : (\mathbf{1} - \mathbf{\Sigma}_{Di}^M)$  denotes the eigenstiffness tensor of the double-inclusions surrounding the family  $i$  of cracks. These double-inclusions practically characterize the spatial distribution of cracks. Recalling that spherical double-inclusions are generally adopted for isotropically distributed cracks, the non-overlapping condition is respected provided that crack densities  $d_i$  remain inferior to  $3/4\pi$  (see Appendix II.B). For higher crack densities, the full-range IDD proposed by Zheng and Du (2001) employs spheroidal double-inclusions to fulfill this non-overlapping condition but leads to complex computations. It is noteworthy that, even with spherical double-inclusions, a simple analytical expression for  $\mathbb{H}^{IDD}$  such as the one in Eq. (IV.4) for the dilute scheme is difficult to reach for materials with at least two families of cracks having different orientations. The matrix representation of  $\mathbb{H}^{IDD}$  then comprises extra-diagonal terms and as a result the expression of  $\mathbf{C}_{IDD}^*$  may be tedious for elastic bodies weakened by many families of cracks. A slightly simplified version of the IDD

model is proposed to circumvent this difficulty. By expanding the expression of  $\mathbb{H}^{IDD}$  in the previous equation, the following relation is obtained:

$$\hat{\mathbb{C}}_{IDD}^* = (\mathbb{S}_M + \hat{\mathbb{H}}^{IDD})^{-1} \text{ with } \hat{\mathbb{H}}^{IDD} = \sum_i \left( \mathbb{I} + \sum_i \mathbb{H}_i^{dil} : \Omega_{Di}^M \right) : \mathbb{H}_i^{dil}. \quad (IV.8)$$

The matrix representation of the compliance increment tensor  $\hat{\mathbb{H}}^{IDD}$  estimated by this simplified IDD model does not contain any extra-diagonal term and simply reads in the case of spherical double-inclusions:

$$\hat{\mathbb{H}}^{IDD} = \sum_i \frac{1}{E_M} \left[ \begin{array}{l} \frac{d_i}{d_c^{dil}} \left( 1 + \frac{d_i}{d_c} \right) \Delta_i \otimes \Delta_i + \\ \frac{d_i}{d_c^{dil} (2-\nu)^2} \left( (2-\nu) + \frac{E_M d_i}{\Omega_{DG} d_c^{dil}} \right) \left( \mathbb{1} \otimes \Delta_i + \Delta_i \otimes \mathbb{1} - 2\Delta_i \otimes \Delta_i \right) \end{array} \right]. \quad (IV.9)$$

As the MT and original IDD model, this simplified IDD scheme can be considered as an improved dilute model (see Fig. II.5), where each family of cracks modeled as a single penny-shaped inclusion is immersed in the unbounded matrix material subjected to a modified far-field stress.

It is worth noting that implicit schemes such as the SC (Budiansky and O'Connell 1976), the GSCS (Huang et al. 1994) and the differential scheme (Hashin 1988) may also be applied but the expressions of these estimates can become very complex even if only one family of cracks is involved. However, with the explicit schemes presented above, the analytical expressions of the effective damaged stiffness tensor may also be quite tedious when many families of cracks are involved. Therefore, three particular cases are treated in the next subsection to draw a comparison between the different explicit schemes: aligned, isotropic and orthotropic.

## 11.2 Comparison of the homogenization schemes in simple cases

### 11.2.1 Comparison for a material with aligned cracks

All the cracks are assumed to be aligned with their normal vectors parallel to the same axis  $\mathbf{e}_1$ . The subscripts can thus be disregarded, since only one family of parallel cracks is involved. The effective damaged material is transversely isotropic, since the undamaged one is assumed to be isotropic. In such case, simple analytical expressions are available for most of the studied schemes (Nemat-Nasser and Hori 1993). A general expression including IDD and MT schemes as particular cases is proposed below.

### 11.2.1.1 A general expression for explicit schemes

By taking benefits of similarities between the compliance increment tensors of MT and IDD schemes written in Eqs. (IV.4) and (IV.9), a general expression denoted  $\mathbb{H}$  for the latter tensor has been found to cast IDD and MT schemes in an identical framework:

$$\mathbb{H} = \frac{1}{E_M} \left[ \alpha \Delta \otimes \Delta + \beta \left( \mathbf{1} \otimes \Delta + \Delta \otimes \mathbf{1} - 2\Delta \otimes \Delta \right) \right], \quad (\text{IV.10})$$

with  $\alpha = \frac{d}{d_c^{dil}} \left( 1 - \frac{d}{d_c} \right)^{-1}$  and  $\beta = \frac{d}{d_c^{dil}} \left( (2-\nu) - \frac{E_M d}{\Omega_{DG} d_c^{dil}} \right)^{-1}$ ,

where  $\Omega_{DG}$  is the deviatoric part of the eigenstiffness tensor  $\Omega_D^M$  of the double-inclusion characterizing the distribution of cracks,  $d_c$  denotes a critical crack density parameter and where  $d_c^{dil}$  corresponds to the critical crack density for which the dilute estimation of the Young modulus goes to zero. The IDD and MT estimates may be retrieved for particular values of  $d_c$  and  $\Omega_{DG}$ . For  $\Omega_{DG} = E_M (7-5\nu) / [15(1-\nu^2)]$  and  $d_c = d_c^{IDD} = 45/128$ , the previous equation coincides with the expression of the compliance increment tensor in Eq. (IV.9) provided by the IDD scheme. Observe that  $d_c^{IDD}$  corresponds to the crack density for which the IDD estimation of the Young modulus goes to zero. Similarly, Eq. (IV.10) coincides with the MT estimate in Eq. (IV.4) for  $\Omega_{DG} = E_M / [2(1+\nu)]$  and  $d_c$  going to infinity.

It is furthermore pointed out that simple general expressions can be obtained from the previous equation for the effective axial Young modulus  $E_1^*$ , the longitudinal Poisson ratio  $\nu_{13}^* = \nu_{12}^*$  and the longitudinal shear modulus  $G_1^* = G_{12}^* = G_{13}^*$  of the damaged material allowing for retrieving IDD, MT and dilute homogenization schemes for particular values of the critical crack density parameter  $d_c$ :

$$\frac{E_1^*}{E_M} = \frac{\nu_{13}^*}{\nu} = \frac{\nu_{12}^*}{\nu} = \left( 1 - \frac{d}{d_c} \right) \left[ 1 - \frac{d}{d_c} \left( 1 - \frac{d_c}{d_c^{dil}} \right) \right]^{-1}, \quad (\text{IV.11})$$

$$\frac{G_1^*}{G_M} = \left[ 1 + \frac{d}{(1+\nu) d_c^{dil}} \left( (2-\nu) - \frac{E_M d}{\Omega_{DG} d_c^{dil}} \right)^{-1} \right]^{-1}.$$

If  $\Omega_{DG} = E_M / [2(1+\nu)]$  and  $d_c$  tends to infinity, the expressions of the Young and shear moduli given in the previous equation coincide with the estimation of the MT model written below:

$$\frac{E_1^{MT}}{E_M} = \left( 1 + \frac{d}{d_c^{dil}} \right)^{-1}, \quad \text{with} \quad d_c^{dil} = \frac{3}{16(1-\nu^2)}, \quad (\text{IV.12})$$

$$\frac{G_1^{MT}}{G_M} = \left( 1 + \frac{d}{(1+\nu)(2-\nu)d_C^{dil}} \right)^{-1} = \left( 1 + \frac{16(1-\nu)d}{3(2-\nu)} \right)^{-1},$$

and if  $d_C = d_C^{dil}$ , they coincide with the dilute estimation:

$$\frac{E_1^{dil}}{E_M} = 1 - \frac{d}{d_C^{dil}} \quad \text{and} \quad \frac{G_1^{dil}}{G_M} = 1 - \frac{16(1-\nu)d}{3(2-\nu)} + O(d^2), \quad (\text{IV.13})$$

where  $d_C^{dil}$  appears clearly to be the critical crack density for which the dilute estimation of the Young modulus goes to zero. Finally, the IDD predictions are also retrieved for  $\Omega_{DG} = E_M(7-5\nu)/[15(1-\nu^2)]$  and  $d_C = d_C^{IDD}$ :

$$\frac{E_1^{IDD}}{E_M} = \left( 1 - \frac{128d}{45} \right) \left[ 1 - \frac{128d}{45} \left( 1 - \frac{45}{128d_C^{dil}} \right) \right]^{-1} = 1 - \frac{60p(1-\nu^2)}{15\pi + 4p(7-15\nu^2)}, \quad (\text{IV.14})$$

$$\frac{G_1^{IDD}}{G_M} = \left[ 1 + \frac{d}{(1+\nu)d_C^{dil}} \left( (2-\nu) - \frac{15(1-\nu^2)d}{(7-5\nu)d_C^{dil}} \right)^{-1} \right]^{-1} = 1 - \frac{60p(1-\nu)}{15\pi(2-\nu) + 8p(4-5\nu)},$$

with  $p = 4\pi d/3$ . The effective Young and shear moduli of the damaged material along  $e_1$  axis predicted by the simplified IDD can be written as:

$$\frac{\hat{E}_1^{IDD}}{E_M} = \left[ 1 + \frac{1}{d_C^{dil}} \left( 1 + \frac{d_1}{d_C^{IDD}} \right) d_1 \right]^{-1}. \quad (\text{IV.15})$$

In the ensuing, these estimations of the elastic moduli obtained with the dilute, IDD, MT and simplified IDD homogenization models are compared to each other and confronted to numerical results.

### 11.2.1.2 Evolution of the explicit estimates with crack density

For the sake of comparison, the respective predictions of the previously mentioned schemes for the effective axial Young modulus, the longitudinal Poisson ratio and shear modulus of a damaged material with aligned cracks are plotted on Fig. IV.1 as functions of the crack density parameter  $p$ . This crack density parameter used by Ponte-Castaneda and Willis (1995) has a very clear geometrical signification. It corresponds to the volume fraction occupied by spheres circumscribing each penny-shaped crack.

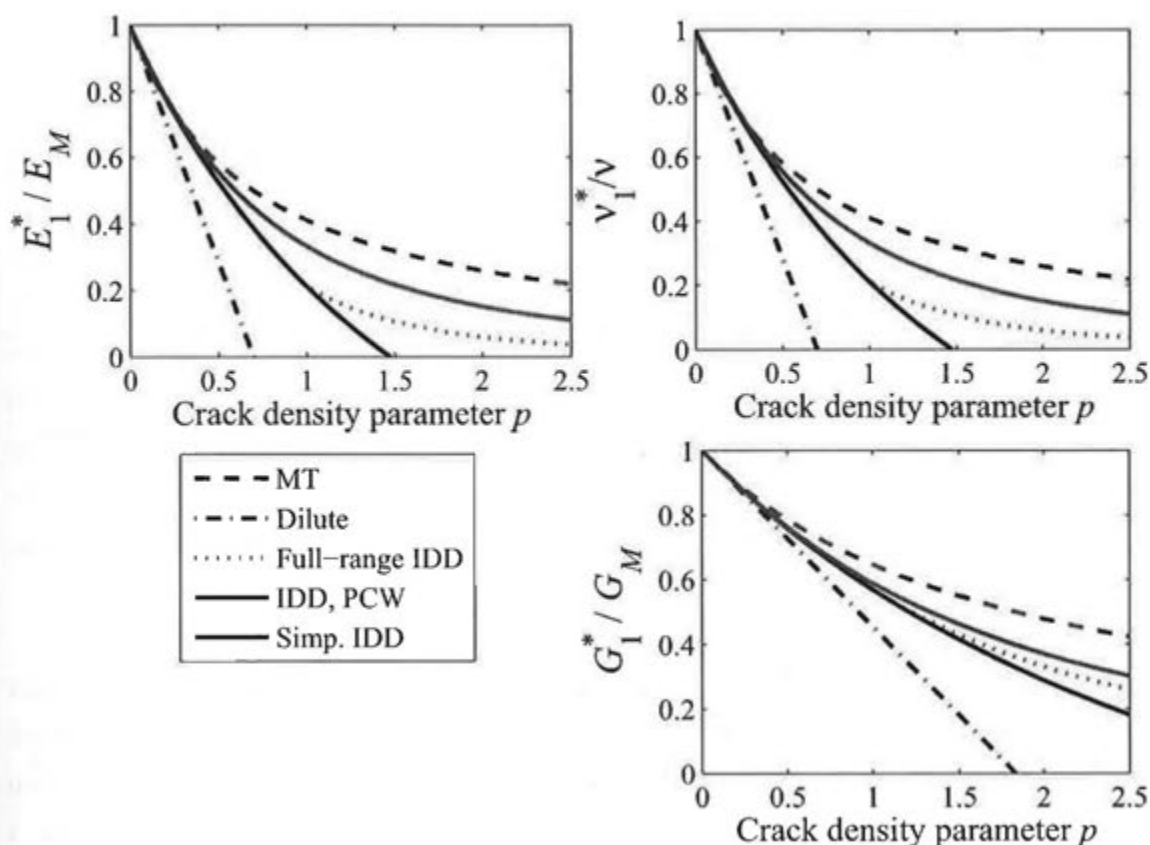


**Figure IV.1:** Evolutions of the effective axial Young modulus, the longitudinal Poisson ratio and the longitudinal shear modulus of an elastic body with  $\nu = 0.25$  weakened by aligned penny-shaped cracks on the  $(e_2, e_3)$  plane estimated by diverse homogenization schemes as functions of the crack density parameter  $p = 4\pi d/3$  (3D).

Clear-cut differences may be observed on Fig. IV.1 between the curves respectively estimated by the dilute, IDD and MT schemes. The elastic properties predicted by MT estimate evolve very slowly when the crack density is high, while the elastic moduli predicted by the dilute model vanish rapidly. By the way, that is why the dilute scheme is considered as a lower bound by Krajcinovic (1996). The curves computed with the IDD method are situated between the dilute and MT ones and go to zero for certain values of the crack density parameter. It is recalled that the interaction effects between cracks are neglected in the dilute estimate and that they are only integrated in an indirect way in IDD and MT schemes, since they can be interpreted as dilute models where the stress applied at infinity is modified to account for the presence of other microcracks, as is shown in Part II (Fig. II.5). Most of the papers dedicated to the calculation of cracks interactions are numerical, since it is a tremendously difficult task to calculate the exact stress intensity factors of a given microcrack, which interacts with all the other microcracks. Thorough numerical simulations taking into account interactions between cracks have been performed by Shen and Yi (2001), Feng and Yu (2003a,b) and Shen and Li (2004) in 2D to predict the damaged mechanical

properties. It is consequently interesting to compare the present estimates with these advanced simulations to gauge which one is the most accurate.

The different results obtained in the case of aligned cracks for the evolution of the Young modulus with crack density are gathered in Fig. IV.2 and compared with the predictions given by micromechanical schemes. It is pointed out that numerical results (Feng et al. 2003a; Shen and Li 2004) are systematically situated between MT and IDD or PCW estimates. These simulations are performed with the Kachanov's method (Kachanov 1987) to account for the interactions between cracks and consider an isotropic distribution of cracks. It is complicated to determine which model between MT and IDD ones is best suited for estimating the damaged effective properties. The IDD scheme seems to be in better agreement with the numerical results for low and moderate crack densities ( $p < 1$ ), whereas the MT predictions lay closer to the simulations for very high density of microcracks.

It would consequently be valuable to find a model capable of scanning all the values comprised between IDD and MT predictions. The full-range IDD defined in Part II, which predictions are situated between the ones of IDD and MT schemes, is thus clearly better than IDD, which suffers from the fact that the effective Young modulus becomes zero for a moderate value of  $p$  on Fig. IV.2. However, even though the full-range IDD is explicit, it is quite difficult to use it in practice, since the expression of the eigenstiffness tensors  $\Omega_{Di}^M$  of the double-inclusions characterizing the distribution of cracks changes for different values of the crack density parameters (see Appendix II.B). The simplified version of IDD proposed in Eq. (IV.8) yields surprisingly good results. It then represents a good compromise, since it is both simple of use and accurate. It is however worth noting that the differential method (Hashin 1988) also provides accurate predictions, according to Feng and Yu (2003a; b) and Shen and Li (2004). But a decisive argument in favour of the different IDD schemes presented is their simplicity compared to implicit models such as the SC, GSCS and the differential one, while providing results close to the differential one.

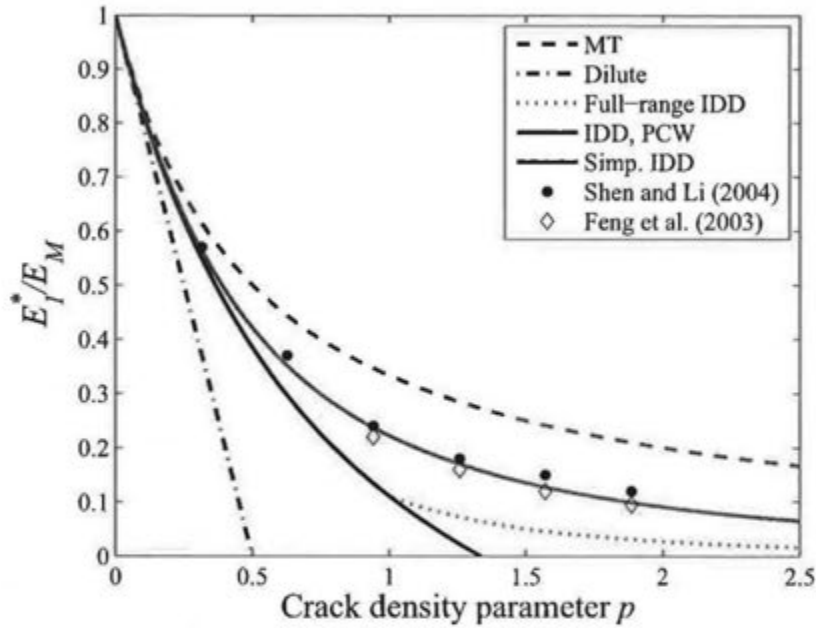


**Figure IV.2:** Evolutions of the effective axial Young modulus of an elastic body with  $\nu = 0.25$  weakened by aligned penny-shaped cracks on the  $(e_2, e_3)$  plane estimated by diverse homogenization schemes and by numerical simulations as functions of the crack density parameter  $p = \pi d (2D)$ .

The differences between IDD and MT models lie on the respective distribution of inhomogeneities considered. While the distribution of cracks is necessarily flat in the MT model (Stora et al. 2006a), this distribution in the PCW or IDD model depends on the aspect ratio of the double-inclusion that could thus constitute an interesting parameter. The choice of a spheroidal double-inclusion may somehow account for the anisotropy induced in the distribution by the mechanical loads. It may thus introduce a further anisotropy aspect due to the distribution of cracks, in addition to the classical anisotropic behaviour of the damaged material, but it leads to complicated calculations. This is the reason for which spherical double-inclusions are adopted in the ensuing for the computations of these models.

### 11.2.2 Comparison for an isotropic damaged material

The analytical expressions for an isotropic damaged material can easily be deduced from the relations derived for the case of aligned cracks by performing the following average operation on all the possible orientations denoted by curly brackets (e.g. Benveniste 1987):

$$\mathbf{Q} = \{\mathbf{T}\} = \frac{1}{3} T_{rrpp} \mathbf{J} + \frac{1}{5} \left( T_{rrpp} - \frac{1}{3} T_{rrpp} \right) \mathbf{K}. \quad (\text{IV.16})$$

The following relations are thus obtained for the concerned schemes:

$$\mathbf{C}_{dil}^* = \mathbf{C}_M : (\mathbf{I} - p \mathbf{Q}), \quad (\text{IV.17})$$

$$\mathbf{C}_{MT}^* = \mathbf{C}_M : (\mathbf{I} + p \mathbf{Q})^{-1}, \quad (\text{IV.18})$$

$$\mathbf{C}_{IDD}^* = \mathbf{C}_M : \left[ \mathbf{I} + \left( \mathbf{I} - \{ \mathbf{H}^{dil} : \boldsymbol{\Omega}_D^M \} \right)^{-1} : p \mathbf{Q} \right]^{-1}, \quad (\text{IV.19})$$

$$\hat{\mathbf{C}}_{IDD}^* = \mathbf{C}_M : \left[ \mathbf{I} + \left( \mathbf{I} + \{ \mathbf{H}^{dil} : \boldsymbol{\Omega}_D^M \} \right) : p \mathbf{Q} \right]^{-1}, \quad (\text{IV.20})$$

with  $\mathbf{Q} = \frac{4}{3\pi} \frac{(1-\nu)}{(1-2\nu)} \mathbf{J} + \frac{8}{15\pi} \frac{(1-\nu)(5-\nu)}{(2-\nu)} \mathbf{K}$ .

The curves proposed on Fig. IV.3 for the evolutions of the effective mechanical properties of an isotropic damaged material are quite similar to the ones obtained for a body containing only aligned cracks. Nevertheless, the decrease of the Young modulus in the  $\mathbf{e}_1$  direction for the case of aligned cracks (see Fig. IV.1) is more marked than for randomly oriented ones. It may be explained by the fact that, at a given crack density parameter value, the aligned cracks mainly affects the material properties in one direction, while randomly oriented ones influence equally on all the possible orientations. The curves on Fig. IV.3 predicted by the full-range IDD and the simplified one are very close. This observation further justifies the interest of the simplified IDD that is much easier to compute than the full-range IDD.

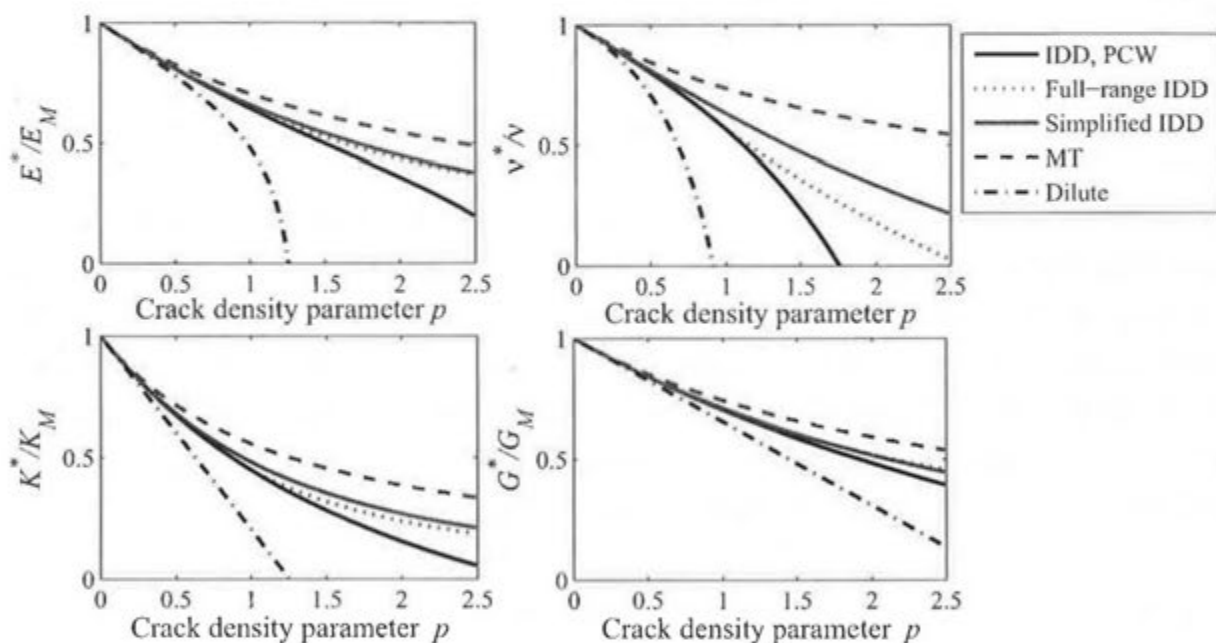


**Figure IV.3:** Evolutions of the effective Young modulus (up left), the Poisson ratio (up right), the bulk (down left) and shear moduli (down right) of an elastic body with  $\nu = 0.25$  weakened by randomly oriented penny-shaped cracks predicted by various homogenization schemes as functions of the crack density parameter  $p$  (3D).

### 11.2.3 Comparison for an orthotropic damaged material

The case of a material containing three families of cracks, which normal vectors are respectively oriented following  $\mathbf{e}_1$ ,  $\mathbf{e}_2$  and  $\mathbf{e}_3$ , is now considered. The resulting material is thus orthotropic:

$$\mathbb{H}^{dil} = \sum_i p_i \mathbb{T}_i : \mathbb{S}_M, \quad (\text{IV.21})$$

where  $i$  denotes the family of microcracks which normal is oriented following  $\mathbf{e}_i$  ( $i = 1, 2, 3$ ). In the present case, the tensor  $\mathbb{H}^{dil}$  has got a simple expression and is not singular if  $d_1$ ,  $d_2$  and  $d_3$  are not equal to zero, on the contrary of the case where all the microcracks are parallel:

$$H_{iii}^{dil} = \frac{16(1-\nu^2)}{3E_M} d_i; \quad H_{1313}^{dil} = \frac{8(1-\nu^2)}{3(2-\nu)E_M} (d_1 + d_3); \quad H_{2323}^{dil} = \frac{8(1-\nu^2)}{3(2-\nu)E_M} (d_2 + d_3);$$

$$H_{1212}^{dil} = \frac{8(1-\nu^2)}{3(2-\nu)E_M} (d_1 + d_2),$$

or written in tensorial form:

$$\mathbb{H}^{dil} = \frac{16(1-\nu^2)}{3E_M(2-\nu)} \left[ \sum_{i=1}^3 d_i \left( \mathbf{1} \otimes \Delta_i + \Delta_i \otimes \mathbf{1} - \nu \Delta_i \otimes \Delta_i \right) \right]. \quad (\text{IV.22})$$

The compliance increment tensor  $\mathbb{H}^{IDD}$  and  $\hat{\mathbb{H}}^{IDD}$  predicted by the original and simplified IDD models are provided by Eqs. (IV.7-8), respectively. The evolutions of the Young moduli  $E_i^*$  and of the shear moduli  $G_{ij}^*$  ( $\{i, j\} \in [1, 3]$  and  $i \neq j$ ) along the three principal directions are presented in Fig. IV.4 as functions of the total crack density parameter in the case where  $d_1 = d_2 = d/2$  and  $d_3 = 0$  and in the cubic one recovered for  $d_1 = d_2 = d_3 = d/3$ . The cubic damaged state does not coincide with the isotropic one, though the curves in Figs. IV.3 and IV.4 are quite close. One of the main questions now consists in finding how many families of cracks should be employed to accurately represent any damaged state of concrete.

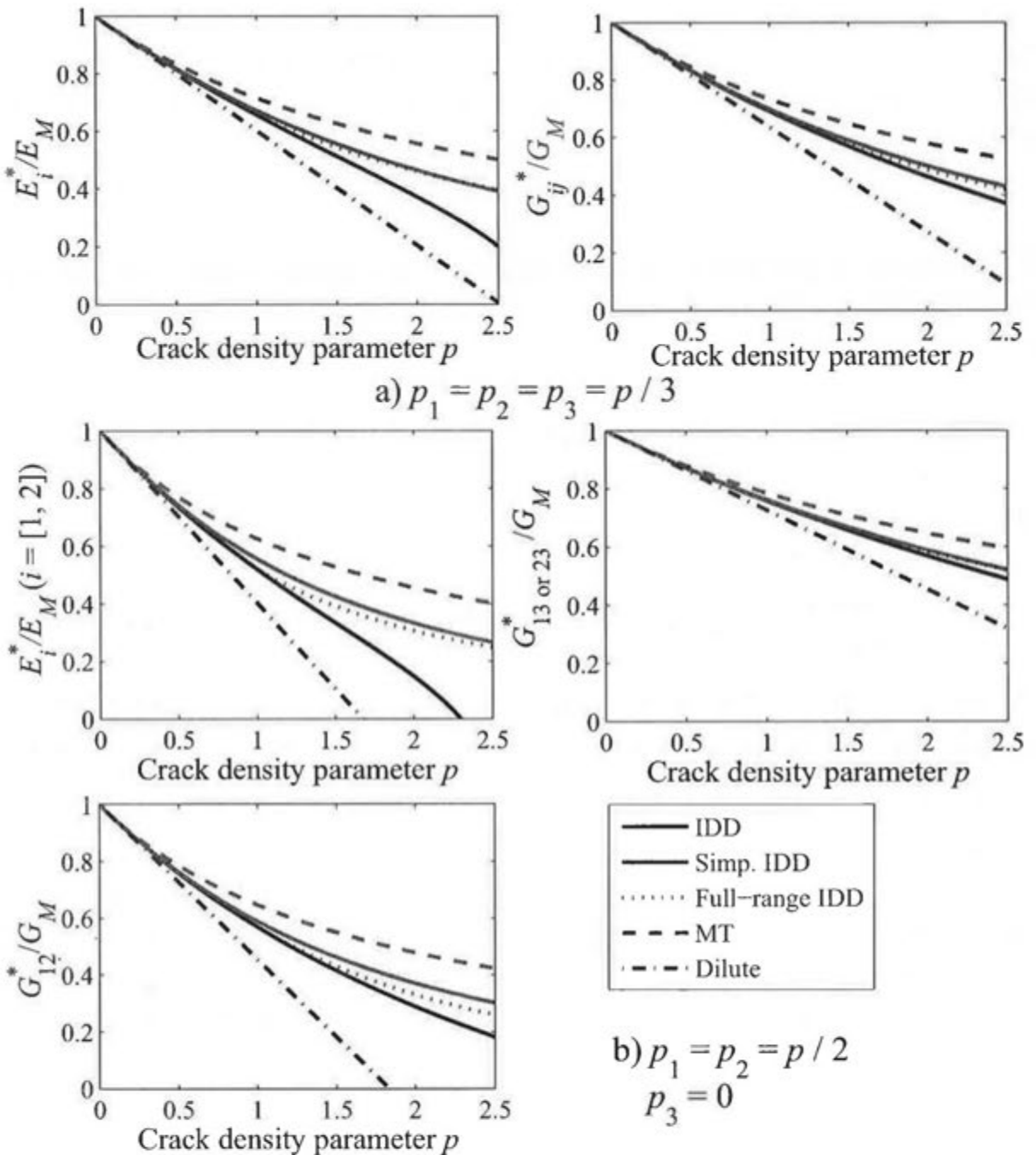


**Figure IV.4:** Evolutions of the effective Young moduli and shear moduli along the three principal axis  $e_1 = e_2 = e_3$  of an elastic body with  $\nu = 0.25$  weakened by three families of penny-shaped cracks oriented according to the principal directions with identical crack densities  $p_1 = p_2 = p_3 = p/3$  (up) and with crack densities  $p_1 = p_2 = p/2$  and  $p_3 = 0$  (down) as functions of the crack density parameter  $p$ .

### 11.3 Link between the macroscopic behavior and the number of microcracks

The number of families of cracks chosen to represent the microdefects of a damaged material is an aspect of primary importance for the use of homogenization procedures detailed before. A compromise needs to be found so that the model developed accurately represents the actual

microdefects and is at the same time tractable analytically. To answer to this problem, the directional dependence of the Young modulus predicted by the IDD model for different numbers of families of cracks is therefore investigated.

Let a damaged material be represented by an elastic body weakened by  $n_C$  families of cracks. The estimation of the effective compliance tensor of the latter material by the IDD model is denoted as  $\mathbb{S}_{IDD}^*$ . The predicted effective Young modulus of the damaged composite along an arbitrary direction of the space can be deduced from this compliance tensor with the help of the subsequent relation:

$$\frac{1}{E^{IDD}(\Delta)} = \Delta : \mathbb{S}_{IDD}^* : \Delta, \quad (IV.23)$$

where  $\Delta = \mathbf{n} \otimes \mathbf{n}$  and  $E^{IDD}(\Delta)$  is the Young modulus of the damaged material predicted by IDD along the direction  $\mathbf{n}$ . As pointed out by many authors (e.g. Cazzani and Rovati 2003), the dependence of the Young modulus on the direction  $\mathbf{n}$  reflects in a certain manner the anisotropy of a given material.

Rosettes representing the relative decrease of the Young modulus with the orientation are proposed on Figs. IV.5 and IV.6 for two and four families, respectively. The damaged material is considered in plane stress conditions. Concerning Fig. IV.5, the two families of cracks numbered 1 and 2 respectively correspond to cracks with normal vectors along  $\mathbf{e}_1$  and  $\mathbf{e}_2$ . Remark that the cracks, which normal direction is for instance  $\mathbf{e}_1$ , do not influence the Young modulus in the directions perpendicular to  $\mathbf{e}_1$ . In the case of four families of cracks respectively numbered from 1 to 4, their normal vectors are  $\mathbf{e}_1$ ,  $\mathbf{e}_2$ ,  $(\mathbf{e}_2 + \mathbf{e}_1)/\sqrt{2}$  and  $(\mathbf{e}_2 - \mathbf{e}_1)/\sqrt{2}$ , respectively. According to Fig. IV.6, the isotropy can already be well reproduced with four families of cracks, which is in good agreement with the observations of Pensée (2003). It appears from Figs. IV.5 and IV.6 that the developed micromechanical model is all the more accurate to reproduce the damage induced anisotropy as many families of microcracks are involved.

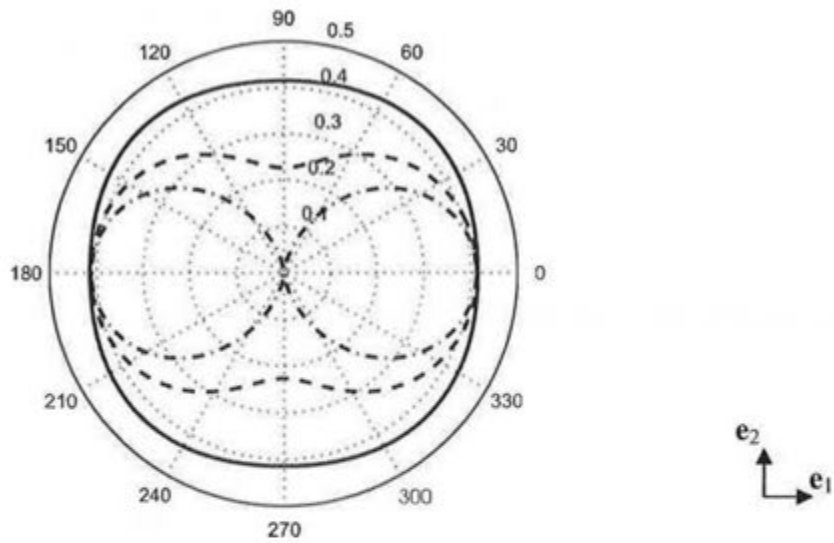


**Figure IV.5:** Rosette representing the relative decrease of the effective Young modulus predicted by the IDD scheme for two families of cracks aligned with the  $e_1$  and  $e_2$  directions which crack densities are  $d_1 = d, d_2 = 0$  with  $d = 0.1$  (dash-dotted),  $d_1 = d, d_2 = d/2$  (dashed) and  $d_1 = d_2 = d$  (plain), respectively.

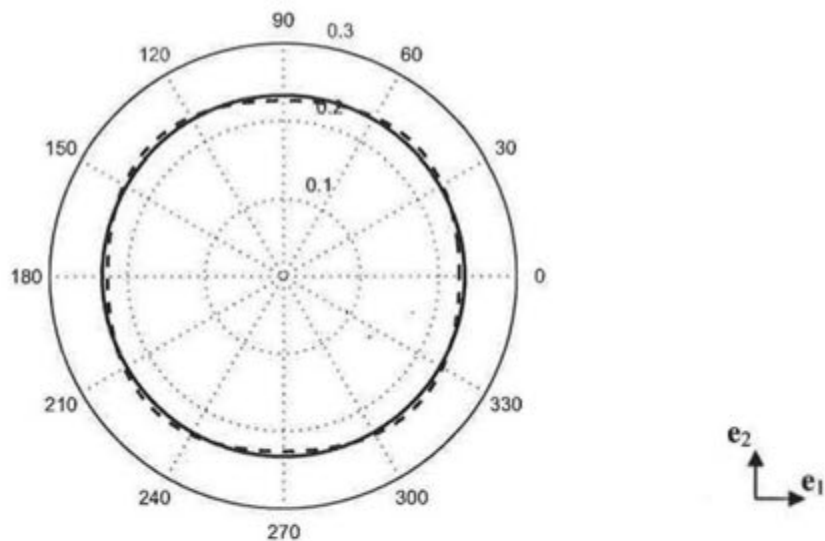


**Figure IV.6:** Rosette representing the relative decrease of the effective Young modulus predicted by the IDD scheme for four families of cracks aligned with the  $e_1$  and  $e_2$  directions which crack densities are  $d_1 = d_2 = d/2$  and  $d_3 = d_4 = 0$  with  $d = 0.1$  (dashed) and  $d_1 = d_2 = d_3 = d_4 = d/4$  (plain), respectively.

#### 11.4 Conclusion of chapter 11

The recent application of micromechanics for modelling damage is a promising way to relate the damaged material behaviour to its microstructure. However, relatively few micromechanically-based models have been incorporated in FE codes (e.g. Bary et al. 2007; Zhu et al. 2007), because they are usually more difficult to handle than phenomenological models especially in anisotropic cases.

In order to build a micromechanically-based damage model incorporable in FE codes, different explicit homogenization schemes have been reviewed. Their predictions of the effective mechanical properties of an elastic body weakened by aligned microcracks have been confronted with 2D numerical simulations accounting for interactions between microcracks. The rather good agreement of the IDD scheme, providing identical predictions as the PCW and DI type models, with these numerical results constitutes an argument in its favour. A simplified version of this estimate that seems better suited for dealing with materials weakened by diverse families of cracks has also been proposed (see Eq. (IV.22)) and is employed in the ensuing to formulate the damaged material behavior.

The crucial question of the number of families of cracks necessary to represent the anisotropy of the damaged material is also addressed. In plane stress conditions, four families seem to be adequate for such representation. Nevertheless, since the damage model developed will only be applied to quite simple cases of loadings, only two families of perpendicular cracks are adopted in the ensuing for simplicity reasons. The model should however not be applied for anisotropic cases that are more complex than orthotropy. The next chapter aims at developing evolution laws for the crack density of these two families.

## 12 ESTABLISHMENT OF THE EVOLUTION LAWS

The establishment of the evolution laws is generally performed in the framework of the thermodynamics of irreversible processes. According to the second principle of thermodynamics, the intrinsic dissipation  $Dis$  has to be non-negative (e.g. Nguyen 2000):

$$Dis = -\frac{\partial \Phi}{\partial d_i} \dot{d}_i = Y_{di} \dot{d}_i (\geq 0), \quad (IV.24)$$

where  $Y_{di}$  are the driving forces associated with the micromechanical damage variables  $d_i$ . The present chapter aims at building suitable evolution laws for these damage variables while taking care that they respect the second principle of thermodynamics, i.e. the Clausius-Duhem inequality written just above.

### 12.1 Criteria based on the generalized standard materials (GSM) formalism

The evolution law of the damage variables are established adopting the GSM formalism detailed below. The framework of GSM constitutes a convenient method to automatically guarantee the fulfillment of the second principle of thermodynamics. The grounding paper of this approach was written by Halphen and Nguyen in 1975 and the underlying mathematics, the theory of convex analysis, can be found in details in several books, for instance Nguyen (2000).

### 12.1.1 Presentation of the GSM formalism

#### 12.1.1.1 Basic definition

The basic definition proposed by Nguyen (2000) for the GSM formalism (e.g. Halphen and Nguyen 1975; Marigo 1985; Nguyen 2000) stipulates that the constitutive laws of a given material are generalized standard if they are associated with a free energy and a dissipation potential having the following characteristics: they depend on the current values of the state variables and the dissipation potential is convex with respect to the flux. According to the GSM model, the constitutive relations are thus fully defined through the choice of a specific internal energy functional  $\Phi$  and of a specific dissipation functional  $\Psi$ , which depend on the local values of the state variables. A simple illustrative example is now given to show the philosophy of the GSM formalism, the mathematical basis of this theory being presented later.

#### 12.1.1.2 Simple illustrative example

To automatically guarantee the fulfillment of the Clausius-Duhem inequality (IV.24), the basic idea carried out by the GSM models consists in finding a convex dissipation potential  $\Psi$  that is minimal in zero and depends only on the internal variables so that:

$$Y_{di} = \frac{\partial \Psi(\dot{d}_i)}{\partial \dot{d}_i}, \quad (\text{IV.25})$$

if  $\Psi$  is differentiable, the case for which  $\Psi$  is not differentiable being treated later. For instance, if the following convex dissipation potential is employed:

$$\Psi(\dot{d}_i, \beta_i) = \sum_i Y_0 \dot{d}_i^2, \quad (\text{IV.26})$$

where  $Y_0$  is the damage threshold in terms of elastic energy density. The positiveness of the intrinsic dissipation is then immediate:

$$Dis = Y_0 \dot{d}_i^2 (\geq 0). \quad (\text{IV.27})$$

However, the driving forces thus obtained depend on the rate of damage:

$$Y_{di} = 2Y_0 \dot{d}_i. \quad (\text{IV.28})$$

Usually, the evolution laws proposed in literature for brittle or quasi-brittle materials are rate-independent (e.g. Marigo 1985). The utilisation of the GSM theory for the case of rate-independent materials treated subsequently requires some more efforts, even though the basic ideas remain the same.

### 12.1.2 Application of the GSM formalism for quasi-brittle materials

In the case of rate-independent materials such as brittle materials considered here, the dissipation potential  $\Psi$  is not necessarily differentiable. Therefore the notion of sub-gradient of  $\Psi$  is introduced to apply the GSM formalism to non differentiable dissipation potentials (e.g. Nguyen 2000):

$$Y_{di} \in \partial\Psi(\dot{d}_i) \Leftrightarrow Y_{di}(\hat{d}_i - \dot{d}_i) + \Psi(\dot{d}_i) \leq \Psi(\hat{d}_i), \quad \forall \hat{d}_i, \quad (\text{IV.29})$$

where  $\partial\Psi$  denotes the sub-gradient of  $\Psi$ . This concept generalizes the definition of derivative and can still apply even if  $\Psi$  is not differentiable. The following equivalency is useful to relate the dissipation potential  $\Psi$  to damage threshold function  $f_i$  (e.g. Nguyen 2000):

$$Y_{di} \in \partial\Psi(\dot{d}_i) \Leftrightarrow Y_{di} \text{ realises } \max_{Y_{di}: f(Y_{di}) \leq 0} (Y_{di} \dot{d}_i). \quad (\text{IV.30})$$

Once that the damage threshold functions have been determined, the consistency conditions and the normal associated flow rules, classically used in plasticity, can be expressed by means of Kuhn-Tucker theorem:

$$Y_{di} \text{ realises } \max_{Y_{di}: f(Y_{di}) \leq 0} (Y_{di} \dot{d}_i) \Leftrightarrow \begin{cases} \dot{d}_i = \lambda_i \frac{\partial f_i}{\partial Y_{di}} \\ f_i \leq 0 \quad \lambda_i \geq 0 \quad \lambda_i f_i = 0. \end{cases} \quad (\text{IV.31})$$

where  $\lambda_i$  designate the damage multipliers, that may be expressed from the consistency condition. The following convex dissipation potential may for instance be employed (e.g. Lorentz and Andrieux 2003):

$$\Psi(\dot{d}_i, \beta_i) = \sum_i \left[ Y_0 \dot{d}_i + \mathcal{I}_{\mathcal{K}^*}(\dot{d}_i) \right] \quad \text{with} \quad \mathcal{I}_{\mathcal{K}}(Y_{di}) = \begin{cases} 0 & \text{if } Y_{di} \in K \\ \infty & \text{if } Y_{di} \notin K \end{cases}, \quad (\text{IV.32})$$

where the indicator function  $\mathcal{I}_{\mathcal{K}^*}(\dot{d}_i)$  enforces the positivity of the damage rates and where  $K$  is a convex domain. By setting  $\hat{d}_i = 0$  in Eq. (IV.29), the intrinsic dissipation appears clearly to be non-negative:

$$\text{Dis} = Y_0 \dot{d}_i \geq \Psi(\dot{d}_i) - \Psi(0) \geq 0. \quad (\text{IV.33})$$

In addition, simple damage threshold functions are derived from the dissipation potential, the details of the demonstration being provided in Appendix IV.A:

$$f_i = Y_{di} - Y_0. \quad (\text{IV.34})$$

The latter fracture-type criterion may be too simple to faithfully represent the evolution of damage. Indeed, if  $Y_{di}$  does not depend on the damage variables, the damage surface does not evolve during the damage process. More versatile evolution laws adopting the GSM formalism are proposed in the next part.

### 12.1.3 Development of evolution laws adopting the GSM formalism

In order to develop more advanced criteria than the one given in the previous equation, the following form is used for the Helmholtz free energy:

$$\Phi = \frac{1}{2} \bar{\epsilon} : \mathbb{C}^*(d_i) : \bar{\epsilon} + \varphi(\beta_i), \quad (\text{IV.35})$$

where  $\beta_i$  are called damage softening variables and the function  $\varphi$  characterizes this damage softening. These softening damage variables are introduced as additional internal variables

and characterize the evolution of the damage surface threshold. They are associated with driving forces denoted  $X_i$ . By analogy with the concept of hardening in plasticity, the function  $\varphi$  corresponds to the free energy stored by damage softening. Practically, it represents the effect of the damage state on the further development of damage. It is noteworthy that, the damage softening parameter  $\beta_i$  being considered as internal variables, the intrinsic dissipation reads as follows:

$$Dis = -\frac{\partial \Phi}{\partial d_i} \dot{d}_i - \frac{\partial \Phi}{\partial \beta_i} \dot{\beta}_i = Y_{di} \dot{d}_i + X_i \dot{\beta}_i (\geq 0). \quad (IV.36)$$

Lorentz and Andrieux (2003) showed that by adopting the following expressions for the dissipation potential and the free energy:

$$\Psi(\dot{d}_i, \dot{\beta}_i) = \sum_i \left[ Y_0 \dot{d}_i + \mathcal{J}_{\kappa^*}(\dot{d}_i) + \mathcal{J}_{\{0\}}(\dot{\beta}_i - \dot{d}_i) \right], \quad (IV.37)$$

$$\Phi(d_i, \beta_i) = \frac{1}{2} \bar{\boldsymbol{\varepsilon}} : \mathbf{C}^*(d_i) : \bar{\boldsymbol{\varepsilon}} + \sum_i \int_0^{\beta_i} (\mathfrak{R}_i(s) - Y_0) ds, \quad (IV.38)$$

the following threshold functions expressed with respect to the thermodynamic forces associated to the internal variables  $d_i$  and  $\beta_i$  are derived:

$$f_i = Y_{di} - \mathfrak{R}_i(\beta_i), \quad (IV.39)$$

where the function  $\mathfrak{R}_i$  represents the evolution of the damage threshold surface. The convexity of the proposed dissipation potential taking its minimal value for  $\dot{\beta}_i = \dot{d}_i = 0$ , with  $i \in [1, 2]$ , guarantees the fulfilment of the second principle of thermodynamics. Furthermore, the indicator function  $\mathcal{J}_{\{0\}}(\dot{\beta}_i - \dot{d}_i)$  enforces that the internal damage variables  $d_i$  and  $\beta_i$  remain equal to each other.

Concerning the damage threshold functions, the forces  $Y_{di}$  are obtained by homogenization, while the expressions of  $\mathfrak{R}_i$  are unknown and may be identified in different manners (e.g. Marigo 1985) so as to find an adequate evolution law. In particular, it is sufficient to adopt the dissipation potential in Eq. (IV.37) and to rewrite the Helmholtz free potential as:

$$\Phi = \frac{1}{2} \bar{\boldsymbol{\varepsilon}} : \mathbf{C}^*(d_i) : \bar{\boldsymbol{\varepsilon}} + \frac{1}{2} Y_0 \omega \left( \sum_i \beta_i^2 - \sum_i \beta_i \right), \quad (IV.40)$$

where  $\omega$  is a damage parameter, to retrieve the ensuing Marigo criterion (1985):

$$f_i = Y_{di} - Y_0 (1 + \omega) d_i. \quad (IV.41)$$

The latter evolution law is further investigated in a simple case.

### 12.1.4 Application in the case of multi-axial tension tests

The Marigo criterion (1985) introduced in the previous subsection is presently employed to define the evolution laws of a mortar subjected to uniaxial and biaxial tension tests. The purpose of this part consists in testing if the Marigo criterion provides an adequate damage evolution law so that the stress-strain curve of a mortar subjected to uniaxial tension predicted by the micromechanically-based damage model shows good accordance with the experimental curve measured by Le Bellégo (2001). The case of biaxial tension tests is also treated to observe how the crack densities of the different families of cracks evolve during non uniaxial tests. The mortar is initially assumed to be linear isotropic and is supposed to be in a plane stress state:

$$\bar{\sigma}_{13} = \bar{\sigma}_{23} = \bar{\sigma}_{33} = 0. \quad (\text{IV.42})$$

In the ensuing, the macroscopic stresses or strains are denoted without any superscript. The stress tensor  $\boldsymbol{\sigma}$  estimated by the present damage model is expressed as:

$$\boldsymbol{\sigma} = \left( -\frac{\partial \Phi}{\partial \boldsymbol{\varepsilon}} \right) = \mathbb{C}^*(d_i) : \boldsymbol{\varepsilon}. \quad (\text{IV.43})$$

In the case of two families of perpendicular cracks, two damage threshold functions for the two crack density parameters are involved and their derivatives read:

$$\begin{cases} \dot{f}_1 = \frac{\partial Y_{d1}}{\partial \boldsymbol{\varepsilon}} : \dot{\boldsymbol{\varepsilon}} + \frac{\partial Y_{d1}}{\partial d_1} \dot{d}_1 + \frac{\partial Y_{d1}}{\partial d_2} \dot{d}_2 - \frac{\partial X_1}{\partial \beta_1} \dot{\beta}_1 \\ \dot{f}_2 = \frac{\partial Y_{d2}}{\partial \boldsymbol{\varepsilon}} : \dot{\boldsymbol{\varepsilon}} + \frac{\partial Y_{d2}}{\partial d_1} \dot{d}_1 + \frac{\partial Y_{d2}}{\partial d_2} \dot{d}_2 - \frac{\partial X_2}{\partial \beta_2} \dot{\beta}_2 \end{cases} \quad (\text{IV.44})$$

The consistency condition imposes that:

$$\begin{cases} \frac{\partial Y_{d1}}{\partial \boldsymbol{\varepsilon}} : \dot{\boldsymbol{\varepsilon}} + \left( \frac{\partial Y_{d1}}{\partial d_1} - \frac{\partial X_1}{\partial \beta_1} \right) \lambda_1 + \frac{\partial Y_{d1}}{\partial d_2} \lambda_2 = 0 \\ \frac{\partial Y_{d2}}{\partial \boldsymbol{\varepsilon}} : \dot{\boldsymbol{\varepsilon}} + \frac{\partial Y_{d2}}{\partial d_1} \lambda_1 + \left( \frac{\partial Y_{d2}}{\partial d_2} - \frac{\partial X_2}{\partial \beta_2} \right) \lambda_2 = 0 \end{cases} \quad (\text{IV.45})$$

In the case of a uniaxial tension following the  $\mathbf{e}_1$  axis, the tension applied merely affects the family of cracks with normal vectors oriented along the  $\mathbf{e}_1$  axis so that we can consider that  $d_2 = 0$  and  $\lambda_2 = 0$ . The set of equations just above then simplifies into:

$$\frac{\partial Y_{d1}}{\partial \boldsymbol{\varepsilon}} : \dot{\boldsymbol{\varepsilon}} + \frac{\partial Y_{d1}}{\partial d_1} \dot{d}_1 + \frac{\partial Y_{d1}}{\partial d_2} \dot{d}_2 - \frac{\partial X_1}{\partial \beta_1} \dot{\beta}_1 = 0. \quad (\text{IV.46})$$

With the Marigo criterion, the derivative of the driving force  $X_i$  with respect to  $\beta_i$  is simply equal to  $\omega$  (see Eq. (IV.41)). Moreover, given the fact that  $d_2 = 0$ , the latter equation yields:

$$\dot{d}_1 = \left( \frac{\partial Y_{d1}}{\partial d_1} - \omega \right)^{-1} \frac{\partial Y_{d1}}{\partial \boldsymbol{\varepsilon}} : \dot{\boldsymbol{\varepsilon}}. \quad (\text{IV.47})$$

The evolution of the internal variable  $d_1$  and the stress-strain curve predicted by different homogenization schemes, namely MT, IDD and simplified IDD, with the Marigo criterion are plotted in Fig. IV.7. The Young modulus and Poisson ratio of the sound mortar are respectively equal to  $E_M = 44$  GPa and  $\nu = 0.25$  (Le Bellégo 2001). By default, the initial damage threshold is taken as  $Y_0 = 8000$  J m<sup>-3</sup> and the value of the parameter  $\omega$  in the Marigo criterion is set to zero by default. The influence of the parameter  $\omega$  on the stress-strain curve predicted by IDD is illustrated in Fig. IV.8 for information. On Fig. IV.7, the results obtained with the three micromechanically-based models are confronted with the experimental measurements from Le Bellégo (2001) on mortar samples. The stress-strain curve predicted by the IDD or PCW model appears to reproduce quite well the post-peak part of the stress-strain curve but goes to zero quite rapidly. Visible differences between the curves obtained with MT, IDD and simplified IDD schemes may be observed on Figs. IV.7, even though the evolutions of damage variables are computed with Marigo criterion using the same parameters ( $Y_0 = 8000$  J m<sup>-3</sup> and  $\omega = 0$ ) for the three models. The MT and simplified IDD models are seen to be far from Le Bellégo's results for this set of parameters but it is difficult to improve their predictions even by changing the values of  $Y_0$  and  $\omega$ . To obtain a better agreement with the experimental results, it would be preferable to adopt a stress formulation for the Helmholtz free energy in Eq (IV.1) (Pensée 2003).

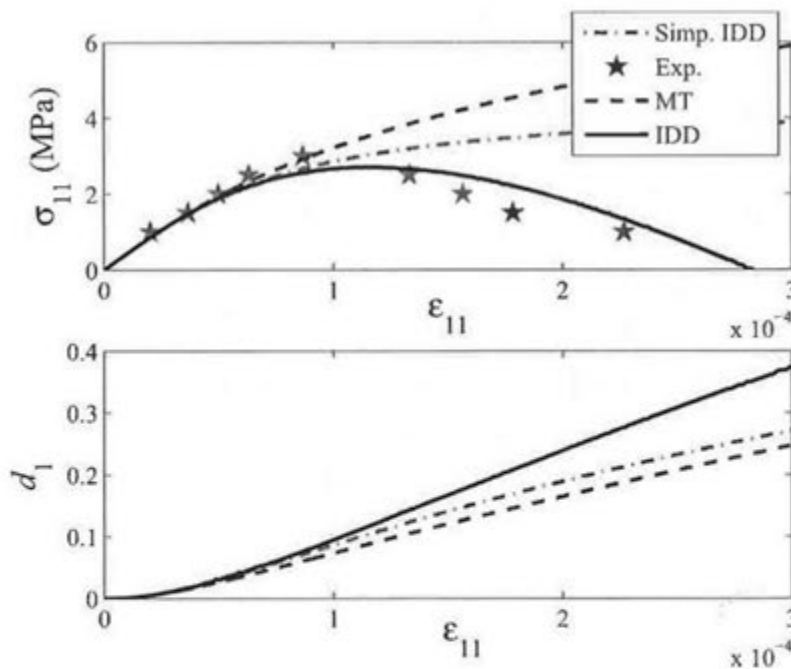


*Figure IV.7: Comparison of the stress-strain curves predicted of a mortar subjected to uniaxial tension along the  $e_1$  axis by different micromechanically based damage models with Marigo criterion with the one experimentally recorded by Le Bellégo (2001) (up); evolution for the crack density parameter  $d_1$  predicted by the latter models (down).*

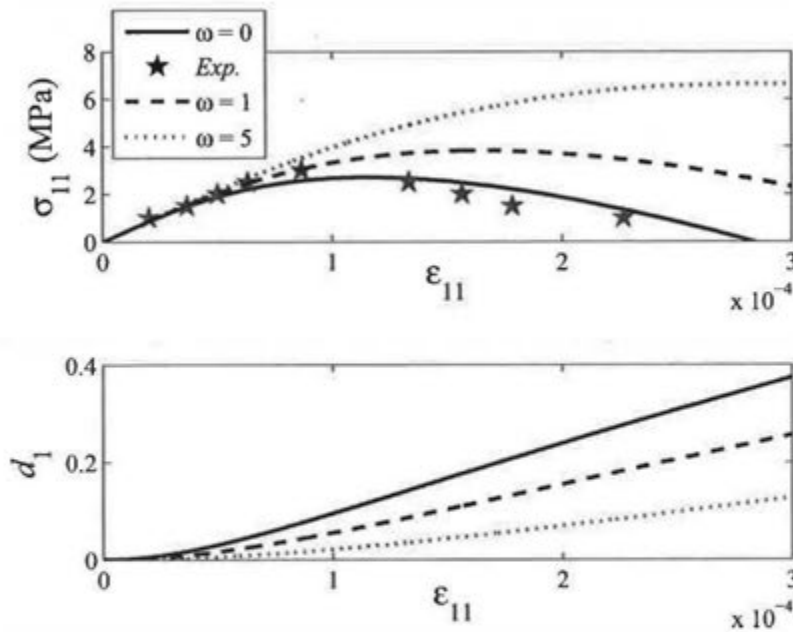


**Figure IV.8:** Comparison of the stress-strain curves predicted of a mortar subjected to uniaxial tension along the  $e_1$  axis by the IDD damage model with Marigo criterion with the one experimentally recorded by Le Bellégo (2001) (up); evolution for the crack density parameter  $d_1$  predicted by the latter model (down).

In more general cases, the system of differential equations in Eq. (IV.45) can be written in a matrix form in order to find the damage amplitudes  $\lambda_1$  and  $\lambda_2$ :

$$\begin{pmatrix} \frac{\partial Y_{d1}}{\partial d_1} - \omega & \frac{\partial Y_{d1}}{\partial d_2} \\ \frac{\partial Y_{d2}}{\partial d_1} & \frac{\partial Y_{d2}}{\partial d_2} - \omega \end{pmatrix} \begin{pmatrix} \lambda_1 \\ \lambda_2 \end{pmatrix} = - \begin{pmatrix} \frac{\partial Y_{d1}}{\partial \epsilon} : \dot{\epsilon} \\ \frac{\partial Y_{d2}}{\partial \epsilon} : \dot{\epsilon} \end{pmatrix}. \quad (\text{IV.48})$$

When the simplified IDD model is used to estimate the free energy, the forces  $Y_{di}$  do not depend on  $d_j$  ( $j \neq i$ ) so that no coupling exists between the two criteria. The system can then be solved using for instance the basic explicit Runge-Kutta algorithms incorporated in MATLAB, since the matrix above is diagonal and the system reduces into two decoupled equations. It should be emphasized that the complexity of computations of the evolution laws further increases if many families of cracks are involved. The main difficulty concerning the use of the IDD estimate arises from the fact that the effective stiffness tensor does not vary linearly with the crack density parameters. A hint used by Zhu et al. (2007) to avoid this problem is to consider a Taylor development at the first order of the driving forces, so that the extra diagonal terms in the previous matrix are annihilated. However, such an assumption might not be fully satisfactory, since the accuracy of the homogenization scheme is lost in this Taylor development at the first order. The stress-strain curves predicted by the micromechanically-based damage model with the Marigo criterion for mortar samples

subjected to biaxial tensions along the two axis  $e_1$  and  $e_2$  with  $\varepsilon_{11} = \varepsilon_{22}$  is plotted on Fig. IV.9. The plotted curves clearly differ from the uniaxial case (Fig. IV.7). This is due to the fact that the stiffness tensors predicted by the MT, IDD and simplified schemes do not vary linearly with damage variables and thus the driving forces  $Y_{di}$  depend from the two involved crack damage variables. This dependence practically results in different stress-strain curves in uniaxial and in biaxial tests. It is furthermore pointed out that the extra diagonal terms of the square matrix in the previous equation do not vanish and the system of ordinary differential equations has to be solved numerically, using preferentially an implicit Runge-Kutta algorithm. As in the uniaxial case, strong differences between the stress-strain curves obtained with MT, IDD and simplified IDD schemes are visible on Fig. IV.9, when the same parameters the evolutions of damage variables are adopted for the three models ( $Y_0 = 8000 \text{ J m}^{-3}$  and  $\omega = 0$ ).

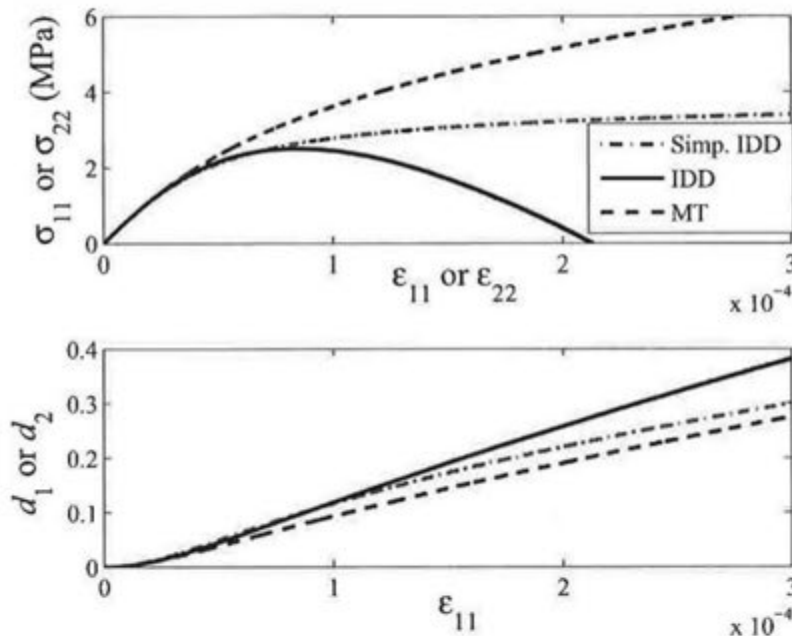


**Figure IV.9:** Stress-strain curves along the two principal axis of a mortar subjected to biaxial tension along the two axis  $e_1$  and  $e_2$  with  $\varepsilon_{11} = \varepsilon_{22}$  predicted by different homogenization models with Marigo criterion (up); evolution for the crack density parameters  $d_1$  and  $d_2$  predicted by the latter model (down).

The application of Marigo evolution law to the micromechanical damage model appears to be rather complicated to implement in a FE code without making simplifying assumptions. The next subchapter is devoted to strain-based criteria that are frequently employed in concrete in order to find a simpler method to establish the evolution laws.

## 12.2 Strain-based criteria

### 12.2.1 Review of strain-based criteria

The damage loading function  $f$  can be expressed using an equivalent strain denoted  $\tilde{\varepsilon}$  :

$$f = \tilde{\varepsilon} - \varepsilon_0, \quad (\text{IV.49})$$

where  $\varepsilon_0$  designates the initial damage threshold. One of the great interests of having a strain-based criterion is that it accounts for the sensitivity of the material to extension. Two forms proposed for the equivalent strain respectively by Mazars (1984) and De Vree et al. (1995) present valuable features for dealing with damage in concrete. In particular, they account for the differences of behavior of cement-based materials in traction and in compression. It is therefore of interest to thoroughly assess and compare these two theories of equivalent strains. The following strain invariants are introduced:

$$\begin{aligned} I_1^{(\varepsilon)} &= \text{tr}\boldsymbol{\varepsilon}, & I_2^{(\varepsilon)} &= \frac{1}{2} \left[ (\text{tr}\boldsymbol{\varepsilon})^2 - \text{tr}\boldsymbol{\varepsilon}^2 \right], & I_3^{(\varepsilon)} &= \det\boldsymbol{\varepsilon}, \\ J_2^{(\varepsilon)} &= \frac{1}{2} \text{tr} \left( \boldsymbol{\varepsilon} - \frac{1}{3} (\text{tr}\boldsymbol{\varepsilon}) \mathbf{1} \right)^2, \end{aligned} \quad (\text{IV.50})$$

where  $\text{tr}$  denotes the trace of a tensor and  $\det$  its determinant. Identical invariants, obtained by substituting  $\boldsymbol{\varepsilon}$  by  $\boldsymbol{\sigma}$  in the previous equation, may be used for the stress tensor. The criteria proposed by Mazars (1984) and De Vree et al. (1995) are respectively recalled below:

$$\tilde{\varepsilon}_{Ma} = \sqrt{\langle \varepsilon_i \rangle_+^2}, \quad \text{with} \quad \langle \varepsilon_i \rangle_+ = \frac{\varepsilon_i + |\varepsilon_i|}{2}, \quad (\text{IV.51})$$

$$\tilde{\varepsilon}_{DV} = \frac{k-1}{2k(1-2\nu)} I_1^{(\varepsilon)} + \frac{1}{2k} \sqrt{\frac{(k-1)^2}{(1-2\nu)^2} I_1^{(\varepsilon)2} + \frac{12k}{(1+\nu)^2} J_2^{(\varepsilon)}}, \quad (\text{IV.52})$$

where  $\varepsilon_i$  ( $i = \text{I, II, III}$ ) are the principal strains,  $\varepsilon_0$  is the strain threshold corresponding to the initiation of damage in traction and  $k$  denotes the ratio of the compressive strength over the tensile one. These two equations are very different at first sight, since the first one is expressed in terms of principal strains and the second uses the first two invariants of the strain tensor.

The surfaces representing these two threshold functions are plotted in Figs. IV.10 and IV.11 for  $\nu = 0.25$  and  $\varepsilon_0 = 10^{-4}$ . A sound criterion should respect some important conditions: (i) to be systematically non negative; (ii) to be closed convex. The Mazars criterion fulfills the first condition but not the second one (Fig. IV.11). The De Vree criterion respects both conditions (De Vree et al. 1995). In addition, the strong connections existing between the De Vree criterion and the one recently proposed by Christensen (2005) are evidenced in Appendix IV.B. The damage threshold surface evolves during the damage process so that a suited law is required to account for this evolution.

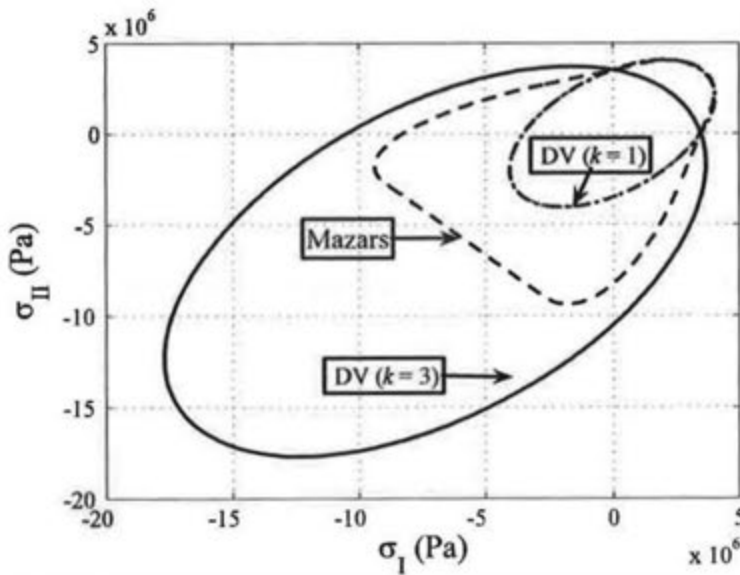


Figure IV.10: Damage yield surfaces respectively representing the Mazars criterion and the De Vree one for  $k = 1$  and  $k = 3$  in the space of principal stresses.

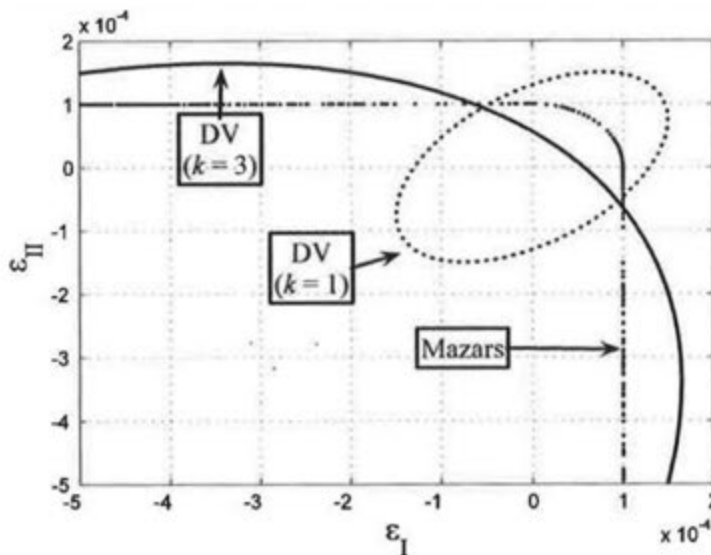


Figure IV.11: Damage yield surfaces respectively representing the Mazars criterion and the De Vree one for  $k = 1$  and  $k = 3$  in the space of principal strains.

### 12.2.2 Review of the Mazars model

The Mazars model is without contest the most popular damage model for concrete. Its success seems mainly due to its simplicity of use in a FE code and to its capacity of accounting in a simple and relatively efficient manner for the differences of behavior of concrete in tension and in compression. It has been extended to fatigue (Papa 1993) and recently to anisotropic damage (Desmorat et al. 2007). A non-local version of the Mazars model was furthermore proposed by Pijaudier-Cabot and Bazant (1987) in order to improve the numerical results and

limit the mesh dependency. Basically, the Mazars model (1984) consists in defining the following criterion:

$$f = \tilde{\varepsilon}_{Ma} - \kappa(\mathcal{D}), \quad (\text{IV.53})$$

where  $\mathcal{D}$  is a scalar macroscopic damage variable expressed as:

$$\mathcal{D} = 1 - \frac{E^*}{E_M}, \quad (\text{IV.54})$$

and where the function  $\kappa(\mathcal{D})$  rules the evolution of the damage surface. This function  $\kappa(\mathcal{D})$  is chosen so as to obtain the following evolution law:

$$\mathcal{D} = 1 - \frac{\varepsilon_0(1-A)}{\tilde{\varepsilon}_{Ma}} - A \exp(-B(\tilde{\varepsilon}_{Ma} - \varepsilon_0)), \quad (\text{IV.55})$$

where  $\tilde{\varepsilon}_{Ma}$  is the Mazars equivalent strain defined in Eq. (IV.52) and where  $A$  and  $B$  are parameters that are identified with different values in traction and in compression. The stress-strain behavior is then given by:

$$\boldsymbol{\sigma} = (1 - \mathcal{D}) \mathbb{C}_M : \boldsymbol{\varepsilon}. \quad (\text{IV.56})$$

Desmorat et al. (2007) proposed a convenient extension of the Mazars evolution to anisotropic cases by adopting a non-associated evolution law deriving from the latter dissipation potential:

$$\Psi^* = \mathbf{Y} : \langle \boldsymbol{\varepsilon}_p \rangle_+^2, \quad (\text{IV.57})$$

where  $\mathbf{Y}$  is the driving force associated with the second order damage tensor  $\mathcal{D}$  and where  $\boldsymbol{\varepsilon}_p$  is the tensor of the principal strains. This tensor admits the following representation:

$$\boldsymbol{\varepsilon}_p = \varepsilon_I \mathbf{e}_I \otimes \mathbf{e}_I + \varepsilon_{II} \mathbf{e}_2 \otimes \mathbf{e}_2 + \varepsilon_{III} \mathbf{e}_3 \otimes \mathbf{e}_3, \quad (\text{IV.58})$$

where  $\otimes$  is recalled to stand for the tensor product and  $\mathbf{e}_i (i=1,2,3)$  are the orthonormal vectors defining the principal strain directions. The derivation of the dissipation potential thus yields the following evolution law:

$$\dot{\mathcal{D}} = \lambda \frac{\partial \Psi^*}{\partial \mathbf{Y}} = \lambda \langle \boldsymbol{\varepsilon}_p \rangle_+^2. \quad (\text{IV.59})$$

In other words, the damage tensor rate is proportional to the square of the positive part of the principal strain tensor. The Mazars criterion is reused by substituting the previous isotropic damage variable  $\mathcal{D}$  by the trace of the second order damage tensor  $\mathcal{D}$  presently considered:

$$f = \tilde{\varepsilon}_{Ma} - \kappa(\text{tr} \mathcal{D}), \quad (\text{IV.60})$$

where different expressions were proposed for  $\kappa(\text{tr} \mathcal{D})$  by Desmorat et al. (2007) to provide a good fitting with the experimental stress-strain curves in tension and in compression. The damage multiplier is then determined from the consistency condition and the damage evolution law takes the general form:

$$\dot{\mathfrak{D}} = \frac{d\kappa^{-1}}{d\bar{\varepsilon}_{Ma}} \frac{\dot{\bar{\varepsilon}}_{Ma}}{\text{tr}\langle \boldsymbol{\varepsilon}_p \rangle_+^2} \langle \boldsymbol{\varepsilon}_p \rangle_+^2. \quad (\text{IV.61})$$

In the next subsection, a similar reasoning is carried out to establish an adequate evolution law for the crack densities parameters that are very different from the macroscopic damage variables employed by Mazars (1984) and Desmorat et al. (2007).

### 12.2.3 Definition of a strain-based evolution law for the micromechanically-based damage model

On the view of the previous considerations, the ensuing type of strain-based criterion is proposed as a starting point:

$$f = \bar{\varepsilon}_{DV} - \kappa(\text{tr}\mathbf{d}), \quad (\text{IV.62})$$

where  $\mathbf{d}$  is a second-order micromechanical damage tensor that reads in the  $(\mathbf{e}_1, \mathbf{e}_2, \mathbf{e}_3)$  orthonormal basis:

$$\mathbf{d} = \begin{pmatrix} d_1 & 0 & 0 \\ 0 & d_2 & 0 \\ 0 & 0 & 0 \end{pmatrix}, \quad (\text{IV.63})$$

since the normal vectors of the two families of perpendicular cracks retained in the micromechanical model are respectively oriented along  $\mathbf{e}_1$  and  $\mathbf{e}_2$ . The next stage consists in identifying a suitable function  $\kappa(\text{tr}\mathbf{d})$ . To perform such task, only one family of aligned cracks with normal vectors parallel to  $\mathbf{e}_1$  is first considered for simplicity. It is pointed out from Eqs. (IV.52-53) that the elastic stiffness deterioration along the direction  $\mathbf{e}_1$  with the Mazars model follows the evolution:

$$\frac{E_1^*}{E_M} = \frac{\varepsilon_0(1-A)}{\bar{\varepsilon}_{Ma}} + A \exp(-B(\bar{\varepsilon}_{Ma} - \varepsilon_0)). \quad (\text{IV.64})$$

In the ensuing computations, the parameter  $A$  is taken equal to 1. It is furthermore recalled that MT, IDD and simplified IDD estimations of the effective Young modulus  $E_1^*$  of the damaged material along the normal direction  $\mathbf{e}_1$  to aligned cracks are expressed analytically as functions of the crack density parameters in Eqs. (IV.11), (IV.14) and (IV.15), respectively. By combining these equations with Eq. (IV.64) where the Mazars equivalent strain is substituted by the one of De Vree et al. (1995), the following damage loading functions  $f$  can be established for MT, IDD and simplified IDD damage models, respectively:

$$f_{MT} = \frac{d_c^{dil} g(\bar{\varepsilon}_{DV})}{1 - g(\bar{\varepsilon}_{DV})} - d_1, \quad (\text{IV.65})$$

$$f_{IDD} = \frac{g(\tilde{\epsilon}_{DV})}{g(\tilde{\epsilon}_{DV}) + \frac{d_c^{IDD}}{d_c^{dil}}(1-g(\tilde{\epsilon}_{DV}))} - d_1, \quad (IV.66)$$

$$\hat{f}_{IDD} = \frac{-b + \sqrt{b^2 - 4ac}}{2a} - d_1, \quad \text{with } g(\tilde{\epsilon}_{DV}) = 1 - \exp(-B(\tilde{\epsilon}_{DV} - \epsilon_0)) \quad \text{and}$$

$$a = \frac{1-g(\tilde{\epsilon}_{DV})}{d_c^{dil} d_c^{IDD}}, \quad b = \frac{1-g(\tilde{\epsilon}_{DV})}{d_c^{dil}}, \quad \text{and } c = -g(\tilde{\epsilon}_{DV}).$$

These damage loading functions can be extended to the case of two families by using the trace of the damage tensor  $\mathbf{d}$ :

$$f = \kappa^{-1}(\tilde{\epsilon}_{DV}) - \text{tr} \mathbf{d}, \quad (IV.67)$$

where the expression of  $\kappa$  depends on the homogenization scheme employed to compute the effective mechanical properties of the damaged material. By analogy with Desmorat et al. (2007), a simple expression is proposed for the dissipation potential:

$$\Psi^* = \mathbf{Y}_d : \langle \mathbf{R} \cdot \boldsymbol{\epsilon}_p \rangle_+^2, \quad (IV.68)$$

where  $\mathbf{Y}_d$  is the driving force associated with the micromechanical damage tensor  $\mathbf{d}$  and  $\mathbf{R}$  is a projection operator that projects the principal strain tensor on the  $(\mathbf{e}_1, \mathbf{e}_2, \mathbf{e}_3)$  reference basis. The derivation of the dissipation potential yields the damage evolution law:

$$\dot{\mathbf{d}} = \lambda \frac{\partial \Psi^*}{\partial \mathbf{Y}_d} = \lambda \langle \mathbf{R} \cdot \boldsymbol{\epsilon}_p \rangle_+^2. \quad (IV.69)$$

An essential difference of the present approach with phenomenological models, such as the one of Desmorat et al. (2007), is that the principal directions of the damage tensor are now fixed. The damage multiplier is then determined from the consistency condition and the damage evolution law takes the general form:

$$\dot{\mathbf{d}} = \frac{d\kappa^{-1}}{d\tilde{\epsilon}_{DV}} \frac{\dot{\tilde{\epsilon}}_{DV}}{\text{tr} \langle \mathbf{R} \cdot \boldsymbol{\epsilon}_p \rangle_+^2} \langle \mathbf{R} \cdot \boldsymbol{\epsilon}_p \rangle_+^2. \quad (IV.70)$$

It was observed that, with the Marigo theory, two criteria are required in the case of two families of perpendicular cracks and that the two damage multipliers have to be solved numerically. In the present case, only one simple criterion given in Eq. (IV.68) provides explicitly the evolutions of the diverse crack density parameters. This characteristic is of high interest in view of an implementation in a FE code. However, on the contrary to the Marigo criterion that systematically respects the Clausius-Duhem inequality, the positivity of the intrinsic dissipation with the present strain-based criterion is not guaranteed and has to be carefully verified. The next subchapter is therefore devoted to the assessment of the thermodynamic admissibility of the damage evolution obtained by means of strain-based criteria.

### 12.2.4 Positivity of the intrinsic dissipation

For the strain-based criterion presented before, the fulfilment of the Clausius-Duhem inequality is not automatically guaranteed, since the GSM formalism was not employed. It is consequently necessary to verify that the second principle of thermodynamics is respected. It is recalled that in the presently developed damage model the intrinsic dissipation reads:

$$Dis = Y_{di} \dot{d}_i, \quad \text{with} \quad Y_{di} = \frac{1}{2} \boldsymbol{\varepsilon} : \left( -\frac{\partial \mathbf{C}^*_{IDD}}{\partial d_i} \right) : \boldsymbol{\varepsilon} \quad (i \in [1,2]). \quad (\text{IV.71})$$

To show the thermodynamic admissibility of the different micromechanically-based damage model with the strain-based criteria defined in Eq. (IV.66), the respective positivities of the thermodynamic forces  $Y_{di}$  and of the damage rates  $\dot{d}_i$  are verified. To prove that  $Y_{di} \geq 0$ , it is sufficient to show that the derivatives of  $\mathbf{C}^*$  with respect to the crack density parameters are semi-definite positive, for example by computing its determinant or by looking at the signs of its eigenvalues. For this purpose, it is convenient to rewrite the stiffness tensor predicted by the different homogenization schemes in a matricial form. Using the fact that:

$$-\frac{\partial \mathbf{C}^*}{\partial d_i} = \mathbf{C}^* : \frac{\partial \mathbf{S}^*}{\partial d_i} : \mathbf{C}^*, \quad \text{with} \quad i \in [1,2], \quad (\text{IV.72})$$

the opposite of the derivatives of the stiffness tensor estimated by MT, IDD and simplified IDD with respect to the crack density parameter  $d_1$  (or similarly  $d_2$ ) read respectively:

$$\begin{aligned} -\frac{\partial \mathbf{C}^*_{MT}}{\partial d_1} &= \mathbf{C}^*_{MT} : \left( \frac{4}{3} \pi \mathbf{T}_1 : \mathbf{S}_M \right) : \mathbf{C}^*_{MT}, \\ -\frac{\partial \mathbf{C}^*_{IDD}}{\partial d_i} &= \mathbf{C}^*_{IDD} : \frac{\partial \mathbf{H}^{IDD}}{\partial d_i} : \mathbf{C}^*_{IDD}, \\ -\frac{\partial \hat{\mathbf{C}}^*_{IDD}}{\partial d_i} &= \hat{\mathbf{C}}^*_{IDD} : \frac{\partial \hat{\mathbf{H}}^{IDD}}{\partial d_i} : \hat{\mathbf{C}}^*_{IDD}, \end{aligned} \quad (\text{IV.73})$$

The three derivatives above all admit three non-vanishing eigenvalues designated by  $\zeta_i$  ( $i \in [1,3]$ ) and obtained with the help of the symbolic toolbox of MATLAB:

$$\begin{aligned} \zeta_1^{MT} &= \frac{E_M d_C^{dil} (1-2\nu+3\nu^2)}{[(1+\nu)(1-2\nu)d_C^{dil} + (1-\nu)d]^2}, \quad \zeta_2^{MT} = \zeta_3^{MT} = \frac{E_M d_C^{dil} (2-\nu)}{[(1+\nu)(2-\nu)d_C^{dil} + d]^2}, \\ \zeta_1^{IDD} &= \frac{81(1-\nu^2)E_M d_C^{dil} (1-2\nu+3\nu^2)}{[9(1-\nu)(1-2\nu)(1+\nu)d_C^{dil} + (6(1-\nu)(1-2\nu)(1+\nu)\Omega_{DG} - 13\nu^2 + 16\nu - 7)d]^2}, \\ \zeta_2^{IDD} = \zeta_3^{IDD} &= \frac{E_M d_C^{dil} (2-\nu)}{[(1+\nu)(2-\nu)d_C^{dil} + (1-\Omega_{DG}(1+\nu))d]^2}, \end{aligned}$$

$$\begin{aligned}\zeta_1^{IDD} &= \frac{9E_M d_C^{dil2} (1-2\nu + 3\nu^2) [9(1-\nu) d_C^{dil} + (12(1-\nu)\Omega_{DG} + 4)d]}{(1-\nu) [(6(1-\nu)\Omega_{DG} + 2)d^2 + 9d_C^{dil} (1+\nu)d + 9(1-2\nu)(1+\nu)]^2}, \\ \zeta_2^{IDD} = \zeta_3^{IDD} &= \frac{E_M d_C^{dil} (2-\nu)^2 (d_C^{dil} (2-\nu) + 2\Omega_{DG}d)}{[\Omega_{DG}d^2 + d_C^{dil} (2-\nu)d + (1+\nu)(2-\nu)^2]^2}.\end{aligned}\quad (IV.74)$$

It is straightforward that all these eigenvalues are positive. The eigenvalues of the opposite of the derivatives of the effective stiffness tensor being all positive or null, the thermodynamic forces are consequently not negative. The form of the damage evolution law written in Eq. (IV.70) furthermore ensures that  $\dot{d}_i \geq 0$  ( $i \in [1, 2]$ ), so that the second principle of thermodynamics is respected for the three homogenization schemes considered.

### 12.2.5 Application in the case of multi-axial tension tests

The strain-based criterion introduced just above is presently employed to define the evolution laws of a mortar subjected to uniaxial and biaxial tension tests. As done previously with the Marigo criterion, the predictive capacity of the micromechanically-based damage model with the strain-based criterion is tested in the case of a mortar subjected to uniaxial tension (Le Bellégo 2001). The case of biaxial tension tests is also treated to observe how the crack densities of the different families of cracks evolve during non uniaxial tests. For concision, the different micromechanically-based approaches will be referred to as MT, IDD or simplified IDD damage models depending on the homogenization scheme chosen to compute the elastic properties of the damaged material. The mortar is initially assumed to be linear isotropic and is supposed to be in a plane stress state.

The consistency condition applied to the criterion defined in Eq. (IV.67) takes the form:

$$\lambda_1 = \frac{\frac{\partial f}{\partial \bar{\epsilon}_{DV}} : \dot{\bar{\epsilon}}_{DV}}{\frac{\partial f}{\partial d_i}}, \quad (IV.75)$$

providing the evolution of the crack density parameter plotted in Fig. IV.12. The post-peak behaviour is ruled by the rate form of the constitutive equation reading:

$$\dot{\sigma} = \mathbf{C}^*(d_i) : \dot{\epsilon} + \left( \frac{\partial \mathbf{C}^*}{\partial d_i} \dot{d}_i \right) : \epsilon, \quad (IV.76)$$

and is also plotted in Fig. IV.12. The values adopted for the damage parameters are respectively  $\epsilon_0 = 7 \times 10^{-5}$  and  $B = 7000$  providing a good fitting of the experimental stress-strain curve from Le Bellégo (2001). In particular, the typical damage softening effect observed in uniaxial tension is well reproduced.

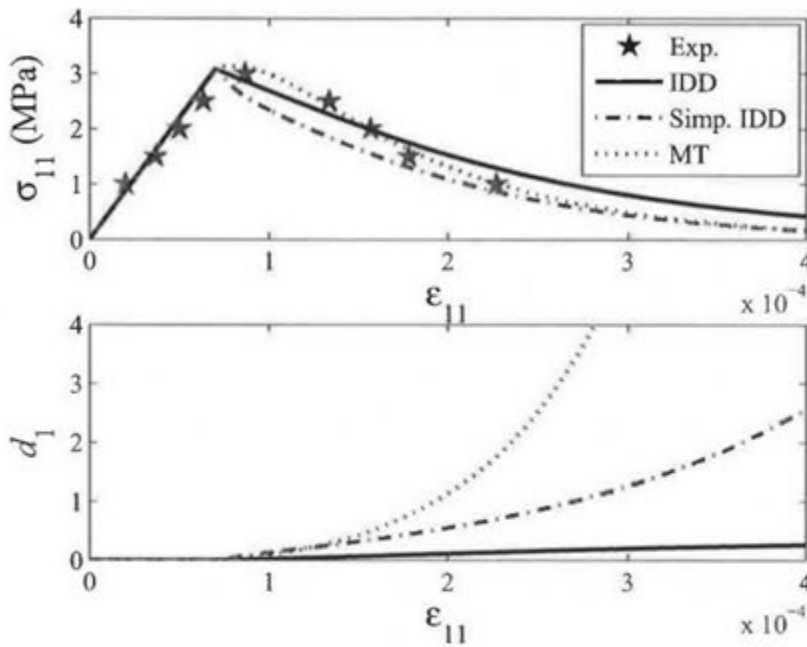


**Figure IV.12:** Comparison of the stress-strain curves predicted of a mortar subjected to uniaxial tension by the damage model with a strain-based criterion with the one experimentally recorded by Le Bellégo (2001) (up); evolution for the crack density parameters  $d_1$  and  $d_2$  predicted by the latter model (down).

The stress-strain curves predicted by the micromechanically-based damage models with the strain-based criterion in Eq. (IV.67) for mortar samples subjected to biaxial tensions along the two axis  $\mathbf{e}_1$  and  $\mathbf{e}_2$  with  $\epsilon_{11} = \epsilon_{22}$  and  $\epsilon_{11} = 3\epsilon_{22}$  are also plotted on Figs. IV.13 and IV.14, respectively. The IDD damage model leads to unexpected results. This shortcoming is due to the evolution law in Eqs. (IV.67-70) failing to work correctly when crack density parameters are not allowed to trespass a critical value. Nonetheless, the stress-strain curves estimated by MT and simplified IDD damage models, which account relatively well for the orthotropy induced by loadings, seem to be more consistent. However, a more involved damage model (e.g. Pensée 2003) would be necessary to reproduce correctly the induced anisotropy by more complex loadings, such as the Willam test.

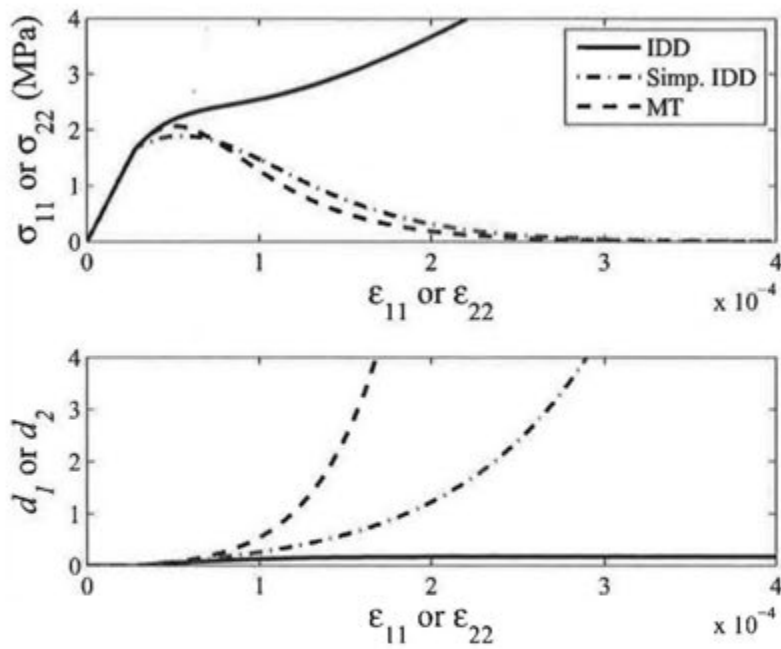


Figure IV.13: Stress-strain curves along the two principal axis of a mortar subjected to biaxial tension along the two axis  $e_1$  and  $e_2$  with  $\epsilon_{11} = \epsilon_{22}$  predicted by the damage model with Marigo criterion (up); evolutions for the crack density parameters  $d_1$  and  $d_2$  predicted by the latter model (down).

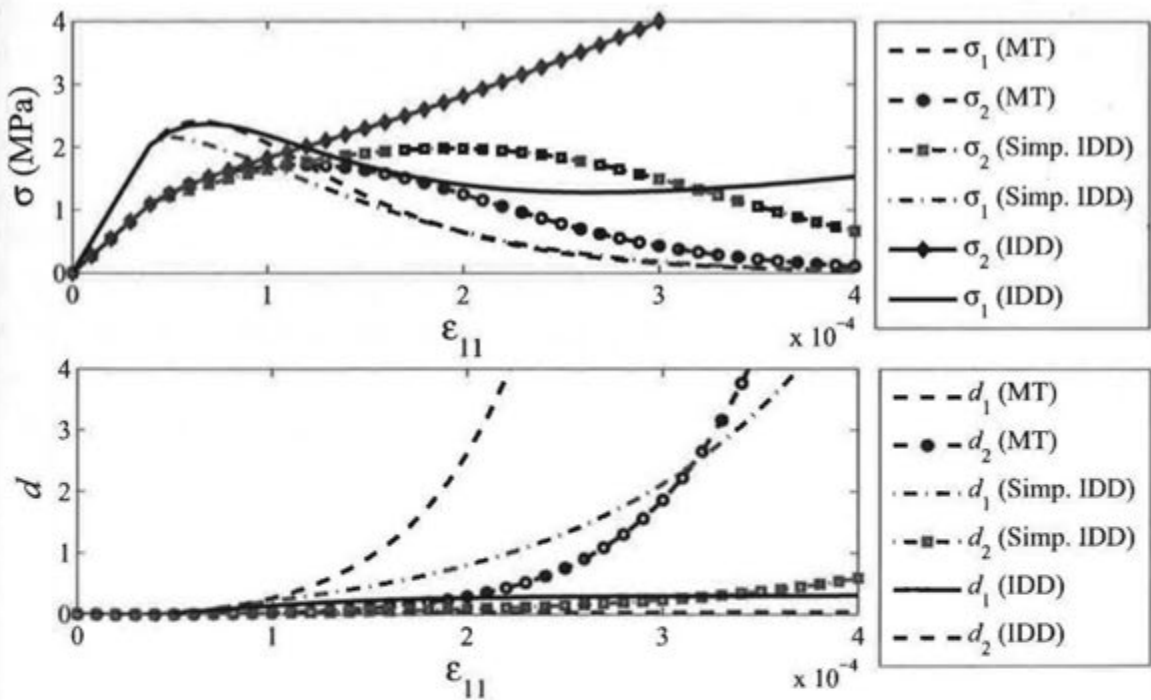


Figure IV.14: Stress-strain curves along the two principal axis of a mortar subjected to biaxial tension along the two axis  $e_1$  and  $e_2$  with  $\epsilon_{11} = 3\epsilon_{22}$  predicted by the damage model with Marigo criterion (up); evolutions for the crack density parameters  $d_1$  and  $d_2$  predicted by the latter model (down).

### 12.3 Conclusions of chapter 12

The evolution law has been established within the framework of thermodynamics of irreversible processes. Two theories, Marigo's one based on the GSM formalism and the other one using the concept of equivalent strain, have been assessed and applied to the micromechanically-based damage model. Their thermodynamical admissibility has also been investigated, showing the coherence of both theories. For our particular orthotropic model comprising two internal damage variables, the strain-based evolution law that seems easier to implement in a FE code is adopted. The criterion proposed by Marigo is attractive but requires some simplifications and perhaps more efforts (Zhu et al. 2007) for its use in numerical computations.

## CONCLUSIONS OF PART IV

An orthotropic damage model based on both micromechanics and thermodynamics of irreversible processes has been developed. The model comprises two damage variables, representing the density of cracks in two perpendicular directions, which is suited to deal with orthotropic damage under plane stress conditions. Different homogenization schemes have been tested for estimating the Helmholtz free energy. The IDD or PCW methods are shown to be of interest provided the damage variables do not trespass a certain critical crack density value. A simplified version of the IDD model has been developed to circumvent this difficulty. However, the original IDD or PCW scheme that is more standard is chosen for computing the damaged material behavior for a given damage state in the ensuing FE simulations.

A strain-based evolution law is established for the two micromechanical damage variables and the thermodynamical admissibility of the developed damage model has been verified. An application to the case of mortar samples subjected to uniaxial and biaxial tension tests has been proposed. In the subsequent Part, the IDD damage model is implemented in the FE code CAST3M and more complicated mechanical problems, such as flexion tests, are addressed.

### Appendix IV.A: Link between the dissipation potential and the damage threshold functions

As an example, we look after the dissipation potential providing the classical fracture-type criterion  $f$  written in Eq. (IV.34). For simplicity only one damage variable is considered. Using the definition of Legendre-Fenchel transform, the following equivalence can be established (e.g. Nguyen 2000):

$$Y_d \in \partial \Psi(\dot{d}) \Leftrightarrow \Psi^*(Y_d) + \Psi(\dot{d}) = Y_d \dot{d}, \quad (\text{IV.A1})$$

where  $\Psi^*$  is the Legendre-Fenchel transform of  $\Psi$ . For the particular case of a dissipation potential  $\Psi$  positive homogeneous of degree one, i.e.  $\forall \dot{d}, \forall k \geq 0, \Psi(k\dot{d}) = k\Psi(\dot{d})$ , its Legendre-Fenchel transform  $\Psi^*$  is immediate:

$$\Psi^*(Y_d) = \sup_{\dot{d}} (Y_d \dot{d} - \Psi(\dot{d})) = \mathcal{I}_K(Y_d) = \begin{cases} 0 & \text{if } Y_d \in K \\ \infty & \text{if } Y_d \notin K \end{cases}, \quad (\text{IV.A2})$$

where  $K$  is a convex domain defined by a threshold function  $f$ . It appears by employing the properties of the Legendre-Fenchel transform and the threshold function  $f$  given in Eq. (IV.34) that:

$$\Psi(\dot{d}) = \sup_{Y: f \leq 0} (Y_d \dot{d}) = \sup_{Y \leq Y_0} (Y_d \dot{d}). \quad (\text{IV.A3})$$

More precisely, the following dissipation potential homogeneous of degree one is deduced (Lorentz and Andrieux 2003):

$$\Psi(\dot{d}) = Y_0 \dot{d} + \mathcal{I}_{\mathbb{R}^+}(\dot{d}), \quad (\text{IV.A4})$$

where  $Y_0$  is the damage threshold in terms of elastic energy density and where the indicator function  $\mathcal{I}_{\mathbb{R}^+}(\dot{d})$  enforces the positivity of the damage rates.

### Appendix IV.B: Links between the De Vree and the Christensen criteria

In order to draw a comparison between the Christensen and the De Vree criteria, the latter is written in terms of stress invariants:

$$f_{DV} = \frac{k-1}{2C} I_1^{(\sigma)} + \frac{1}{2} \sqrt{\frac{(k-1)^2}{C^2} I_1^{(\sigma)2} + \frac{12k}{C^2} J_2^{(\sigma)}} - 1, \quad (IV.B1)$$

using those relations:

$$\frac{J_2^{(\sigma)}}{(1+\nu)^2} = \frac{J_2^{(\sigma)}}{E^2}; \frac{I_1^{(\sigma)}}{(1-2\nu)} = \frac{I_1^{(\sigma)}}{E}; C = kE\varepsilon_0^T. \quad (IV.B2)$$

It is easy to demonstrate that, when the De Vree criterion is verified  $f_{DV} = 0$ , the Christensen one is then automatically verified. The previous equation is first elevated to power square:

$$\left( \frac{k-1}{2C} I_1^{(\sigma)} + \frac{1}{2} \sqrt{\frac{(k-1)^2}{C^2} I_1^{(\sigma)2} + \frac{12k}{C^2} J_2^{(\sigma)}} \right)^2 = 1, \quad (IV.B3)$$

and is then expanded yielding the following relation:

$$\frac{1}{2} \left( \frac{k-1}{C} I_1^{(\sigma)} \right)^2 + \frac{1}{2} \frac{k-1}{C} I_1^{(\sigma)} \sqrt{\frac{(k-1)^2}{C^2} I_1^{(\sigma)2} + \frac{12k}{C^2} J_2^{(\sigma)}} + \frac{3k}{C^2} J_2^{(\sigma)} = 1. \quad (IV.B4)$$

By factorizing the terms with the first invariant of the stress tensor, we notice that:

$$\frac{k-1}{C} I_1^{(\sigma)} \left( \frac{k-1}{2C} I_1^{(\sigma)} + \frac{1}{2} \sqrt{\frac{(k-1)^2}{C^2} I_1^{(\sigma)2} + \frac{12k}{C^2} J_2^{(\sigma)}} \right) + \frac{3k}{C^2} J_2^{(\sigma)} = 1, \quad (IV.B5)$$

which simplifies into the form proposed by Christensen (2005):

$$\frac{k-1}{C} I_1^{(\sigma)} + \frac{3k}{C^2} J_2^{(\sigma)} = 1. \quad (IV.B6)$$

Conversely, supposing the latter equation verified, it can be recast in the following form:

$$\left( \frac{k-1}{2C} I_1^{(\sigma)} + \frac{3k}{C^2} J_2^{(\sigma)} \right)^2 = \left( 1 - \frac{k-1}{2C} I_1^{(\sigma)} \right)^2. \quad (IV.B7)$$

The left-hand member is then expanded:

$$\left( \frac{k-1}{2C} I_1^{(\sigma)} \right)^2 + \frac{3k}{C^2} J_2^{(\sigma)} \left( \frac{k-1}{C} I_1^{(\sigma)} + \frac{3k}{C^2} J_2^{(\sigma)} \right) = \left( 1 - \frac{k-1}{2C} I_1^{(\sigma)} \right)^2, \quad (IV.B8)$$

leading to:

$$\frac{1}{4} \left[ \left( \frac{k-1}{C} I_1^{(\sigma)} \right)^2 + \frac{12k}{C^2} J_2^{(\sigma)} \right] = \left( 1 - \frac{k-1}{2C} I_1^{(\sigma)} \right)^2. \quad (IV.B9)$$

If  $\left[ \left( \frac{k-1}{C} I_1^{(\sigma)} \right)^2 + \frac{12k}{C^2} J_2^{(\sigma)} \right] \left( 1 - \frac{k-1}{2C} I_1^{(\sigma)} \right) \geq 0$ , the De Vree criterion is retrieved.

## Part V

# SIMULATIONS OF THE CHEMO-MECHANICAL DEGRADATIONS BY LEACHING OF CEMENT-BASED MATERIALS

The service life of cement-based materials, which can serve as engineering barriers for the disposal of long-term nuclear wastes, is affected by the deterioration factors due to chemical attacks and mechanical damage, but also by the detrimental interactions between these phenomena. Precisely, the concrete underground structures can be both altered by: (i) dissolution – precipitation reactions caused by ionic migration, governed by the material transport properties, between the interstitial solution and ground water; (ii) damage due to external mechanical loadings and possibly precipitation of secondary solid phases generating internal pressures (e.g. sulfate attack).

Various experimental studies evidence significant negative interactions between these deterioration factors. For example, some authors (Tognazzi 1998) showed the existence of highly degraded areas around artificial cracks similar to those originated by mechanical damage. Hence, the nucleation and growth of cracks in the concrete may accelerate the transport phenomena and then enhance the chemical degradation process, which in turn creates an additional porosity that affects its overall mechanical behaviour. In addition, numerous investigations on the influence of calcium leaching on the residual mechanical behaviour of cement-based materials (e.g. Carde 1996; Gallé et al. 2004; Heukamp et al. 2005; Le Bellégo et al. 2003; Nguyen 2005) have concluded on the significant reduction of their elastic moduli and of their residual strength. They generally consist in performing mechanical tests such as uniaxial compression or traction tests (e.g. Carde 1996; Le Bellégo 2001; Nguyen 2005; Heukamp et al. 2005) or 3 points flexion tests (e.g. Le Bellégo 2001), on samples previously submitted to an accelerated leaching. Unfortunately, these experiments, designated as « residual resistance » tests, do not account for the effects of damage on the chemical degradation process. Nevertheless, some fully coupled experiments, designated as “life-time”, have been performed among others by Le Bellégo (2001) and Schneider and Chen (2005), where the material is submitted to a mechanical sollicitation and undergoes simultaneously a chemical attack by an aggressive solution of ammonium nitrate. These experiments may lead to the complete rupture after a few months.

Some approaches to model chemo-mechanical degradations of cement-based materials have been developed by the CEA/LECBA (Bary 2006) but also elsewhere (e.g. Gérard 1996; Heukamp 2002; Kuhl et al. 2004a; b; Le Bellégo et al. 2003; Nguyen 2005). They are however mostly based on simplifying assumptions, since it is generally supposed that only calcium ions governs the chemical equilibrium and/or that the influence of damage on diffusion is not accounted for.

The French Atomic Energy Commission (CEA) has developed in collaboration with ANDRA and EDF a numerical integration platform ALLIANCES capable of simulating problems that couple chemistry, transport and mechanics (Montarnal et al. 2006; 2007). This platform may allow for a more thorough modelling of chemo-mechanical degradations compared to existing approaches (e.g. Gérard 1996; Kuhl et al. 2004a; Bary 2006) by gathering within the same simulation environment a code resolving chemical equilibrium and a finite volume or element software dealing with transport and mechanical problems. The aim of the present work is to implement a comprehensive multi-physical model in this platform that:

- allows for predicting the effects of coupled chemo-mechanical deteriorations on cementitious materials;
- may be applied to any cement-based material, provided its initial composition and the physical properties of its elementary phases are known.

For this purpose, the multi-scale homogenization model developed in Parts II and III and the micromechanical damage model proposed in Part IV are implemented into the numerical platform to estimate the material mechanical behavior as well as its diffusive properties. One of the interests of these homogenization theories is to propose a deductive approach that may apply to diverse cementitious materials, provided the elastic and diffusive properties of their elementary phases are known. The integration in the ALLIANCES platform of a comprehensive homogenization model could thus permit to develop an advanced prediction tool of the degradation of real concrete structures. Furthermore, these upscaling methods help for a better comprehension of the influence of the microstructure and its evolution with time on the chemical and mechanical behaviors of these materials.

The scope of the present Part is two-fold. The first chapter is specifically devoted to the simulations of chemical degradations. After a brief presentation of how to model chemical degradations with the ALLIANCES platform, one-dimensional simulations of pure water and accelerated leaching of cement-based materials are thus proposed and validated. In the second chapter dedicated to the interactions between damage and chemical deteriorations, coupled chemo-mechanical simulations of simple structures subjected to decalcification and solicited in flexion are performed; confrontation of the numerical results with available experimental data (Le Bellégo 2001) is carried out and analyzed.

## **13 MODELLING AND SIMULATIONS OF THE CHEMICAL DEGRADATION WITH ALLIANCES PLATFORM**

### **13.1 Presentation of ALLIANCES**

The scope of this part is to detail the main steps for modelling chemo-mechanical degradations of cement-based materials with the ALLIANCES platform that is briefly

presented below. For more details concerning the latter platform, the reader should refer to Montarnal et al. (2006; 2007). The ALLIANCES platform allows for combining and connecting together diverse numerical codes dealing with different physical problems. This platform is developed in collaboration between CEA, ANDRA and EDF for the simulation of nuclear waste disposal. This tool programmed in Python is presently employed to couple chemistry, with the code CHESS (van der Lee and de Windt 2002), transport and mechanics, with the finite elements software CAST3M (CEA), so as to perform numerical simulations of the multi-physical degradation of cement-based materials. In the present context of long-term deterioration of concrete underground structures in nominal phase of waste storage, the following simplifying assumptions are made:

- the material is in saturated and isothermal conditions;
- electro-diffusive phenomena are neglected, ionic transfers being only due to molecular diffusion;
- the effects of creep are disregarded;
- the same diffusion coefficient is affected to all aqueous species;
- the chemical reactions are instantaneous compared to the diffusion process.

### *13.1.1 Coupled chemical-transport problem solved by ALLIANCES*

The chemical degradation of cement-based materials is a chemical-transport coupled problem. For example, in the case of the concrete underground structures in contact with ground water, the existence of concentrations gradients of ions between the interstitial solution and ground water provokes ionic migration inside the interstitial solution, governed by the material transport properties. This movement of ions disturbs the chemical equilibrium state between the solid skeleton and the pore solution of the material and causes dissolution-precipitation reactions in the material. Therefore, the evolutions of the diffusion coefficients of ions in the material are important data for predicting its chemical alteration, as already mentioned in Part III.

Different types of chemical-transport coupled simulations have been performed on concrete materials. Some authors (e.g. Adenot 1992; Gérard 1996) proposed simplified approaches, where only calcium ions are supposed to govern the main chemical reactions. More complete simulations are recently available (e.g. Moranville et al. 2004; Planel 2002), where the current chemical equilibrium state is obtained by means of a chemical equilibrium code. Planel (2002) thus modelled the sulfate attack of HCP with HYTECH (van der Lee et al. 2003), based on both geochemistry and transport codes. Moranville et al. (2004) ran with the help of the CEMHYD3D model of NIST (Bentz et al. 2002) simulations of pure water degradations that are quite comparable to the ones presently realized. It is pointed out that the ALLIANCES platform is capable of treating multi-species reactive transport problems on the contrary to many simplified coupled approaches developed for cement-based materials (e.g.

G erard 1996). This is important in the case of decalcification for modelling for instance the migration of alkalis or simulating accelerated leachings by  $\text{NH}_4\text{NO}_3$  because of the penetration of  $\text{NO}_3^-$ .

### 13.1.1.1 Transport equations solved by CAST3M

To present in a simple manner the transport equations solved by CAST3M, transport is first supposed to occur in a non reactive porous medium representing the cement-based material. Inside this medium, the species that may move are the fluid filling the porosity and the chemical species concentrated in the fluid. The finite volume method is used for the computations. The medium is thus represented by a number  $w$  of subvolumes  $V_i$  each comprising  $M_i$  mineral phases supposed homogeneous. The interstitial solution in each subvolume contains  $N$  aqueous species, most of them being ions. For simplicity, the cinematic dispersion is neglected. Under such conditions, the conservation law imposes that the divergence of the sum of the average diffusive flux vector of ions  $j$  denoted  $\bar{\mathbf{J}}_j$  through a given subvolume  $V_i$  and of the average velocity vector denoted  $\bar{\mathbf{U}}$  is equal to the variation of concentration designated by  $C_j$  of ions  $j$  in  $V_i$ :

$$-\text{div}(\bar{\mathbf{J}}_j + C_j \bar{\mathbf{U}}) = c_p \frac{\partial C_j}{\partial t}, \quad (\text{V.1})$$

where  $c_p$  is the average porosity inside the subvolume  $V_i$ . In the present case, the velocity vector  $\bar{\mathbf{U}}$  of the fluid is null because it is assumed that no pressure gradient provokes water transport by permeation and the previous equation simplifies into:

$$-\text{div}(\bar{\mathbf{J}}_j) = c_p \frac{\partial C_j}{\partial t}. \quad (\text{V.2})$$

The ions flux vectors depend on gradients of ions concentration and/or on electric gradients. However, the possible influence of the electric charges of ions on diffusion being presently neglected, the ions flux vectors are expressed by Fick's law.

At the scale of the heterogeneities of the material, Fick's law, stipulating that the microscopic flux of ions  $j$  is proportional to the microscopic gradient of concentration, reads:

$$\mathbf{J}_j(x) = -\mathbf{D}_j(x) \cdot \text{grad} C_j(x), \quad \forall x \in V, \quad (\text{V.3})$$

where  $\text{grad} C_j(x)$  is the gradient of concentration of ions  $j$  and the operator ' $\cdot$ ' indicates a simple contraction. The ensuing relations are obtained by averaging in each subvolume  $V_i$ :

$$\bar{\mathbf{J}}_j = -\mathbf{D}_j^* \cdot \overline{\text{grad} C_j(x)}. \quad (\text{V.4})$$

The diverse homogenization techniques (e.g. Torquato 2001) can provide estimations for the effective second order diffusion tensors  $\mathbf{D}_j^*$  of the diverse ionic species through the material. In the ALLIANCES platform, all these tensors are supposed to be identical for all the species,

so that only one effective tensor  $\mathbf{D}^*$  is involved. Furthermore, the cementitious materials are considered to be macroscopically isotropic so that this effective second order diffusion tensor  $\mathbf{D}^*$  simplifies into  $D^*\mathbf{1}$ , where  $D^*$  is a scalar. By combining Eqs. (V.2) and (V.4), the transport equations solved by CAST3M are written in the following way:

$$c_p \frac{\partial C_i}{\partial t} = \text{div}(\mathbf{D}^* \overline{\text{grad } C_i}), \forall i \in \{1, \dots, N\}, \quad (\text{V.5})$$

where  $N$  refers to the total number of aqueous species. In addition to the transport process, the effects of chemical reactions in the case of concrete have to be accounted for. The cement-based material is initially taken in a stable chemical state. The possible leak of aqueous species such as  $\text{Ca}^{2+}$  precised by the transport equations may disturb this equilibrium state. The new equilibrium state of the perturbed system can be computed by means of the chemical equilibrium code CHESS (van der Lee and de Windt 2002), assuming that the chemical reactions are instantaneous in comparison with the transport process.

#### 13.1.1.2 Chemical reactions computed by CHESS

The dissolution reaction of a mineral specie denoted  $e_m$  in contact with an aggressive ionic specie, designated by  $e_{ia}^{z+}$  with  $z$  being an integer, forms aqueous species  $e_i^{z+}$  in the interstitial solution:



where  $\chi_{im}$  designates the stoichiometric coefficients of the dissolution reaction. This reaction is controlled by the following mass action law:

$$K_m^d = \prod_{i=1}^N [e_{ia}^{z+}]^{-1} [e_m]^{-1} [e_i^{z+}]^{\chi_{im}}, \quad (\text{V.7})$$

where  $K_m^d$  is the equilibrium constant of the dissolution reaction and the brackets surrounding a given specie designates its activity. The activity of a component is generally related to its concentration by:

$$[e_i] = \gamma_i p_i, \quad (\text{V.8})$$

where  $\gamma_i$  is the activity coefficient that can be considered equal to one for dilute solutions and  $p_i$  designates the concentration in mol per liter of solution of the component or specie  $i$ . For higher concentrations, diverse methods accounting for example for ion interactions exist to relate the concentrations and activities of the species. The CHESS software proposes several models for computing the activity coefficient, and in the following we retain the modified Davies method. It must be borne in mind that the dissolution of a mineral, such as portlandite

in the case of leaching (see Eq (I.6)), can also occur by itself without requiring a reaction with aggressive ionic specie.

The precipitation reaction of a mineral specie  $e_m$  from aqueous species over the saturation limit inside the interstitial solution reads:



with the following action mass law:

$$K_m^p = \prod_{i=1}^N [e_m] [e_i^{z+}]^{-\chi_{im}}. \quad (\text{V.10})$$

### 13.1.1.3 Coupled chemical-transport equations solved by ALLIANCES

The ALLIANCES platform solves the chemical-transport problem by coupling the chemical equilibrium code (CHESS) with transport (finite volume, CAST3M) in the following manner:

$$\begin{cases} \frac{\partial(c_p C_j)}{\partial t} = \text{Tr}(c_p, c_m, C_j), \\ (C_j, p_m) = \text{Ch}_{0j}(C_j), \\ c_p = \left(1 + \sum_{m=1}^{Mi} V_m p_m\right)^{-1}, \forall j \in \{1, \dots, N\}, \forall m \in \{1, \dots, Mi\}, \end{cases} \quad (\text{V.11})$$

where  $c_m$ ,  $c_p$  respectively denote the volume fractions of the mineral phase  $m$  and of porosity,  $V_m$  designates the molar volume (L/mol) of the mineral  $m$ ,  $Mi$  is the total number of mineral species and the concentration  $C_j$  of ions  $j$  is expressed in mol per liter of solution.

The operators Tr and Ch, respectively computed by CAST3M and CHESS, are such as:

$$\text{Tr}(c_p, c_m, C_j) = \text{div}(\mathbf{D}^*(c_p, c_m) \cdot \overline{\text{grad}(C_j)}), \quad (\text{V.12})$$

$$\text{Ch}_{0j}(C_j) = \begin{cases} \text{precipitation} & K_m^p = \prod_{i=1}^N [e_m] [e_j^{z+}]^{-\chi_{jm}}, \\ \text{dissolution} & K_m^d = \prod_{i=1}^N [e_{ja}^{z+}]^{-1} [e_m]^{-1} [e_j^{z+}]^{\chi_{jm}}, \end{cases}$$

where  $K_m^p$ ,  $K_m^d$  and  $\chi_{jm}$  have been defined previously. The effective diffusion coefficient  $\mathbf{D}^*$  depends of the porosity and of the volume fractions of minerals. Eq. (V.11) presents how these quantities are computed with ALLIANCES. It is noteworthy that diverse empirical diffusion laws, such as the ones of Winsauer and Tognazzi, are already implemented in ALLIANCES (Nozourtier-Mazauric 2004). In order to show the importance of the evolution law chosen for the macroscopic diffusion coefficient, different types of laws, such as Tognazzi's one (1998), are tested in the first simulations of leaching on cement pastes.

#### 13.1.1.4 Computations of the chemical-transport loop with ALLIANCES

A schematic description of the modelling of chemo-mechanical degradations is presented in Fig. V.1. The first step consists in implementing a homogenization model in order to estimate the material effective diffusive properties from its composition. By communicating with a chemical equilibrium code (CHESS), ALLIANCES in a second step updates at each time step the mineral composition and the porosity of the cement and computes the evolution of the diffusivity inside the material from its current composition. This practically corresponds to the chemical-transport loop depicted on the left-hand side of Fig. V.1. The coupling algorithm is sequential iterative (Yeh and Tripathi 1989) and has been validated on different tests (Montarnal et al. 2007). The fixed-point algorithm used to solve the transport equations is implicit in time (Nozourtier-Mazauric 2004), but the scheme employed to solve the chemical part is explicit. The precision concerning the chemical resolution is fixed by the user and is defined at a given time step  $t + 1$  from the total concentrations of the constituting species as follows:

$$\frac{\|F^{t+1,j+1} - F^{t+1,j}\|}{\|F^{t+1,j+1}\|} < \text{Pr}, \quad \text{with} \quad F^{t+1,j} = \sum_j \sum_{m=1}^{M_j} \chi_{jm} P_m \quad (l \in \{1, \dots, I_{\max}\}), \quad (\text{V.13})$$

where Pr designates the precision,  $l$  is the iteration index and  $I_{\max}$  is the maximal number of iterations desired. ALLIANCES then adapts the time steps so that convergence is obtained within this number of steps. It is often necessary to impose a precision less than  $10^{-6}$  resulting in small time steps, practically a few hundreds of seconds, to ensure convergence of the computations.

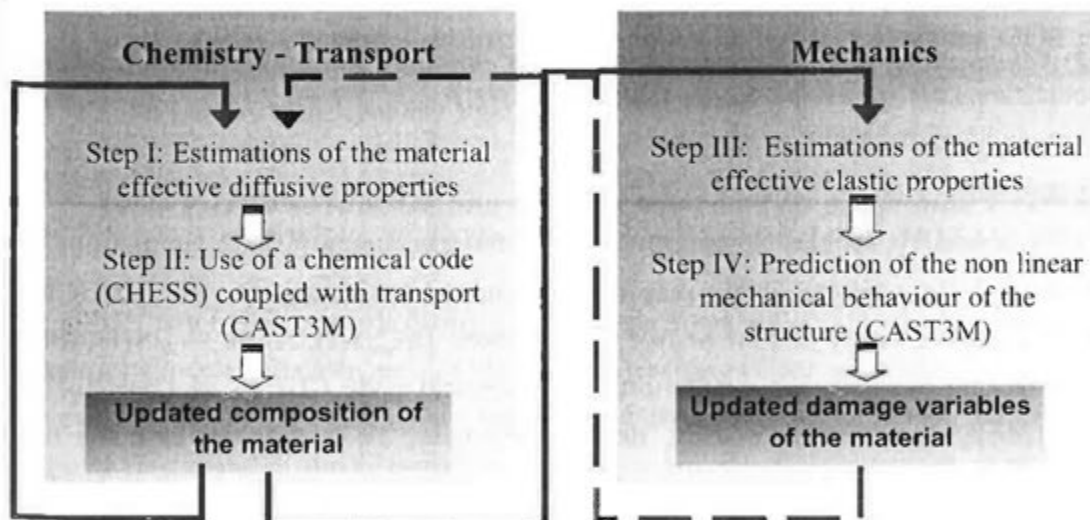
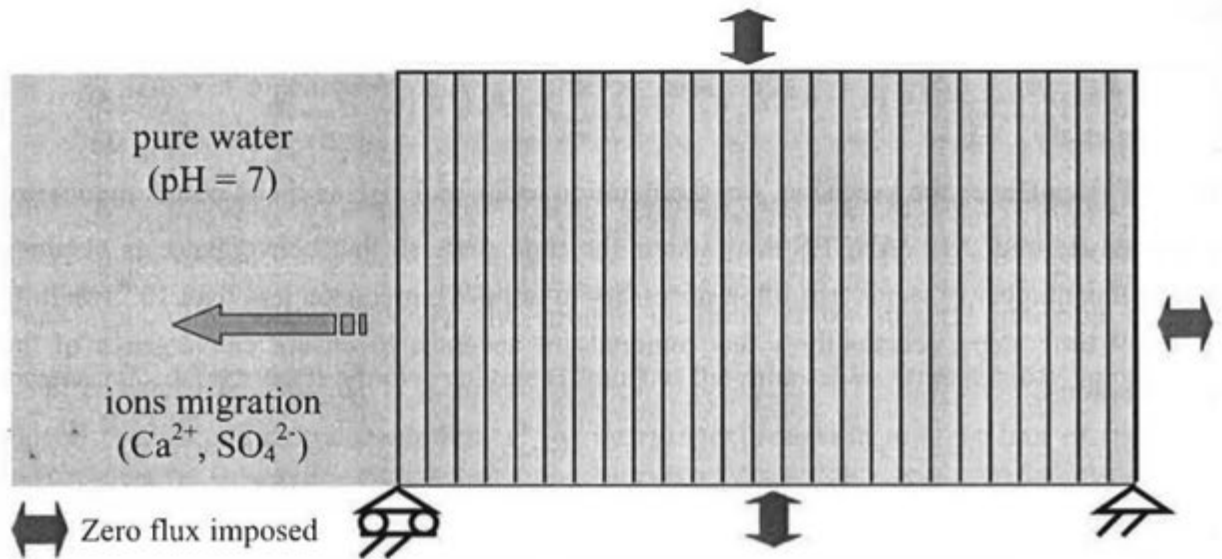


Figure V.1: Schematic of the modelling of chemo-mechanical degradations of cement-based materials with ALLIANCES.

## 13.2 Simulations of the decalcification of cement pastes

### 13.2.1 System considered

The following one-dimensional system (Fig. V.2) is adopted for the simulations of leaching process. A hydrated cement paste sample, simply modelled as a rectangle with 3 mm of length and 1 mm of height, is in contact on its left extremity with pure water (pH = 7), while a zero flux condition is imposed on the other one. The mesh used is composed of 30 rectangular subvolumes. The computations of the chemistry - transport loop are then performed with the finite volume method and provide the mineral composition at each center of the subvolumes. For simplicity, alkalis are not taken into account in the interstitial solution, since they rapidly disappear during the leaching process as observed in the leaching simulations of Moranville et al. (2004). Consequently, the pH of the interstitial solution is fixed by the equilibrium with portlandite and is initially about 12.5. The temperature considered constant is 25°C.



*Figure V.2: Schematic of the one-dimensional system employed for the simulations of pure water leaching of HCP.*

### 13.2.2 Input data

The input data necessary for the chemistry - transport - mechanics (CTM) simulations are listed in Table V.1. In order to obtain reasonable computations times, non altered HCP is assumed to be composed only of four or five main phases: [UC, CH, AFm, C<sub>1.65</sub>SH, AFt or hydrogarnet]. During the leaching simulations, the chemical code CHESS searches for the new mineral phases that precipitate using its huge database. To further decrease the time computation, the database is reduced to the following system for altered HCP: [CH, AFt, AFm, C<sub>1.65</sub>SH, C<sub>1.25</sub>SH, C<sub>0.90</sub>SH, SiO<sub>2</sub>(am), diaspore, gypsum, hydrogarnet], where SiO<sub>2</sub>(am) refers to the amorphous silicon gel. The chemical formulae and the equilibrium constants of

these mineral phases are given in Appendix V.A. On the contrary to portlandite that can totally dissolve during the degradation of a cement paste, the decalcification of CSH rather implies a progressive decrease of their C/S ratio. As a consequence, their diffusive and elastic properties are gradually diminished. To model this degradation in a simplified way, three types of CSH with diverse C/S ratios ( $C/S = 1.65, 1.25, 0.90$ ) corresponding to more or less decalcified states, are introduced in CHESS. Silicon gel  $SiO_2(am)$  is furthermore introduced in the chemical system to represent the most decalcified state of CSH. The anhydrous residuals are supposed to be unreactive, since they only represent a few percent in terms of volume fractions and modelling their hydration would require very long computation times. With this system, the following chemical species mainly appear in the interstitial solution:  $[Ca^{2+}, SO_4^{2-}, Al^{3+}, SiO_2(aq)]$ . Alkalis ( $Na^+, K^+$ ) and ions such as  $Fe^{3+}$  or  $Mg^{2+}$  are not taken into account, even though they are usually present in the interstitial solution.

| Chemistry  | Mechanics   |
|--|---|
| <ul style="list-style-type: none"> <li>Concentrations of the initial mineral species: <math>p_m, m \in [CH, AFm, CSH_{1.65}, AFt \text{ or Hydrogarnet}]</math>;</li> <li>pH and composition of the external solution .</li> </ul>   | <ul style="list-style-type: none"> <li>Elastic properties of mineral species: <math>E_m, \nu_m</math>, with <math>m \in [CH, AFt, AFm, C_{1.65}SH, C_{1.25}SH, C_{0.90}SH, SiO_2(am), \text{diaspore, gypsum, hydrogarnet}]</math>;</li> <li>Parameters of the damage model;</li> <li>Initial and boundary conditions.</li> </ul> |
| Transport  |   |
| <ul style="list-style-type: none"> <li>Diffusivities of all the mineral species: <math>E_m, \nu_m</math>, with <math>m \in [CH, AFt, AFm, C_{1.65}SH, C_{1.25}SH, C_{0.90}SH, SiO_2(am), \text{diaspore, gypsum, hydrogarnet}]</math>;</li> <li>Diffusivities of gel and capillary pores: <math>D_{GP}, D_{CP}</math>;</li> <li>MCSA parameters: <math>f^{int}</math> and <math>f^{ext}</math> (Part III)</li> </ul> |   |
| Coupling Chemistry –transport  | Coupling CTM  |
| Parameters of the coupling algorithm.  | Frequency of the computations of the damage state with CAST3M.  |

**Table V.1: Table summarizing the main input data for performing CTM coupled simulations using the homogenization model with ALLIANCES.**

The  $CSH^{int}$  and  $CSH^{ext}$  are not distinguished in the chemical computations, since their relative proportions inside the paste are not affected by leaching (Constantinides and Ulm 2004). It is however necessary to differentiate them in the homogenization model, because they have different elastic and diffusive properties, as shown previously in the manuscript. Their relative volume fractions are given by Tennis and Jennings (2000). Constantinides and Ulm (2004) have measured the Young moduli of  $CSH^{int}$  and  $CSH^{ext}$  both for sound and asymptotically leached states, their C/S ratio decreasing to 0.8 (Heukamp 2002). By asymptotically leached,

it is intended that the sample has been so severely attacked that it reaches a uniform degraded state. It is supposed that the effective diffusivities and Young moduli of the two heterogeneous CSH evolve as a function of their  $C/S$  ratios comprised between 0 and 1.65 in the following manner:

$$\begin{cases} \text{if } C/S > 0.8, & E_{CSH_{int\ or\ ext}} = \left(1 - \frac{C/S - 0.8}{1.65 - 0.8}\right) E_{CSH_{int\ or\ ext}}^{UL} + \frac{C/S - 0.8}{1.65 - 0.8} E_{CSH_{int\ or\ ext}}^S; \\ \text{if } C/S \leq 0.8, & E_{CSH_{int\ or\ ext}} = E_{CSH_{int\ or\ ext}}^{UL}; \\ \text{if } C/S > 0.8, & D_{CSH_{int\ or\ ext}} = \left(1 - \frac{C/S - 0.8}{1.65 - 0.8}\right) D_{CSH_{int\ or\ ext}}^{UL} + \frac{C/S - 0.8}{1.65 - 0.8} D_{CSH_{int\ or\ ext}}^S; \\ \text{if } C/S \leq 0.8, & D_{CSH_{int\ or\ ext}} = D_{CSH_{int\ or\ ext}}^{UL}, \end{cases} \quad (V.14)$$

where the superscripts S and UL mean sound and uniformly leached, respectively. The values of the Young moduli  $E_{CSH_{int\ or\ ext}}^S$  and  $E_{CSH_{int\ or\ ext}}^{UL}$  are taken from Constantinides and Ulm (2004) and the diffusivities  $D_{CSH_{int\ or\ ext}}^S$  and  $D_{CSH_{int\ or\ ext}}^{UL}$  are estimated by means of the MCSA model developed in Part III. The Poisson ratio is assumed to remain constant during leaching (Stora et al. 2006a).

The reference cement paste used for the simulations is the Origny CEM I 42.5 paste with  $w/c = 0.40$ , since it corresponds to the one used by Le Bellégo (2001) in her experiments. Furthermore, this type of cement paste is well characterized (e.g. Adenot 1992; Baroghel-Bouny 1994) and its mechanical behavior has also been studied (Carde 1996; Le Bellégo 2001). The CEM I 42.5 paste is presently assumed to be initially composed only of five phases (Le Bellégo 2001): UC,  $C_{1.65}SH$ , CH, AFm and AFt. The initial composition of the material (in mol/L), computed by Le Bellégo (2001) by means of the simplified model from Adenot (1992), is given in Table V.2. The hydration rate is estimated in the calculations of phase volume fractions so as to retrieve the same value for total porosity as the water porosity measured experimentally (Le Bellégo 2001). The composition of the paste is a little particular because of its high concentration in AFm.

| Phases                          | Origny CEM I 42.5<br>paste (w/c = 0.40)<br>(Le Bellégo 2001;<br>Adenot 1992) | Lafarge CEM I 52.5<br>HTS paste (w/c = 0.45)<br>(Gallé et al. 2004) |
|---------------------------------|--|---|
| Estimated hydration rate        | 0.80   | 0.88  |
| CH (mol/L)                      | 3.54   | 4.56  |
| AFt (mol/L)                     | 0.0873   | 0.00  |
| AFm (mol/L)                     | 0.45   | 0.199   |
| Hydrogarnet (mol/L)             | 0.00   | 0.478   |
| CSH (mol/L)                     | 3.86   | 4.44  |
| UC                              | 0.074  | 0.043   |
| Water porosity                  | 0.27   | 0.319   |
| $D_{ini}^*$ (m <sup>2</sup> /s) | $2.80 \cdot 10^{-12}$<br>(Tognazzi 1998)                                     | $5.21 \cdot 10^{-12}$<br>(Richet et al. 1997)                       |

**Table V.2: Initial composition of the two CEM I pastes used for the simulations.**

### 13.2.3 Influence of the diffusion law on the chemical degradation

Simulations with three different diffusion laws enlisted below are performed on the CEM I 42.5 paste to put in evidence the influence of the evolution of diffusivity on the leaching process. The first simulation is thus made employing a simple proportional law designated by  $D_{prop}^*$ :

$$D_{prop}^* = D_{ini}^* \frac{c_p}{c_p^{ini}}, \quad (V.15)$$

the second one adopts Tognazzi's law denoted as  $D_{Togn}^*$  for predicting the evolution of the diffusion coefficients:

$$D_{Togn}^* = D_{ini}^* \exp(9.95(c_p - c_p^{ini})), \quad (V.16)$$

while the third one uses the multi-scale homogenization model defined in Part II for estimating the diffusivities. In the equations above,  $D_{ini}^*$  refers to the effective diffusivity of the non altered paste,  $c_p$  and  $c_p^{ini}$  denote the current and initial total porosities of the paste, respectively. The mineral compositions of the CEM I 42.5 paste with w/c = 0.40 degraded by pure water after 50 days, computed at each center of the subvolumes (see Fig. V.3) with ALLIANCES using respectively the three types of laws, as a function of the depth of the simulated samples are plotted on Fig. V.3. As a complement, Fig. V.4 shows the evolutions of the diffusion coefficient inside the CEM I paste for the three simulations.

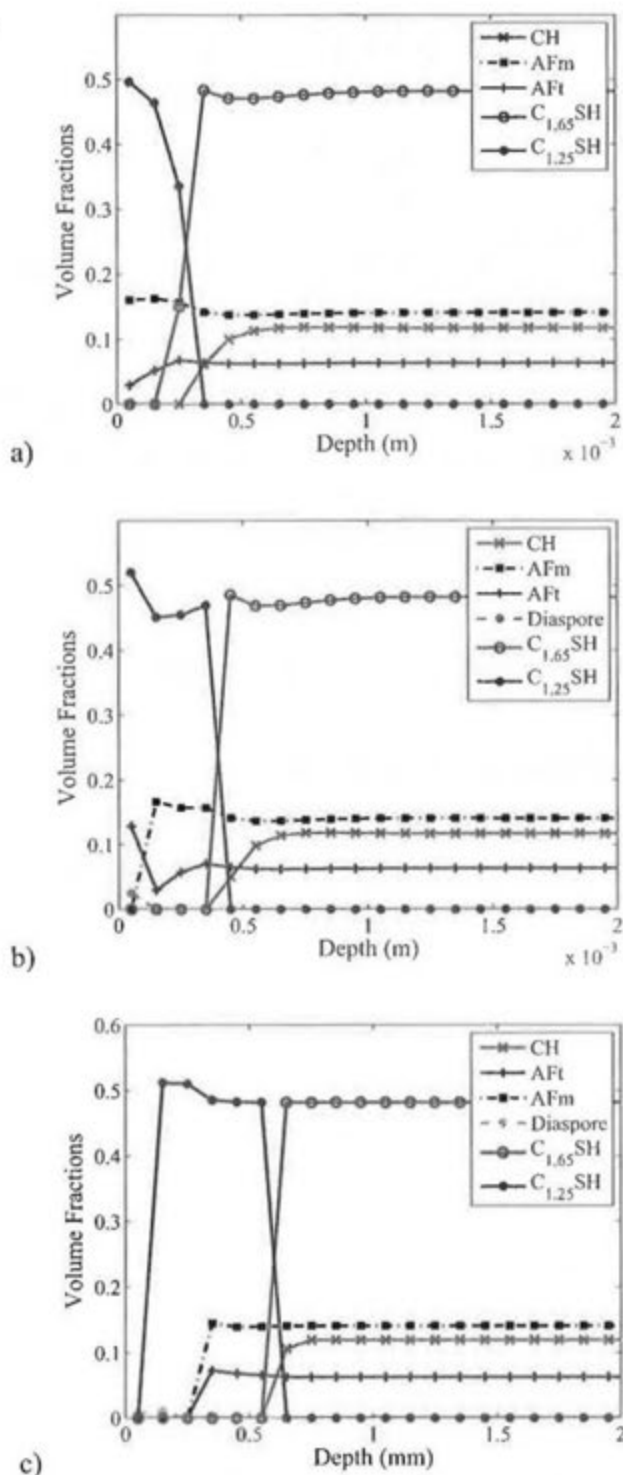


**Figure V.3: Mineral compositions in terms of volume fractions inside a sample of CEM I 42.5 paste with  $w/c = 0.40$  subjected to a 50 days attack by pure water simulated with ALLIANCES using a) a proportional law, b) Tognazzi's law and c) the multi-scale homogenization model, respectively.**

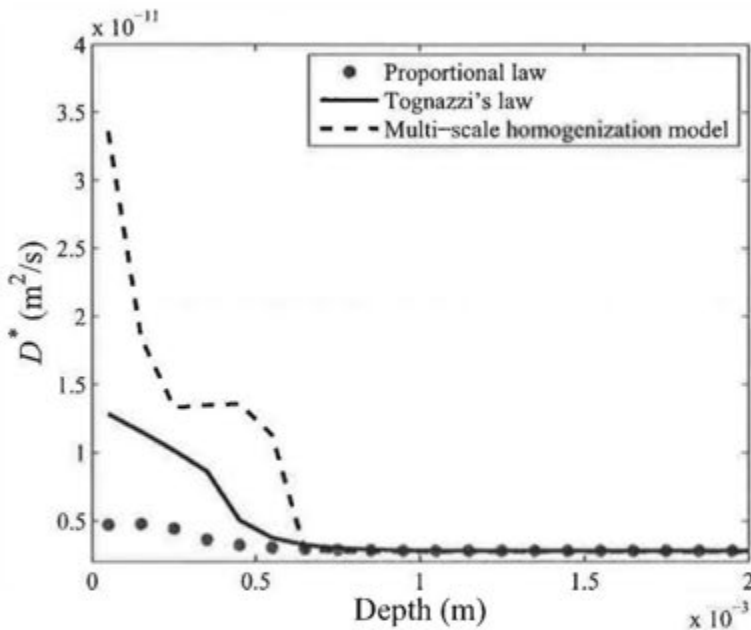


**Figure V.4: Evolutions of the macroscopic diffusivity inside a sample of CEM I 42.5 paste ( $w/c = 0.40$ ) subjected to a 50 days attack by pure water simulated with ALLIANCES using a proportional law (red), Tognazzi's law (blue) and our homogenization model (dashed), respectively.**

On Fig. V.3, the volume fractions of the different mineral phases inside the HCP strongly evolve near the left-hand zone in contact with pure water but these evolutions are different for the three simulations computed with diverse diffusion laws. In parallel, the ionic diffusivities are seen to increase on Fig. V.4 in this altered zone due to the additional porosity created by the dissolution of certain mineral phases. These augmentations in the deteriorated zone are much more significant with Tognazzi's law and the homogenization model than with the proportional law. It thus appears clearly by comparing Figs. V.3 and V.4 that the evolution of the diffusion coefficient inside the paste significantly impacts the degradation process.

In the three simulations, portlandite is the phase that is most affected by leaching, since its complete dissolution may be observed on the left-hand sides of Fig. V.3 in good accordance with the experimental observations (e.g. Adenot 1992). The two aluminous phases, AFt and AFm, dissolve at a lower calcium concentration in pore solution. It should also be noted on Fig. V.3b) that with Tognazzi's law AFt reprecipitates in the zone where AFm has dissolved, as is habitually viewed experimentally. Conservely, no reprecipitation of AFt is observed with the proportional law and furthermore AFt starts to dissolve before AFm. This is contradictory with the dissolution sequences evidenced by Adenot (1992). According to his work, CH dissolves before AFm that should themselves dissolve before AFt. On the contrary, the decalcification of CSH should occur in a progressive manner, as already mentioned. On the three figures, the CSH are thus progressively decalcified: as the  $C_{1.65}SH$  dissolve (where the

subscript 1.65 refers to the C/S ratio), CSH with a lower C/S ratio,  $C_{1.25}SH$ , simultaneously precipitate.

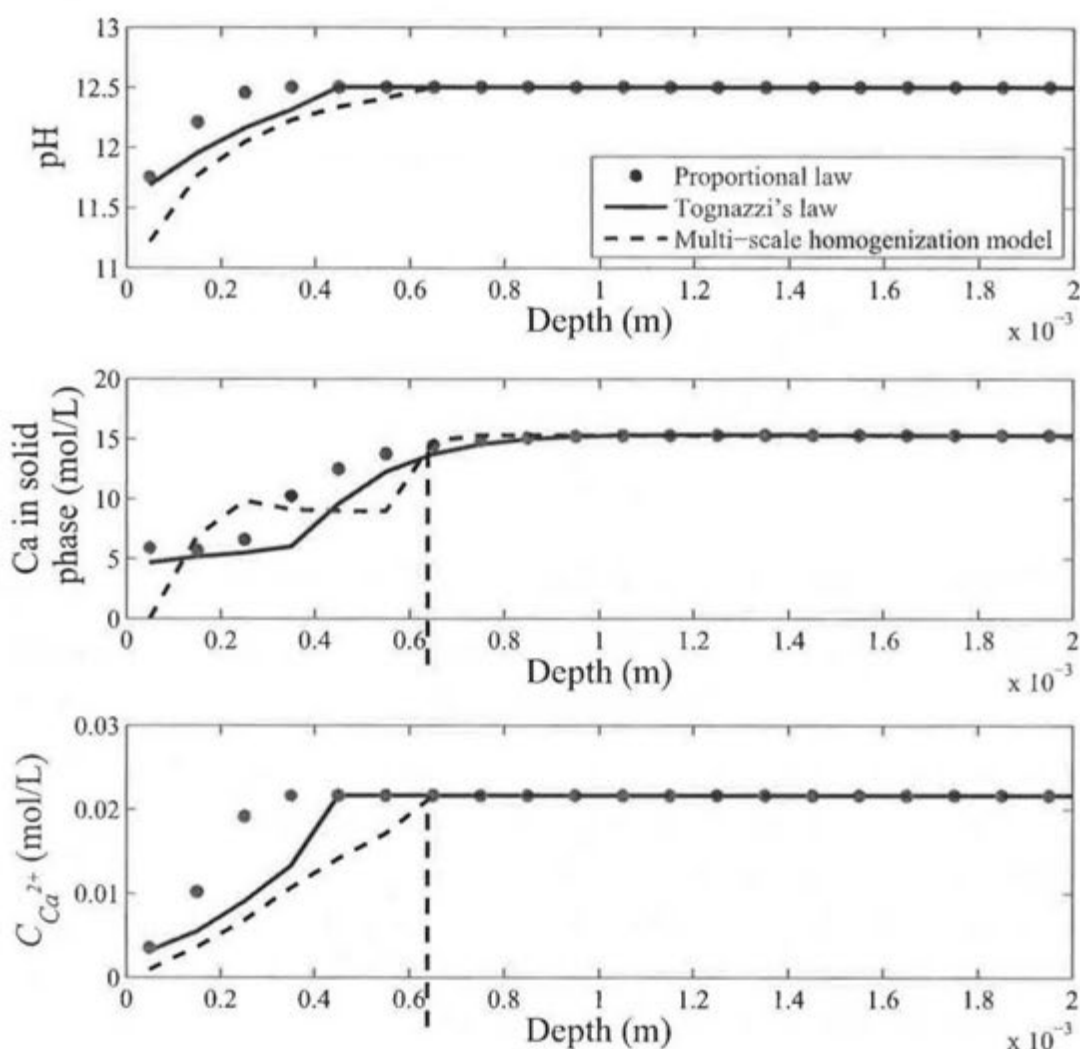


**Figure V.5:** Evolutions of the pH of the interstitial solution and of the calcium concentrations in solid phase and in solution inside a CEM I 42.5 paste with  $w/c = 0.40$  subjected to a 50 days attack by pure water simulated with ALLIANCES using a proportional law (red), Tognazzi's law (blue) and the multi-scale homogenization model (dashed), respectively.

The calcium concentration profiles in solution and in solid phase and the pH curve plotted on Fig. V.5 are quite comparable with those from Moranville et al. (2004). As expected, these profiles strongly depend on the presence of CH. Indeed, the calcium concentration in solid phase decreases as soon as CH starts to dissolve. Furthermore, its presence controls the pH and the calcium concentration in solution and both decrease whenever CH is totally dissolved. The dissolution of CH usually occurs very rapidly so that the degradation depths on Fig. V.5 can be estimated by quoting the beginning of the decrease in the profile of calcium either in solution or in solid phase. This dissolution front is represented by vertical bars on Fig. V.5 for

the calcium profiles obtained with the homogenization model. The two bars logically coincide and thus allow for determining the leaching front propagation. For Tognazzi's law and for the proportional one, it is difficult to make such a determination, since the beginnings of the decrease in the two different calcium profiles are far one from another. This discrepancy may be caused by the poor increase of the diffusivity when CH starts to dissolve (see Fig. V.4).

The depths predicted with the simulations done with Tognazzi's law and the homogenization model are bigger than those obtained with the proportional law. This may be explained easily: the higher the diffusivity of the paste (see Fig. V.4), the faster the concentration of aqueous species, such as  $\text{Ca}^{2+}$ , diminishes in the interstitial solution, thus enhancing the dissolution process. Experimentally, the degradation depth can be measured by different ways, for example from electronic microprobe or by phenolphthalein (Le Bellégo 2001). The dissolution front propagations provided by the numerical tries with the homogenization model are quite close from the degradation front propagation experimentally measured by SEM (Adenot and Buil 1992) on a similar paste that is about  $0.15 \text{ mm} / \text{days}^{0.5}$  (see Table V.3).

The results obtained with Tognazzi's law and with our model are far better than those provided with a proportional law. This shows the importance of using a realistic diffusion law. The multi-scale homogenization model presents the benefit to be more general than the empirical Tognazzi's law that has been specifically developed for CEM I pastes on the basis of diffusion experiments on several pastes with different porosity (Tognazzi 1998). This law that was proved to be reliable for the standard pastes chosen for our simulations is not necessarily applicable for other types of cement pastes, such as CEM V. The multi-scale homogenization model is therefore adopted for the subsequent simulations.

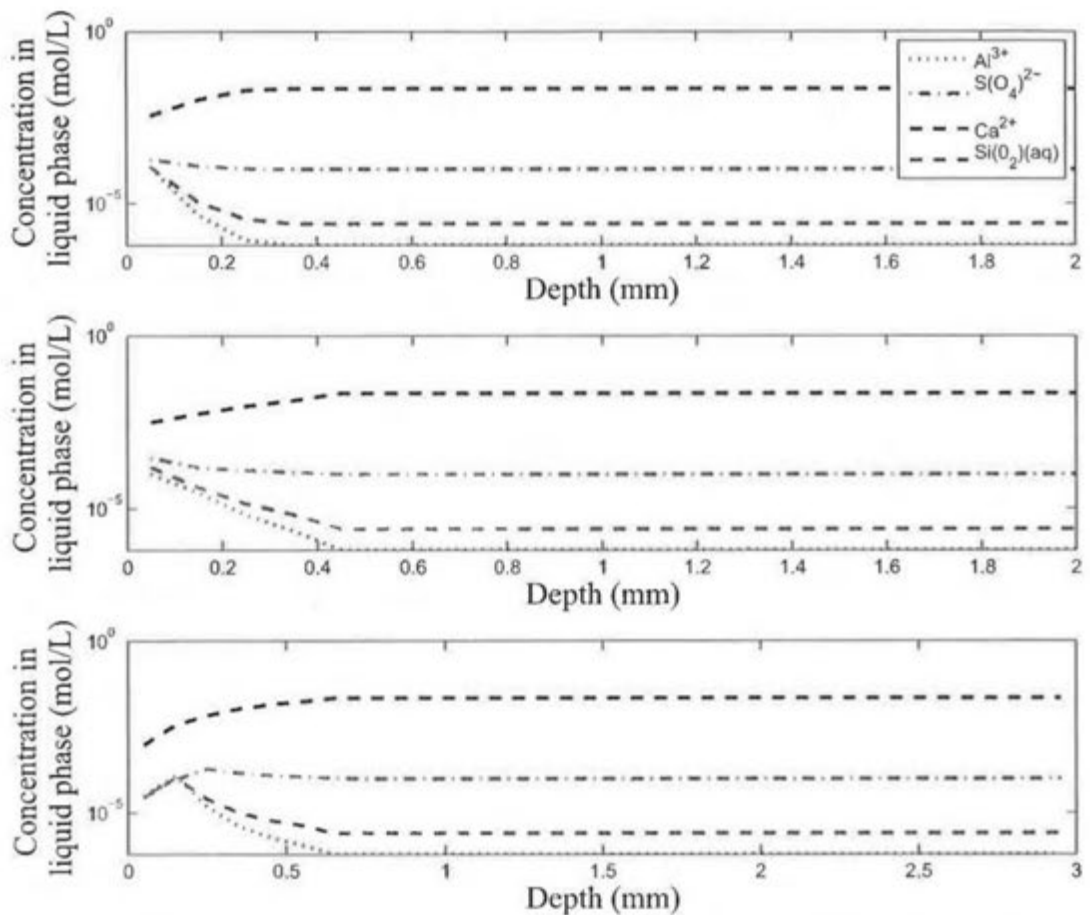


**Figure V.6:** Evolution of the concentrations in solution of the main aqueous species compared with the initial ones as a function of the depth of the sample of CEM I 42.5 with  $w/c = 0.40$  paste after 50 days of pure water degradation simulated with ALLIANCES using a proportional law (up), Tognazzi's law (middle) and the multi-scale homogenization model (down), respectively.

The variations of the concentration of the main aqueous species in the interstitial solution depend on the diffusion law chosen, as is shown on Fig. V.6. One of the shortcomings of ALLIANCES is that it is presently not possible to affect different diffusion coefficients to each aqueous species, which might lead to unrealistic results. For example, we observe on Fig. V.6 that  $\text{SiO}_2(\text{aq})$  move inside the interstitial solution towards the exterior of the paste, while they should hardly move in theory because of the big size of the  $\text{SiO}_2(\text{aq})$  molecules.

Since there is a large number of factors that affect the chemical degradation of cement, it is of practical significance to identify factors that strongly affect the deterioration. For this purpose, the respective effects of the composition of the cement paste, of the aggressive solution, of the inclusion shape of CH and of the CSH percolating porosity on the leaching of HCP are investigated below. The last two factors are parameters of the multi-scale homogenization model that significantly modify the macroscopic diffusive and mechanical properties of cement pastes (Stora et al. 2006a; b).

### 13.2.4 Influence of the composition of cement pastes on the chemical degradation

In order to perform a rigorous validation of the simulations and investigate the influence of the composition of the cement pastes on their chemical degradations, two CEM I pastes, that are well characterized (Adenot and Buil 1992; Baroghel-Bouny 1994; Gallé 2001) and which mechanical behavior has also been studied (Carde 1996; Le Bellégo 2001; Gallé et al. 2004; Moranville et al. 2004) are employed: a CEM I 42.5 of Origny with  $w/c = 0.40$  (Tognazzi 1998; Le Bellégo 2001) and a CEM I 52.5 HTS from Lafarge (Gallé 2001; Gallé et al. 2004; Moranville et al. 2004). The comparison between the two cement pastes provides furthermore some insights about the effect of the hydration rate and of the  $w/c$  ratio on the chemical degradation. The CEM I 52.5 HTS paste with  $w/c = 0.45$  (Gallé et al. 2004) has a quite different composition from the other one with five phases supposed present initially (Béjaoui and Bary 2007): UC,  $C_{1.65}SH$ , CH, AFm and hydrogarnet (Table V.2). This initial composition is obtained by means of the Jennings model (Béjaoui and Bary 2007). The simulations of chemical degradations of the CEM I HTS paste are confronted with experimental results from pure water leaching tests (Gallé et al. 2004) but also with other results from recent simulations (Moranville et al. 2004).

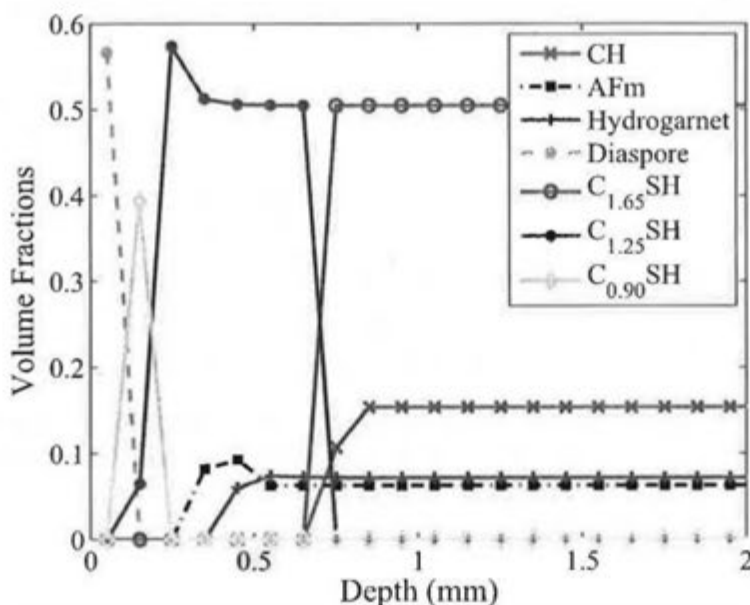


**Figure V.7: Mineral compositions in terms of volume fractions inside a sample of CEM I 52.5 HTS paste with  $w/c = 0.45$  subjected to a 50 days attack by pure water simulated with ALLIANCES.**

The figure above presents the mineral profile in a CEM I HTS paste with  $w/c = 0.45$  leached with pure water during 50 days. The complete dissolution of phases, such as CH, hydrogarnet and AFm, may be observed on the left-hand side of the top of Fig. V.7, corresponding to the altered zone. It is noteworthy that there is a reprecipitation of AFm in the zone where

hydrogarnet starts to dissolve and low C/S ratio CSH,  $C_{0.90}SH$ , precipitate near the interface with pure water.

The dissolution front of portlandite propagates faster in a CEM I HTS paste than in a CEM I 42.5, since the CEM I 52.5 HTS is much more porous and has a higher diffusivity (see Tables V.2 and V.3). An additional possible reason why the CEM I 42.5 paste resists better to leaching than the CEM I 52.5 HTS one is that it contains less portlandite and more aluminates showing a better resistance to pure water. Fig. V.8 confirms that the degradation propagates faster in the CEM I HTS paste. The decrease of the pH and of the concentration of calcium in solid phase is much more significant than inside the CEM I 42.5 paste due to the decalcification of the  $C_{1.25}SH$ .

The calcium fluxes are furthermore underestimated in both simulations (see Table V.3) and appear to be much smaller than the values measured experimentally by Adenot (1992) and Bourdette (1994) on a CEM I 42.5 paste with  $w/c = 0.40$ . It is consequently necessary to adjust the MCSA parameter of the multi-scale homogenization model in order to obtain a better agreement with the experimental results.

| Leaching front propagation   | Origny CEM I 42.5 paste<br>( $w/c = 0.40$ )   | Lafarge CEM I 52.5<br>HTS paste ( $w/c = 0.45$ )  |
|--|---|---|
| Experimental decalcification front propagation                                     | 0.15 mm $d^{-0.5}$<br>(Adenot 1992)   | 0.19 mm $d^{-0.5}$<br>(Gallé et al. 2002)         |
| Decalcification front propagation (after 50 days of simulated pure water leaching) | 0.10 mm $d^{-0.5}$  | 0.12 mm $d^{-0.5}$                                |
| Calcium Flux measured experimentally   | 1.4 mol $m^{-2} d^{-0.5}$ (Adenot 1992)<br>1.1 mol $m^{-2} d^{-0.5}$ (Bourdette 1994) | 1.75 mol $m^{-2} d^{-0.5}$<br>(Gallé et al. 2002) |
| Calcium Flux (after 50 days of simulated pure water leaching)                      | 0.55 mol $m^{-2} d^{-0.5}$  | 0.82 mol $m^{-2} d^{-0.5}$                        |

*Table V.3: Comparison of the decalcification front propagations obtained in the simulations performed with ALLIANCES of pure water leaching with experimental values.*

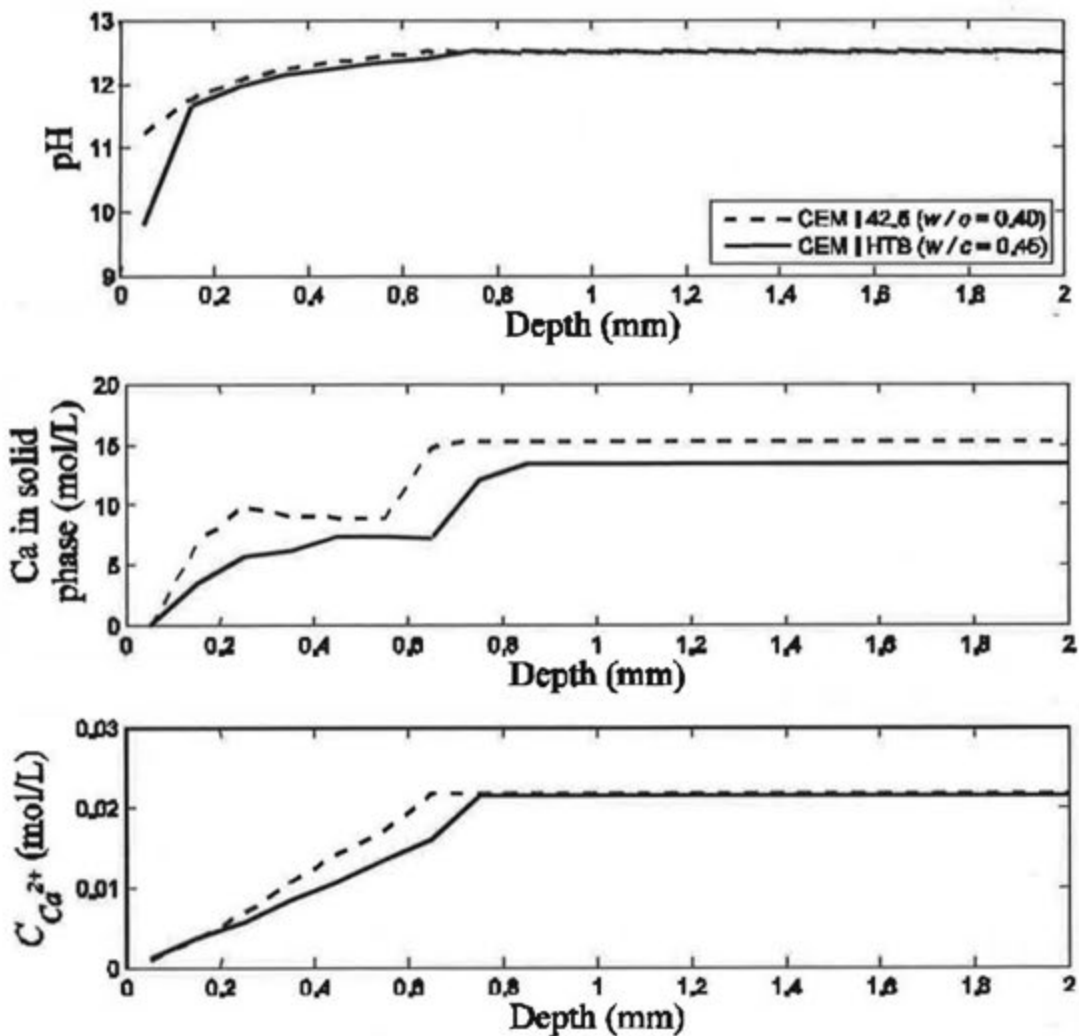


Figure V.8: Evolutions of the pH of the interstitial solution and of the concentrations of calcium ions in solid phase and in solution inside 42.5 (w/c = 0.40) and 52.5 HTS (w/c = 0.45) CEM I pastes subjected to a 50 days attack by pure water.

### 13.2.5 Influence of the aggressive solution on the chemical degradation

Although the degradation of the small cement samples in the previous subsection is significant, the effect of leaching by water at the scale of a real concrete structure are only observable for very long times, since it roughly takes 300 years to leach 4 cm of a concrete structure by extrapolating results from leaching experiments (Adenot 1992). More aggressive solutions, such as ammonium nitrate ( $\text{NH}_4\text{NO}_3$ ), are consequently commonly used by experimentalists to enhance the degradation process (Carde 1996). In particular, a very concentrated solution containing 6 mol/L (6M) of  $\text{NH}_4\text{NO}_3$  is generally employed for the coupled chemo-mechanical degradation experiments (see e.g. Le Bellégo 2001). It is therefore necessary to be able to simulate accelerated leaching by this 6M  $\text{NH}_4\text{NO}_3$  solution to reproduce the available chemo-mechanical degradation experiments. The rectangle with 3 mm

of length used for pure water leaching simulations (see Fig. V.2) is not adapted for the 6M  $\text{NH}_4\text{NO}_3$  attack due to the very fast propagation of the dissolution front. A bigger rectangle with 1 cm of length and 1 mm of height and a bigger mesh composed of 20 rectangular subvolumes are consequently employed to obtain reasonable computation times. The mineral profiles obtained for a CEM I 42.5 paste with  $w/c = 0.40$  respectively attacked by pure water and by a 6M  $\text{NH}_4\text{NO}_3$  solution during 10 days is plotted on Fig. V.9. The dissolution front is at least one order of magnitude deeper for the accelerated attack. The decalcification front propagations obtained for different cement pastes are presented in Table V.4 and appear to be at least one hundred times faster than for pure water leaching. However, the simulated dissolution front propagations are clearly underestimated compared to those measured experimentally. This shortcoming may be caused by a too low diffusion coefficient in the degraded zone. It is furthermore pointed out that the calculations of ion activities by the Davis modified are inaccurate and probably overestimated, which should rather enhance the simulated propagation of the dissolution front. According to Heukamp (2002), the Davis modified law used by default in ALLIANCES does not suffice for computing the right activities and equilibrium concentrations in the case of a 6M  $\text{NH}_4\text{NO}_3$  solution and other laws such as Pitzer equations should be used. Indeed, the equilibrium concentrations of the hydration products are strongly modified in the presence of a 6M  $\text{NH}_4\text{NO}_3$  solution.

| Accelerated leaching front propagation (6M $\text{NH}_4\text{NO}_3$ ) | Origny CEM I 42.5<br>$w/c = 0.40$ | Lafarge CEM I 52.5 HTS<br>$w/c = 0.45$<br>(Gallé et al. 2004) |
|---|-----------------------------------|---|
| Experimental measure  | -                                 | 1.74 mm $d^{-0.5}$  |
| After 10 days of simulations of degradation                           | 1.11 mm $d^{-0.5}$                | 1.27 mm $d^{-0.5}$  |
| Acceleration factor<br>(compared to pure water degradation)           | 111                               | 104   |

*Table V.4: Comparison of the decalcification front propagations obtained in the different simulations performed with ALLIANCES of accelerated leaching by a 6M  $\text{NH}_4\text{NO}_3$  solution with experimental values (Gallé et al. 2004).*

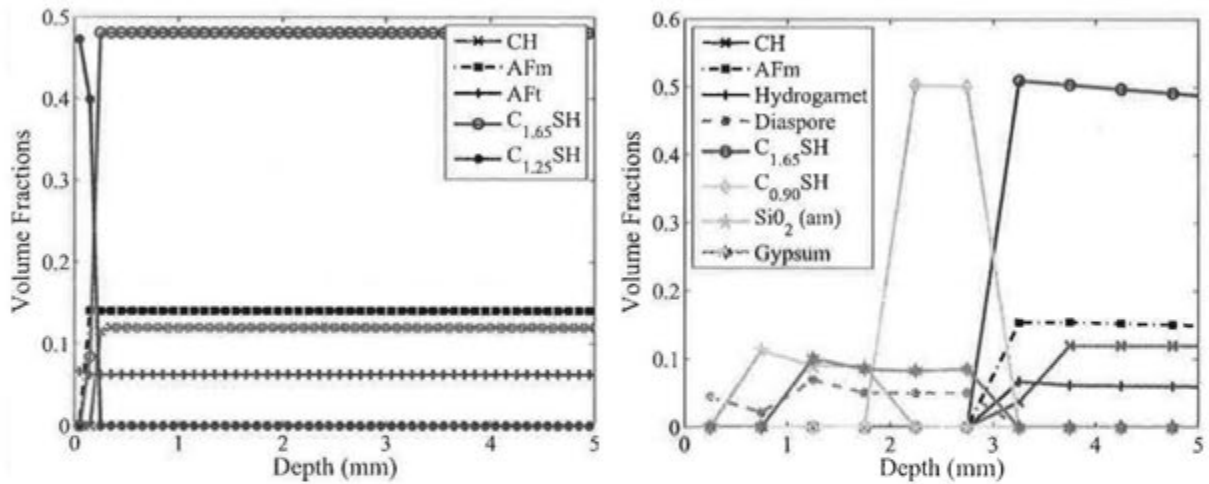


**Figure V.9: Mineral compositions in terms of volume fractions inside a sample of CEM I 42.5 paste with a  $w/c = 0.40$  (Le Bellégo 2001) subjected to a 10 days attack on its left side by pure water (left) and by a  $6M NH_4NO_3$  solution (right).**

Even though the simulations of chemical degradations of HCP obtained with ALLIANCES using the multi-scale homogenization model are quite conform to leaching experiments (see Tables V.3 and V.4), they tend to underestimate the degradation depths. Nevertheless, the results may be further improved by modelling portlandite as spheroidal inclusions instead of spherical ones (Stora et al. 2006a) or by increasing the volume fractions of percolating gel pores (Stora et al. 2006b).

### 13.2.6 Improving the leaching simulations by adjusting the parameters of the homogenization model

#### 13.2.6.1 Influence of the inclusion shapes

To investigate the impact of the inclusion shapes used in the homogenization model on the chemical degradation of HCP, a simulation of 50 days pure water leaching is performed using an oblate spheroid with an aspect ratio  $r = 0.1$  to model portlandite in the multi-scale representation of HCP. The influence of the CH inclusion shape on the evolutions of diffusivity being quite modest (Figs. V.10 and V.11), the depth of the CH dissolution front remains practically unchanged for a 50 days pure water leaching simulation. In the ensuing part devoted to the chemo-mechanical couplings, the chemical deteriorations are exclusively simulated adopting the multi-scale homogenization model with CH represented for simplicity as a sphere for estimating the diffusivity evolutions.

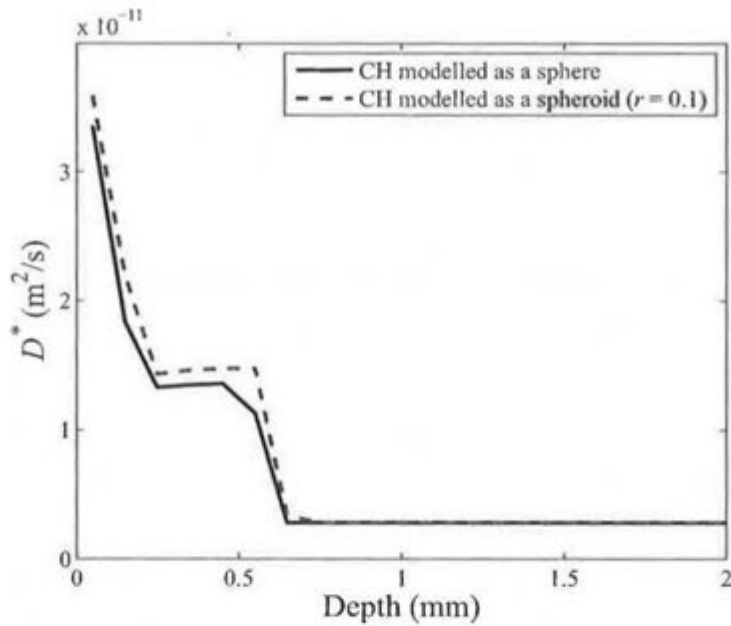


**Figure V.10:** Evolutions of the macroscopic diffusivity inside a sample of CEM I 42.5 paste ( $w/c = 0.40$ ) subjected to a 50 days attack by pure water simulated with the multi-scale homogenization model with CH modelled as a sphere (blue) and as oblate spheroids (dashed), respectively.

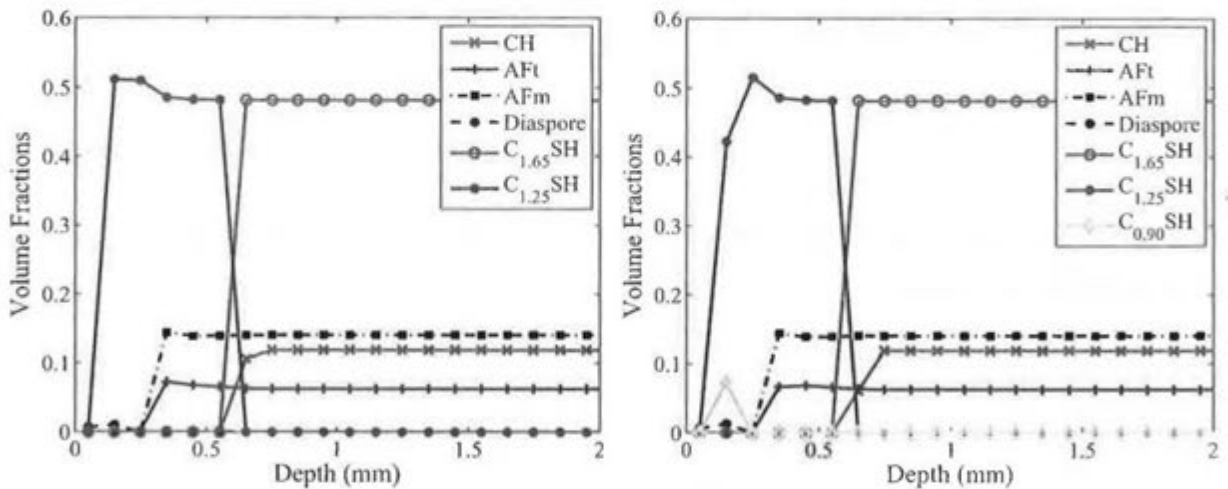


**Figure V.11:** Mineral compositions in terms of volume fractions inside a sample of CEM I 42.5 paste with  $w/c = 0.40$  subjected to a 50 days attack by pure water simulated with the multi-scale homogenization model with CH modelled as a sphere (left) and as an oblate spheroid (right), respectively.

### 13.2.6.2 Influence of the percolating gel porosity

In absence of experimental values for the diffusivities of uniformly leached CSH and HCP, these quantities have to be estimated by the homogenization model based on assumptions of the quantities of additional percolating gel and capillary porosity, designated as  $\Delta c_{GP}^{(p)}$  and

$\Delta c_{CP}^{(p)}$  respectively, appearing during the decalcification. These suppositions formulated in Part III are now revised so as to obtain a higher diffusivity for the totally leached zone. Instead of supposing that, in the uniformly leached state, 5 % of the CSH are dissolved and replaced by capillary pores (Bary and Béjaoui 2006), it is presently assumed that they are substituted by additional percolating gel pores. As a consequence, an additional volume fraction  $\Delta c_{GP}^{(p)} = 0.065$  of gel porosity is supposed to percolate through the uniformly leached paste. By summing these additional percolating gel pores and capillary ones replacing the dissolved hydration products (CH, AFt), the total quantity of additional porosity measured by mercury porosimetry (Gallé et al. 2004) is retrieved. As may be seen in Fig. V.12, the diffusivity obtained with this new hypothesis augments by a factor three in the most leached zone and the depth of the CH dissolution front is increased by about 0.1 mm for a 50 days pure water leaching simulation (see Fig. V.13) thus leading to a better agreement with the experimental decalcification front propagation.

In addition, the calcium flux computed that is about  $1.0 \text{ mol m}^{-2} \text{ d}^{-0.5}$  (Fig. V.14) is almost doubled in comparison with the previous simulations and appears to be closer to the experimental measure (Adenot 1992; Bourdette 1994), even though the calcium flux is still underestimated. In the case of the HTS cement paste, the calcium flux and leaching front propagation are also much higher thus significantly improving the agreement with experimental data (see Table V.5).

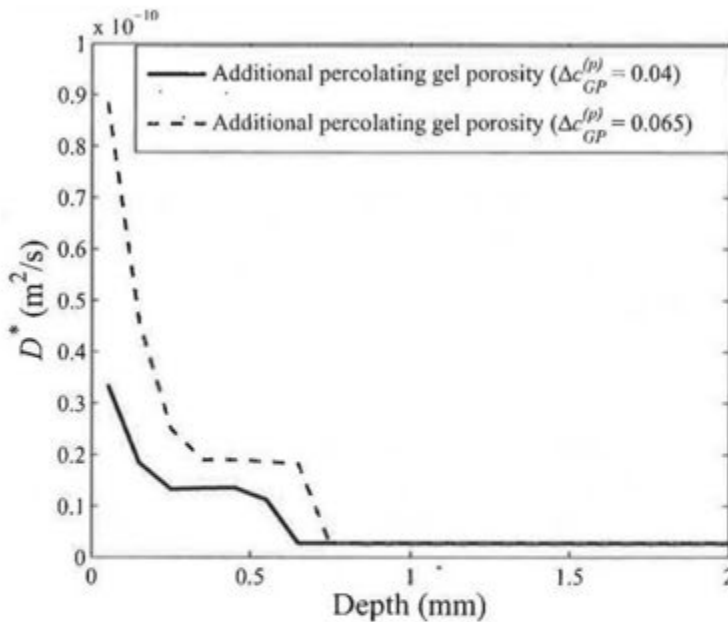


**Figure V.12: Evolutions of the macroscopic diffusivity inside a sample of CEM I 42.5 paste ( $w/c = 0.40$ ) subjected to a 50 days attack by pure water simulated with the multi-scale homogenization model by considering different quantities of additional percolating gel pores ( $\Delta c_{GP}^{(p)} = 0.04$  and  $\Delta c_{GP}^{(p)} = 0.065$ ).**

| Decalcification front propagation  | Origny CEM I 42.5 paste<br>w/c = 0.40   | Lafarge CEM I 52.5<br>HTS paste w/c = 0.45                        |
|--|---|---|
| Experimental decalcification front propagation                                     | 0.15 mm d <sup>-0.5</sup><br>(Adenot 1992)  | 0.19 mm d <sup>-0.5</sup><br>(Gallé et al. 2002)                  |
| Decalcification front propagation (after 50 days of simulated pure water leaching) | 0.12 mm d <sup>-0.5</sup>   | 0.15 mm d <sup>-0.5</sup>   |
| Calcium Flux measured experimentally   | 1.4 mol m <sup>-2</sup> d <sup>-0.5</sup> (Adenot 1992)<br>1.1 mol m <sup>-2</sup> d <sup>-0.5</sup> (Bourdette 1994) | 1.75 mol m <sup>-2</sup> d <sup>-0.5</sup><br>(Gallé et al. 2002) |
| Calcium Flux (after 50 days of simulated pure water leaching)                      | 1.0 mol m <sup>-2</sup> d <sup>-0.5</sup>   | 1.7 mol m <sup>-2</sup> d <sup>-0.5</sup>                         |

**Table V.5: Comparison of the decalcification front propagations obtained in the new simulations performed with ALLIANCES of pure water leaching with experimental values.**

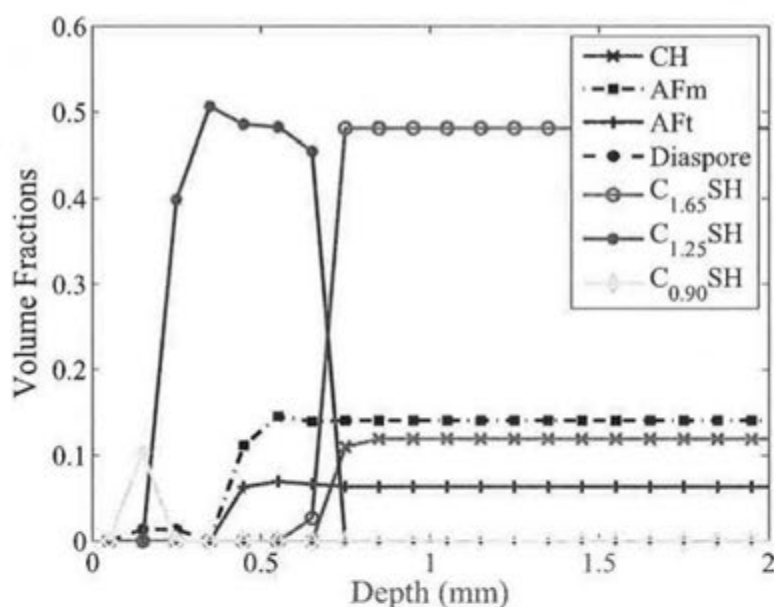


**Figure V.13: Mineral compositions in terms of volume fractions inside a sample of CEM I 42.5 paste with w/c = 0.40 subjected to a 50 days attack by pure water simulated with the multi-scale homogenization model by considering an increased quantity of additional percolating gel pores ( $\Delta c_{GP}^{(p)} = 0.065$ ).**

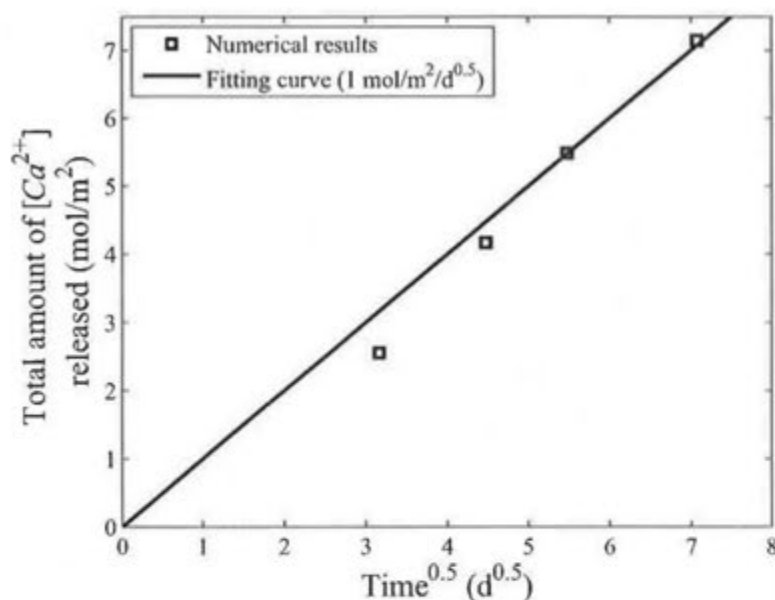


**Figure V.14: Evolutions with square root of time of the total amount of released calcium from a CEM I 42.5 paste with  $w/c = 0.40$  subjected to an attack by pure water simulated with the multi-scale homogenization model.**

These results highlight the importance of the amount of the percolating porosity in the MCSA model (Stora et al. 2006b). In the ensuing chapter devoted to the chemo-mechanical couplings, the chemical deteriorations are exclusively simulated adopting this increased quantity of percolating gel pores for the homogenization computations.

### 13.3 Conclusions of chapter 13

The multi-scale homogenization model developed in Part III has been implemented within the ALLIANCES platform to compute the evolutions of the diffusive properties of concrete materials. Simulations of both pure water and accelerated leaching of these materials have been run and confronted to both experiments (e.g. Adenot 1992) and recent numerical results (Moranville et al. 2004). The concentration profiles of the aqueous and mineral species inside the paste predicted by the simulations are quite close from what is generally observed experimentally. The results obtained with the latter model are better than those obtained with empirical laws (e.g. Tognazzi 1998). However, the dissolution front propagation and the calcium flux tend to be underestimated in comparison with the experimental measures but the results have been improved by increasing the quantity of percolating gel pores in the multi-scale representation of HCP. After this presentation of the coupled chemical-transport problem solved by ALLIANCES, the next chapter is specifically devoted to the couplings between chemistry and mechanics.

## 14 SIMULATIONS OF THE CHEMO-MECHANICAL DEGRADATIONS BY LEACHING OF CEMENT-BASED MATERIALS

The next step of modelling consists in estimating the material effective elastic properties by means of homogenization techniques. The non-linear mechanical behaviour of the sample is then evaluated by FE with CAST3M using a micromechanically based damage model detailed in Part IV. The present chapter focuses on the influence of the chemical deterioration on the residual mechanical behaviour. The impact of damage on the leaching process has been treated at the very end of the PhD thesis. Some results have been obtained after the defense of my thesis and are not presented in this manuscript. They are however gathered in a paper submitted to Cement and Concrete Research (Stora et al. 2008).

Residual mechanical resistance tests on cement pastes have been performed both in compression (e.g. Carde 1996; Heukamp 2002) and in traction or flexion (e.g. Le Bellégo 2001). For simplicity, the chemo-mechanical simulations are limited to traction or flexion tests. The present chapter aims at simulating the different flexion tests performed by Le Bellégo (2001) on mortars that constitute a very good example of chemo-mechanical coupled experiments.

### 14.1 Stiffness reduction of cement-based materials after leaching

The multi-scale homogenization approach developed in Part III to estimate the evolutions of the diffusivity of cement-based materials is also applied to predict their elastic properties in both sound and leached states. The Young moduli of each subvolume of the simulated cement-based material can be estimated by implementing this model into ALLIANCES. The volume fractions of each mineral phase necessary for applying the homogenization model are provided by the previous simulations of the chemical deterioration performed with the multi-scale homogenization model for diffusion. The volume fractions given on Fig. V.3 and the measurements by nanoindentation of the elastic properties of each mineral phase (see Table I.3) then serve as input parameters for the estimations of the elastic properties.

The doubly-coated spheres model, representing the microstructure of HCP and mortars, is computed with the aid of the GSCS and provides the estimations plotted on Fig. V.15 for the Young modulus of the HCP inside the degraded sample. The latter modulus is significantly reduced in the altered zone because of the dissolution of rigid phases, such as CH and AF. It may be seen on Fig. V.15 that the decrease occurs in two steps: the first one is attributed to the dissolution of CH and the second one is caused by the decalcification of the CSH. This sharp diminution due to leaching is in good agreement with the experimental works of Carde (1996), Constantinides and Ulm (2004) and Gallé et al. (2004) that evidence a significant effect of leaching on the macroscopic Young modulus of cement pastes. Constantinides and

Ulm (2004) further measured that the stiffness modulus of an asymptotically leached paste decreased to about 3 GPa. The homogenized Young modulus of the most decalcified subvolume on the left-hand side of Fig. V.15 is of the same order.

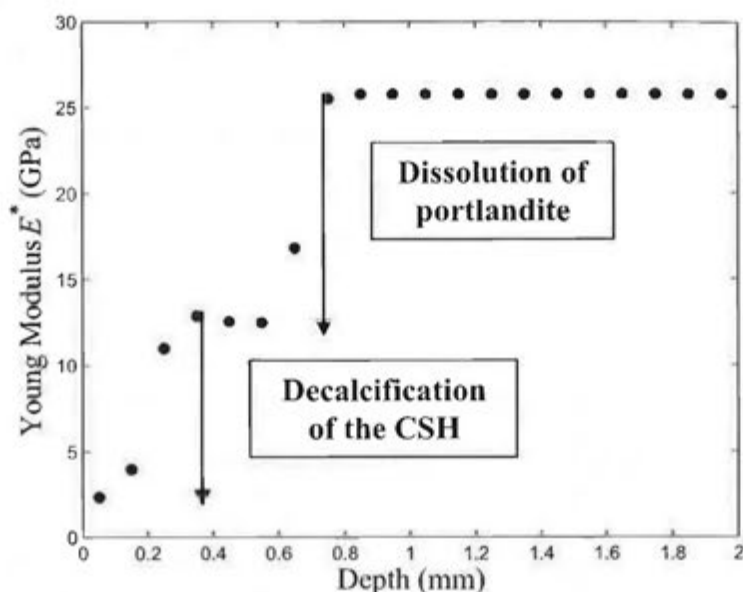


Figure V.15: Evolution of the Young modulus inside a sample of CEM I 42.5 paste with  $w/c = 0.40$  (Le Bellégo 2001) subjected to a 50 days pure water attack.

## 14.2 Simulations of the mechanical residual resistance tests on cement-based materials

### 14.2.1 Tensile tests on uniformly leached specimens

Heukamp (2002) performed interesting types of experiments testing in traction or compression both sound and asymptotically leached samples of cement or mortar. By asymptotically leached, it is intended that the sample has been so severely attacked that it reaches a uniform degraded state with much lower elastic properties and strength. To simulate such deterioration, the previous one-dimensional system in Fig. V.2 is reused except that a 6M  $\text{NH}_4\text{NO}_3$  solution is now employed instead of pure water. The initial mineral composition of the OPC type I cement paste with  $w/c = 0.50$  is computed by means of the Tennis and Jennings model and displayed in Appendix V.B. After 50 days, the sample is already entirely leached and a uniaxial tensile test along the  $e_1$  axis is simulated on this specimen.

The eventual cracks inside the paste solicited in traction along the vertical axis on the beam should mainly appear oriented along the horizontal axis. For simplicity, the normal vectors of all the cracks in the present damage model are thus assumed to be parallel to the horizontal axis  $e_1$ . The subscripts can thus be disregarded, since only one family of parallel cracks is involved. The undamaged material being isotropic, the effective damaged one is consequently transversely isotropic, according to our model.

The damage parameters such as tensile strength in the sound and uniformly leached specimens are obtained from Heukamp et al. (2005) and enlisted on Table V.6. After simulating a 100 days attack by a 6M  $\text{NH}_4\text{NO}_3$  solution, the sample is uniformly leached. The stress-strain curves of these two samples obtained by FE are plotted in Fig. V.16, illustrating the strong degradation of the mechanical properties of chemically deteriorated cements. The relative decrease obtained for the Young moduli are quite close to the ones measured by Heukamp et al. (2005). Unfortunately these tests did not record the post-peak behavior. Therefore, the developed tool, and in particular the micromechanically based damage model, needs to be further validated by comparing with the more detailed experiments from Le Bellégo (2001).

| Parameters of the damage model | OPC type I paste<br>(w/c = 0.50) | Mortar<br>(w/c = 0.40) |
|--------------------------------|----------------------------------|------------------------|
| $\varepsilon_0$                | $8.6 \times 10^{-4}$             | $5 \times 10^{-5}$     |
| A                              | 1                                | 1                      |
| B                              | 10000                            | 3000                   |
| $k$                            | 28.9<br>(Heukamp et al. 2005)    | 9.84                   |

**Table V.6: Mechanical input data adopted for the micromechanically-based damage model in the cases of a HCP sample (Heukamp et al. 2005) submitted to a uniaxial traction and of the mortar beam tested in flexion (Le Bellégo 2001).**

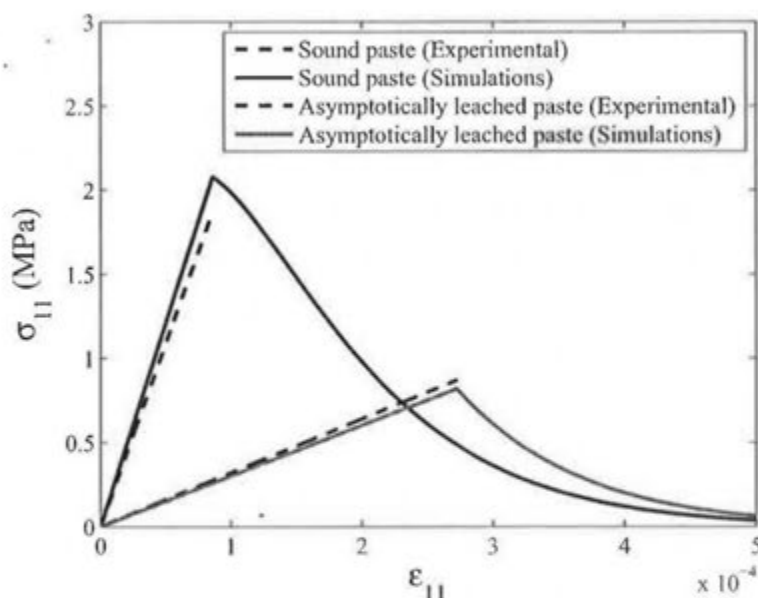


**Figure V.16: Stress-strain curves of a sound and an asymptotically leached cement paste with a w/c ratio equal to 0.50 (Heukamp et al. 2005) submitted to a uniaxial traction following the  $e_1$  axis.**

## 14.2.2 Three-points flexion tests

### 14.2.2.1 System considered

For testing the mechanical residual resistance of cement-based materials, the case of a beam in flexion is now simulated so as to reproduce existing experiments (e.g. Le Bellégo 2001; Schneider and Chen 2005). Le Bellégo (2001) in particular conducted a large series of three-point bending tests of partially leached mortars and recorded the whole curve linking the displacement imposed and the reaction force. It is emphasized that their results are more detailed than the ones of Schneider and Chen (2005), who performed the same kind of tests but have only recorded the ultimate strength. In the present simulations, the smallest beam tested by Le Bellégo (2001) is used. Its total length and height are 320 mm and 80 mm, respectively. The lateral surfaces and the 60 mm long sections at the corners of the beam are insulated by an epoxy coating (see Fig. V.17). Therefore only the central part of the lower face, which will be subsequently subjected to tensile stresses, is in contact with a 6M  $\text{NH}_4\text{NO}_3$  solution. The 2D mesh depicted on Fig. V.17 is employed for the chemical and mechanical computations on the beam. The chemical attack of the beam by this aggressive solution lasts 114 days. Le Bellégo measured with phenolphthalein that the degradation depth reached 18.2 mm from the bottom of the beam. After this attack, the deteriorated beam is further subjected to a three-point flexion test schematically represented in Fig. V.17. The following mechanical boundary conditions are imposed:

$$u_y(x=0, y=0.08, t=114\text{d})=u_0; \quad u_x(x=0, y, t)=0; \quad u_y(x=0.12, y=0, t)=0. \quad (\text{V.17})$$

After 114 days of leaching, an increasing displacement  $u_0$  is thus imposed on the center of the upper face (Fig. V.17). The non-linear mechanical behaviour of the leached sample is then evaluated by FE using the micromechanically based damage model detailed in Section 2. The beam is assumed to be in plane stress conditions. In the present system, eventual cracks inside the chemically degraded zone presently sollicitated in traction along the horizontal axis because of the flexural displacement imposed on the beam should mainly appear oriented along the vertical axis.

A rather coarse 2D mesh comprising 1600 elements is employed for the chemical and mechanical computations on the mortar beam, since the smallest element of the mesh should be bigger than the typical size of the RVE. It is recalled that this size is about 10-100  $\mu\text{m}$  for cement pastes and about 1-10 mm for mortars. According to the work of Pensée and He (2007) accounting for the effects of the size of the RVE, the latter should be significantly bigger than the typical sizes of the particulate phases. Lutz et al. (1997) for example considered an average equivalent diameter of 700  $\mu\text{m}$  for sand aggregates. Consequently, the

average size of a mesh element should be at least superior to 2 mm in the case of mortars. In a first attempt, a coarse mesh composed of 200 elements was used to ensure reasonable calculations times (about one hour) but a 2D mesh with 1600 elements (more than two hours) was finally preferred to examine more precisely the dissolution front propagation. This propagation was observed to be independent of the mesh adopted. The area of a mesh element is  $8 \text{ mm}^2$  for the mesh with 1600 elements and its dimensions are  $2 \text{ mm} \times 4 \text{ mm}$ . This choice is a compromise between the RVE size condition ( $> 2 \text{ mm}$ ) and the computation precision for damage, for which it is generally recommended to avoid too big elements.

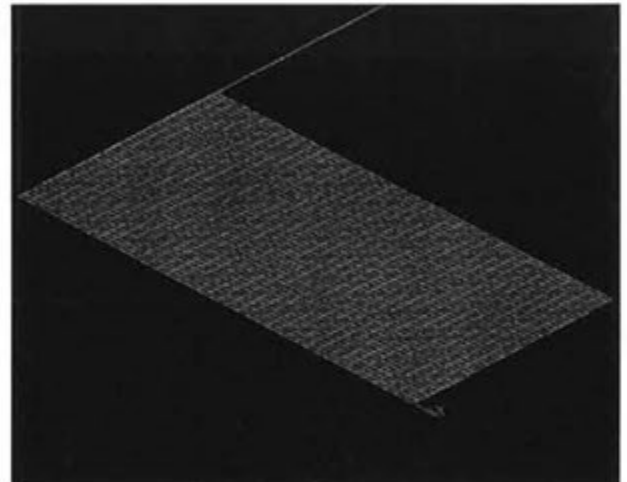
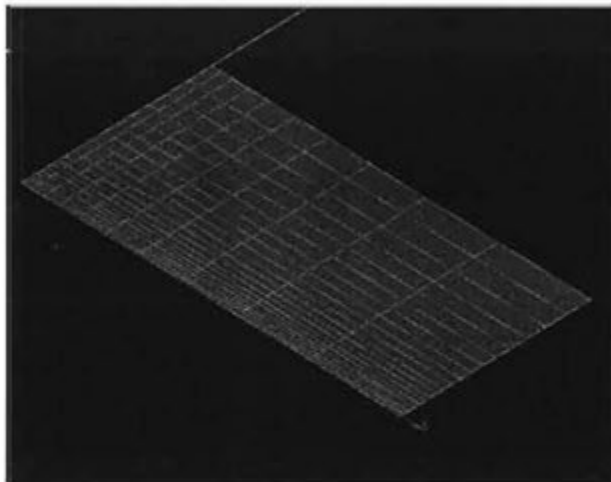
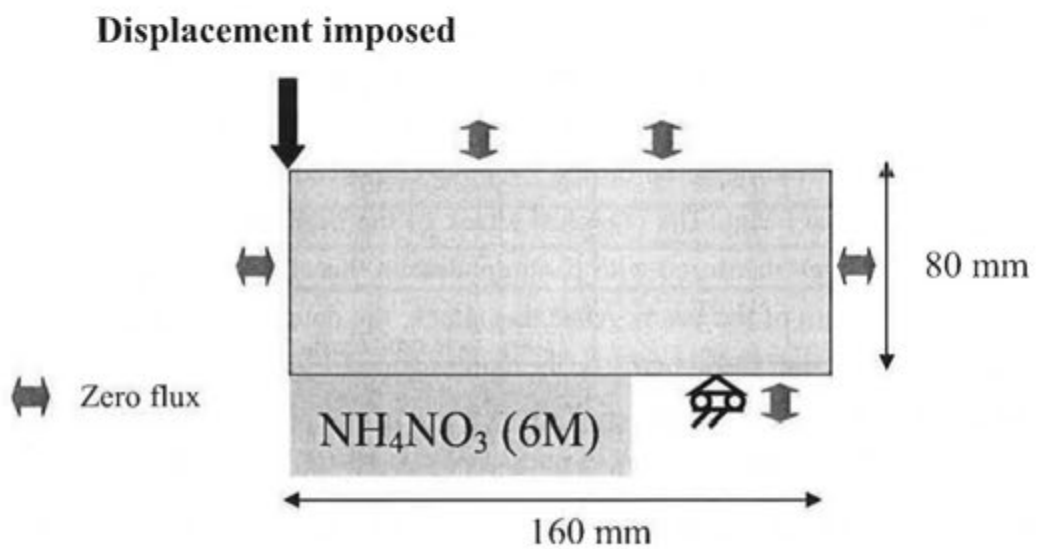


*Figure V.17: Schematic of the two-dimensional mesh employed for the simulations of mechanical resistance tests (up); meshes of 200 elements (down left) and of 1600 elements (down right) used for the computations.*

Concerning the representation of cracks, strong assumptions are made in the micromechanically-based damage model. They may grow in the bulk cement paste, through

the interface between sand aggregates and paste and through the sand aggregates themselves. The micromechanical damage model consequently assumes that the cracks are embedded in an effective medium having the same properties as undamaged mortars, according to the fact that the cracks may grow anywhere. Another argument for representing the cracks inside the already homogenized undamaged mortars is that they may be very extended and have a correlation length that is much longer than the particulate phase such as sand or clinker grains. In the case of concrete, cracks are also likely to grow inside and span over the coarse aggregates.

The chemical-transport input data are collected in Appendix V.B. It is necessary to pay attention to the fact that the mineral composition of the cement paste inside mortar is different from the plain HCP. Indeed, the total water porosity inside the mortar presently considered with 50 % of sand grains is measured to be equal to 0.18, whereas the total water porosity of the plain HCP is 0.27 (Le Bellégo 2001). Assuming that the sand aggregates are impermeable, the total water porosity of the cement paste inside mortar that is more porous than the plain HCP is then about 0.36.

The mechanical input data for the damage model (see Table V.6) are computed or fitted from the results of Le Bellégo (2001) in the case of mortars and of Heukamp et al. (2005) in the case of cement pastes. The ratio of the compressive strength over the tensile one  $k$  is for example determined from the uniaxial compressive and tensile strengths provided by Le Bellégo (2001), equal to 44.3 MPa and 4.5 MPa, respectively. The possible evolutions of the damage parameters are discussed in the next subsection.

#### *14.2.2.2 Evolutions of the damage threshold with leaching*

As already mentioned previously, the experiments performed on both sound and asymptotically leached cement-based materials (e.g. Heukamp et al. 2005) clearly evidence the fact that the compressive or tensile strengths are strongly modified in the leached state. It raises an important question: how does the stress or strain damage threshold evolve during the decalcification process? Unfortunately, the decrease of strength for intermediate leached states is very difficult to measure because of the inhomogeneous degradation of the samples in the typical degradation tests. That's why the following assumption is made: damage occurs when the right line corresponding to the elastic part of the stress-strain curve of the decalcified material intersects the stress-strain curve of the damaged unleached material, as may be seen on Fig. V.18. These curves are obtained by applying the IDD damage model both to the asymptotically degraded and sound cement pastes tested in tension by Heukamp et al. (2005). The strain damage threshold  $\varepsilon_0^{UL} = 2.37 \times 10^{-4}$  provided by this quite empirical method appears to be quite close from the one  $\varepsilon_0^{UL} = 2.72 \times 10^{-4}$  measured by Heukamp for the uniformly leached cement paste.

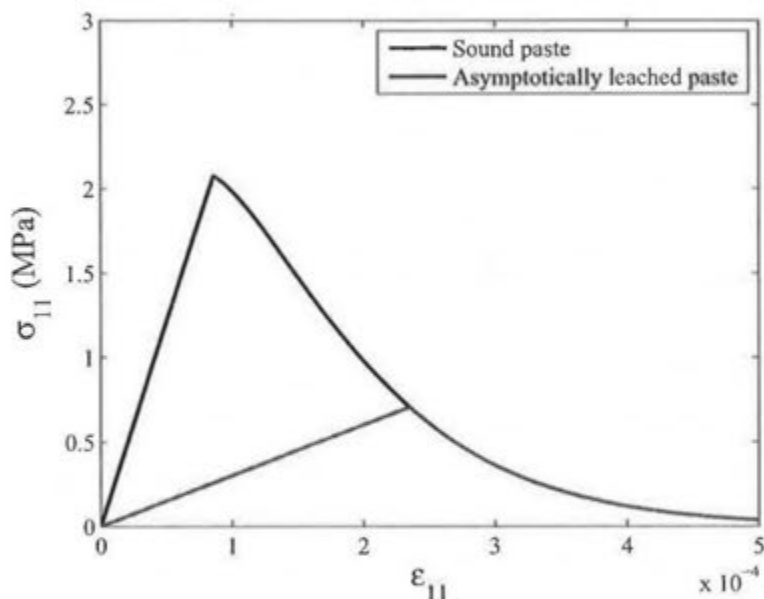


**Figure V.18: Identification of the strain damage threshold of a leached OPC type I paste (Heukamp et al. 2005) from the stress-strain curve of the damaged unleached one.**

#### 14.2.2.3 Results and comments

Before testing the residual mechanical resistance of the mortar beam, it is indispensable to first correctly reproduce the chemical deterioration of the leached material. The computation time for the numerical test of the accelerated leaching is about three hours on a standard PC-Linux machine depending on the precision defined in Eq. (V.13), presently  $10^{-8}$ . The CH dissolution front reaches about 17 mm (Fig. V.19) on mortar beams after 114 days of accelerated leaching. This depth is in quite good agreement with the one obtained experimentally by Le Bellégo despite the fact that the ion activities evaluated with the Davis modified method should be computed more accurately in the case of  $\text{NH}_4\text{NO}_3$  attack.

It appears on Fig. V.20 that the liquid calcium concentration in contact with the 6M  $\text{NH}_4\text{NO}_3$  solution goes up to about 2 mol/L near the portlandite dissolution front. This value is not far from the one considered by Tognazzi (1998) and Heukamp (2002), who assert that the CH dissolution front in presence of a 6M  $\text{NH}_4\text{NO}_3$  solution occurs for a liquid calcium concentration inferior to 2.7 mol/L. In addition, the diffusivity in the leached zone of the beam (Fig. V.20) augments by more than two orders of magnitude compared with the sound part.

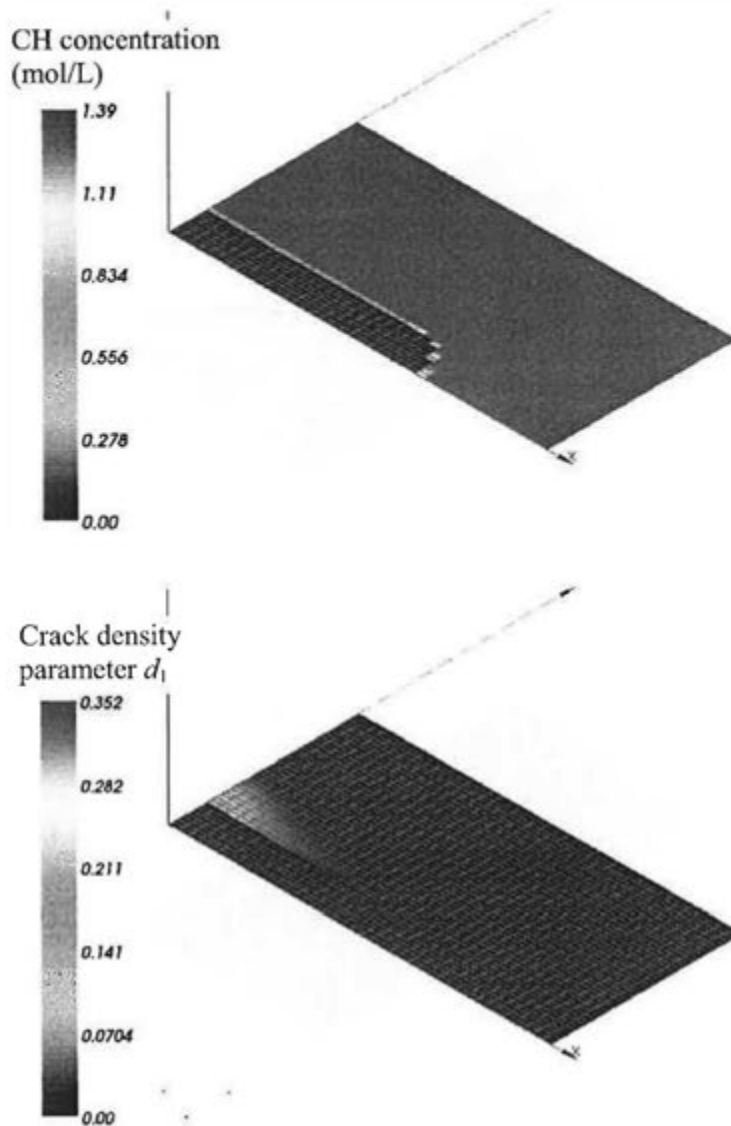


**Figure V.19:** Profile of the portlandite concentration (mol/L) in a mortar beam after a 114 days attack by a  $\text{NH}_4\text{NO}_3$  solution (up); crack density parameter  $d_1$  predicted by the IDD damage model in the leached beam submitted to a flexural displacement of  $39 \mu\text{m}$  (down).

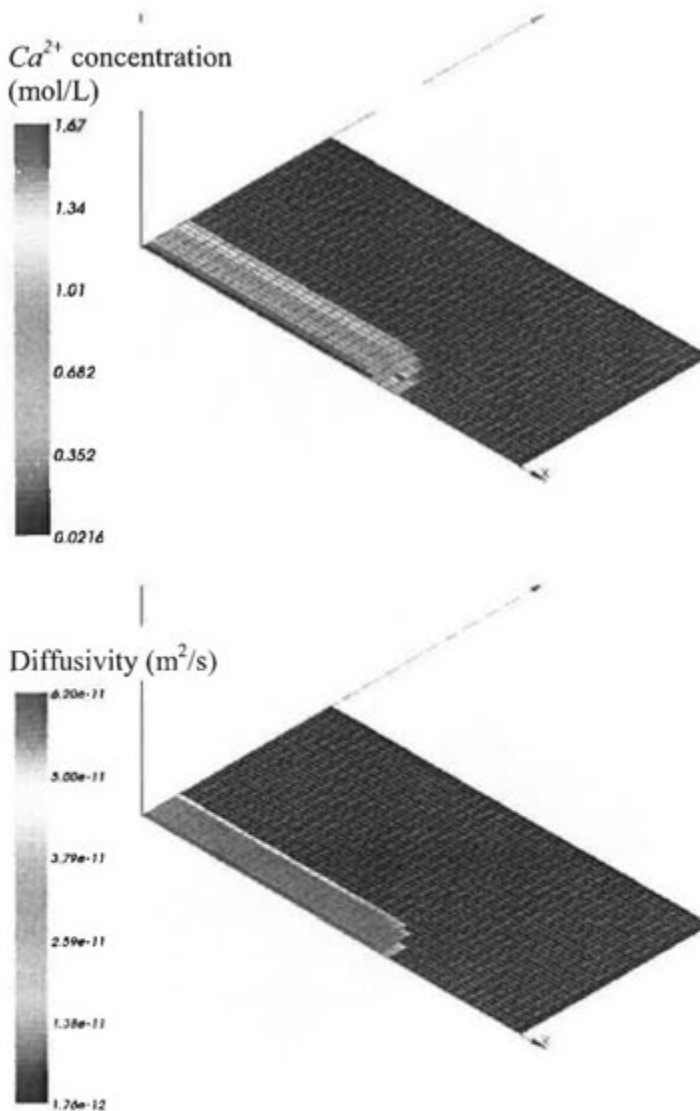


*Figure V.20: Profiles of the diffusion coefficients (down) and of the liquid calcium concentration (mol/L) (up) in a mortar beam after a 114 days attack by a 6M  $\text{NH}_4\text{NO}_3$  solution.*

The evolution of the mineral profile of mortar in the leached zone of the beam is plotted on Fig. V.21. The sequences of dissolution are similar to the ones observed in Adenot (1992) on a CEM I 42.5 paste after a pure water leaching. The degradation induced by a 6M  $\text{NH}_4\text{NO}_3$  solution being yet more severe than the one with pure water, the presence of a completely decalcified zone only composed with  $\text{SiO}_2(\text{am})$  and diaspore may be seen on the left-hand side of Fig. V.21.

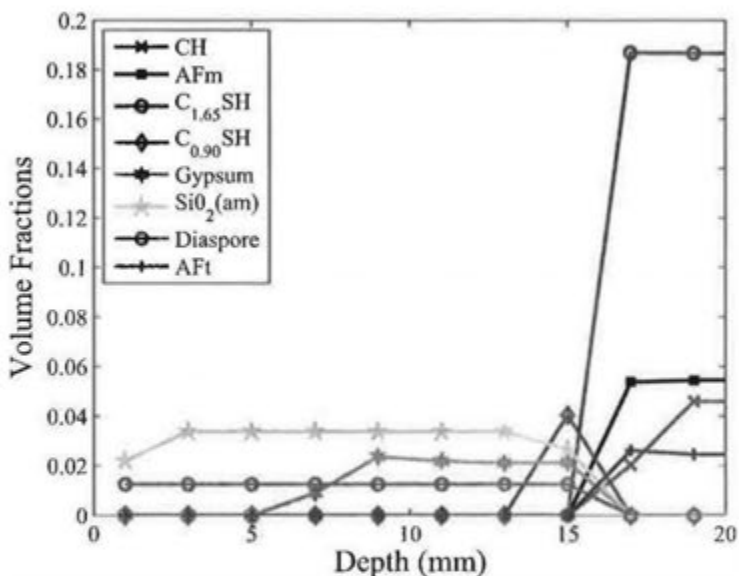
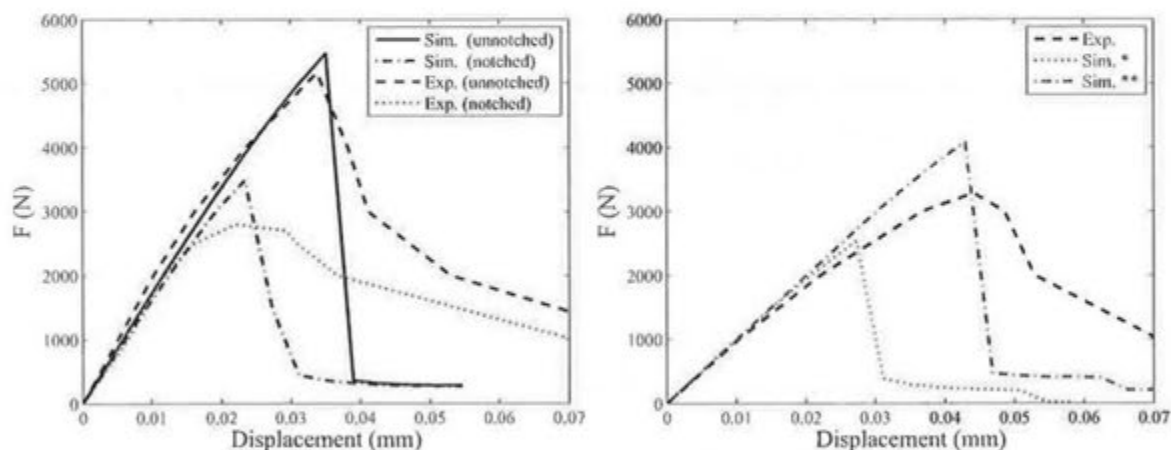


**Figure V.21: Evolutions of the mineral compositions in terms of volume fractions inside a mortar beam after a 114 days attack by a  $\text{NH}_4\text{NO}_3$  solution along the vertical symmetry axis beam.**

Before simulating the residual mechanical tests of Le Bellégo (2001), it is necessary to first try to reproduce the results of her flexion tests performed on sound mortar beams. The post-peak part of the simulated curve poorly fits with the experimental data, according to Fig. V.22 (left). This is mainly due to the fact that only a local version of the micromechanically-based model has been implemented in the platform. A non-local version of the model based on the work of Pijaudier-Cabot and Bazant (1987) should however be incorporated in the future.

In a first attempt, simulations of flexion tests on the leached mortar have been run using exactly the same values for the damage parameters as for the sound specimen (see Table V.6). The results obtained appear on Fig. V.22 (right) to be unsatisfactory thus confirming the fact that the damage threshold is modified by the leaching process. The empirical method described in previously has therefore been employed to have the strain damage threshold  $\varepsilon_0$  evolved. The pre-peak part of the numerical curve then agrees relatively well with the experimental curve on Fig. V.22 (right) but the forces predicted by the simulations tend to be overestimated. There are diverse reasons to explain this difference. The first explanation could be that the Young modulus in the most leached zone, which is estimated to be equal to about 4.9 GPa by the multi-scale homogenization model, is overestimated, even though this value already seems to be quite low. For instance, Heukamp (2002) measured that the effective Young modulus on a uniformly leached mortar is equal to 4.3 GPa. Another reason may be that the dissolution front propagation, that affects the material residual mechanical behavior, is slightly underestimated in comparison with the one gained experimentally, as

already asserted previously. Moreover, it could be also useful to adopt other values for the damage parameters  $A$ ,  $B$  and  $k$  in order to better predict the residual resistance on leached mortars.



\* with the same strain damage threshold as for the sound material

\*\* with a different strain damage threshold in the sound and leached cases

**Figure V.22: Comparison of the simulations results with the experimental curve of the vertical forces plotted against the imposed flexural displacement recorded during a three-point flexion test on a sound mortar beam (left) and another one leached during 114 days by  $NH_4NO_3$  (right).**

Fig. V.19 also reveals the presence of a main damaged domain at the interface between the degraded and chemically sound parts of the beam. Conversely, the chemically leached zone is only slightly damaged, since the strain damage threshold in the decalcified region is assumed to increase rapidly with leaching (see Fig. V.18). Further investigations concerning this evolution of the damage threshold with leaching would however be desirable to confirm this observation.

## CONCLUSIONS OF PART V

The present Part is devoted to the development of a tool incorporated in the ALLIANCES numerical platform that allows for predicting the long-term evolutions of the mineral composition of leached cementitious materials and of their mechanical and diffusive properties. This numerical instrument is built up by incorporating the multi-scale homogenization approach proposed in Parts II and III to predict respectively the evolutions of the diffusivity and of the elastic behavior of cement-based materials into ALLIANCES. The micromechanical damage model developed in Part IV has also been integrated to estimate the damage propagation in these materials.

Owing to the numerical device developed, simulations of the chemical behavior of decalcified cement-based materials have been carried out. The good agreement of the simulated dissolution front propagation and stiffness reduction with experimental data constitute a further validation of the multi-scale homogenization approach proposed in the manuscript. Residual resistance experiments illustrating the couplings between damage and leaching have also been simulated. The numerical results confronted with experimental tests are encouraging but may require some further refinement for the predictions of damage inside the material. Nevertheless, they give some interesting interpretations summarized below for the measures gained from these tests that are particularly useful for assessing the durability of cement-based materials. The simulated behaviour of sound and leached mortar beams in flexion has underlined the necessity to have the damage threshold presently expressed in deformations evolved with decalcification. An empirical method that assimilates the decrease of the Young modulus due to leaching to the one caused by damage is then employed to predict more accurately the maximum load that the deteriorated material can sustain. According to this method, the formation of cracks is then influenced by decalcification, the leached zones being less damaged than the chemically sound ones.

#### Appendix V.A: Chemical formulae and equilibrium constants of the mineral phases in the reduced database.

| Mineral phases             | Chemical formula  | Equilibrium constant | References                      |
|----------------------------|---|----------------------|---------------------------------|
| CH                         | $\text{Ca(OH)}_2$   | $10^{-22.90}$        | Bary (2005)                     |
| AFt                        | $6 \text{ CaO} - \text{Al}_2\text{O}_3 - 3 \text{ SO}_3 - 24 \text{ H}_2\text{O}$ | $10^{-57.00}$        | - // -                          |
| AFm                        | $4 \text{ CaO} - \text{Al}_2\text{O}_3 - \text{SO}_3 - 12 \text{ H}_2\text{O}$    | $10^{-70.25}$        | - // -                          |
| Hydrogarnet                | $3 \text{ CaO} - \text{Al}_2\text{O}_3 - 6 \text{ H}_2\text{O}$                   | $10^{-78.80}$        | - // -                          |
| $\text{C}_{1.65}\text{SH}$ | $1.65 \text{ CaO} - \text{SiO}_2(\text{aq}) - 1.65 \text{ H}_2\text{O}$           | $10^{-29.36}$        | - // -                          |
| $\text{C}_{1.25}\text{SH}$ | $1.25 \text{ CaO} - \text{SiO}_2(\text{aq}) - 1.25 \text{ H}_2\text{O}$           | $10^{-20.25}$        | - // -                          |
| $\text{C}_{0.90}\text{SH}$ | $0.90 \text{ CaO} - \text{SiO}_2(\text{aq}) - 0.90 \text{ H}_2\text{O}$           | $10^{-13.01}$        | - // -                          |
| $\text{SiO}_2(\text{am})$  | $\text{SiO}_2(\text{aq})$   | $10^{+2.16}$         | van der Lee and de Windt (2002) |
| Diaspore                   | $\text{AlO}_2\text{H}$  | $10^{-7.13}$         | - // -                          |
| Gypsum                     | $\text{Ca(SO}_4) - 2 \text{ H}_2\text{O}$   | $10^{-4.48}$         | - // -                          |

**Appendix V.B: Chemical-transport input data used for the simulations of chapter 14.**

| <b>Phases</b>   | <b>OPC type I paste<br/>w/c = 0.50<br/>(Heukamp et al. 2005)</b>                  |
|---|---|
| Estimated hydration rate                                  | 0.90  |
| CH (mol/L)  | 3.78  |
| AFt (mol/L)   | 0.00  |
| AFm (mol/L)   | 0.18  |
| Hydrogarnet (mol/L)                                       | 0.00  |
| CSH (mol/L)   | 5.26  |
| UC  | 0.012   |
| Total water porosity                                      | 0.328   |
| parameter $f$ of the MCSA representing CSH <sup>ext</sup> | 0.64  |
| $D_{ini}^*$ (m <sup>2</sup> /s)                           | $7.6 \cdot 10^{-12}$<br>(value estimated by the multi-scale homogenization model) |

**Table V.B.2: Mineral composition of the OPC type I paste with w/c = 0.50 (Heukamp et al. 2005).**

| <b>Phases</b>  | <b>Mortar (w/c = 0.40)<br/>(Le Bellégo 2001)</b> |
|--|--|
| CH (mol/L)   | 1.37   |
| AFt (mol/L)  | 0.034  |
| AFm (mol/L)  | 0.17   |
| Hydrogarnet (mol/L)  | 0.00   |
| CSH (mol/L)  | 1.49   |
| UC volume fraction   | 0.068  |
| Water porosity   | 0.18   |
| Volume fraction of sand aggregates                                 | 0.50   |
| ITZ volume fraction  | 0.103  |
| Parameter $f^{ext}$ of the MCSA representing CSH <sup>ext</sup>    | 0.78   |
| $D_{ini}^*$ estimated by the multi-scale model (m <sup>2</sup> /s) | $1.8 \cdot 10^{-12}$                             |
| Diffusivity measured experimentally                                | $1.7 \cdot 10^{-12}$<br>(Bourdette 1994)         |

**Table V.B.2: Initial composition of the mortar and input data used for the simulations of flexion tests.**

## 15 GENERAL CONCLUSIONS AND PERSPECTIVES

The present chapter recapitulates the main findings and conclusions of the thesis. Some discussions and proposals for future research are also formulated.

### 15.1 Main conclusions

The findings or achievements of the thesis concern different domains that can be separated in the subsequent categories:

- (i) homogenization theories;
- (ii) modelling and prediction of the macroscopic properties of cement-based materials;
- (iii) numerical simulations of coupled chemo-transport-mechanical degradations of cement-based materials.

In the first Parts of the manuscript, diverse homogenization techniques have been assessed using different criteria and tested on particular cases that have been solved numerically. Among the reviewed schemes, double-inclusion type models and GSCS exhibit the most suited attributes for estimating the linear elastic properties of cement-based materials. By revisiting the DIM of Hori and Nemat-Nasser (1993), a modified version of this model overcoming some of its original shortcomings in the case of coated inclusions has been derived.

The merits of homogenization theories for predicting the effective diffusive properties of porous media presenting high contrast between phase diffusivities have also been examined. Many models such as the matrix-inclusion type schemes are pointed out to be inappropriate, since they are inadequate for modelling percolating or connected pores. A novel estimate associated to a space-filling assemblage mixing two types of composite spheres pertinent to account for pore connectivity has thus been developed. By construction, this MCSA scheme automatically respects HS rigorous bounds and depends only on one geometric parameter which variation allows the realization of any diffusivity ranging within these bounds.

By taking benefit of EMTs retained from the preceding review, a two-step homogenization model is developed for the prediction of the macroscopic linear elastic properties of HCP and mortars and validated by comparison with experimental measurements. The developed model is also validated in the case of cement pastes and mortars submitted to severe leaching. The influence of inclusion shape on the micromechanical estimations of the effective elastic properties of HCP has also been investigated. The spherical particle phase approximation that is generally adopted for simplicity is shown to be valid in most cases, except for very porous leached pastes. Using the same framework as the two-scale approach developed in elasticity, a

more sophisticated model surmounting the lack of knowledge on CSH diffusivities is proposed for predicting the macroscopic diffusivities of cement pastes and mortars. In this multi-scale model, the two types of CSH containing connected gel porosity are estimated with the help of the MCSA scheme presently developed.

An orthotropic damage model has been developed for concrete materials by combining the Mazars model (1984) and micromechanical concepts. It comprises two damage variables, representing the density of cracks in two perpendicular directions, which is suited to deal with orthotropic damage under plane stress conditions. It is less involved than other similar approaches in the literature (e.g. Pensée and Kondo 2003) but presents the advantage to be relatively simple to implement numerically.

Simulations of chemical and of coupled chemo-mechanical degradations of leached cement-based materials have been performed by integrating into ALLIANCES the different models developed in the rest of the thesis to predict the evolutions of the diffusivity and of the mechanical behavior of cement-based materials. The numerical results obtained have been confronted with experimental tests and are encouraging.

The possible benefits of the present work are multiple. First, the homogenization schemes proposed, such as the MCSA estimate, appear well suited for cementitious materials but are also of potential interest for other kinds of composites (e.g. porous media, granular materials). Second, the analytical multi-scale approach can be employed for computing the elastic and diffusive properties of any cement paste or mortar, which composition is accurately known, and their evolution with time. It furthermore requires very few parameters and is therefore useful for engineering applications. Finally, the chemo-mechanical simulations performed with the aid of this deductive model can be easily applied to other cement pastes and mortars. Moreover, the numerical results are instructive and help for better understanding the mechanisms of degradation. For instance, they clearly show the detrimental impact of Portlandite dissolution and of the progressive CSH decalcification on the elastic and diffusive properties of HCP.

## 15.2 Proposals for future research

The models and simulations proposed in the manuscript may obviously be further improved. Many interesting paths for future ameliorations can be envisaged. Double-inclusion type models have been shown to be of interest for their simplicity and versatility but they could be further developed as proved by the proposed derivation of a modified DIM. Recent progress in analytical techniques of homogenization (e.g. Berryman 2006; Duan et al. 2006) may for instance be very promising for predicting with better accuracy the effective properties of cement-based materials.

The prediction of the non-linear mechanical behavior of cement-based materials needs to be improved. For this purpose, it would be desirable to develop and implement a more advanced damage model, including phenomena such as plasticity or creep. The integration of a non-local formulation is also central to get better estimations of the post-peak behavior of the damaged material.

The chemo-mechanical simulations presented in the thesis are promising. Still, some more work should be done. Important aspects of the chemical degradation process, such as the progressive CSH decalcification, could be described more thoroughly. The retroactive effects of cracks on the chemical degradation have also to be taken into account in order to reproduce fully coupled chemo-mechanical experiments (Le Bellégo 2003; Schneider and Chen 2005). This numerical work should then be extended to chemical attacks generating internal pressures and possibly microcracks, such as sulphatic attacks. It is also possible to extend the simulations to concrete and eventually to real underground structures.

### **15.3 Perspectives**

The present manuscript provides results that are particularly interesting in the context of nuclear waste disposal. But the present work is more generally justified by the increasing necessity of adopting coupled multi-physical approaches for the assessment of the lifetime of existing structures. In the perspective of concrete durability, more and more investigations are dedicated to coupled multi-physical problems, like the present one or thermo-hydro-mechanical ones (e.g. Gawin et al. 1999). This study put together with other approaches (e.g. Bary et al. 2007) could lead at term to the development of powerful prediction tools for the durability of concrete facilities. It constitutes a huge task because of the necessity of solving thorny issues, such as unsaturated conditions. These tools would then find very wide industrial applications, from nuclear reactors to CO<sub>2</sub> storage.

## REFERENCES

- Adenot, F. (1992). "Durabilité du Béton: Caractérisation et Modélisation des Processus Physiques et Chimiques de Dégradation du Ciment," PhD thesis, Université Orléans, France.
- Adenot, F., and Buil, M. (1992). "Modelling of the corrosion of the cement paste by deionized water." *Cem. Concr. Res.*, 22(2-3), 489-496.
- Baroghel-Bouny, V. (1994). "Caractérisation des pâtes de ciment et des bétons. Méthodes, analyse et interprétations," PhD thesis, LCPC, France.
- Bary, B. (2006). "Simplified coupled chemo-mechanical modeling of cement pastes behavior subjected to combined leaching and external sulfate attack." *Submitted to Int. J. Num. Ana. Meth. Geomech.*
- Bary, B., and Béjaoui, S. (2006). "Assessment of diffusive and mechanical properties of hardened cement pastes using a multi-coated sphere assemblage model." *Cem. Concr. Res.*, 36(2), 245-258.
- Bary, B., Durand, S., Ranc, G., and Carpentier, O. "A coupled thermo-hygro-mechanical model for concrete subjected to moderate heating." *CONSEC'07*, Tours, France, June 4-6 2007.
- Bear, J., and Bachmat, Y. (1991). "Introduction to modeling of transport phenomena in porous media."
- Béjaoui, S., and Bary, B. (2007). "Modeling of the link between microstructure and effective diffusivity of cement pastes using a simplified composite model." *Cem. Concr. Res.*, 37(3), 469.
- Béjaoui, S., Bary, B., Nitsche, S., Chaudanson, D., and Blanc, C. (2006). "Experimental and modeling studies of the link between microstructure and effective diffusivity of cement pastes." *Rev. Eur. Gén. Civ.*, 10(9), 1073-1106.
- Bentz, D. P. (1997). "Three-Dimensional Computer simulation of Portland Cement Hydration and Microstructure Development." *J. Am. Ceram. Soc.*, 80(1), 3-21.
- Bentz, D. P., Mizell, S., Satterfield, S. G., Devaney, J. E., George, W., Ketcham, P. M., Graham, J. R., Porterfield, J. E., Quenard, D. A., Vallee, F., and Sallee, H. (2002). "The visible cement data set." *J. Res. Natl. Inst. Stand. Technol.*, 107, 137-148.
- Benveniste, Y. (1987). "A new approach to the application of Mori-Tanaka's theory in composite materials." *Mech. Mater.*, 6(2), 147-157.
- Beran, M. (1965). *Nuovo Cim.*, 38, 771-782.
- Bergman, D. J. (1976). "Calculation of bounds for some average bulk properties of composite materials." *Phys. Rev. B*, 14, 4304-4312.
- Bernard, O., Ulm, F. J., and Lemarchand, E. (2003). "A multiscale micromechanics-hydration model for the early-age elastic properties of cement-based materials." *Cem. Concr. Res.*, 33, 1293-1309.
- Berryman, J. G. (2005). "Bounds and estimates for transport coefficients of random and porous media with high contrasts." *J. Appl. Phys.*, 97(6), 1-11.
- Berryman, J. G. (2006). "Measures of microstructure to improve estimates and bounds on elastic constants and transport coefficients in heterogeneous media." *Mech. Mater.*, 38(8-10), 732-747.
- Berryman, J. G., and Berge, P. A. (1996). "Critique of two explicit schemes for estimating elastic properties of multiphase composites." *Mech. Mater.*, 22(2), 149.

- Bohn, R. B., and Garboczi, E. J. (2003). "User manual for finite element and finite difference programs: a parallel version of NIST IR 6269." NIST Internal Report.
- Boumiz, A., Sorrentino, D., Vernet, C., and Cohen Tenoudji, F. "Modelling the development of the elastic moduli as a function of the degree of hydration of cement pastes and mortars." *2nd RILEM Workshop on Hydration and Setting*, Dijon, France.
- Bourdette, B. (1994). "Durabilité du mortier, prise en compte des auréoles de transition dans la caractérisation et la modélisation des processus physiques et chimiques d'altération," PhD Thesis, INSA de Toulouse, France.
- Broadbent, S. R., and Hammersley, J. M. (1957). "Percolation processes. I. Crystals and mazes," *Proc. Camb. Phil. Soc.*, 53, 629.
- Brown, P., and Hooton, R. D. (2002). "Ettringite and thaumasite formation in laboratory concretes prepared using sulfate-resisting cements." *Cem. Concr. Compos.*, 24(3-4), 361.
- Bruggeman, D. A. G. (1935). "Berechnung verschiedener physikalischer Konstanten von heterogenen Substanzen: I. Dielectrizitätskonstanen und Leitfähigkeiten der Mischkörper aus Isotropen Substanzen." *Ann. Phys. (Leipzig)*, 24, 636-679.
- Budiansky, B., and O'Connell, R. J. (1976). "Elastic moduli of a cracked solid." *Int. J. Solids Struct.*, 12, 81-97.
- Burlion, N., Bernard, D., and Chen, D. (2006). "X-ray microtomography: Application to microstructure analysis of a cementitious material during leaching process." *Cem. Concr. Res.*, 36(2), 346-357.
- Carde, C. (1996). "Caractérisation et modélisation de l'altération des propriétés mécaniques due à la lixiviation des matériaux cimentaires," PhD Thesis, INSA de Toulouse, France.
- Caré, S., and Hervé, E. (2004). "Application of a n-phase model to the diffusion coefficient of chloride in mortar." *Transp. Por. Med.*, 56(2), 119-135.
- Cazzani, A., and Rovati, M. (2003). "Extrema of Young's modulus for cubic and transversely isotropic solids." *Int. J. Solids Struct.*, 40(7), 1713-1744.
- Christensen, R. M. (1990). "A critical evaluation for a class of micro-mechanics models." *J. Mech. Phys. Solids*, 38(3), 379.
- Christensen, R. M. (2005). "Exploration of ductile, brittle failure characteristics through a two-parameter yield/failure criterion." *Mater. Sci. Eng. A*, 394(1-2), 417.
- Christensen, R. M., and Lo, K. H. (1979). "Solutions for effective shear properties in 3 phase sphere and cylinder models." *J. Mech. Phys. Solids*, 27(4), 315-330.
- Constantinides, G., and Ulm, F.-J. (2004). "The effect of two types of C-S-H on the elasticity of cement-based materials: Results from nanoindentation and micromechanical modeling." *Cem. Concr. Res.*, 34(1), 67-80.
- Cormery, F., and Weleman, H. (2002). "A critical review of some damage models with unilateral effect." *Mech. Res. Commun.*, 29(5), 391-395.
- Cui, L., and Cahyadi, J. H. (2001). "Permeability and pore structure of OPC paste." *Cem. Concr. Res.*, 31, 277-282.
- Daimon, M., Abo-El-Enein, S. A., Hosaka, G., Goto, S., and Kondo, R. (1977). "Pore structure of calcium silicate hydrate in hydrated tricalcium silicate." *J. Am. Ceram. Soc.*, 60, 110-114.
- Damidot, D., Velez, K., and Sorrentino, F. "Characterisation of Interstitial Zone (ITZ) of high performance cement by nanoindentation technique." *11th Int. Conference on Cement Chemistry*, Durham, South Africa.

- De Vree, J., Brekelmans, W., and Van Gils, M. (1995). "Comparison of nonlocal approaches in continuum damage mechanics." *Comp. Struct.*, 55, 581-588.
- Delagrave, A., Marchand, J., and Pigeon, M. (1998). "Influence of microstructure on the tritiated water diffusivity of mortars." *Adv. Cem. Res.*, 7(2), 60-65.
- Desmorat, R., Gatuingt, F., and Ragueneau, F. (2007). "Nonlocal anisotropic damage model and related computational aspects for quasi-brittle materials." *Eng. Fract. Mech.*, 74(10), 1539.
- Deudé, V., Dormieux, L., Kondo, D., and Pensée, V. (2002). "Propriétés élastiques non lineaires d'un milieu mésos fissuré." *C. R. Meca.*, 330(8), 587.
- Diamond, S. (2000). "Mercury porosimetry—an inappropriate method for measurement of pore size distributions in cement-based materials." *Cem. Concr. Res.*, 30, 1517-1525.
- Dormieux, L., Kondo, D., and Ulm, F. J. (2006). *Microporomechanics*, John Wiley & Sons, Chichester.
- Douglas, J. F., and Garboczi, E. J. (1995). "Intrinsic viscosity and the polarization of particles having a wide range of shapes." *Adv. Chem. Phys.*, 91(85-153).
- Duan, H. L., Jiao, Y., Yi, X., Huang, Z. P., and Wang, J. (2006). "Solutions of inhomogeneity problems with graded shells and application to core-shell nanoparticles and composites." *J. Mech. Phys. Solids*, 54(7), 1401.
- Dullien, F. A. L. (1992). *Porous Media, Fluid Transport and Pore Structure*, Academic Press.
- Eshelby, J. D. (1957). "The determination of the elastic field of an ellipsoidal inclusion and related problems." *Proc. Roy. Soc. London Series A-Math. Phys. Sci.*, 241(1226), 376-396.
- Feng, X.-Q., Li, J.-Y., Ma, L., and Yu, S.-W. (2003a). "Analysis on interaction of numerous microcracks." *Comput. Mater. Sci.*, 28(3-4), 454.
- Feng, X.-Q., Li, J.-Y., and Yu, S.-W. (2003b). "A simple method for calculating interaction of numerous microcracks and its applications." *Int. J. Solids Struct.*, 40(2), 447.
- Gallé, C. (2001). "Effect of drying on cement-based materials pore structure as identified by mercury intrusion porosimetry: A comparative study between oven-, vacuum-, and freeze-drying." *Cem. Concr. Res.*, 31(10), 1467-1477.
- Gallé, C., Peycelon, H., and Le Bescop, P. (2004). "Effect of an accelerated chemical degradation on water permeability and pore structure of cement-based materials." *Adv. Cem. Res.*, 16(3), 105-114.
- Garboczi, E. J. (1998). "Finite element and finite difference programs for computing the linear electric and elastic properties of digital images of random materials." *NISTIR 6269*, U.S. Department of Commerce/ NIST.
- Garboczi, E. J. (2002). "Three-dimensional mathematical analysis of particle shape using X-ray tomography and spherical harmonics: Application to aggregates used in concrete." *Cem. Concr. Res.*, 32(10), 1621.
- Garboczi, E. J., and Bentz, D. P. (1997). "Analytical formulas for interfacial transition zone properties." *Adv. Cem. Bas. Mater.*, 6(3-4), 99.
- Garboczi, E. J., and Bentz, D. P. (2001). "The effect of statistical fluctuation, finite size error, and digital resolution on the phase percolation and transport properties of the NIST cement hydration model." *Cem. Concr. Res.*, 31(10), 1501.
- Garboczi, E. J., and Berryman, J. G. (2001). "Elastic moduli of a material containing composite inclusions: effective medium theory and finite element computations." *Mech. Mater.*, 33(8), 455.

- Garboczi, E. J., and Bullard, J. W. (2004). "Shape analysis of a reference cement." *Cem. Concr. Res.*, 34(10), 1933.
- Garboczi, E. J., Snyder, K. A., Douglas, J. F., and Thorpe, M. F. (1995). "Geometrical percolation threshold of overlapping ellipsoids." *Phys. Rev. E*, 52(1), 819-828.
- Gawin, D., Majorana, C. E., and Schrefler, B. A. (1999). "Numerical analysis of hygro-thermal behaviour and damage of concrete at high temperature." *Mech. Cohesive-Frictional Mater.*, 4(1), 37-74.
- Gérard, B. (1996). "Contribution des couplages mécanique-chimie-transfert dans la tenue long terme des ouvrages de stockage de déchets radioactifs," PhD Thesis, ENS Cachan, France.
- Gilormini, P. (2001). "Realizable compressibility and conductivity in isotropic two-phase composites." *C. R. Acad. Sci. Paris Ser. IIB*, 329, 851-855.
- Halphen, B., and Nguyen, Q. (1975). "Sur les matériaux standards généralisés." *J. Mech. Th. Appl.*, 14(39-63).
- Hashin, Z. (1988). "The differential scheme and its application to cracked materials." *J. Mech. Phys. Solids*, 36(6), 719.
- Hashin, Z., and Monteiro, P. J. M. (2002). "An inverse method to determine the elastic properties of the interphase between the aggregate and the cement paste." *Cem. Concr. Res.*, 32(8), 1291.
- Hashin, Z., and Shtrikman, S. (1962). "A variational approach to the theory of the elastic behaviour of polycrystals." *J. Mech. Phys. Solids*, 10(4), 343-352.
- He, Q.-C., and Curnier, A. (1995). "A more fundamental approach to damaged elastic stress-strain relations." *Int. J. Solids Struct.*, 32(10), 1433-1457.
- Hervé, E. (2002). "Thermal and thermoelastic behaviour of multiply coated inclusion-reinforced composites." *Int. J. Solids Struct.*, 39(4), 1041.
- Hervé, E., and Zaoui, A. (1993). "N-layered inclusion-based micromechanical modeling." *Int. J. Eng. Sci.*, 31(1), 1-10.
- Heukamp, F. H. (2002). "Chemomechanics of calcium leaching of cement-based materials at different scales: the role of CH dissolution and CSH degradation on strength and durability performance of materials and structure," PhD Thesis, Cambridge.
- Heukamp, F. H., Ulm, F.-J., and Germaine, J. T. (2005). "Does calcium leaching increase ductility of cementitious materials? Evidence from direct tensile tests." *J. Mater. Civ. Eng.*, 307.
- Hill, R. (1963). "Elastic properties of reinforced solids: some theoretical principles." *J. Mech. Phys. Solids*, 11, 357.
- Holzer, L., Gasser, P., and Münch, B. "Three Dimensional analysis of the Pore-network in cement Pastes using FIB-nanotomography." *Nanostructure*, Monte Verità - Switzerland.
- Hori, M., and Nemat-Nasser, S. (1993). "Double-inclusion model and overall moduli of multi-phase composites." *Mech. Mater.*, 14(3), 189.
- Hu, G. K., and Weng, G. J. (2000). "The connections between the double-inclusion model and the Ponte Castaneda-Willis, Mori-Tanaka, and Kuster-Toksoz models." *Mech. Mater.*, 32(8), 495-503.
- Huang, Y., Hu, K. X., and Chandra, A. (1994a). "A generalized self-consistent mechanics method for microcracked solids." *J. Mech. Phys. Solids*, 42(8), 1273.
- Huang, Y., Hu, K. X., and Chandra, A. (1994b). "Several variations of the generalized self-consistent method for hybrid composites." *Compos. Sci. Tech.*, 52(1), 19.

- Igarashi, S., Kawamura, M., and Watanabe, A. (2004). "Analysis of cement pastes and mortars by a combination of backscatter-based SEM image analysis and calculations based on the Powers model." *Cem. Concr. Compos.*, 26(8), 977-985.
- Jacobsen, S., Marchand, J., and Boisvert, L. (1996). "Effect of Cracking and Healing on Chloride Transport in OPC concrete." *Cem. Concr. Res.*, 26(6), 869-881.
- Jennings, H. M. (2000). "A model for the microstructure of calcium silicate hydrates in cement paste." *Cem. Concr. Res.*, 30(1), 101-116.
- Jennings, H. M., Thomas, J. J., Gevrenov, J. S., Constantinides, G., and Ulm, F.-J. (2007). "A multi-technique investigation of the nanoporosity of cement paste." *Cem. Concr. Res.*, 37(3), 329.
- Kachanov, M. (1987). "Elastic solids with many cracks: A simple method of analysis." *Int. J. Solids Struct.*, 23(1), 23.
- Kachanov, M. (1992). "Effective elastic properties of cracked solids: critical review of some basic concepts." *Appl. Mech. Rev.*, 45, 304-335.
- Kamali, S. (2003). "Comportement et simulation des matériaux cimentaires en environnements agressifs: lixiviation et température," PhD Thesis, ENS Cachan, France.
- Katz, A. J., and Thompson, A. H. (1987). "Prediction of rock electrical conductivity from mercury injection measurements." *J. Geophys. Res.*, 92(B1), 599-607.
- Kirkpatrick, S. (1971). "Classical transport in disordered media: scaling and effective-medium theories." *Phys. Rev. Lett.*, 27, 1722-1725.
- Kirkpatrick, S. (1973). "Percolation and conduction." *Rev. Mod. Phys.*, 45, 574-588.
- Krajcinovic, D. (1996). *Damage mechanics*, North-Holland, Amsterdam.
- Kuhl, D., Bangert, F., and Meschke, G. (2004a). "Coupled chemo-mechanical deterioration of cementitious materials Part II: Numerical methods and simulations." *Int. J. Solids Struct.*, 41(1), 41-67.
- Kuhl, D., Bangert, F., and Meschke, G. (2004b). "Coupled chemo-mechanical deterioration of cementitious materials. Part I: Modeling." *Int. J. Solids Struct.*, 41(1), 15-40.
- Kuster, G. T., and Toksoz, M. N. (1974). "Velocity and attenuation of seismic waves in two-phase media: Part I. Theoretical formulation." *Geophys.*, 39(5), 587-606.
- Ladevèze, P. (1983). "Sur une théorie de l'endommagement anisotrope." 34, Laboratoire de Mécanique et Technologie, Cachan, France.
- Landauer, R. (1952). "The electrical resistance of binary metallic mixtures." *J. Appl. Phys.*, 23, 779-784.
- Le Bellégo, C. (2001). "Couplages chimie-mecanique dans les structures en béton attaquées par l'eau: Etude expérimentale et analyse numérique," PhD Thesis, ENS Cachan, France.
- Le Bellégo, C., Pijaudier-Cabot, G., Gérard, B., Dubé, J. F., and Molez, L. (2003). "Coupled mechanical and chemical damage in calcium leached cementitious structures." *J. Eng. Mech.*, 129(3), 333-341.
- Lorentz, E., and Andrieux, S. (2003). "Analysis of non-local models through energetic formulations." *Int. J. Solids Struct.*, 40(12), 2905.
- Lu, B., and Torquato, S. (1992). "Nearest-surface distribution functions for polydispersed particle systems." *Phys. Rev. A*, 45(8), 5530-5544.
- Lutz, M. P., Monteiro, P. J. M., and Zimmerman, R. W. (1997). "Inhomogeneous interfacial transition zone model for the bulk modulus of mortar." *Cem. Concr. Res.*, 27(7), 1113-1122.

- Lutz, M. P., and Zimmerman, R. W. (2005). "Effect of an inhomogeneous interphase zone on the bulk modulus and conductivity of a particulate composite." *Int. J. Solids Struct.*, 42(2), 429.
- Ma, H. L., Hu, G. K., and Huang, Z. P. (2004). "A micromechanical method for particulate composites with finite particle concentration." *Mech. Mater.*, 36(4), 359-368.
- Marigo, J. J. (1985). "Modelling of brittle and fatigue damage for elastic material by growth of microvoids." *Eng. Frac. Mech.*, 21(4), 861-874.
- Mazars, J. (1984). "Application de la mécanique de l'endommagement au comportement non linéaire et à la rupture du béton de structure," PhD Thesis, Université de Paris VI, France.
- Mazars, J. (1985). "Description of micro- and macroscale damage of concrete structures." *Eng. Frac. Mech.*, 25(5-6), 729-737.
- McLachlan, D. S. (1987). "An equation for the conductivity of binary mixtures with anisotropic grain structures." *J. Phys. C: Solid State Phys.*, 20, 865-877.
- Mélé, P., Marceau, S., Brown, D., and Albérola, N. D. (2005). "Consequences of the aggregation and the percolation of fillers on the viscoelastic behaviour of nanocomposites." *C. R. Meca.*, 333, 155-161.
- Milton, G. W. (1985). *Commun. Math. Phys.*, 99, 463-500.
- Milton, G. W. (2002). *The theory of composites*, Cambridge University Press, New York.
- Mindess, S., and Young, J. F. (1981). "Concrete."
- Montarnal, P., Bengaouer, A., Chavant, C., and Loth, L. "ALLIANCES: Simulation Platform for Nuclear Waste Disposal." *CMWR'06*, Copenhagen, Denmark.
- Montarnal, P., Mügler, C., Colin, J., Descotes, M., Dimier, A., and Jacquot, E. (2007). "Presentation and use of a reactive transport code in porous media." *to appear in Phys. Chem. Earth*.
- Monteiro, P. J. M., and Chang, C. T. (1995). "The elastic moduli of calcium hydroxide." *Cem. Concr. Res.*, 25(8), 1605-1609.
- Monteiro, P. J. M., and Ostertag, C. P. (1989). "Analysis of the aggregate-cement paste interface using grazing incidence X-ray scattering." *Cem. Concr. Res.*, 19(6), 987.
- Moranville, M., Kamali, S., and Guillon, E. (2004). "Physicochemical equilibria of cement-based materials in aggressive environments--experiment and modeling." *Cem. Concr. Res.*, 34(9), 1569.
- Mura, T. (1987). *Micromechanics of defects in solids*, Martinus Nijhoff, The Hague.
- Nemat-Nasser, S., and Hori, M. (1993). *Micromechanics: overall properties of heterogeneous solids*, Elsevier, Amsterdam.
- Neubauer, C. M., Jennings, H. M., and Garboczi, E. J. (1996). "A three-phase model of the elastic and shrinkage properties of mortar." *Adv. Cem. Bas. Mater.*, 4(1), 6.
- Nguyen, Q. (2000). *Stability and Nonlinear Solid Mechanics*, Wiley, Chichester.
- Nguyen, V. H. (2005). "Couplage dégradation chimique - comportement en compression du béton." PhD Thesis, ENPC, France.
- Nguyen, V. H., Nedjar, B., Colina, H., and Torrenti, J. M. (2006). "A separation of scales homogenization analysis for the modelling of calcium leaching in concrete." *Comput. Meth. Appl. Mech. Eng.*, 195(52), 7196-7210.
- Norris, A. N. (1989). "An examination of the Mori-Tanaka effective medium approximation for multiphase composites." *ASME J. Appl. Mech.*, 56, 83-88.

- Nozourtier-Mazauric, E. (2004). "Prise en compte des variations de porosité dans le couplage transport-chimie mis en œuvre dans ALLIANCES." Technical note CEA.
- Oh, B. H., and Jang, S. Y. (2004). "Prediction of diffusivity of concrete based on simple analytic equations." *Cem. Concr. Res.*, 34(3), 463.
- Papa, E. (1993). "A damage model for concrete subjected to fatigue loading." *Eur. J. Mech. A/Solids*, 12, 429-440.
- Pensée, V. (2003). "Contribution de la micromécanique à la modélisation tridimensionnelle de l'endommagement par mésofissuration," PhD Thesis, University Lille I, France.
- Pensée, V., and Kondo, D. (2003). "Micromechanics of anisotropic brittle damage: comparative analysis between a stress based and a strain based formulation." *Mech. Mater.*, 35(8), 747-761.
- Pensée, V., and He, Q.-C. (2007). "Generalized self-consistent estimation of the apparent isotropic elastic moduli and minimum representative volume element size of heterogeneous media." *Int. J. Solids Struct.*, 44, 2225-2243.
- Pham, D. C. (1997). *Acta Mech.*, 121, 177-190.
- Pijaudier-Cabot, G., and Bazant, Z. P. (1987). "Non local damage theory." *J. Eng. Mech.*, 113, 1512-1533.
- Pivonka, P., Hellmich, C., and Smith, D. (2004). "Microscopic effects on chloride diffusivity of cement pastes - a scale-transition analysis", *Cem. Concr. Res.*, 34(12), 2251-2260.
- Planel, D. (2002). "Les Effets Couplés de la Précipitation d'Espèces Secondaires sur le Comportement Mécanique et la Dégradation Chimique des Bétons," PhD thesis, Université de Marne la Vallée, France.
- Pólya, G., and Szegő, G. (1951). *Isoperimetric Inequalities in Mathematical Physics*, Princeton University Press, Princeton.
- Ponte Castaneda, P., and Willis, J. R. (1995). "The effect of spatial distribution on the effective behavior of composite materials and cracked media." *J. Mech. Phys. Solids*, 43(12), 1919-1951.
- Powers, T. C. B., T.L. (1948). "Studies of the physical properties of hardened cement pastes." *J. Am. Concr. Inst.*, 43.
- Ramesh, G., E.D., S., and Chen, W. F. (1996). "Effect of transition zone on elastic moduli of concrete materials." *Cem. Concr. Res.*, 26, 611-622.
- Rattanasak, U., and Kendall, K. (2005). "Pore structure of cement/pozzolan composites by X-ray microtomography." *Cem. Concr. Res.*, 35(4), 637.
- Riccardi, A., and Montheillet, F. (1999). "A generalized self-consistent method for solids containing randomly oriented spheroidal inclusions." *Acta Mech.*, 133, 39-56.
- Richardson, I. G. (2000). "The nature of the hydration products in hardened cement pastes." *Cem. Concr. Compos.*, 22, 97-113.
- Richet, C., Pin, M., Adenot, F., Maury, J., Lalle, J. P., and Fokedey, C. (1997). "Amélioration de la fiabilité du modèle DIFFUZON." Technical note CEA.
- Rintoul, M. D., and Torquato, S. (1997). "Precise determination of the critical threshold and exponents in a three-dimensional continuum percolation model." *J. Phys. A*, 16.
- Roberts, A. P., and Garboczi, E. J. (2000). "Computation of the linear elastic properties of random porous materials with a wide variety of microstructure." *R. Soc. Proc. Math. Phys. Eng. Sci.*, 458, 1033-1054.

- Schneider, U., and Chen, S. W. (1998). "The Chemomechanical Effect and the Mechanochemical Effect on High-Performance Concrete Subjected to Stress Corrosion." *Cem. Concr. Res.*, 28(4), 509.
- Schneider, U., and Chen, S. W. (2005). "Deterioration of high-performance concrete subjected to attack by the combination of ammonium nitrate solution and flexure stress." *Cem. Concr. Res.*, 35(9), 1705.
- Scrivener, K. (2004). "Backscattered electron imaging of cementitious microstructures: understanding and quantification." *Cem. Concr. Compos.*, 26(8), 935-945.
- Scrivener, K. L., and Nematì, K. M. (1996). "The percolation of pore space in the cement paste/aggregate interfacial zone of concrete." *Cem. Concr. Res.*, 26(1), 35.
- Segurado, J., and Llorca, J. (2002). "A numerical approximation to the elastic properties of sphere-reinforced composites." *J. Mech. Phys. Solids*, 50(10), 2107.
- Shante, V. K. S., and Kirkpatrick, S. (1971). "An introduction to percolation theory." *Adv. Phys.*, 325-356.
- Shen, L., and Li, J. (2004). "A numerical simulation for effective elastic moduli of plates with various distributions and sizes of cracks." *Int. J. Solids Struct.*, 41(26), 7471.
- Shen, L., and Yi, S. (2001). "An effective inclusion model for effective moduli of heterogeneous materials with ellipsoidal inhomogeneities." *Int. J. Solids Struct.*, 38(32-33), 5789.
- Shodja, H. M., and Roumi, F. (2005). "Overall behavior of composites with periodic multi-inhomogeneities." *Mech. Mater.*, 37(2-3), 343.
- Shodja, H. M., and Sarvestani, A. S. (2001). "Elastic fields in double inhomogeneity by the equivalent inclusion method." *J. Appl. Mech.*, 68(3), 3-10.
- Stora, E., He, Q. C., and Bary, B. (2006a). "Influence of inclusion shapes on the effective linear elastic properties of hardened cement pastes." *Cem. Concr. Res.*, 36(7), 1330-1344.
- Stora, E., He, Q. C., and Bary, B. (2006b). "A mixed composite spheres assemblage model for the transport properties of random heterogeneous materials with high contrasts." *J. Appl. Phys.* 100(8), 084910.
- Stora, E., Bary, B., and He, Q.-C. (2007). "On estimating the transport properties of hardened cement pastes." Accepted for publication in *Transp. Por. Med.*
- Sun, Z., Garboczi, E. J., and Shah, S. P. (2007). "Modeling the elastic properties of concrete composites: Experiment, differential effective medium theory, and numerical simulation." *Cem. Concr. Compos.*, 29(1), 22.
- Taylor, H. F. W. (1997). *Cement Chemistry*, Thomas Telford, London.
- Tennis, P. D., and Jennings, H. M. (2000). "A model for two types of calcium silicate hydrate in the microstructure of Portland cement pastes." *Cem. Concr. Res.*, 30 (6), 855-863.
- Tognazzi, C. (1998). "Couplage fissuration-dégradation chimique dans les matériaux cimentaires: caractérisation et modélisation," INSA Toulouse.
- Torquato, S. (2001). *Random Heterogeneous Media: Microstructure and Macroscopic Properties*, Springer-Verlag, New York.
- Torquato, S., Donev, A., Evans, A. G., and Brinker, C. J. (2005). *J. Appl. Phys.*, 97(12), 1-5.
- van der Lee, J., and de Windt, L. (2002). "Chess tutorial and Cookbook, updated for version 3.0." ENSMP-CIG LHM/RD/02/13.
- van der Lee, J., de Windt, L., Lagneau, V., and Goblet, P. (2003). "Module-oriented modeling of reactive transport with HYTECH." *Comput. Geosci.*, 29(265-275).

- Velez, K., Maximilien, S., Damidot, D., Fantozzi, G., and Sorrentino, F. (2001). "Determination by nanoindentation of elastic modulus and hardness of pure constituents of Portland cement clinker." *Cem. Concr. Res.*, 31(4), 555.
- Wang, J. A., Lubliner, J., and Monteiro, P. J. T. (1988). "Effect of ice formation on the elastic moduli of cement paste and mortar." *Cem. Concr. Res.*, 18(6), 874-885.
- Wriggers, P., and Moftah, S. O. (2006). "Mesoscale models for concrete: Homogenisation and damage behaviour." *Finite Elements in Analysis and Design*, 42(7), 623.
- Wu, T. (1966). "The effect of inclusion shape on the elastic moduli of a two-phase material." *Int. J. Solids Struct.*, 2(1), 1-8.
- Yang, C. C. (1998). "Effect of the Transition Zone on the Elastic Moduli of Mortar." *Cem. Concr. Res.*, 28(5), 727.
- Yang, Z., Weiss, W. J., and Olek, J. (2006). "Water Transport in Concrete Damaged by Tensile Loading and Freeze-Thaw Cycling." *J. Mater. Civ. Eng.*, 18(3), 424-434.
- Ye, G. (2005). "Percolation of capillary pores in hardening cement pastes." *Cem. Concr. Res.*, 35(1), 167-176.
- Yeh, G. T., and Tripathi, V. S. (1989). "A critical evaluation of recent developments in hydrogeochemical transport models of reactive multichemical components." *Water Resour. Res.*, 25(1), 93-108.
- Zaoui, A. (1997). "Matériaux hétérogènes et composites, lecture notes Paris." Ecole Polytechnique.
- Zheng, Q. S., and Du, D. X. (2001). "An explicit and universally applicable estimate for the effective properties of multiphase composites which accounts for inclusion distribution." *J. Mech. Phys. Solids*, 49(11), 2765-2788.
- Zheng, Q. S., Zhao, Z. H., and Du, D. X. (2006). "Irreducible structure, symmetry and average of Eshelby's tensor fields in isotropic elasticity." *J. Mech. Phys. Solids*, 54(2), 368.
- Zhu, Q., Kondo, D., Shao, J., and Pensee, V. (2007). "Micromechanical modelling of anisotropic damage in brittle rocks and application." *Int. J. Rock Mech. Mining Sci.*, In Press.
- Zimmerman, R. W., King, M. S., and Monteiro, P. J. M. (1986). "The elastic moduli of mortar as a porous-granular material." *Cem. Concr. Res.*, 16(2), 239.